SVEUČILIŠTE U SPLITU

FAKULTET GRAĐEVINARSTVA, ARHITEKTURE I GEODEZIJE

Matej Šodan, mag.ing.aedif.

NUMERICAL MODEL WITH EMBEDDED STRONG DISCONTINUITIES AND STOCHASTIC IDENTIFICATION OF PARAMETERS IN MATERIAL FAILURE PROCESSES

Doctoral Dissertation

Split, 2025.

Matej Šodan, mag.ing.aedif.

Number: xxx

**This doctoral dissertation has been submitted for evaluation
to the University of Split, Faculty of Civil Engineering, Architecture and
Geodesy, for the purpose of obtaining the doctoral academic degree
in Technical Sciences, field of Fundamental Technical Sciences**

Supervisor (mentor): izv. prof. dr. sc. Mijo Nikolić

Committee for the assessment of doctoral dissertation:

<div align="right">

prof. dr. sc. Vedrana Kozulić

izv. prof. dr. sc. Hrvoje Smoljanović

prof. dr. sc. Vedrana Cvitanić

prof. dr. sc. Leo Škec

izv. prof. dr. sc. Nina Čeh

</div>

Committee for the doctoral dissertation defense:

prof. dr. sc. Xxxxxxxxx _____

prof. dr. sc. Xxxxxxxxx _____

prof. dr. sc. Xxxxxxxxxx _____

prof. dr. sc. Xxxxxxxxxx _____

izv. prof. dr. sc. Xxxxxxx_____

The dissertation has been defended on the xx.xx.20xx

Secretary:

Saša Delić, dipl. iur.

The dissertation contains:

162 pages of text

44 figures

4 tables

94 references

Mottos, dedications, acknowledgments, etc…

Mottos, dedications, acknowledgments, etc…

Matej Šodan (dipl. ing. građ.)

Numerical model with embedded strong discontinuities and stochastic identification of parameters in material failure processes

Abstract:

The subject of this dissertation is the problem of crack initiation and propagation in structural materials. Analysis of material fracture processes represents an complex problem due to the heterogeneous structure of materials and nonlinear laws that govern their behavior. The aim of this work is to improve existing knowledge and methods for analyzing these phenomena and thus contribute to improving the quality and safety of existing and future structures through the development of a comprehensive methodological framework that includes an advanced numerical model and methodology for parameter identification.

For the analysis of physical fracture processes, a two-dimensional model based on the finite element method has been developed that uses the embedded strong discontinuities method (ED-FEM) for simulating crack initiation and propagation. This method models cracks locally as a jump in the displacement field within each finite element, which makes results independent of element mesh size. A damage model based on exponential softening law has been incorporated to describe crack behavior and energy dissipation. The time of initiation as well as the location and orientation of cracks are defined through implemented fracture criteria: the Rankine criterion and the Maximum shear stress criterion, which enables simulation of fracture under tensile and compressive loading. These criteria depend only on the stress state within individual finite elements, thereby achieving physical relevance of the approach. To enable simulation of more complex heterogeneous structures at the mesostructural level, which includes different constituents of various dimensions and material properties, algorithms for clustering and tracking of crack initiation and propagation have been developed and incorporated within the model. These algorithms enable global tracking of material fracture, formation of macrocracks, their continuous propagation and interconnection, and consequently the final failure of the heterogeneous structure.

Given the significant dependence of fracture simulation results on the values of input model parameters, a methodology for their reliable identification has been developed. A stochastic approach using the inverse Bayesian method has been selected, which treats unknown parameters as random variables described by probability distributions. The procedure is based on defining the prior distribution of unknown parameter values and updating it based on Bayes' theorem of conditional probability through selected experimental measurements and numerical model results. Since these measurements do not need to be directly related to the parameters, the possibility of using simple measurements such as horizontal and vertical displacements has been investigated. The method enables the inclusion of uncertainties in the identification process, the existence of multiple solution combinations, and assessment of the reliability of obtained results. Since analytical solution of the posterior distribution is usually not feasible, the Markov chain Monte Carlo (MCMC) method has been applied. Within this method, the application of various mathematical proxy models that enable efficient and precise approximation of numerical model solutions has been investigated. General polynomial chaos expansion (gPCE) and neural networks models are applied, including autoencoder models for reducing the dimensionality of measurement data. The selection of the optimal approach for parameter identification has been

examined on simple and complex fracture examples using synthetic measurements, through comparison of computational efficiency and accuracy of identified results.

The developed numerical model and parameter identification methodology have been verified on experimental measurements conducted on specimens of aluminium alloy 6060. Since aluminium is a ductile material, the developed numerical model has been modified and extended with implementation of a linear hardening law based on the Von Mises yield criterion and a deformation model with exponential softening law to describe crack behavior. Parameter identification was conducted using uniaxial tensile tests in two phases. In the first phase, elastic material parameters were identified on a rectangular specimen. In the second phase, these identified parameters were adopted and elastoplastic and fracture parameters were identified on a single-notched dogbone specimen. The used measurements, force-displacement and lateral deformation, were verified before conducting the experiment using Sobol sensitivity analysis to confirm their suitability for identification. The identification results were then validated to confirm their accuracy and applicability. For this purpose, results of numerical simulations with identified parameter values were compared with experimental measurements that included displacement and strain field values of the single-notched dogbone specimen through digital image correlation (DIC), as well as comparison of the force-displacement curve for a double-notched dogbone specimen.

Keywords: Fracture propagation problem, Finite element method, Embedded strong discontinuity, Stohastic identification, Bayesian inference, proxy modelling, experimental testing.

Matej Šodan (dipl. ing. građ.)

Numerički model s ugrađenim jakim diskontinuitetima i stohastička identifikacija parametara u procesima loma materijala

Sažetak:

Predmet ovog rada je problem inicijacije i propagacije pukotina u konstruktivnim materijalima. Analiza procesa sloma materijala predstavlja složen problem zbog heterogene strukture materijala i nelinearnih zakona koji upravljaju njegovim ponašanjem. Cilj ovog rada je poboljšanje postojećih znanja i metoda za analizu ovih fenomena te tako pridonijeti poboljšanju kvalitete i sigurnosti postojećih i budućih konstrukcija kroz razvoj sveobuhvatnog metodološkog okvira koji uključuje napredni numerički model i metodologiju za identifikaciju parametara.

Za analizu fizikalnih procesa sloma razvijen je dvodimenzionalni model temeljen na metodi konačnih elemenata koji koristi metodu ugrađenih jakih diskontinuiteta (ED-FEM) za simulaciju inicijacije i propagacije pukotina. Ova metoda modelira pukotine lokalno kao skok u polju pomaka unutar svakog konačnog elementa, što čini rezultate neovisnima o veličini mreže elemenata. Ugrađen je model oštećenja temeljen na eksponencijalnom zakonu omekšavanja za opisivanje ponašanja pukotina i disipacije energije. Vrijeme inicijacije kao i lokacija i orijentacija pukotina definirani su kroz implementirane kriterije sloma: Rankineov kriterij i kriterij maksimalnog posmičnog naprezanja, što omogućava simulaciju sloma pod vlačnim i tlačnim opterećenjem. Ovi kriteriji ovise samo o stanju naprezanja unutar pojedinih konačnih elemenata, čime se postiže fizikalna relevantnost pristupa. Za omogućavanje simulacije složenijih heterogenih struktura na mezostruktualnoj razini, koja uključuje različite konstituente različitih dimenzija i materijalnih svojstava, razvijeni su i ugrađeni algoritmi za grupiranje i praćenje inicijacije i propagacije pukotina unutar modela. Ovi algoritmi omogućavaju globalno praćenje sloma materijala, formiranje makropukotina, njihovu kontinuiranu propagaciju i međusobno povezivanje, te posljedično konačno otkazivanje heterogene strukture.

S obzirom na značajnu ovisnost rezultata simulacije sloma o vrijednostima ulaznih parametara modela, razvijena je metodologija za njihovu pouzdanu identifikaciju. Odabran je stohastički pristup koristeći inverznu Bayesovu metodu koja tretira nepoznate parametre kao slučajne varijable opisane distribucijama vjerojatnosti. Postupak se temelji na definiranju prior distribucija nepoznatih vrijednosti parametara i njihovom ažuriranju na temelju Bayesovog teorema uvjetne vjerojatnosti kroz odabrana eksperimentalna mjerenja i rezultate numeričkog modela. Budući da ova mjerenja ne moraju biti izravno povezana s parametrima, istražena je mogućnost korištenja jednostavnih mjerenja poput horizontalnih i vertikalnih pomaka. Metoda omogućava uključivanje nesigurnosti u proces identifikacije, postojanje višestrukih kombinacija rješenja i procjenu pouzdanosti dobivenih rezultata. S obzirom na to da analitičko rješenje posterior distribucije obično nije izvedivo, primijenjena je metoda Markov lanac Monte Carlo (MCMC). Unutar ove metode je istražena primjena različitih matematičkih proxy modela koji omogućavaju efikasnu i preciznu aproksimaciju rješenja numeričkog modela. Primijenjeni su modeli generalnog polinomnog kaosa (gPCE) i neuronskih mreža, uključujući autoencoder modele za reduciranje dimenzionalnosti mjernih podataka. Odabir optimalnog pristupa za identifikaciju parametara ispitan je na jednostavnim i složenim primjerima sloma koristeći sintetička mjerenja, kroz usporedbu računalne efikasnosti i točnosti identificiranih rezultata.

Razvijeni numerički model i metodologija identifikacije parametara verificirani su na eksperimentalnim mjerenjima provedenim na uzorcima aluminijske legure 6060. Budući da je aluminij duktilan materijal, razvijeni numerički model je modificiran i proširen implementacijom linearnog zakona očvršćavanja temeljenog na von Misesovom kriteriju popuštanja i deformacijskog modela s eksponencijalnim zakonom omekšavanja za opisivanje ponašanja pukotina. Identifikacija parametara provedena je koristeći jednoosne vlačne testove u dvije faze. U prvoj fazi identificirani su elastični parametri materijala na pravokutnom uzorku. U drugoj fazi, ti identificirani parametri su prihvaćeni te se provela identifikacija elastoplastičnih i parametra loma na uzorku tipa "dogbone" s jednim zarezom. Korištena mjerenja, sila-pomak i bočna deformacija, verificirana su prije provođenja eksperimenta koristeći Sobolovu analizu osjetljivosti za potvrdu njihove prikladnosti za identifikaciju. Rezultati identifikacije su zatim verificirani radi potvrde njihove točnosti i primjenjivosti. U tu svrhu, rezultati numeričkih simulacija s identificiranim vrijednostima parametara uspoređeni su s eksperimentalnim mjerenjima koja su uključivala vrijednosti polja pomaka i polja deformacija "dogbone" uzorka s jednim zarezom kroz digitalnu korelaciju slike (DIC), kao i usporedbu krivulje sila-pomak za "dogbone" uzorak s dva zareza.

Ključne riječi: Problem propagacije pukotina, Metoda konačnih elemenata, Metoda ugrađenih jakih diskontinuiteta, Stohastička identifikacija, inverzna Bayesova metoda, Proxy modeliranje, Eksperimentalno testiranje.

List of appended papers and my contributions

The thesis is based on three papers (see Appendix), referred by Roman numerals in the text of the thesis:

No.	Paper Title	SJR Rank*
I	**Šodan, Matej**; Stanić, Andjelka; Nikolić, Mijo Enhanced solid element model with embedded strong discontinuity for representation of mesoscale quasi-brittle failure // International journal of fracture, 248 (2024), 1-25. doi: 10.1007/s10704-024-00797-0	Q1
II	**Šodan, Matej**; Urbanics, András; Friedman, Noémi; Stanic, Andjelka; Nikolić, Mijo Comparison of Machine Learning and gPC-based proxy solutions for an efficient Bayesian identification of fracture parameters // Computer methods in applied mechanics and engineering, 436 (2025), 117686, 31. doi: 10.1016/j.cma.2024.117686	Q1
III	**Šodan, Matej**; Divić, Vladimir; Friedman, Noémi; Nikolić, Mijo Investigating Bayesian Parameter Identification Using Non-Standard Laboratory Specimens // Applied sciences (Basel), 15 (2025), 11; 6194, 28. doi: 10.3390/app15116194	Q2

*Quartiles are determined for the year of 2024.

My contributions in papers are listed below:

- Development and programming of numerical model,
- Participation in design and execution of virtual tests,
- Participation in analysis of numerical results,
- Participation in development and programming of stochastic methodology for parameter identification,
- Running computations on high-performance cluster computer,
- Writing program scripts for large-scale data processing,
- Participation in design and execution of fracture parameter identification procedures,
- Participation in preparation and execution of experimental tests,
- Participation in analysis of experimental results,
- Participation in development of research findings and conclusions,
- Writing original drafts of all three research papers,
- Design of figures, diagrams, and tables,
- Participation in peer review processes.

TABLE OF CONTENTS

1. INTRODUCTION

1.1. Problem and subject of a research

Fracture is a physical process in which a material separates due to the initiation and propagation of cracks. Cracks form when internal tensile or shear stresses exceed the material's strength, which results in nonlinear behavior. The character of the fracture process depends on the type of the material and may include phenomena such as yielding, hardening, plastic mechanisms, or other forms of damage. As cracks open and grow, energy is dissipated. Based on the amount of energy needed to cause fracture, materials are typically classified into three categories: brittle, quasi-brittle, and ductile [1]. This thesis focuses mainly on quasi-brittle materials.

Quasi-brittle materials, such as concrete, brick, mortar, ceramics, rocks, and certain hard steels, are widely used in civil engineering. Under the loading, the appearance of cracks in these materials is expected and is usually considered during the design phase. However, unexpected crack formation and growth can indicate underlying structural issues that warrant closer inspection. Unstable crack propagation in quasi-brittle materials can compromise the structural integrity, leading to costly repairs or, in extreme cases, total failure. For this reason, ongoing research into their fracture behavior is essential to improve the safety, reliability, and durability of engineering structures.

Despite many advancements, simulation of the fracture of quasi-brittle materials remains a significant challenge. This is largely due to the complex fracture mechanisms and the heterogeneous internal structure of these materials, which often contain different constituents of varying sizes and mechanical properties, as well as pre-existing defects. Fracture usually begins with the formation of microcracks at weak points within the material. These weak areas may include softer phases such as weaker constituents, regions around pre-existing defects, notches, or sharp corners. As loading continues, these microcracks grow and merge into larger cracks. Eventually, a network of cracks develops, which leads to a progressive failure. During this process, the material accumulates permanent damage.

Accurately simulating this behavior is challenging and often requires significant computational resources. To overcome these challenges, many large-scale simulations simplify material heterogeneity by adopting macroscopic models. Detailed consideration of material heterogeneity in large structural models is generally not feasible and is therefore mostly limited to small-scale material samples. However, developing models that can simulate fracture mechanisms at the local heterogeneous scale is essential. Such models will enable precise description and simulation of mechanisms at a smaller material level, thereby contributing to a better understanding of the global material failure process.

Regardless of the modeling approach, all numerical models require input parameters that de-

scribe the material's internal behavior through the implemented constitutive laws. The accuracy of simulation results depends heavily on the reliability of these parameter values. For simpler problems, the parameters can often be estimated using analytical expressions based on experimental data and well-established procedures. However, for more complex phenomena such as material failure, analytical solutions are generally not available. In such cases, the unknown model parameters cannot be directly measured, and alternative approaches must be utilized.

Successful determination of parameter values for such complex problems is as important as developing accurate numerical models. This is especially true for fracture problems, where fracture-related parameters strongly influence when and where cracks will form and how they will evolve. A major difficulty in obtaining precise parameter values is that all models inevitably include some level of uncertainty due to simplifications in the equations and approximations of nonlinear material behavior. Additional uncertainty arises from the material itself, which may change over time due to environmental exposure, leading to both chemical and mechanical changes that reduce the reliability of previously determined parameters. Moreover, measurement equipment is also prone to uncertainty, with potential errors in the measurements further contributing to the overall uncertainty.

Therefore, it is clear that the use of numerical models to simulate material failure must be supported by a reliable process for identifying and calibrating model parameters in order to achieve reliable simulation results. This process must also take into account all associated uncertainties. By combining advanced numerical modeling with a robust approach to parameter identification, the simulation results become more reliable and applicable to real engineering problems. Together, these methods enable meaningful and trustworthy simulations that can address the uncertainties present in real-world materials and structures.

1.2. Literature review of a research field

The research field of this thesis can be divided into two main areas: the development of numerical models for simulating material fracture, and the development of methodologies for identifying uncertain parameter values.

Simulating the fracture of quasi-brittle materials is a complex task that requires accurate modeling of the processes and mechanisms occurring within the material under load. These processes include crack initiation, crack propagation, and eventual material failure. The accuracy of such simulations depends on how well the material's heterogeneous structure is represented. This structure is typically modeled using one of three approaches: macro, meso, or micro (see Figure 1.1). [2]–[11].

Macro-modeling assigns uniform material properties to every point in the material and neglects its heterogeneity. This method is computationally efficient and widely used for large-scale structures or in problems where fracture is expected to be driven by a single macrocrack [5]–[8]. On the other hand, mesoscale and micromodeling incorporate the material's heterogeneity structure by

modeling its individual constituents. At the meso level, for example, concrete is represented as a composite made of aggregates, cement paste and interfacial transition zones (ITZ). Micromodeling goes a step further by including finer structural details such as grains, crystals, fibers and capillary pores. Although these approaches are more computationally demanding, they offer a realistic representation of material heterogeneity.
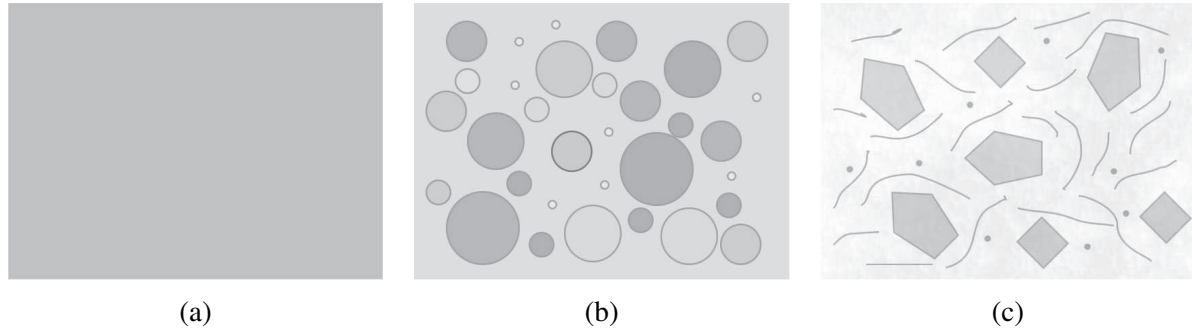

(a) (b) (c)

Figure 1.1: Heterogeneous structure modelling: a) Macroscale, b) Mesoscale, c) Microscale.

Regardless of the modeling scale, accurate and advanced numerical models must be developed to successfully simulate the fracture of quasi-brittle materials. In the literature, these models are generally classified into two main categories: continuum and discontinuum approaches [12], [13].

Continuum models are based on the continuity of the spatial domain to ensure continuity between different points. One of the most applied techniques within continuum models is the finite element method (FEM) [12], [13]. The basic idea of the FEM method involves discretizing the material domain into a set of finite elements, within which local calculations are performed. However, traditional FEM approaches require systematic re-meshing of the domain to model the formation and propagation of cracks within elements. Moreover, these approaches often yield subjective results when simulating material softening and fracture, as the results strongly depend on the size of the elements. Specifically, the size of the finite element affects the width of the localized damage zone, which in turn influences the energy dissipation and the global structural response [13]–[16].

To overcome these limitations, enhanced FEM models such as the Extended Finite Element Method (X-FEM) and Embedded Discontinuity FEM (ED-FEM) have been developed [17]. These methods enrich the element fields with discontinuity functions, which enables the modeling of cracks without the need for re-meshing and results are independent of the size of the used elements. In X-FEM, displacements are enriched globally at the nodes to simulate crack growth [18]. A limitation of this approach is the introduction of additional degrees of freedom, which prevents condensation of the stiffness matrix and requires that cracks remain continuous. In contrast, ED-FEM introduces displacement enrichment locally within elements, enabling stiffness matrix condensation and allowing for the modeling of cracks without enforcing its strict continuity (see Figure 1.2a) [1], [6], [7], [19], [20].

On the other hand, discontinuum models treat the material as a collection of discrete elements that can undergo displacements, rotations, separations, and mutual interactions. These models

were originally developed to simulate materials that are inherently discontinuous, such as rocks and granular materials. The most widely used method in this category is the Discrete Element Method (DEM), which simulates the motion and contact between particles by calculating interaction forces and moments of each individual element [12], [13]. With further development, cohesive bonds were introduced between the particles, which enabled DEM to simulate continuum materials that fracture under stress [21]. Among discontinuum models, lattice models are commonly used (see Figure 1.2b) [10], [22]–[28]. These models represent materials as a web of one-dimensional elements and Voronoi cells, preserving the initial connectivity of the system. Material failure is simulated by computing cohesive forces inside these elements, and checking for fracture criteria. Cracks are then introduced either by deleting cracked elements or for instance implementing embedding strong discontinuities within cohesive elements, which allows modeling of fracture and material softening with mesh-independent results.

In addition to continuum and discontinuum approaches, hybrid models that combine both methods are also found in literature, referred to as the Finite-Discrete Element Method (FDEM) [8], [12]. These models treat the material as continuous until cracks form, after which cracks propagate through contact elements inserted between continuum elements (see Figure 1.2c). This enables large displacements, rotations, and contact interactions once the material separates.

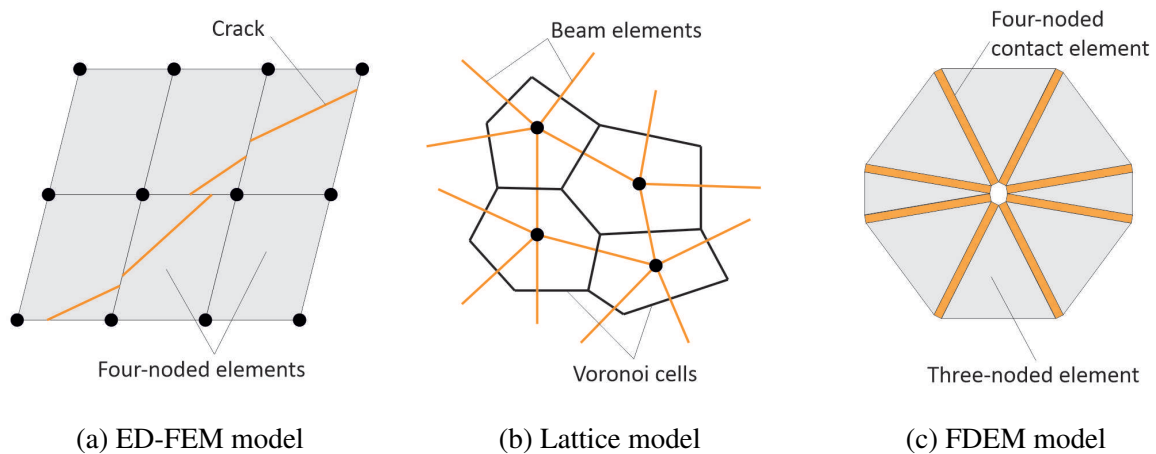(a) ED-FEM model   (b) Lattice model   (c) FDEM model

Figure 1.2: Numerical models for fracture simulation.

Considering the different modeling strategies and their advantages and limitations, different approaches are often favored depending on the problem. Continuum models allow for accurate representation of stress distributions and enable realistic simulation of crack patterns within finite elements, with clearly defined positions and orientations. However, using continuum models for fracture simulation comes with certain challenges. A key issue is the difficulty in maintaining crack continuity, as well as the problem of stress-locking. These limitations are especially relevant when simulating complex crack paths such as a single macrocrack that changes directions or more advanced cases where multiple macrocracks with different orientations merge into a single crack that ultimately causes material failure.

To address these issues, several techniques have been developed, such as crack tracking algorithms [7], [20], [29] and strain injection methods [30], [31]. Additionally, some successful

approaches have employed the incompatible modes method combined with symmetrical and kine-matically non-symmetric (SKON) embedded strong discontinuities, eliminating the need for explicit crack tracking algorithms [6]. However, most of these applications are focused on fracture sim-ulation of beams and plates [5]–[7], [17]–[19], [32], [33], as well as some larger-scale structural frame problems [34], where typically fracture is caused by single dominant macrocrack. Successful applications involving heterogeneous quasi-brittle fracture are rare due to the mentioned difficul-ties. A few notable exceptions include simulations of heterogeneous mesoscale materials using layer elements inserted between solid finite elements [9] and combinations of weak and strong discontinuities [35].

In contrast, discontinuum models are more frequently used for simulation of complex fracture phenomena, which involves heterogeneous structures and manifestation of multiple macrocracks. Their advantage lies in their simplicity: cracks are directly modeled within contact elements (FEM/DEM models [8]) or along one-dimensional beam elements (lattice models [21]). This definition naturally avoids issues such as crack path continuity and stress locking. As crack growth in discrete models is confined to well-defined boundaries, these methods offer computational efficiency and robustness for complex fracture scenarios. Literature examples include simulations involving multiple crack propagation [4], [8], [10], [21]–[23] and fracture of heterogeneous materials [2], [24], [36]. Nevertheless, discrete models have their own disadvantages. They lack stress state representation and the resulting fracture patterns are mesh-dependent as cracks are restricted to predefined element orientations.

Regardless of the type of numerical model used, constitutive models are required to represent both the linear and nonlinear behavior of materials. For instance, the elastic response of materials is typically modeled using Hooke's law within a linear elasticity. Material yielding and hardening are often approximated using perfect plasticity or isotropic, kinematic, and combined hardening models. These hardening models can be formulated through either linear or exponential laws. Fracture behavior is commonly represented through plasticity or damage softening models, or a combination of both, often governed by linear or exponential degradation laws. Each of these constitutive models requires a specific set of input parameters that define the material behavior [1].

Generally, the more complex the problem, the greater the number of input parameters is needed. These parameters must be carefully identified to ensure meaningful and reliable simulation results. Using numerical models without properly determining the parameter values, especially in fracture mechanics, can lead to dubious predictions, as small variations in input values can cause substantial deviations in output results [37]–[40]. Therefore, the identification of fracture parameters represents a mandatory aspect of research in fracture mechanics field.

One commonly used approach for parameter identification is direct measurement through standardized laboratory tests, which provide deterministic values for material parameters. In the context of fracture problems, typical tests include uniaxial tensile tests and Brazilian splitting tests to evaluate tensile strength, as well as three-point or four-point bending tests on notched beams to determine fracture energy. However, a major limitation of this approach is that the measured

quantities must directly correspond to the model parameters. For many complex or nonlinear parameters, establishing such direct relationships is difficult or even impossible. Furthermore, even when such direct measurements are possible, several challenges can affect the reliability of the results [41], [42]. These include sensitivity to the quantity of the measurement data used, inconsistencies due to varying test termination criteria, particularly in the determination of fracture energy [43], and the influence of stress concentrations around notches, which are often not considered in the analysis. As a result, test outcomes become highly sensitive to specimen geometry [44], [45]. Additionally, direct measurements do not account for uncertainties originating from the numerical model or the measurement devices, which further limits the overall reliability of this approach.

To address these issues, parameter identification can instead be formulated as an inverse problem. In this context, the aim is to determine the set of model parameters values that leads to numerical predictions matching experimental data. This typically involves iteratively adjusting parameter values to minimize the discrepancy between predicted and measured responses. Importantly, the used measurements in this approach do not need to be directly related to the parameters being identified, as long as a reliable numerical model is used to simulate the physical behavior of the system.

A widely used method is traditional calibration, where a loss function is defined as the difference between numerical predictions and experimental results. This function is then minimized using optimization algorithms [40], [46], [47]. The parameter set that produces the smallest loss function value serves as the most optimal estimate. This approach is commonly used due to its straightforward nature and practical implementation. However, this approach has a couple of limitations that keeps it unfavored for complex physical problems. It provides a deterministic solution and therefore lacks the ability to quantify uncertainty. Like direct measurements, it also fails to account for uncertainty from experimental noise or model assumptions. Furthermore, inverse problems are often ill-posed, meaning that different parameter sets can yield similar low loss values. To address this, regularization techniques are commonly introduced to improve solution stability and ensure a well-posed problem [40], [48]. However, these regularization methods are often sensitive to initial conditions, which increases the risk of convergence to local minima, potentially reducing the accuracy and reliability of the results.

To overcome the limitations of traditional calibration, more robust methods have been developed that better address uncertainty and improve the formulation of the inverse problem [37]–[40]. These approaches are generally categorized into two main frameworks: frequentist and probabilistic.

In the frequentist framework, probability is interpreted as the relative frequency of an event occurring across repeated realizations [37], [49], [50]. Within this framework, model parameters are treated as deterministic, while measurement uncertainties are modeled probabilistically, accounting for factors such as noise and modeling errors. A commonly used method is the Maximum Likelihood Estimator (MLE) [49], [50], which aims to find the set of parameters that maximizes the likelihood of observing the experimental data, or equivalently, minimizes the error between model predictions and

observed results. The outcome is a single point estimate, often accompanied by confidence intervals, based solely on the observed data. Despite its advantages, this approach requires well-defined, repeatable experiments, which may not always be feasible in complex systems. Additionally, high-dimensional parameter spaces demand many results to ensure statistically meaningful results, increasing computational cost.

In contrast, probabilistic approaches define both parameters and measurements within a probabilistic framework. A widely adopted method is Bayesian inference, which is based on Bayes' theorem of conditional probability [40]. In this approach, uncertain parameters are initially described using prior distributions, which reflect existing knowledge derived from previous experiments, expert opinion, or non-informative assumptions. These priors are updated using new experimental measurements and numerical model predictions through the application of Bayes' theorem. Here method is able to incorporate all sources of uncertainty within the identification process, including those associated with measurements, numerical modeling, and material behavior. This is achieved by the formulation of the error model through the likelihood function, similar to the MLE method. However, unlike frequentist methods, Bayesian inference results in a posterior probability distribution that represents the updated knowledge about the parameters after incorporating both prior information and measured data (see Figure 1.3). As a result, it provides a more robust and comprehensive framework for uncertainty quantification and parameter identification, which is beneficial for ensuring reliability of engineering applications [40], [51]–[53].

As this work adopts Bayesian inference for the development of a parameter identification methodology, the following text provides further details of its application.
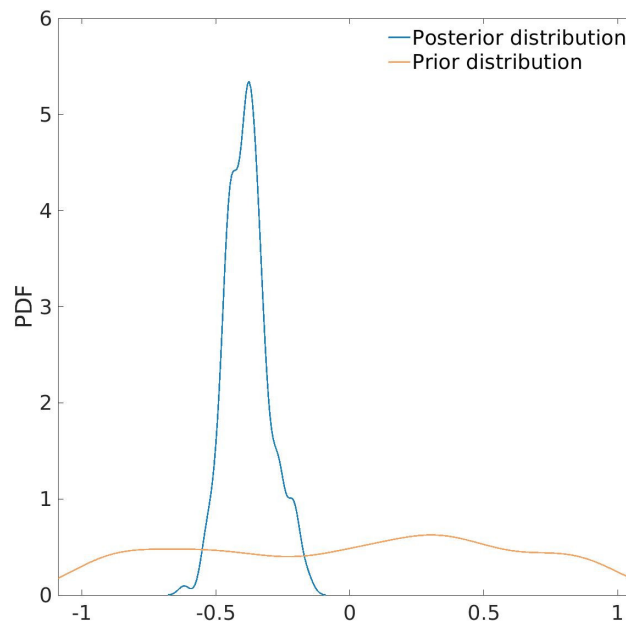

Figure 1.3: Bayesian inference: Prior and posterior distributions

A common challenge with this method is that these posterior distributions are rarely in closed form or match known distributions, making their analytical calculation complex or infeasible. Therefore, various approximation methods have been developed to estimate these distributions

[54]. These methods statistically analyze numerous generated solutions to approximate the target parameter distributions. The most commonly used methods are the Markov Chain Monte Carlo (MCMC) method and the Kalman filter.

MCMC is a robust, simple, and model-independent method that combines Monte Carlo simulation with Markov chains [49], [54], [55]. It uses a "random walk" process to analyze different parameter values combinations in search of the target posterior distribution. The most commonly used algorithm is Metropolis-Hastings, which starts multiple Markov chains from different points in the prior distribution space. Each new sample depends only on the previous accepted value and is selected based on the posterior probability ratio between the new and current values.

The Kalman filter estimates sequential states of linear systems in discrete time based on uncertain measurements [56]. The basic Kalman filter assumes a Gaussian posterior distribution, defined by a mean and covariance. The process includes a prediction step, where the current state is estimated from the previous one, and an update step, where the prediction is combined with measured data [54], [56]. This method is also applied in Bayesian inverse problems, using structural measurements to identify model parameter distributions. Since many engineering problems are nonlinear, various Kalman filter variants have been developed, such as the Ensemble Kalman Filter, which handles nonlinearities [49], [54], [56], [57].

However, these methods often require many numerical simulations to approximate the posterior distributions of uncertain parameters. This can be computationally expensive, particularly for complex fracture mechanics problems. As a result, the practical implementation of these methods often depends on the development of effective mathematical proxy models. By providing accurate approximations with significantly reduced computational demand, proxy models offer a solution to this challenge. Proxy models, also known as surrogate or meta-models, do not require a deep understanding of the underlying mechanisms. Instead, they are constructed using input-output data through a black-box approach. Once trained on a dataset of input parameters and corresponding numerical model simulation results, these models can predict outcomes for new input combinations with high accuracy. Common proxy modeling techniques include Generalized polynomial chaos expansion (gPCE), Gaussian process regression (GPR), and Neural networks (NN) [58].

The construction of a proxy model using the Generalized polynomial chaos expansion (gPCE) method involves approximating the solution of a numerical model through a linear combination of selected multidimensional polynomials and their corresponding coefficients [54], [59], [60]. Once the polynomial basis is selected, the model is trained by computing the polynomial coefficients based on numerical model solutions generated for selected input parameters. After training, the proxy model is validated on a larger set of model outputs to assess its accuracy. Further improvements in model accuracy can be achieved by employing higher-order polynomials and/or by increasing the number of used numerical model results for training.

The Gaussian process regression (GPR) method is a proxy modeling approach that assumes the outputs of a numerical model follow Gaussian distributions [61]–[63]. These distributions are characterized by a mean function and a covariance function. The covariance function defines the

correlation between different input parameter values and is governed by a set of hyperparameters. The GPR calibration process involves selection of an appropriate covariance function and tuning hyperparameters values by using a set of numerical model solutions. The resulting GPR model is then validated against additional model outputs to evaluate its predictive accuracy. If needed, the hyperparameters are iteratively adjusted until the desired level of precision is achieved.

Neural networks (NN) are a class of approximation algorithms that process input data through a series of interconnected layers composed of neurons [64], [65]. Starting from the input layer, data pass through one or more hidden layers before reaching the output layer. Each neuron processes the input by applying weighted connections and adding a bias term, followed by an activation function that introduces nonlinearity. This transformation enables the network to capture complex relationships between inputs and outputs. The training process, known as backpropagation, iteratively adjusts the weights and biases by comparing the network's predictions to results from the numerical model, minimizing the error and improving accuracy.

Bayesian inverse identification has become an increasingly popular approach in civil engineering for identification of material parameters, calibration of numerical models, and monitoring structural health. Numerous studies have demonstrated its effectiveness for different types of model parameters. For example, in [38], a combination of the Kalman filter and Generalized Polynomial Chaos Expansion (gPCE) was used to determine the mechanical properties of cement mortar from experimental data obtained through a notched three-point bending test. In another study [66], transmission and hysteretic parameters of large aluminum plates were identified using ultrasonic and cyclic tests, applying the Markov Chain Monte Carlo (MCMC) method without the use of proxy modeling. Bayesian methods have also been applied to full scale structures. In [51], the elastic constants of a timber building were identified using a combination of gPCE and MCMC, based on vibration test data. In [67], elastic parameters of a historic building were estimated using MCMC method without proxy modeling, relying on ambient vibration measurements. Additionally, gPCE and MCMC have been applied to identify elastic parameters of concrete dams [68]. A probabilistic approach combining Gaussian process surrogate models with MCMC was used in [69] to identify mechanical parameters of masonry arch bridges based on observed damage patterns.

Several research have also focused on identification of parameters related to fracture mechanics. One application involved identification of elastic and strength properties of concrete tram poles through vibration testing combined with notched three-point bending experiments, utilizing Kriging surrogate modeling together with MCMC method. Another study used gPCE and Kalman filter to identify fracture parameters of concrete and bond properties of a steel-concrete interfaces, based on tensile test data from concrete beams. Similarly, [70] applied the Kalman filter without a proxy modeling to identify the mechanical properties of mortar and concrete from compression tests and notched bending experimental data. Finally, in [71], fracture parameters of brittle cement mortar were estimated using gPCE and MCMC, based on data from notched three-point bending tests.

2.   THE PURPOSE AND GOALS OF THE RESEARCH

The main goal of this dissertation is to develop a comprehensive and reliable methodology for simulating crack initiation and propagation mechanisms. This approach aims to improve the accuracy of structural behavior predictions, both in the design of new structures and in the assessment of existing ones.

To achieve this, several goals must be fulfilled and integrated into a unified methodological framework:

- Development of a precise and efficient numerical model for simulating fracture mechanisms. Numerical models are essential tools for analyzing complex physical phenomena, and their accuracy is a fundamental requirement on a way of producing reliable results.

- Development of a parameter identification methodology based on ED-FEM model to ensure the model realistically simulate physical processes. A precise model alone is insufficient without reliable parameters values to represent the analyzed material or structure.

- Experimental validation of the methodology framework in laboratory settings to confirm its practical applicability and robustness. It provides insight into the experimental measurement design process and definition of the uncertainties.

To accomplish the first goal, this work takes a continuum model based on the Embedded Discontinuity Finite Element Method (ED-FEM) as a base for simulating crack initiation and propagation. The numerical model is developed in FEAP software [72]. The model relies solely on basic fracture parameters, such as material strengths and fracture energies, which ensures both physical consistency and easier applicability. By integrating crack initiation criteria, the model accurately captures material failure under tensile and compressive loading at the macrostructural level. Furthermore, the model has been extended to simulate complex fracture mechanisms at the mesostructural scale, including the behavior of heterogeneous materials with constituents of differing sizes and material properties. This is made possible through enhancement such as machine learning and crack tracking algorithm, programmed in MATLAB 2021b software [73], and connected with the FEAP through the MATFEAP interface [74]. Its successful application offers deeper insights into failure processes of quasi-brittle material.

The second goal, methodology for identification of fracture parameter values based on ED-FEM model, is achieved by solving an inverse problem using a probabilistic framework. Methodology is developed inside the MATLAB 2021b software, by using SGLIB library [75]. This methodology is based on the Bayesian inference method in combination with the Markov Chain Monte Carlo (MCMC) approach. Here, uncertain parameters are treated through probability distributions that are then updated based on measured data from analyzed materials or structures. Here, the focus

is on usage of simpler, easy to collect measurements like horizontal and vertical displacements of the points. To ensure reliability when developing such methodology, the identification procedure was developed by using synthetic (virtual) measurements with known parameter values. As the MCMC method requires numerous simulation results to approximate the posterior distributions, proxy mathematical models were introduced to approximate results of numerical model and thus significantly reduce computational cost. Several types of proxy modelling methods were used and evaluated to determine the most efficient and accurate approach for this task.

Finally, to assess the methodology under realistic conditions, experimental tests were conducted on aluminum alloy specimens of non-standard geometries with unknown material parameters. Since aluminum is a ductile material, the numerical model was extended to accurately capture its fracture behavior by adding the linear hardening constitutive law. For parameter identification, uniaxial tensile tests by universal testing machine (UTM) were done on different specimens. For the identification purpose, simple measurements such as force-displacement and horizontal point displacements were used. The successful application of the methodology in laboratory settings confirmed its effectiveness and demonstrated its general applicability to both quasi-brittle and ductile materials.

3. NUMERICAL MODELING OF FRACTURE PROBLEM

The first part of the research focuses on accomplishing the goal of developing a precise and efficient numerical model for simulating fracture mechanisms of quasi-brittle materials at both the macroscale and mesoscale levels. To achieve this, the finite element method (FEM) is enhanced using incompatible modes and embedded discontinuity methods. The incompatible modes method increases the accuracy of stress field calculations, which is important for realistic and reliable fracture simulations. Embedded strong discontinuities provide an effective way to simulate crack initiation and propagation while avoiding remeshing and sensitivity to element size. The model integrates both Rankine and Maximum shear stress criteria to initiate cracks under tensile and compressive loading conditions. Additionally, the machine learning and crack tracking algorithms are incorporated to enable accurate modeling of complex fracture networks in heterogeneous mesoscale structures. Through the Section 3.1 to 3.7, a overview of the used methodology and results from the paper (I) (see Appendix A) are presented.

3.1. Enhanced quadrilateral finite element

The numerical model for simulating material fracture is based on the Finite Element Method (FEM), specifically an isoparametric quadrilateral (Q4) element with four integration points and standard bilinear Lagrange interpolation functions. This element is selected for its simplicity and robustness. Additional enhancements are achieved through incompatible mode techniques and embedded strong discontinuity approaches. The incompatible mode technique enriches the element's displacement field by adding extra modes ρ_b and quadratic shape functions M_b [1], [76], [77]. This achieves the increase of the accuracy of stress calculations, particularly for distorted elements and in bending dominating problems. To simulate crack propagation, the element is further enhanced using the Embedded Strong Discontinuity Approach (SDA) [1], [6]. More specifically, by Statically and Kinematically Optimal Nonsymmetric (SKON) formulation, due to its demonstrated efficiency in macroscopic fracture modeling [78]. This approach further expands the displacement field of the elements with separation modes α_i and corresponding interpolation functions $\boldsymbol{p}_i$, enabling precise modeling of material fracture processes. Here, the cracks are introduced locally as displacement jumps over an embedded discontinuity (crack) line within the element, which makes the results independent of the element size. This crack line, denoted as Γ^e, divides the element domain into two subdomains, Ω^{e+} and Ω^{e-}. The behavior of the subdomains after cracking is governed by separation modes. In this work, two constant separation modes are adopted: Mode I (crack opening and closing) and Mode II (crack sliding), as illustrated in Figure 3.1. Each corresponding separation parameter $\alpha = [\alpha_1, \alpha_2]^T$, defines the magnitude of the fracture. For α_1, positive values represent tensile opening, while negative values indicate compressive crushing. The
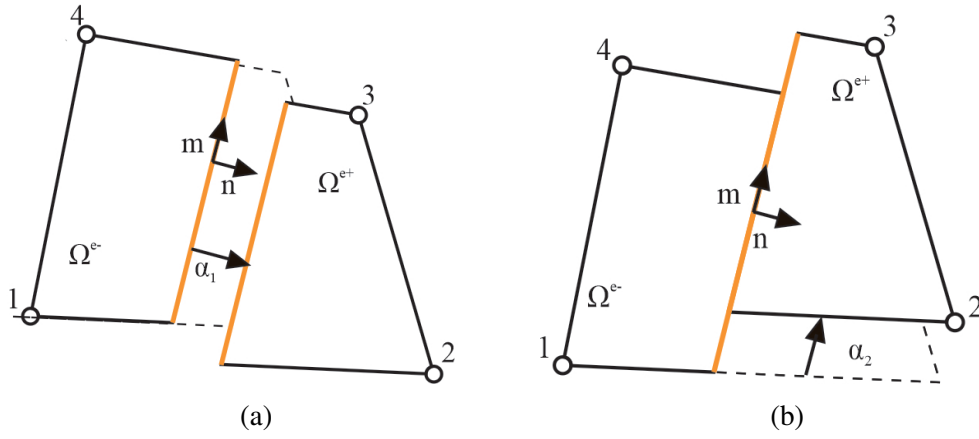
Figure 3.1: Embedded discontinuity separation modes: a) Tensile opening, b) Shear sliding.

parameter α_2 can take both positive and negative values for shear sliding, as it is possible in either direction. The model allows for cracks to develop in either mode individually or in combination.

As the load increases, the stress values within each element increase. All elements are checked according to the fracture criteria. If no fracture occurs, the element keeps the standard quadrilateral finite element formulation enhanced by incompatible modes. After the crack is initiated, the element formulation adds the separation parameters related to the embedded discontinuity method. To ensure the efficiency of the model, the operator-split calculation scheme is used. With this approach, the incompatible and separation modes of each element are calculated locally which reduces the number of global unknowns and increase the speed and efficiency of the model.

3.2.   Crack initiation

The determination of crack initiation time, location, and orientation is performed using a Gauss-point-based fracture criteria. With this approach, only the stress state within each element is considered to define the crack line. Two fracture criteria are implemented and checked at every pseudo-time increment for all uncracked elements: the Rankine criterion and the Maximum shear stress criterion. When either of these criteria is satisfied, the orientation and position of the discontinuity line are defined, and the crack is embedded. In this work, the crack is characterized by the point $\boldsymbol{x}_{ED}^e = [x_{ED}^e, y_{ED}^e]^T$ and angle α_{ED}^e. The angle α_{ED}^e defines the direction of the normal vector **n** to the discontinuity line (see Figure 3.2). Once embedded, the crack's location and orientation remain fixed throughout the simulation. Consequently, only one crack can form within each finite element, but multiple cracks can initiate simultaneously at the mesh level within a single pseudo-time increment.

The Rankine failure criterion [6] identifies tensile fracture by comparing the maximum principal stress with the material tensile strength σ_n. At each pseudo-time increment, principal stresses are
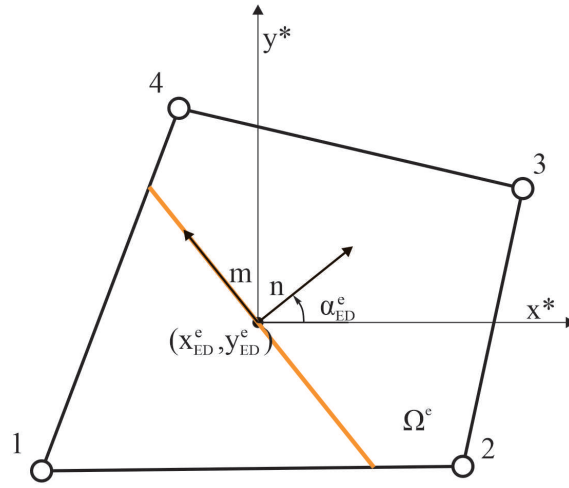
Figure 3.2: Finite element with an embedded crack line. The crack is defined by a point $\boldsymbol{x}_{ED}^e$ and angle α_{ED}^e. The local coordinate axes x^* and y^* are parallel to the global coordinate system.

evaluated at all four integration points of an element:

$$\sigma_{p1,p2}^{e,i} = \frac{\sigma_{xx}^{e,i} + \sigma_{yy}^{e,i}}{2} \pm \sqrt{\left(\frac{\sigma_{xx}^{e,i} - \sigma_{yy}^{e,i}}{2}\right)^2 + \left(\sigma_{xy}^{e,i}\right)^2}. \tag{3.1}$$

From the computed values, the larger of the two is selected as the maximum principal stress at each point, i.e., $\sigma_p^{e,i} = \max[\sigma_{p1}^{e,i}, \sigma_{p2}^{e,i}]$. The element's overall maximum principal stress is then determined as: $\sigma_p^e = \max\limits_{i=1,\ldots,4} \sigma_p^{e,i}$. If this value σ_p^e exceeds the tensile strength σ_n of the material, a tensile crack is initiated in the element.

To define the crack, all integration points with stress close to σ_p^e (within the tolerance) are grouped into the set $B^e = \{id \in \{1, 2, 3, 4\} : \sigma_p^{e,id} = \sigma_p^e\}$. The crack's location is determined by the geometric center of these points:

$$\boldsymbol{x}_{ED}^e = \frac{1}{N_{B^e}} \sum_{i \in B^e} \boldsymbol{x}^{e,i}, \tag{3.2}$$

where N_{B^e} is the number of points in B^e. Next, the average stress at these points is computed:

$$\boldsymbol{\sigma}_{ED}^e = \frac{1}{N_{B^e}} \sum_{i \in B^e} \boldsymbol{\sigma}^{e,i}, \tag{3.3}$$

from which the principal angle is derived:

$$\alpha_{ED}^e = \frac{1}{2} \arctan\left(\frac{2\sigma_{xyED}^e}{\sigma_{xxED}^e - \sigma_{yyED}^e}\right). \tag{3.4}$$

The crack is then defined by the point $\boldsymbol{x}_{ED}^e$ and angle α_{ED}^e, with the tangential vector $\boldsymbol{m}$ being perpendicular to the normal $\boldsymbol{n}$. Once embedded, the element can simulate tensile crack opening and shear sliding.

The maximum shear stress criterion is used to detect shear crack initiation by comparing the maximum shear stress and material shear strength σ_m. At each integration point i, the maximum shear stress is calculated as:

$$\tau_p^{e,i} = \frac{1}{2}|\sigma_{p1}^{e,i} - \sigma_{p2}^{e,i}| \tag{3.5}$$

Shear fracture is triggered if:

$$\tau_p^{e,i} \geq \sigma_m, \tag{3.6}$$

where σ_m is the shear strength of the material. If this condition is satisfied at any integration point, shear crack initiation occurs. The corresponding points with a maximum shear stress $\tau_p^e = \max(\tau_p^{e,i})$ are collected in the set $B^e = \{id \in \{1, 2, 3, 4\} : \tau_p^{e,id} = \tau_p^e\}$. The crack location is computed using the coordinates of the points in B^e as in Eq. (3.2), while the average stress components for these points are calculated using Eq. (3.3). The crack orientation is then determined from the average stress state values using:

$$\alpha_{ED}^e = \frac{1}{2}\arctan\left(\frac{-\sigma_{xx_{ED}}^e + \sigma_{yy_{ED}}^e}{2\sigma_{xy_{ED}}^e}\right), \tag{3.7}$$

where α_{ED}^e is the angle of the normal $\boldsymbol{n}$ to the discontinuity line, measured with respect to the global x-axis (see Figure 3.2).

When this criterion is met, the element fractures in Mode II (shear sliding), as opposed to Mode I (tensile opening) governed by the Rankine criterion. To ensure proper crack propagation under shear, compressive stress acting across the discontinuity is limited by a threshold σ_c, preventing excessive negative traction [21].

3.3. Constitutive relations

To simulate the failure behavior of the material, two constitutive laws are employed within the model: Linear elasticity and damage softening laws. The bulk response of each finite element is described by linear elasticity law, where the stress is defined as $\boldsymbol{\sigma} = \boldsymbol{C}\bar{\boldsymbol{\epsilon}}$. Here, $\boldsymbol{C}$ is the constitutive matrix (applicable to either plane stress or plane strain), and $\bar{\boldsymbol{\epsilon}}$ denotes the strain in the bulk material.

Failure and material degradation at the embedded discontinuity are governed by two uncoupled damage softening laws, corresponding to Mode I and Mode II fracture [79]. These are formulated within a thermodynamic framework for interfaces. The Helmholtz free energy associated with Mode I crack opening is given by:

$$\Psi(\bar{\bar{D}}_n, \bar{\bar{u}}_1, \bar{\bar{\xi}}_n) = \frac{1}{2}\bar{\bar{D}}_n^{-1}\bar{\bar{u}}_1^2 + \bar{\bar{\Xi}}(\bar{\bar{\xi}}_n), \tag{3.8}$$

where $\bar{\bar{D}}_n$ is the compliance modulus, $\bar{\bar{u}}_1$ is the displacement jump in the normal direction at the crack line, $\bar{\bar{\xi}}_n$ is the internal softening variable, and $\bar{\bar{\Xi}}$ is the associated softening potential. The

softening failure function for Mode I tensile opening is then defined as:

$$\bar{\bar{\phi}}_n(t_1, \bar{\bar{q}}_n) = t_1 - (\sigma_n - \bar{\bar{q}}_n) \leq 0, \tag{3.9}$$

where $\bar{\bar{q}}_n$ denotes the softening traction:

$$\bar{\bar{q}}_n = \frac{\partial \bar{\bar{\Psi}}_n}{\partial \bar{\bar{\xi}}_n} = \sigma_n \left(1 - \exp\left[-\frac{\sigma_n}{G_{fn}} \bar{\bar{\xi}}_n \right] \right), \tag{3.10}$$

Here, the σ_n represents the material's tensile strength and G_{fn} tensile fracture energy.

These constitutive relations are illustrated in Figure 3.3, where the stress–strain response is shown for a single element. The same type of response applies when other separation modes are active, although the sign of the stress may differ.
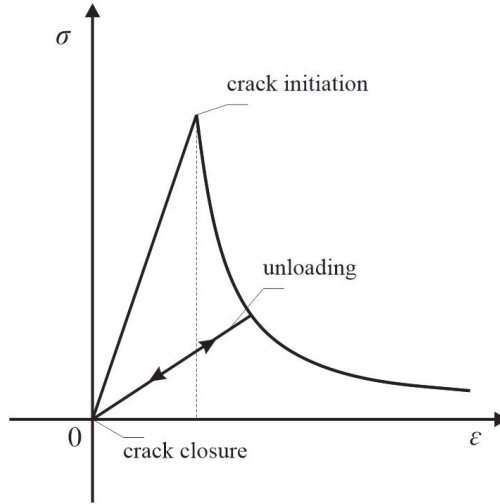

Figure 3.3: Constitutive laws for quasi-brittle material (stress–strain curve for one element). The material first follows a linear elastic law. After crack initiation, the response follows exponential softening law. During unloading, the stress–strain path returns to zero with no permanent deformation but with reduced stiffness.

A similar formulation is used for Mode II shear failure. For compressive loading cases, here only the unconfined compression scenarios are considered, where the typical macroscopic hardening effects observed under confinement are absent. This is consistent with other models in the literature [21], [80], [81], which show that compressive stress along shear cracks must be limited and followed by softening to allow crack propagation under low-confinement conditions. When limiting compressive stresses by the negative traction t_1 along the shear failure line, additional constitutive equations must be introduced:

$$\bar{\bar{\phi}}_c(t_1, \bar{\bar{q}}_c) = t_1 + (\sigma_c - \bar{\bar{q}}_c) \geq 0, \tag{3.11}$$

where σ_c and G_{fc} denote the maximum compressive strength and compressive fracture energy, respectively.

The constitutive equations for Mode I (Eq. 3.8)–(Eq.3.10) are also applied to Mode II, using analogous notation. Specifically, σ_m and G_{fm} represent the material's shear strength and shear fracture energy. The failure function for Mode II is expressed as:

$$\bar{\bar{\phi}}_m(t_2, \bar{\bar{q}}_m) = |t_2| - (\sigma_m - \bar{\bar{q}}_m) \leq 0. \tag{3.12}$$

Here, the absolute value of traction t_2 reflects the fact that sliding in Mode II can occur in both directions along the discontinuity line. The internal softening variable ξ_m accumulates with the maximum shear displacement in either direction. In contrast, tensile and compressive tractions are treated independently by defining separate failure functions (Eq. 3.9) and (Eq. 3.11), along with two distinct internal variables ξ_n and ξ_c.

3.4. Simulation results: macroscale homogeneous specimen fracture

This section presents a simple numerical simulation of fracture of a macroscale homogeneous plate to demonstrate the failure mechanisms of the numerical model. The specimen is a rectangular plate with a thickness of $t = 1$ mm, length $L = 150$ mm, and height $H = 300$ mm. Two distinct imposed displacement load cases are applied. The specimen is discretizing using 240 finite elements, each capable of developing crack. The bottom edge is fixed, and loading is applied as illustrated in Figure 3.4.
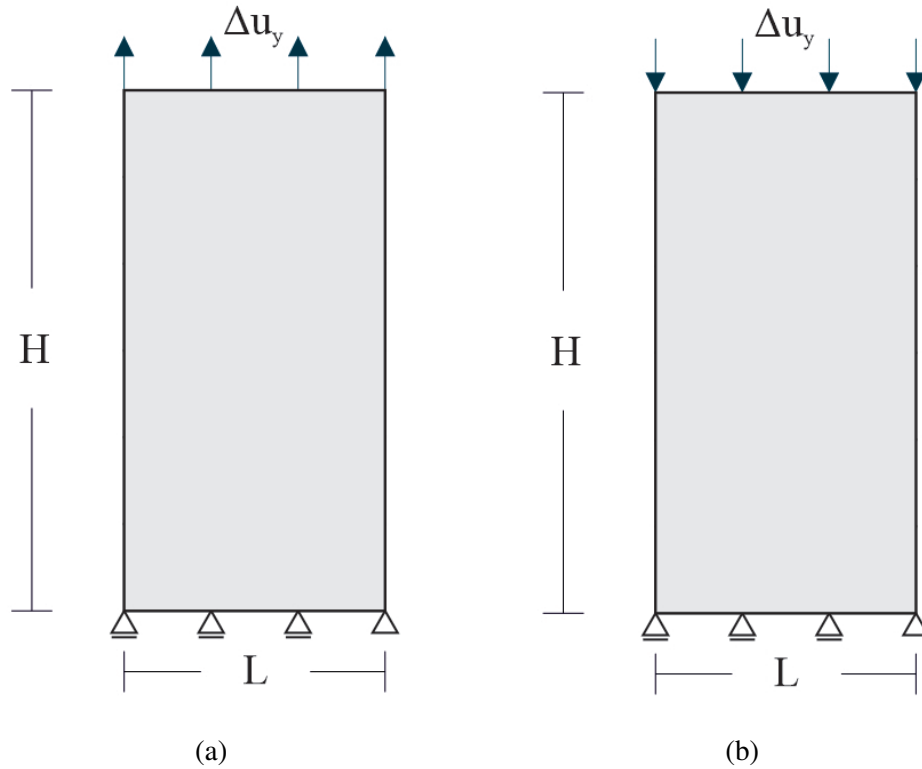

Figure 3.4: Homogeneous specimen test: a) Tensile load case, b) Compressive load case.

The chosen material parameters represents a cementitious quasi-brittle material (see Table 3.1).

Table 3.1: Homogeneous specimen: material properties[1]

Material	ν	E	σ_c	σ_m	σ_n	G_{fc}	G_{fm}	G_{fn}
Homogeneous	0.2	30,000	7	3	2	0.5	0.3	0.1

To initiate a crack in the otherwise homogeneous material, the material strengths in a single element at the specimen center are reduced by 5%. Figure 3.5 shows the final crack patterns at the end of the simulation for both loading cases. In the tensile load case, a horizontal crack

(a)   (b)
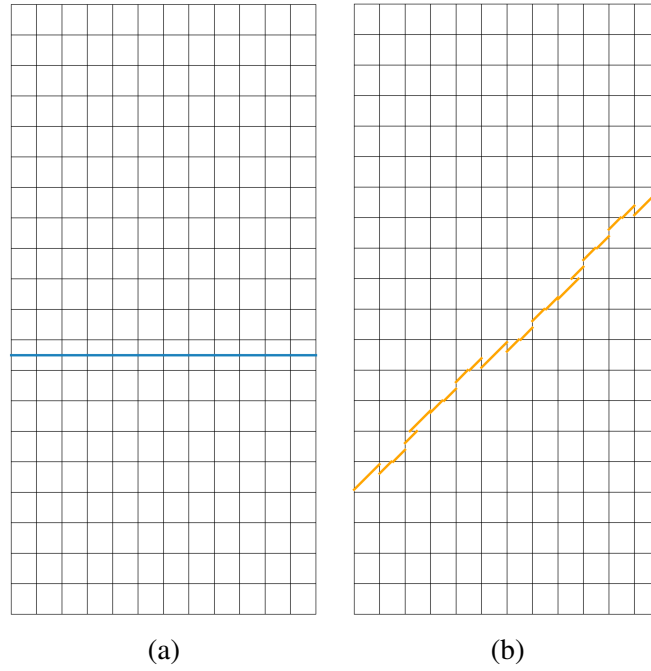
Figure 3.5: Final crack patterns of homogeneous specimen: a) Tensile load case, b) Compressive load case. Localized discontinuity lines are shown in blue (Rankine criterion) and orange (Maximum shear stress criterion).

propagates through the mesh as a result of the activation of the Rankine failure criterion. In the compressive load case, shear stresses lead to the formation of a diagonal crack at approximately 45°, in accordance with the Maximum shear stress criterion. The total failure is confirmed by the reaction-displacement curves for both cases, shown in Figure 3.6. In both cases, the curves exhibit a sudden drop as a macrocrack develops, which leads to a complete loss of load-carrying capacity.

3.5. Development of a numerical model for fracture of heterogeneous media

Further development of the numerical model is focused on simulation of crack formation and propagation at the mesoscale level for complex heterogeneous materials structures. In contrast to

---

[1]Material parameters: ν – Poisson's ratio, E – Young's modulus (N/mm^2), σ_c – compressive strength (N/mm^2), σ_m – shear strength (N/mm^2), σ_n – tensile strength (N/mm^2), G_{fc} – compressive fracture energy (N/mm), G_{fm} – shear fracture energy (N/mm), G_{fn} – tensile fracture energy (N/mm).
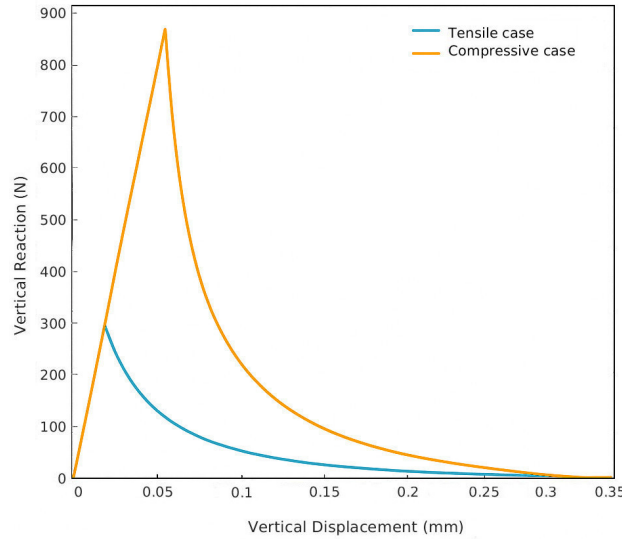
Figure 3.6: Reaction-displacement curves of the homogeneous specimen for tensile and compressive load cases.

the commonly used discontinuum models [2], [4], [12], [21], [82], a continuum-based approach represents a novelty approach. This method provides a more accurate representation of stress distribution within the material and enables an objective simulation of the fracture process.

The work deals with cementitious composites made out of different constituents: aggregates, cement paste, the interfacial transition zone (ITZ) between aggregates and cement paste, and voids. Fracture in such heterogeneous structures is inherently complex, involving multiple stages: initial cracking in weaker regions (such as the ITZ and areas surrounding voids), the formation of multiple macrocracks, their subsequent propagation and coalescence, which eventually leads to material failure.

3.6. Clustering with crack tracking algorithm

A key challenge in continuum-based fracture modeling is the stress-locking phenomenon. This occurs when crack propagation is impeded due to unfavorable geometrical configurations, such as misaligned adjacent cracks or finite element nodes positioned between cracks. While the SKON formulation has been successful at mitigating this effect at the macroscale [6], [78], it proves insufficient at the mesoscale, where fracture mechanisms are significantly more intricate and densely distributed.

To address this, the proposed model incorporates a machine-learning based clustering algorithm (DBSCAN) that identifies and tracks clusters of localized cracks. Initially, multiple finite elements fractures based on the fulfillment of either the Rankine or Maximum shear stress criterion. At each timestep, the DBSCAN algorithm detects clusters of localized elements based on their spatial proximity, assigning each cluster a centroid of the crack (see Figure 3.7). Once identified, each cluster is processed by a crack tracking algorithm that searches for continuous tensile cracks.

Figure 3.7: Clustering of the localized elements. Each cluster is represented by a different color.

The crack tracking algorithm enables the growth and merging of cracks into macroscopic cracks, thereby avoiding stress-locking. The algorithm starts by identifying the most stressed localized element in each cluster. From this point, it searches for neighboring localized elements that share an edge intersected by a potential crack (Figure 3.8). The continuous crack is defined by the sequence of connected elements and bounded by crack tips at the element edges. Elements that do not contribute to the formation of a continuous crack are disregarded and reverted to a non-localized state. This procedure is repeated at every timestep. As stress increases, new elements may localize.
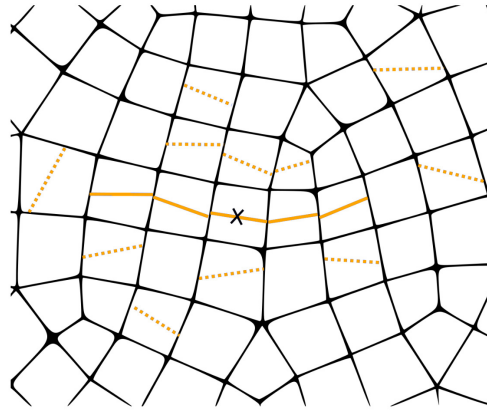

Figure 3.8: Crack tracking algorithm: the most stressed localized element (cross-marked) is used to identify neighboring localized elements (orange color). The remaining localized elements (dashed orange) are rejected and returned to the non-localized state.

These are clustered via DBSCAN and evaluated by the tracking algorithm, which accepts only those elements that extend existing tensile cracks. This approach ensures physically realistic crack evolution and efficient computational handling of complex fracture topologies. Additionally, the crack tracking algorithm is able to recognize two near macrocraks in order to connect them into the single one.

3.7.   Simulation results: mesoscale heterogeneous specimen fracture

This section presents numerical simulation results that illustrate the model's capability to capture failure mechanisms in heterogeneous cementitious materials at the mesoscale level. Material properties are selected to represent a cementitious composite. Aggregates are randomly embedded in a cement matrix and surrounded by an ITZ. Aggregates are modeled as stiff, elastic constituents, while the cement matrix and ITZ are modeled using the enhanced strong discontinuity formulation. The ITZ is represented as a 5 mm-thick layer surrounding the aggregates, with reduced fracture strength. Additionally, several voids with a 10 mm diameter are randomly added. The specimen is a square plate of dimensions 150 mm × 150 mm × 1 mm. It is fixed along the bottom edge and subjected to vertical loading at the top. Figure 3.9 illustrates the geometry, mesh, and boundary conditions. Material properties are summarized in Table 3.2. These specimens are subjected to
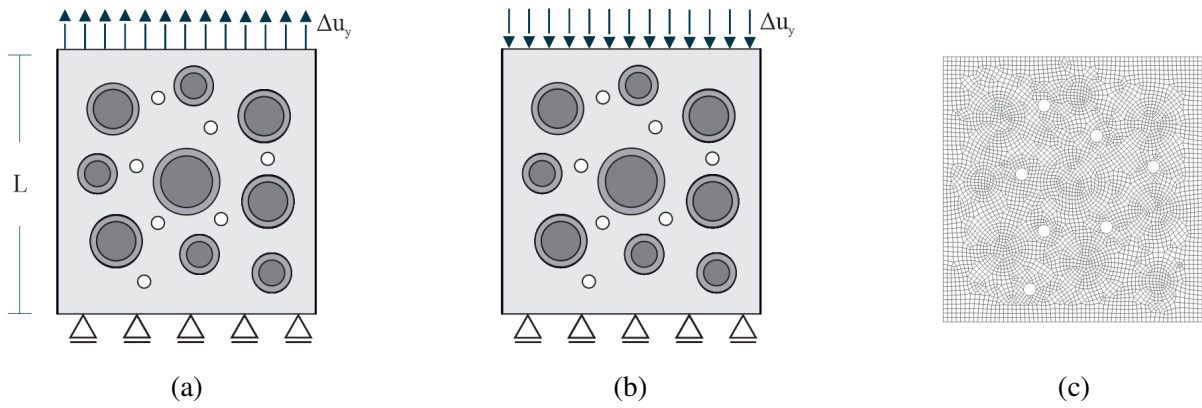

Figure 3.9: Heterogeneous specimen test: a) Tensile load case, b) Compressive load case and c) 4948 finite element mesh.

both tensile and compressive loading to analyze crack propagation.

Table 3.2: Heterogeneous specimen: Material Properties[1]

Material	ν	E	σ_c	σ_m	σ_n	G_{fc}	G_{fm}	G_{fn}
Cement matrix	0.2	30,000	5	2	1	0.05	0.01	0.003
ITZ	0.2	30,000	2.5	1	0.5	0.015	0.003	0.001
Aggregate	0.2	70,000	–	–	–	–	–	–

Tensile loading produces heterogeneous stress state within the material. As shown in Figures 3.10a–3.10c, stress concentrations before cracking develop around aggregates and voids. This leads to the initiation of microcracks within both the ITZ and the cement matrix around the voids. As loading progresses, the microcracks propagate and merge, forming multiple macrocracks. The dominant macrocracks continue to evolve, while other cracks gradually close. This process ultimately results in a single, continuous horizontal macrocrack across the lower half of the specimen, linking the voids and ITZ regions, as shown in the final displacement field (Figure 3.10f). Energy dissipation plots (Figures 3.10d–3.10e) confirm that Mode I tensile cracking is the dominant fracture

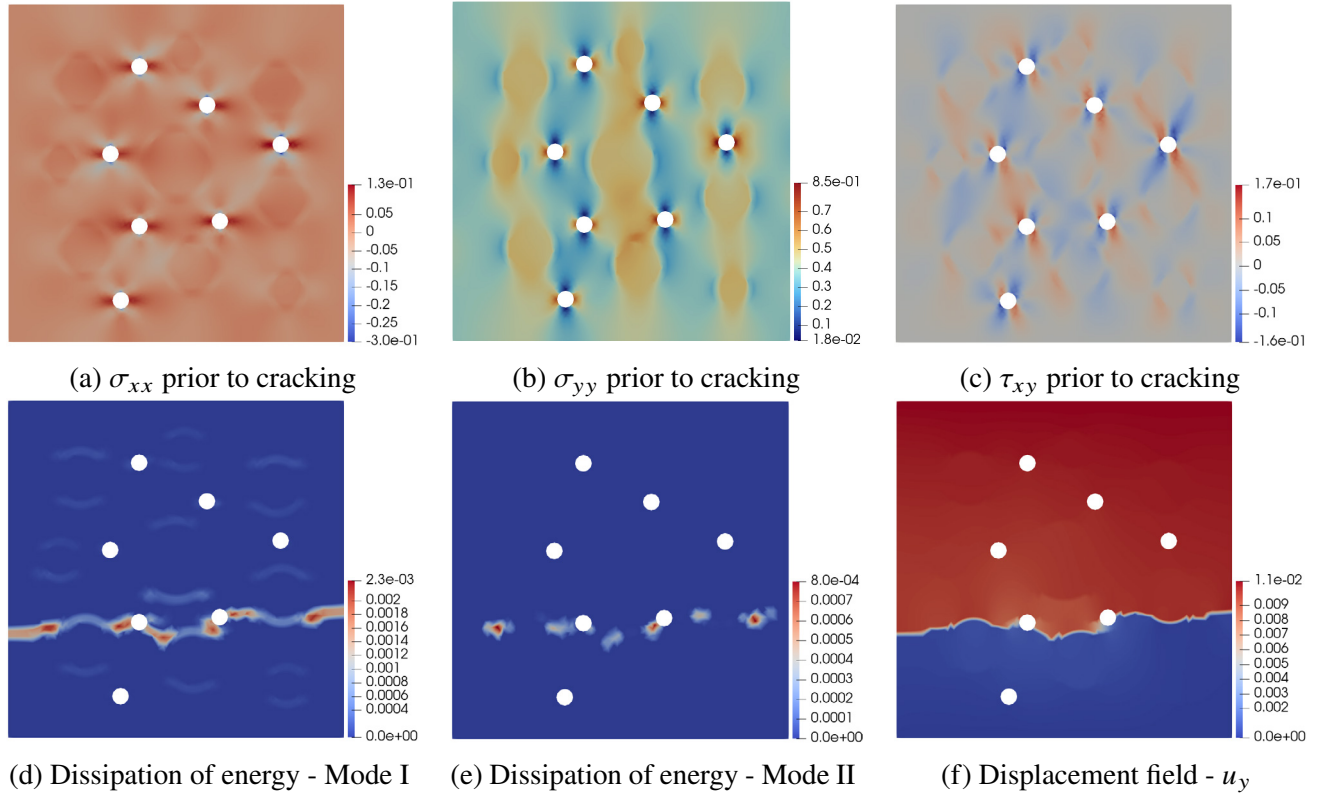mechanism. This it further emphasizes in the Figure 3.11 which visualize the localized elements

(a) σ_{xx} prior to cracking

(b) σ_{yy} prior to cracking

(c) τ_{xy} prior to cracking

(d) Dissipation of energy - Mode I

(e) Dissipation of energy - Mode II

(f) Displacement field - u_y

Figure 3.10: Heterogeneous specimen tensile load case results with stress (N/mm^2) and energy dissipation (N/mm) plots.

and crack patterns. Initially, 25 clusters of cracks are detected, centered around ITZ regions and voids. The crack tracking algorithm refines these by retaining only those that contribute to crack propagation. From it, development of dominant macrocrack in tensile is visible with small shear cracking near the places of macrocrack connection. The reaction-displacement curve of tensile loading case (Figure 3.12) shows complete loss of load-carrying capacity of the specimen and thus complete failure.

Under compression loading, the stress concentrations also form around aggregates and voids (see Figures 3.14a–3.14c). Firstly, entire ITZ zones fractures through Maximum shear stress criterion, followed by tensile cracking around the voids. These cracks propagate through the cement matrix, merging into a series of macrocracks that ultimately lead to complete specimen failure. The final crack path emerges from the top-center of the specimen, propagating asymmetrically through voids and ITZ regions. Figures 3.14d–3.14e clearly illustrate the dominant dissipation of energy due to Mode II shear cracking. In this case, the tracking algorithm allows shear cracks to evolve in a more localized manner, resulting in complex crack topologies, as seen in Figure 3.13. This structural heterogeneity leads to higher energy dissipation before failure, reflected in the compressive load-displacement curve (Figure 3.12).
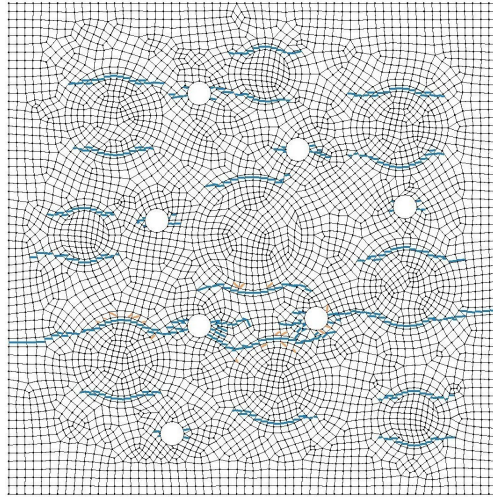
Figure 3.11: Crack formation at the end of tensile load case for heterogeneous specimen test. Localized discontinuity lines are shown in blue (Rankine) and orange (Maximum shear stress)
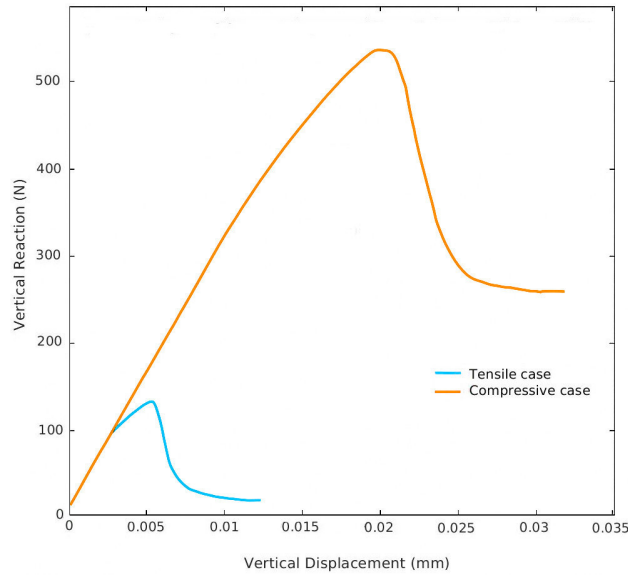

Figure 3.12: Reaction-displacement curves of the heterogeneous specimen for tensile and compressive load cases.
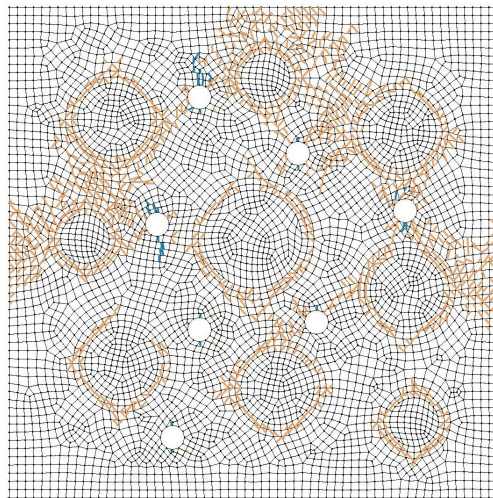

Figure 3.13: Crack formation at the end of compressive load case for heterogeneous specimen test. Localized discontinuity lines are shown in blue (Rankine) and orange (Maximum shear stress)
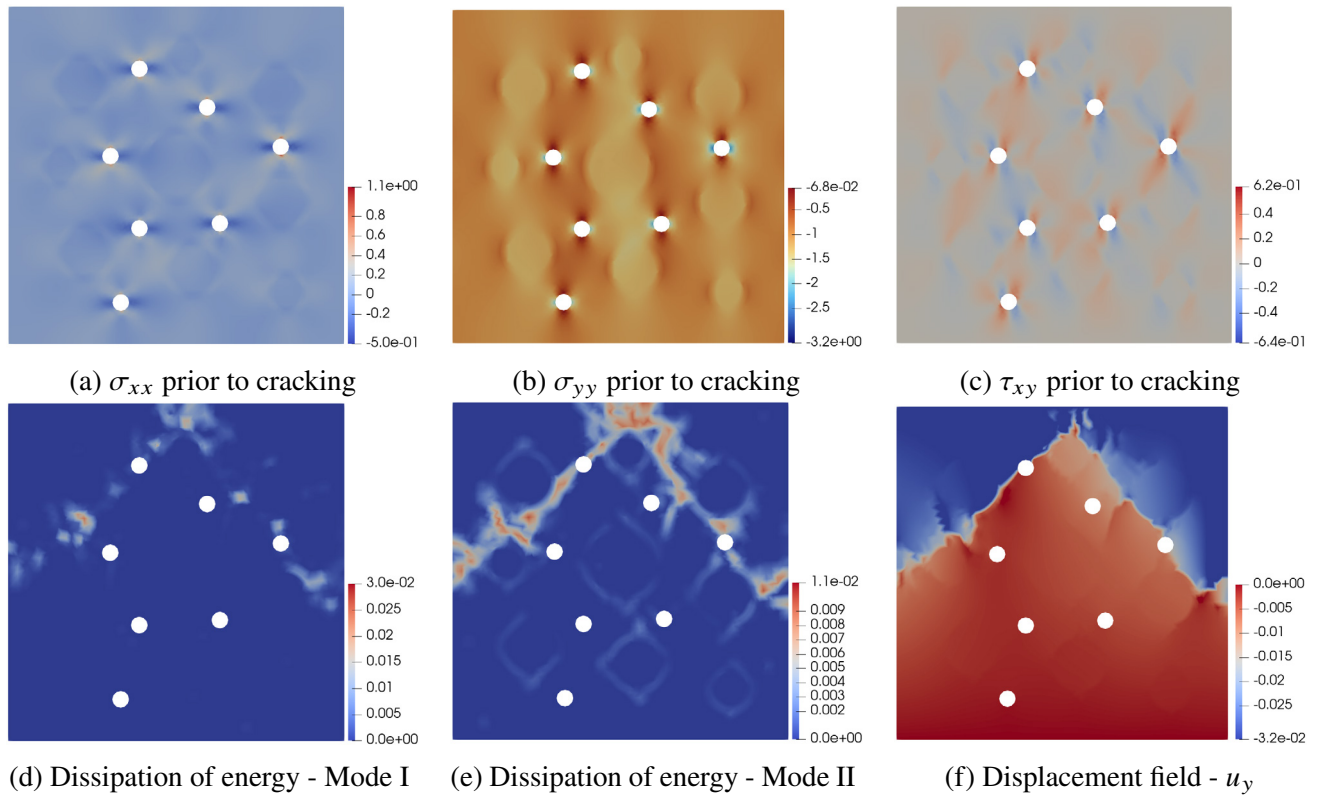
(a) σ_{xx} prior to cracking (b) σ_{yy} prior to cracking (c) τ_{xy} prior to cracking

(d) Dissipation of energy - Mode I (e) Dissipation of energy - Mode II (f) Displacement field - u_y

Figure 3.14: Heterogeneous specimen compressive load case results with stress (N/mm^2) and energy dissipation (N/mm) plots.

4. STOHASTIC METHODOLOGY FOR IDENTIFICATION OF PARAMETERS

Due to the strong nonlinearity of the analyzed fracture problems, the input parameters of the numerical model play a crucial role in reliability of the simulation results. Thus, the second part of this research is focused on development of a methodology for identifying fracture parameters in fracture propagation problems. This is based on a stochastic approach based on Bayes' theorem of conditional probability, also known as the Bayesian inverse identification method or Bayesian inference. The Bayesian inverse method allows for the inclusion of uncertainties in the identification process, such as measurement errors, as well as uncertainties in initial parameter estimates through the prior distribution. By combining numerical model solutions with various types of measurements from the structure, this method identifies the values of the required parameters in the form of probabilistic posterior distributions. This approach enables the existence of multiple "correct" solutions with an estimation of their reliability, resulting in a well-defined formulation of the inverse problem. Through the Section 4.1 to 4.5, a overview of the used methodology and results from the Paper (II) (see Appendix B) are presented.

4.1. Bayesian inverse method

The methodology for reliably identifying numerical model parameters is built upon the Bayesian inverse method, which offers a robust probabilistic framework for solving the stochastic inverse problems. This approach updates prior knowledge about input uncertainties by integrating measurements of structural (material) responses and numerical model outputs [37], [38], [48], [49], [51], [54], [83], [84].

Within this framework, the fracture parameters of the numerical model from Section 3.3 are treated as random variables that can be collectively represented by the vector $\mathbf{z} : \Omega \rightarrow \mathbb{R}^n$:

$$\mathbf{z}(\omega) = \left[\sigma_n(\omega), G_{fn}(\omega), \sigma_m(\omega), G_{fm}(\omega) \right], \tag{4.1}$$

where ω denotes a sample from the set of all possible realizations Ω, reflecting the stochastic nature of the parameters.

Each parameter z_i within $\mathbf{z}$ is described by its probability density function $\pi(z_i)$. Assuming mutual independence among the input parameters, their joint probability function $\pi(\mathbf{z})$ can be expressed as [49], [51]:

$$\pi(z) = \pi(z_1, ..., z_{N_i}) = \prod_{i=1}^{N_i} \pi_i(z_i). \tag{4.2}$$

Here, $\pi(z)$ represents the prior distribution of the parameter values. The selection of this distribution depends on factors such as prior experience/identification results, available measurements, or reasonable assumptions. Although any distribution type is theoretically possible, uniform, beta, normal, and lognormal distributions are usually used in practice [49], [51].

Ideally, the forward (numerical) model $\mathcal{G}$, evaluated with the true parameter set values $\mathbf{z}_{\text{true}}$, should perfectly match the observed measurement data. However, discrepancies arise due to model approximations and measurement errors. Thus, a measured data point $\mathbf{d}_m$ is considered a realization of a random variable defined as [49], [51]:

$$\mathbf{d}_m(\omega_e) = \mathbf{u}_{\text{true}} + \boldsymbol{\epsilon} = \mathcal{G}(\mathbf{z}_{\text{true}}) + \boldsymbol{\epsilon}(\omega_e), \tag{4.3}$$

where $\mathbf{u}_{\text{true}}$ is the predicted response for the true parameters, and $\boldsymbol{\epsilon}(\omega_e)$ represents measurement and modeling errors, characterized by a probability density function π_ϵ. These errors are assumed to be independent of the uncertain input parameters $\mathbf{z}$.

The Bayesian method updates the prior distribution $\pi(\mathbf{z})$ using observed measurements $\mathbf{d}_m$ via Bayes' theorem of conditional probability [51], [84]:

$$\pi(z|\boldsymbol{d}_m) = \frac{\pi(\boldsymbol{d}_m|z)\pi(z)}{\pi(\boldsymbol{d}_m)}. \tag{4.4}$$

The components of Bayes' theorem are the following. Likelihood function $\pi(\boldsymbol{d}_m|z)$ quantifies the probability of observing $\mathbf{d}_m$ given a parameter set $\mathbf{z}$. It is derived by assessing the probability that the error $\boldsymbol{\epsilon}$ equals $\boldsymbol{d}_m - \boldsymbol{u}$, where $\boldsymbol{u} = \mathcal{G}(z)$. With the the assumption that all components of the error vector $\boldsymbol{\epsilon}$ are statistically independent, the likelihood function can be expressed as the product of the probability distributions for each component of the measurable vector $\boldsymbol{u}$:

$$\pi(\boldsymbol{d}_m|z) = \prod_{i=1}^{Q} \pi_{e_i}(d_{m_i} - u_i(z)). \tag{4.5}$$

The evidence function $\pi(\boldsymbol{d}_m)$ acts as a normalization constant, ensuring that the posterior distribution $\pi(z|\boldsymbol{d}_m)$ has a total integral equal to 1. The posterior distribution $\pi(z|\boldsymbol{d}_m)$ is final outcome of the Bayesian inverse approach, providing the refined understanding of parameter distribution values after incorporating the measurement data $\boldsymbol{d}_m$.

In most nonlinear problems, posterior distributions cannot be expressed in closed form and do not follow some standard probability distributions. Consequently, various computational techniques, such as sampling methods, have been developed to approximate these distributions. These approaches work by generating representative samples that characterize the posterior distribution. Here, we employ the Markov Chain Monte Carlo (MCMC) sampling method to approximate such approximations.

4.2. Markov Chain Monte Carlo method

Markov chain Monte Carlo (MCMC) method is one of the most widely used for static and dynamic problems in engineering practice [48], [49], [54], [55], [84]. MCMC is known as a robust, simple, and model-independent technique that combines two methods: Markov chains and Monte Carlo simulations. By employing a random walk process, the method constructs Markov chains that gather solutions from the desired posterior distribution. Several algorithms exist for solving the MCMC procedure. Here we use the Metropolis-Hastings algorithm [48], [49], [55], [83], [84].

The algorithm begins by randomly selecting parameter candidates z^* from the prior distribution, where each selection depends only on the previously accepted value z_i (the Markov chain property). Specifically, the random selection (the Monte Carlo property) of a new potential candidate of the Markov chain z^* is governed by the proposed distribution $q(z^*|z_i)$. The proposed distribution is chosen to be strictly positive and simple, with a symmetric value around the currently selected candidate z_i. Once the value of the random variable is chosen, the forward model calculation $\mathcal{G}(z^*)$ is performed to obtain the solution. By comparing the obtained solution with the measurement data, the likelihood function from Eq. (4.5) can be defined.

The decision to accept the proposed parameter candidate z^* as part of the posterior distribution is based on the calculated value of the acceptance parameters α, which for Metropolis Hastings algorithm is given in its final form:

$$\alpha = \min\left(1, \frac{\pi(z^*|\mathbf{d}_m)}{\pi(z_i|\mathbf{d}_m)}\right). \tag{4.6}$$

Here, the expression $\pi(z^*|\mathbf{d})_m$ stands for the calculated unnormalized posterior distribution value for candidate z^*, while $\pi(z_i|\mathbf{d}_m)$ denotes the unnormalized posterior distribution value at the current location of the chain z_i.

If the value of the parameter α exceeds 1, the candidate z^* lies in the area of higher probability than the previously chosen parameter. Therefore, it is accepted as the new value of the posterior distribution. On the other hand, if the value of the acceptance parameter α is less than 1, a random value r is selected from the uniform distribution $U[0, 1]$. If $\alpha \geq r$, then the candidate is accepted; otherwise, it is rejected, and the entire procedure is repeated with a new parameter candidate. This process is shown in Figure 4.1, which illustrates one step of the Metropolis-Hastings algorithm.

The method's primary limitation lies in its computational demands for which to successfully identify uncertain parameters, all areas of prior distribution values needs to be analyzed. In the case of demanding numerical models, this represents a big problem in terms of the computer capacity. Consequently, there is often a need for the development of mathematical proxy models. These models efficiently, accurately, and computationally inexpensively approximate the required solutions of demanding numerical models.
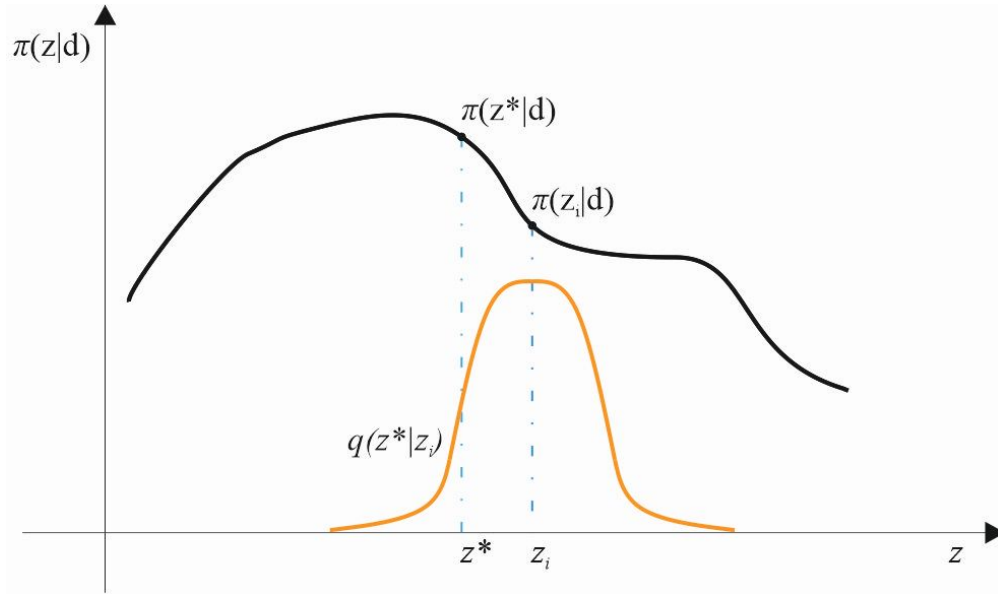
Figure 4.1: Metropolis Hastings algorithm step of finding new values of posterior distribution.

4.3. Proxy models

Running numerous fracture simulations is computationally expensive, which makes usage of MCMC methods for Bayesian identification often impractically slow. To overcome this, proxy models, also known as surrogate or response surface models, are employed to approximate the original numerical model and reduce the computational burden [83]–[85]:

$$\mathcal{G}(z) \approx \tilde{\mathcal{G}}(z), \tag{4.7}$$

where $\tilde{\mathcal{G}}(z)$ is a simplified approximation of the numerical model $\mathcal{G}$.

These models can be developed without deep insight into the internal structure of the numerical model, by using only selected input-output data, following a "black-box" approach. While various types of proxy models exist, most share a similar construction methodology [58], [83]. In this study, Generalized polynomial chaos (gPCE) methods and Neural networks (NN) are utilized. For the given example, several variants of the proxy model are developed to determine the optimal combination of hyperparameters in terms of approximation accuracy. In addition to basic proxy models, the role of autoencoder models based on neural networks is also explored, which are used to reduce the dimensionality of data. Autoencoders have the capability to filter noise from measurements, which may improve the success of the fracture parameter identification process.

General polynomial chaos expansion (gPCE)

The General polynomial chaos expansion (gPCE) method approximates the solution of a numerical model as a linear combination of multivariate polynomials weighted by corresponding

coefficients [54], [59], [60]:

$$\boldsymbol{u} = \mathcal{G}(z) \approx \tilde{\mathcal{G}}(z) = \tilde{\mathbf{u}} = \sum_{k=0}^{K-1} \boldsymbol{v}_k \Phi_k(z) = \boldsymbol{\Upsilon}\boldsymbol{\Phi}(z). \tag{4.8}$$

Here, $\tilde{\mathbf{u}}$ is the approximate model output, $\boldsymbol{\Phi}(z)$ is a vector of basis polynomials, and $\boldsymbol{\Upsilon}$ contains the corresponding coefficient vectors $\boldsymbol{v}_k \in \mathbb{R}^Q$.

The aim is to construct an accurate proxy $\tilde{\mathcal{G}}$ that closely approximates the true model response $\mathcal{G}(z)$ by minimizing the mean square error (MSE) between them [84]. The polynomial basis is chosen according to the defined prior distributions of the input parameters, using orthogonal polynomials with respect to the input space [54], [84].

The coefficients are obtained through solving a regression problem that minimizes the mean squared error:

$$\mathbb{E}[(\mathbf{u} - \tilde{\mathbf{u}})^2] = \int_{\mathbb{R}^n} (\mathbf{u}(\mathbf{z}) - \tilde{\mathbf{u}}(\mathbf{z}))^2 \pi(\mathbf{z}), d\mathbf{z} \approx \frac{1}{N} \sum_{i=1}^{N} (\boldsymbol{u}(z_i) - \tilde{\boldsymbol{u}}(z_i))^2. \tag{4.9}$$

Once constructed, the gPCE model offers an analytical form of the original simulation, making it efficient for statistical analysis and sensitivity studies. One key benefit of this approach is that sensitivities can be directly derived from the expansion coefficients. However, in cases of highly nonlinear or irregular responses, such as those common in fracture simulations, gPCE may require higher-order polynomials to achieve sufficient accuracy. This, in turn, can lead to unstable behavior or poor extrapolation between sample points [86].

Neural networks model

To overcome the potential limitations of gPCE, we also investigate Neural networks (NNs), which offer high flexibility or data representation which can be beneficial in capturing complex, nonlinear behaviors. Unlike gPCE, NNs do not rely on predefined basis functions. Instead, their parameters are learned through iterative optimization processes aimed at minimizing a loss function. However, this training process can be computationally demanding.

A typical feedforward neural network consists of an input layer, one or more hidden layers, and an output layer (see Figure 4.2). Each layer is composed of neurons connected by weighted links. For an input vector $\boldsymbol{x}^0 = (z_1, z_2, \ldots, z_n)$, which represents the model parameters, the network output is computed via forward propagation through the layers. In layer l, the j-th neuron output is given by:

$$\boldsymbol{u} = \mathcal{G}(z) \approx \tilde{\mathcal{G}}(z) = \tilde{\boldsymbol{u}} = \boldsymbol{x}^L(z), \qquad x_j^l = g^l\left(\hat{y}j^l\right), \qquad \hat{y}j^l = \sum_{i=1}^{n^{l-1}} w_{ij}^l x_i^{l-1} + b_j^l, \qquad \boldsymbol{x}^0 = z. \tag{4.10}$$

Here, w_{ij}^l and b_j^l are the weights and biases of neuron j in layer l, and $g^l(\cdot)$ denotes the activation

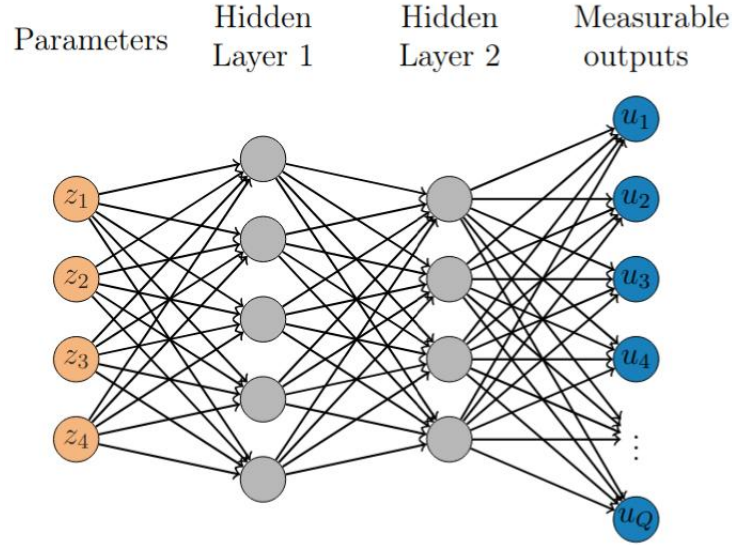function. The final layer output x^L provides the approximation $\tilde{u}$ of the model response.

Figure 4.2: Structure of the Neural network proxy model.

Key hyperparameters influencing NN performance include the number of layers, number of neurons per layer, and choice of activation functions. During training, the network adjusts its internal parameters iteratively through forward and backward propagation, gradually minimizing the loss function using methods such as gradient descent. This contrasts with gPCE, where the proxy is built through a single-step procedure. Nevertheless, once trained, the NN serve as a fast and accurate approximation of forward model evaluations [55], [87]–[89].

Low-rank representation of the measurable processes

For the both proxy modeling approaches chosen, the full measurable response vector u is used without explicitly addressing the internal correlations among its N_u time dependent components. However, since these components are often correlated, the effective dimensionality of the data can be significantly reduced without substantial loss of information. To exploit this, we employ an autoencoder, a type of neural network specifically designed for dimensionality reduction. An autoencoder consists of two parts: an encoder and a decoder. The encoder, denoted $\mathcal{L}(u)$, compresses the high-dimensional response vector $u \in \mathbb{R}^Q$ into a lower-dimensional latent vector $u_r \in \mathbb{R}^{Q_r}$, where $Q_r \ll Q$. This compressed representation (bottleneck layer) is intended to retain the most important features of the original data while reducing noise and redundancy. The decoder $\mathcal{L}^{-1}(u_r)$ then attempts to reconstruct the original data from this reduced representation. The autoencoder is trained by minimizing the reconstruction error between the input and the output (see Figure 4.3). This reduced dimensionality data is used for the training of both proxy models (gPCE and NN), in order to reduce model complexity, accelerates computation, and enhances the ability of the model to capture key data patterns.

To adapt this transformation in the Bayesian inference framework, we reformulate the likelihood computation in the latent space. Specifically, the measured data d_m is first mapped through the
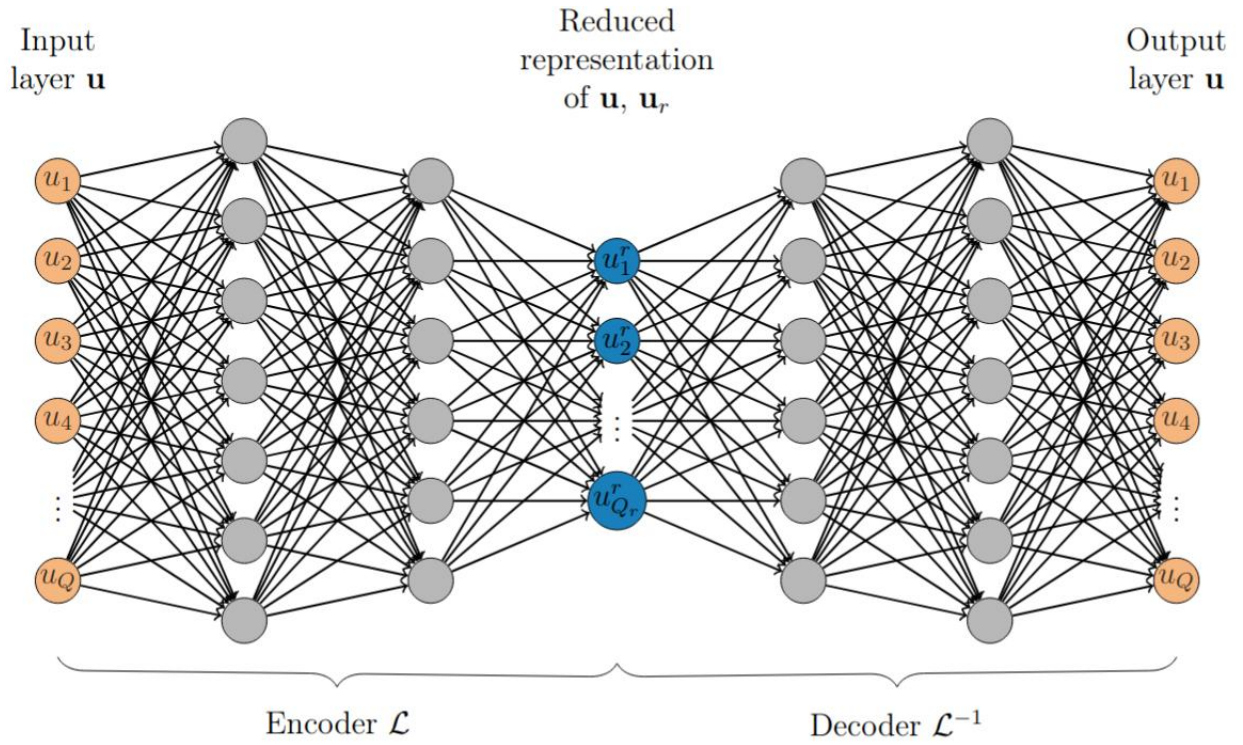
Figure 4.3: Structure of the Autoencoder model for dimensionality reduction of the measured response.

encoder, giving $\boldsymbol{d}_{mr} = \mathcal{L}(\boldsymbol{d}_m)$. The Bayesian update then takes place directly in this reduced space:

$$\pi(z|\boldsymbol{d}_{mr}) = \frac{\pi(\boldsymbol{d}_{mr}|z)\pi(z)}{\pi(\boldsymbol{d}_{mr})}, \tag{4.11}$$

$$\pi(\boldsymbol{d}_{mr}|z) = \pi_{e_r}(\boldsymbol{d}_{mr} - \boldsymbol{u}_r(z)). \tag{4.12}$$

Here, π_{e_r} represents the error distribution in the latent space, which differs from the original error model due to the nonlinear transformation introduced by the autoencoder. To approximate π_{e_r}, we map multiple samples of both exact and noisy outputs through the encoder and analyze their differences in the latent space. These deviations can then be effectively modeled, for instance, using Gaussian mixture models, to accurately reflect uncertainty in the reduced space.

4.4. Sobol sensitivity analysis

Sensitivity analysis plays a crucial role in experimental design by identifying which input parameters most influence the system's response. This insight can guide decisions such as sensor placement and the selection of the most informative measurable outputs [90]. Using proxy models not only makes Bayesian updating computationally fast but also provides the way for sensitivity analysis. In particular, Generalized polynomial chaos expansions (gPCE) offer a unique advantage: the orthogonality of their polynomial basis functions to the input distribution allows for efficient computation of partial variances directly from the expansion coefficients. Partial variance quantifies how much of the output variability can be attributed to one or a combination of uncertain input

variables. Sobol indices provide a normalized measure of this variance, expressing the relative importance of each parameter or parameter interaction. The first-order Sobol index captures the effect of a single input z_i, while second-order indices account for the combined influence of two inputs, z_i and z_j. These indices are defined as:

$$S_i = \frac{V_i}{V} = \frac{\mathrm{var}_{z_i}(\mathbb{E}_{\boldsymbol{z}_{\sim i}}[\boldsymbol{u}|z_i])}{\mathrm{Var}(\boldsymbol{u})} \qquad S_{i,j} = \frac{V_{i,j}}{V} = \frac{\mathrm{var}_{z_i,z_j}(\mathbb{E}_{\boldsymbol{z}_{\sim i,j}}[\boldsymbol{u}|z_i,z_j])}{\mathrm{var}(\boldsymbol{u})}, \qquad (4.13)$$

where $\boldsymbol{z}_{\sim i}$ denotes the set of all input variables except z_i, V is the total output variance, and V_i, $V_{i,j}$ are the partial variances associated with z_i and the interaction between z_i and z_j, respectively. These variances—and hence the Sobol indices—can be estimated using sampling-based methods such as Monte Carlo simulations [91], [92]. However, when combined with a surrogate model, especially one based on gPCE, this process becomes significantly more efficient. The polynomial structure of gPCE allows analytical computation of partial and total variances directly from its coefficients $\boldsymbol{v}$, exploiting their orthogonality [93]:

$$V_{i_1,\ldots i_s} = \mathrm{var}\left(\sum_{\boldsymbol{\alpha}\in\mathcal{J}_{i_1,\ldots,i_s}} \boldsymbol{v}_{\boldsymbol{\alpha}}\Phi_{\boldsymbol{\alpha}}(z_{i_1},\ldots,z_{i_s})\right) = \sum_{\boldsymbol{\alpha}\in\mathcal{J}_{i_1,\ldots,i_s}} v_{\boldsymbol{\alpha}}^2\gamma_{\boldsymbol{\alpha}}, \qquad (4.14)$$

Here, $\mathcal{J}_{i_1,\ldots,i_s}$ represents the set of multi–indices corresponding to basis polynomials that depend only on the selected input parameters $z_{i_1},\ldots,z_{i_s}$, and $\gamma_{\boldsymbol{\alpha}}$ denotes the norm of the polynomial basis function $\Phi_{\boldsymbol{\alpha}}$.

It's worth noting that sensitivity analyses can also be performed using other types of proxy models. Although these approaches do not provide analytical solutions like gPCE, they enable fast approximation of the numerical model results and thus allow for efficient sensitivity analysis.

4.5. Identification results: asymmetric four-point bending test

The application of the methodology is analyzed through the developed numerical model, with an emphasis on the macrostructural level of modeling and corresponding fracture parameters. Since this approach does not require direct measurement of the required parameters, the possibility of using simpler measurements, such as vertical and horizontal displacements on the structure, is explored.

For that purpose, the asymmetric four-point bending test is selected. This example introduces a challenging scenario of crack propagation in a concrete beam. The beam is 1322 mm long, 306 mm high, and 156 mm thick, with a notch (14 mm in length and 82 mm in height). The structure is asymmetrically supported and loaded. Figure 4.4 illustrates the beam geometry, support and loading conditions, and the positions of displacement measurements. The notch in the middle introduce stress concentrations and triggers crack initiation. Depending on the values of fracture parameters, crack propagation variate with its paths. But the overall cracking zone generally spans
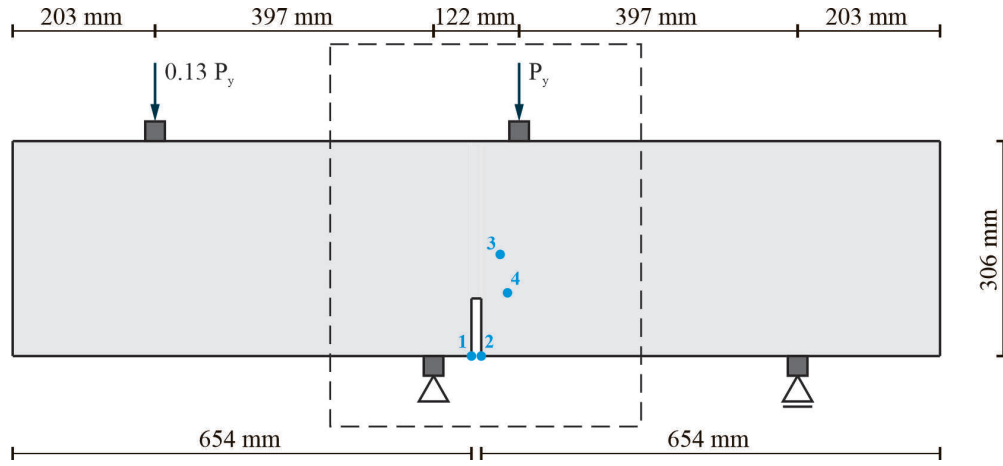
Figure 4.4: Asymetric four-point bending test: boundary conditions scheme, region of interest (dashed lines), and measurements locations (blue dots with indices).

from the notch tip toward the upper right stiff cap, where loading is applied. This zone is indicated by dashed lines in Figure 4.4. The failure process of the beam can be defined into three stages: elastic phase, crack propagation phase, and failure of the system.

As loading begins, internal stresses increase linearly. The stress concentration near the notch leads to tensile crack opening. During this initial cracking phase, multiple cracks may appear, but as loading progresses, one dominant crack tends to propagate, while others unload and close. Figure 4.5 shows Mode I and II degradation patterns for 20 randomly sampled parameter sets. As

(a)   (b)
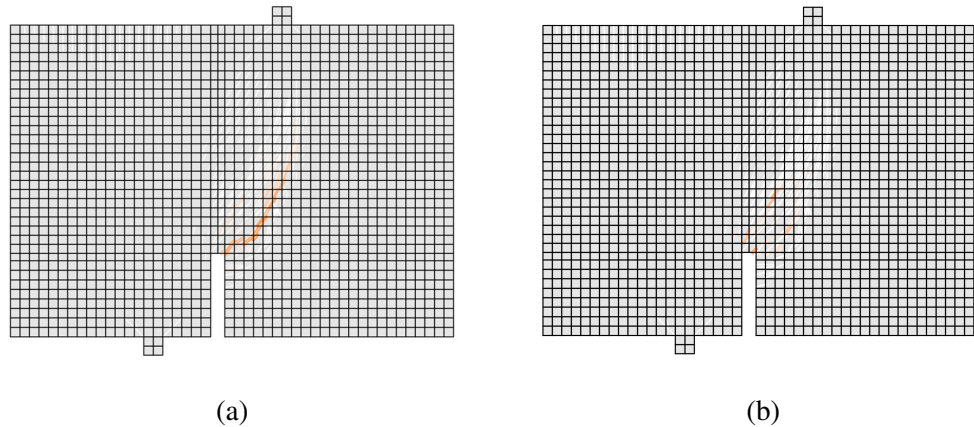
Figure 4.5: Material degradation during crack propagation phase: a) Mode I (tensile opening), b) Mode II (shear sliding). The level of material degradation is shown using a color scale ranging from white to dark orange, where darker shades indicate higher levels of degradation. The results are visualized for 20 randomly selected samples of parameter values.

the crack advances, beam stiffness degrades, leading to rotation of the right section and vertical redirection of the crack path. This marks the transition into the final failure state. As the macrocrack reaches the beam's upper region, the structure becomes unstable, which leads to total failure.

Simulation of this process is computationally intensive. Arc-length methods are used to track notch displacements to ensure numerical stability. The displacement and timestep parameters must be carefully selected. Here, we focus on the crack propagation phase where both fracture modes are

active. This maintains numerical stability but also reduce the computational costs of simulations.

4.5.1.   Problem definition

The elastic parameters of the concrete beam are predefined with values $E = 32{,}000$ N/mm^2 and $\nu = 0.2$. For the stiff caps, which are assumed not to crack, the elastic parameters are set to $E = 3.2 \times 10^9$ N/mm^2 and $\nu = 0.2$. The tensile and shear fracture parameters are treated as uncertain and thus represented by the vector $\mathbf{z}$ from Eq. (4.1). Their prior distributions are assumed to be uniform: $\sigma_n \sim U(2.4 \text{ N/mm}^2, 2.8 \text{ N/mm}^2)$, $G_{fn} \sim U(0.085 \text{ N/mm}, 0.12 \text{ N/mm})$, $\sigma_m \sim U(0.85 \text{ N/mm}^2, 1 \text{ N/mm}^2)$, and $G_{fm} \sim U(0.085 \text{ N/mm}, 0.12 \text{ N/mm})$.

Due to the complexity of fracture phenomena, four measurement points are positioned on the beam to be used for identification: two along the expected crack trajectory and two at the ends of the notch. This configuration captures both local and global effects of crack propagation. From it, four displacement datasets are defined to represent strain gauge outputs: $\boldsymbol{u}^{(1)}$: vertical displacement difference between middle positions (3 and 4). $\boldsymbol{u}^{(2)}$: vertical displacement difference between notch positions (1 and 2). $\boldsymbol{u}^{(3)}$: horizontal displacement difference between notch positions (1 and 2). $\boldsymbol{u}^{(4)}$: horizontal displacement difference between middle positions (3 and 4). These measurements are then combined into a single vector:

$$\boldsymbol{u} = [\boldsymbol{u}^{(1)}, \boldsymbol{u}^{(2)}, \boldsymbol{u}^{(3)}, \boldsymbol{u}^{(4)}]^T \in \mathfrak{R}^{4 \cdot \hat{M}}, \qquad \boldsymbol{u}^{(i)} = [u^{(i)}(\hat{\tau}_1), u^{(i)}(\hat{\tau}_2), ..., u^{(i)}(\hat{\tau}_{\hat{M}})]^T \in \mathfrak{R}^{\hat{M}}, \quad (4.15)$$

where $\hat{M} = 450$ corresponds to the number of timesteps: 87 steps of 0.001 seconds and 363 steps of 0.0001 seconds.

To develop and evaluate the identification methodology, synthetic measurements are employed. These are generated by evaluating the numerical model $\mathcal{G}(\mathbf{z}_{\text{true}})$, where $\mathbf{z}_{\text{true}}$ is randomly sampled from the prior. This approach ensures that the true values of the identified parameters are known in advance, which enables a reliable assessment of the methodology's accuracy. Data are collected from the locations shown in Figure 4.4. Each of the four synthetic measurement sets $\mathbf{u}^{(1)}, \mathbf{u}^{(2)}, \mathbf{u}^{(3)}, \mathbf{u}^{(4)}$ contains 450 timesteps, resulting in a combined synthetic measurement vector of 1800 timesteps. This combined measurement is then split into two phases: Phase 1: Uses the initial 150 timesteps from each individual measurement (totaling 600 steps), indicated by the gray regions in Figure 4.6; Phase 2: Utilizes the full 1800-step measurement vector.

This phased approach facilitates sequential parameter identification. In particular, Phase 1 enables a reduction in proxy model complexity by narrowing the parameter uncertainty before addressing the full problem. This mitigates difficulties in training proxy models caused by large variability in model outputs under the initial prior distribution.
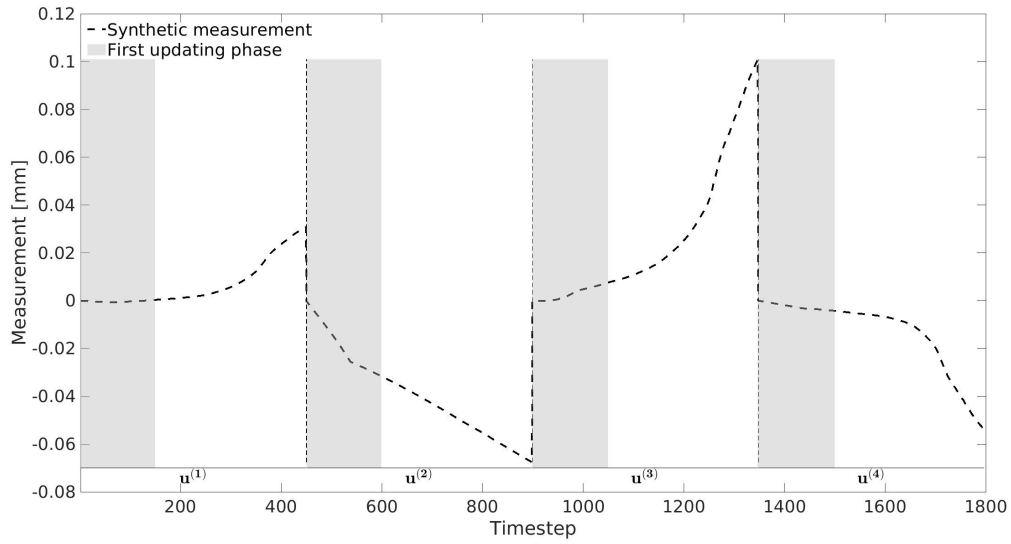
Figure 4.6: Asymmetric four-point synthetic measurement. The measurements $\boldsymbol{u}^{(1)}, \boldsymbol{u}^{(2)}, \boldsymbol{u}^{(3)}, \boldsymbol{u}^{(4)}$ are defined by Eq. (4.15). Each synthetic measurement contains 450 timesteps. Combined, they form a single 1800 timestep measurement, shown as a black dashed line. The gray region highlights the first identification phase, while the entire time domain is used in the second phase.

4.5.2. First updating phase

This phase addresses crack initiation and early macrocrack development. Based on the defined prior distributions, 25,000 QMC parameter samples were generated to train the proxy models, with an additional 5000 samples used for accuracy assessment. Each simulation required approximately 5 minutes to complete, with total of 25 hours of computational time on the cluster computer. Figure 4.7a shows the training set solutions alongside synthetic measurements. A low-rank representation of this set was created using an autoencoder with 52 bottleneck neurons and sigmoid activation (Figure 4.7b). This reduced the original 600 timesteps data to 52 dimensions. These both training sets were used to train proxy models.
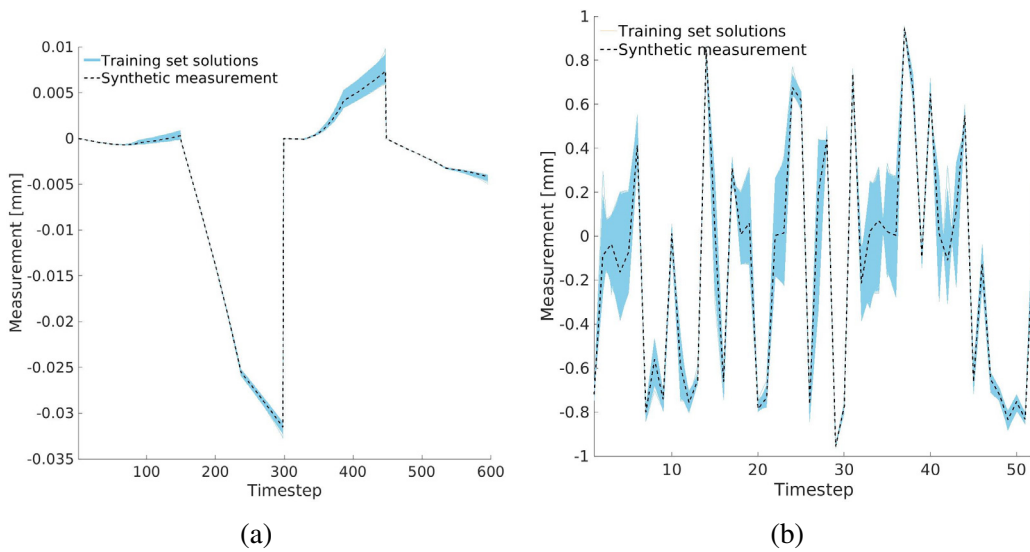

(a)

(b)

Figure 4.7: First updating phase: a) Training set results and synthetic measurement, b) Low-rank representation by autoencoder of a).

Proxy model training

The gPCE model was trained by varying the polynomial degree and evaluating accuracy against the testing set. An 8th-degree polynomial with 495 coefficients per timestep was found to offer the best approximation. Sobol sensitivity analysis using this model (Figure 4.8b) showed that output variance is dominantly influenced by the tensile strength parameter σ_n, particularly during the early stages of cracking. As the fracture progresses, the tensile fracture energy G_{fn} and shear strength σ_m start to influence the results. The shear fracture energy G_{fm} is not visible in this analysis.
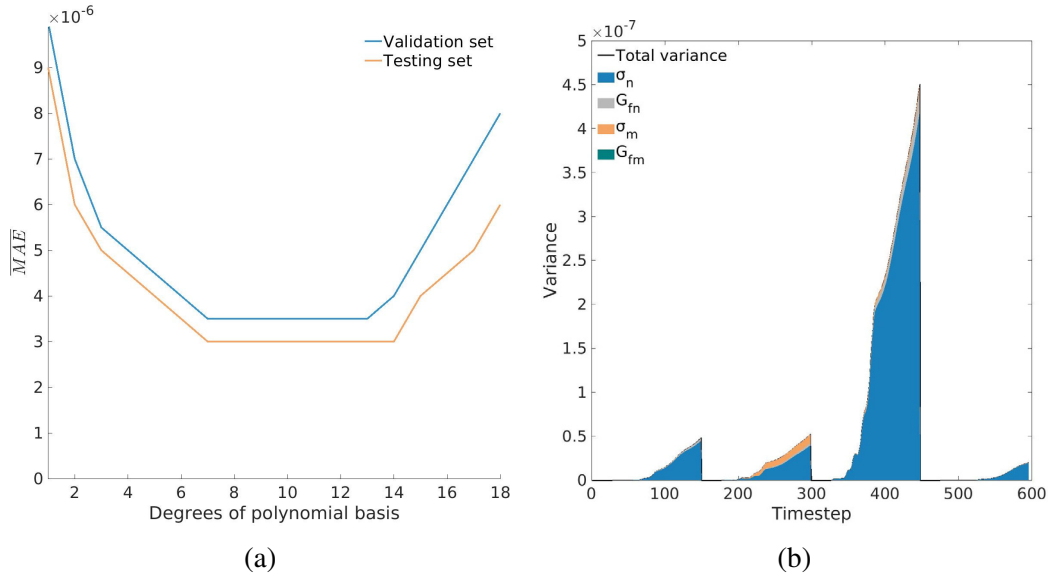
Figure 4.8: First updating phase: a) Accuracy analysis of the gPCE proxy model based on the polynomial degree, b) Sobol sensitivity analysis using trained gPCE proxy model.

The NN model is trained by exploring various architectures and activation functions. Table 4.1 summarizes the configurations and their performance. The best-performing architecture consisted of 128 neurons in the hidden layer and 600 neurons in the output layer, using ReLU and sigmoid activation functions, respectively.

Table 4.1: First updating phase: Training of NN models by changing the model architecture and type of activation functions. Notations used: S-sigmoid, $\emptyset$-there is no activation function, R-ReLu.

Neurons/layer	Activation Function of Layer	$\overline{MAE}$	Max MAE	$\overline{RMSE}$	Max RMSE
4-64-128-64-128-600	S-S-S-S-$\emptyset$	6.83E-06	4.23E-05	1.06E-05	8.79E-05
4-128-600	**R-S**	**4.67E-06**	**3.76E-05**	**8.87E-06**	**8.58E-05**
4-128-128-600	R-R-S	4.85E-06	3.84E-05	8.78E-06	8.17E-05
4-64-600	R-S	4.81E-06	3.84E-05	9.35E-06	8.57E-05
4-64-64-600	R-R-S	4.81E-06	3.92E-05	8.97E-06	8.73E-05

The low-rank gPCE model followed the same training procedure as the gPCE model, but used

the 52 dimensional reduced data. Again, the 8th-degree polynomial with 495 coefficients per timestep showed to be optimal.

For the low-rank NN model, the best configuration consisted of two hidden layers with 16 neurons each using tanh activation, and an output layer with 52 neurons using sigmoid activation.

After training and optimizing all four proxy models, their approximation accuracy was compared. As shown in Figure 4.9a, all models demonstrated very similar and accurate performance. The current updating phase did not involve significant fracture behavior, and the errors for all proxy models remain small. This is also observable from Figure 4.9b where error vales are significantly smaller compared to plotted dataset. Regarding the computational efficiency, the gPCE model
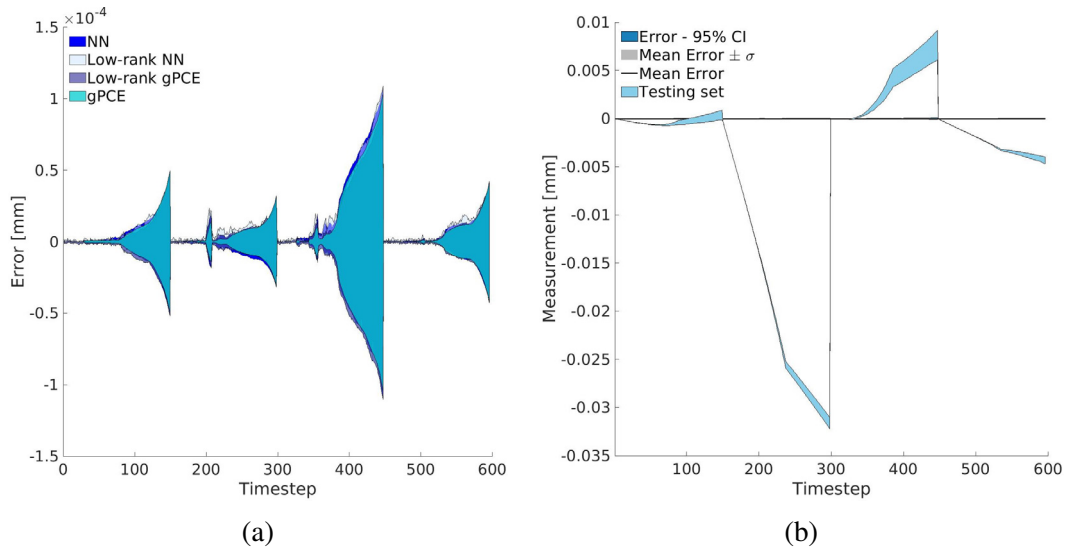
Figure 4.9: First updating phase: a) 95% CI errors of used proxy models, b) gPCE model's error metrics together with the results of the testing set.

proved to be most efficient, followed by the NN model. The low-rank models required additional training of the autoencoder, which increased overall computational cost.

Identification results

The trained proxy models were employed in MCMC analyses to identify the fracture parameters. The comparison of the results obtain by each proxy model enables assessment of effectiveness and reliability of each approach within given methodology. The MCMC analysis was conducted with 2000 steps across 100 Markov chains. With each simulation requiring approximately 5 minutes, the total computational time without proxy models would amount to around 166.7 hours. The use of proxy models substantially reduced this computational burden.

Figure 4.10 presents the identified parameter distributions. The tensile strength σ_n was well identified with narrow posterior distributions by all proxy models. The tensile fracture energy G_{fn} showed some minor variations among the models. More noticeable differences showed in the identification of the shear strength σ_m, where low-rank models exhibited higher accuracy. In contrast, the shear fracture energy G_{fm} remained unidentifiable across all models, which aligns with its negligible influence as indicated by the earlier sensitivity analysis (Figs.4.8b. Overall, none

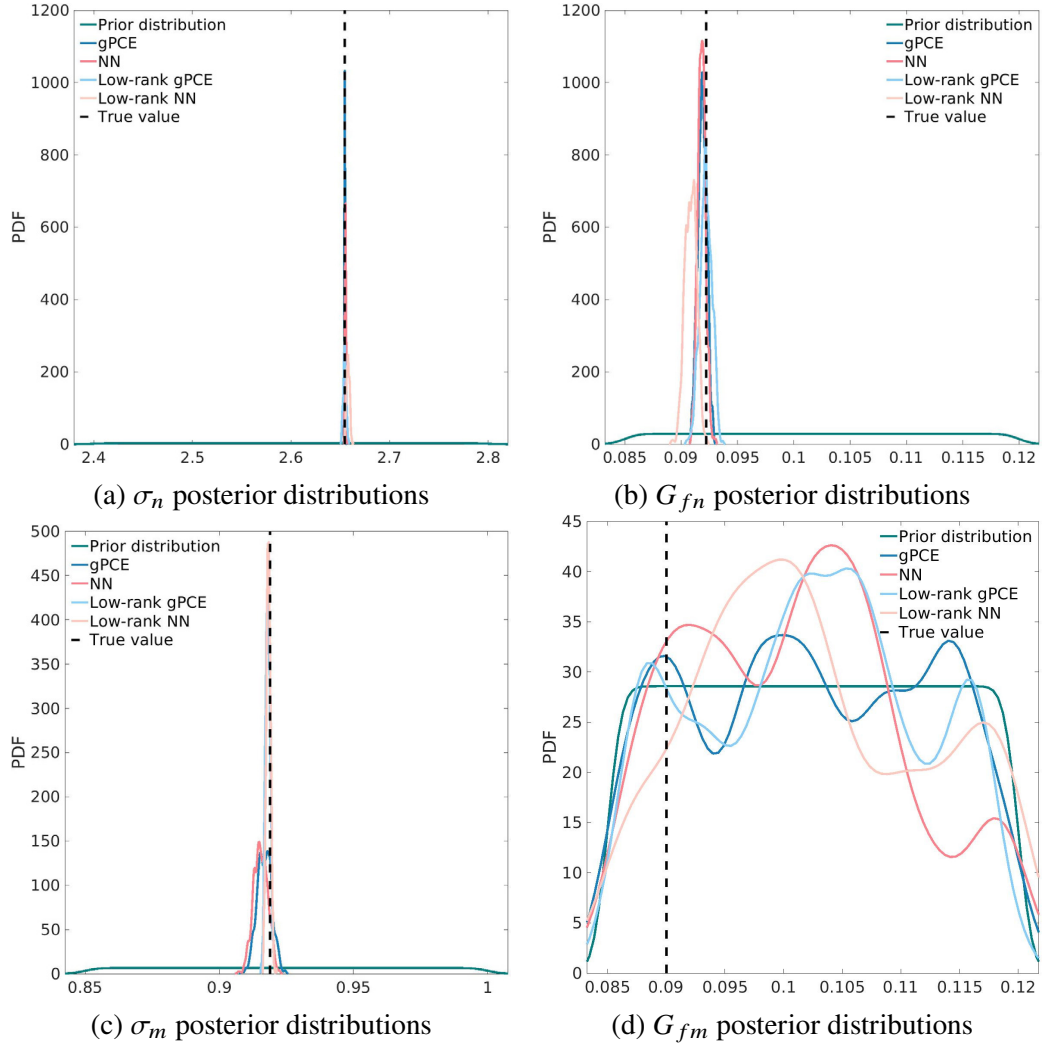of the models demonstrated a clear advantage in this updating phase.

(a) σ_n posterior distributions

(b) G_{fn} posterior distributions

(c) σ_m posterior distributions

(d) G_{fm} posterior distributions

Figure 4.10: First updating phase: Posterior distributions of tensile strength σ_n, tensile fracture energy G_{fn}, shear strength σ_m, and shear fracture energy G_{fm}.

Although the dataset from the first updating phase did not capture pronounced crack propagation or structural instability, the sensitivity analysis demonstrated a significant influence of the parameters σ_n, G_{fn}, and σ_m. This confirms that the onset of crack initiation was sufficient to activate these parameters. As a result, the first updating phase effectively reduced their uncertainty.

Based on these outcomes, updated prior distributions with reduced uncertainty were defined for the second updating phase. These refined distributions aimed to improve identification of the remaining unidentifiable parameter G_{fm} and to further enhance the accuracy of the previously identified parameters.

4.5.3. Second updating phase

To improve the parameter identification, a second updating phase was carried out using refined prior distributions. These new prior distributions were drawn from the posterior distributions of

the first updating phase. For the first three parameters, a multivariate Beta distribution with $\alpha = 3$ and $\beta = 3$ was used. This distribution was shifted and scaled to match the mean and variance of the posterior samples from the first updating phase, with the covariance further upscaled. For the fourth parameter G_{fm}, original prior was kept. Figure 4.11 shows the new defined prior distributions (Training distribution second phase) together with the previously obtained posterior distributions. A total of 20,000 QMC samples were generated for training and 5000 for testing. Each simulation
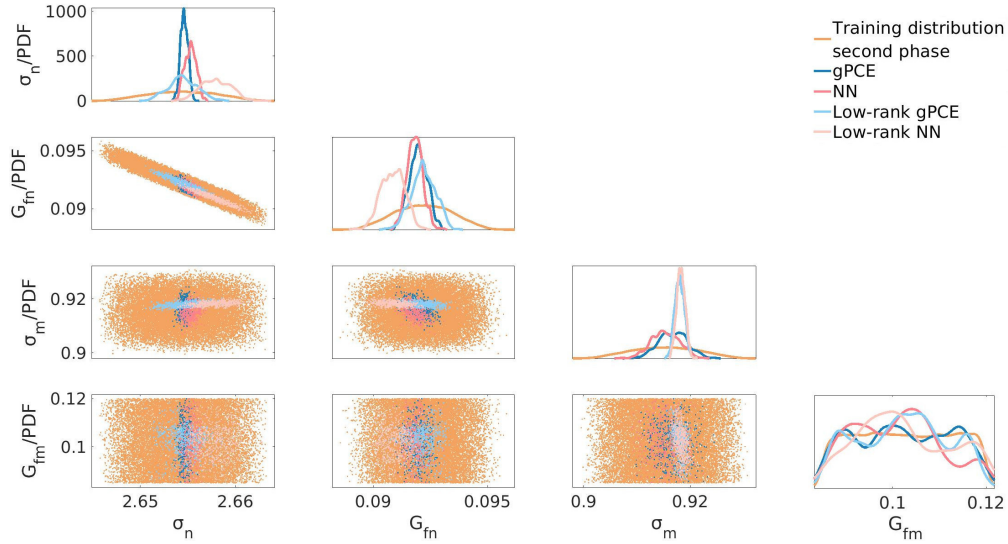
Figure 4.11: Second updating phase: New prior distributions (training distribution for the second updating phase) are shown together with the posterior distributions of first updating phase of each proxy model.

required approximately 25 minutes of computational time, with total of roughly 4.5 days to compute the full set. Solutions of the new training set, togethew with synthetic measurements, are shown in Figure 4.12a.

Proxy Model Training

Based on accuracy analysis, the gPCE model with a 9th-degree polynomial basis with 715 coefficients per timestep was selected. The corresponding Sobol sensitivity analysis is presented in Figure 4.12b. As in the first updating phase, the tensile strength parameter σ_n remains the most influential to the variance of the solutions. However, with the extended crack propagation in this phase, additional parameters exhibit increased influence. The tensile fracture energy G_{fn} becomes more dominant due to the further opening of the crack. The shear strength σ_m also gains relevance as the crack trajectory turns. Notably, the shear fracture energy G_{fm} now also exhibits a measurable influence on the model output.

For the neural network (NN) model, the best performance was achieved with an architecture consisting of three hidden layers of 64 neurons each, followed by an output layer with 1800 neurons. The hidden layers used GeLU activation functions, while a sigmoid function was applied in the output layer.

For the low-rank gPCE model, an 8th-degree polynomial basis with 495 coefficients per timestep provided the most accurate approximation of the 64-dimensional data.
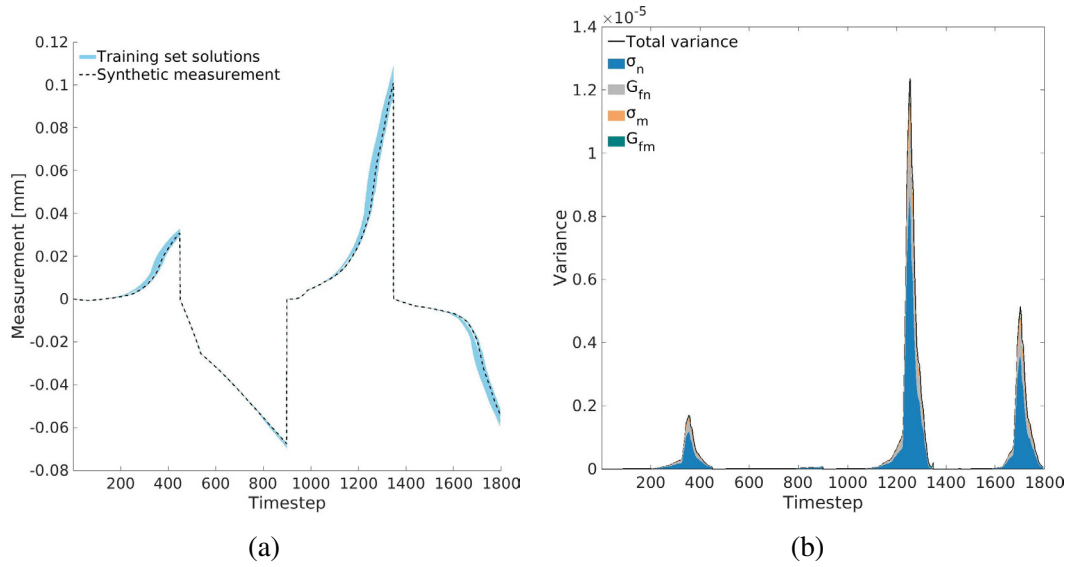
Figure 4.12: Second updating phase: a) Training set solution and synthetic measurement, b) Sobol sensitivity analysis using trained gPCE proxy model.

For the low-rank NN model, the best configuration included three hidden layers with 128, 128, and 64 neurons, respectively, and a 64-neuron output layer. All layers employed ReLU activation functions.

A comparison of proxy model accuracy is shown in Figure 4.13. Notably, the error metrics are significantly higher than those observed in the first updating phase. This increase is attributed to the greater complexity of the dataset in the second phase, which reflects more advanced stages of fracture propagation. As loading continues, some samples exhibit early and severe cracking, while others follow delayed or alternative crack paths, resulting in bifurcated behavior. These variations introduce discontinuities in the data, making accurate approximation more difficult for the proxy models. Here, the neural network (NN) based proxy models demonstrated higher performance, as shown in Figure 4.13a, where the NN models achieved nearly twice the accuracy of the gPCE based approaches.

The required computational time for training the proxy models remained comparable to that in the first phase. Among the methods, gPCE was the most computationally efficient, while the low-rank NN model was the slowest to train.

Identification results

The trained proxy models were employed in MCMC analyses to run the identification of fracture parameters for the second updating phase. The MCMC analysis was conducted using 2000 steps and 100 chains. If performed with the full forward numerical model, this would require approximately 34 days of computation. By using proxy models, the total runtime (including the time for obtaining training dataset) was reduced by an estimated 29.5 days. This highlights the significant benefits of employing proxy modeling within Bayesian updating framework.

The identified parameter distributions are presented in Figure 4.14. The posterior distributions for σ_n narrowed even further for all proxy models. The tensile fracture energy G_{fn} also showed
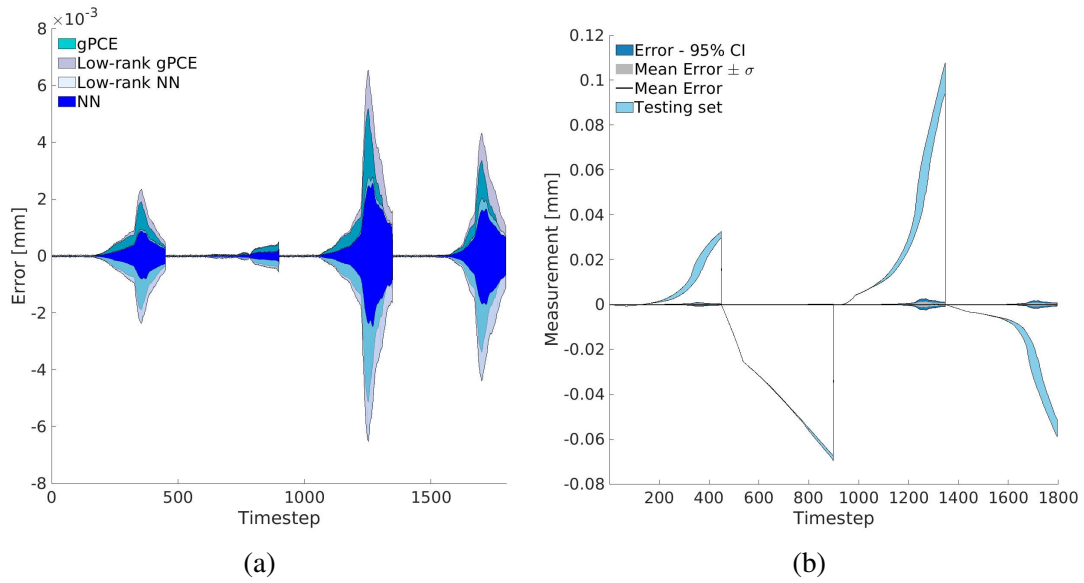
Figure 4.13: Second updating phase: a) 95% CI errors of used proxy models, b) NN model's error metrics together with the results of the testing set.

reduced uncertainty in most models, with the exception of the low-rank NN model. A similar trend was observed for σ_m, where the less accurate results from the low-rank NN model reflect its weaker performance in the first updating phase.

A notable improvement was achieved in the identification of the G_{fm} parameter. The extended crack propagation in this phase led to activation of this parameter, as previously indicated by the Sobol analysis (Figure 4.12b). All models achieved a significant reduction in the uncertainty of G_{fm}, with the NN model producing a posterior mean closest to the true value. Although its distribution remains broader than those of the other parameters, it is considered sufficient for engineering purposes. Nevertheless, further improvement for G_{fm} would likely require a additional testing approaches to achieve its more effective activation.
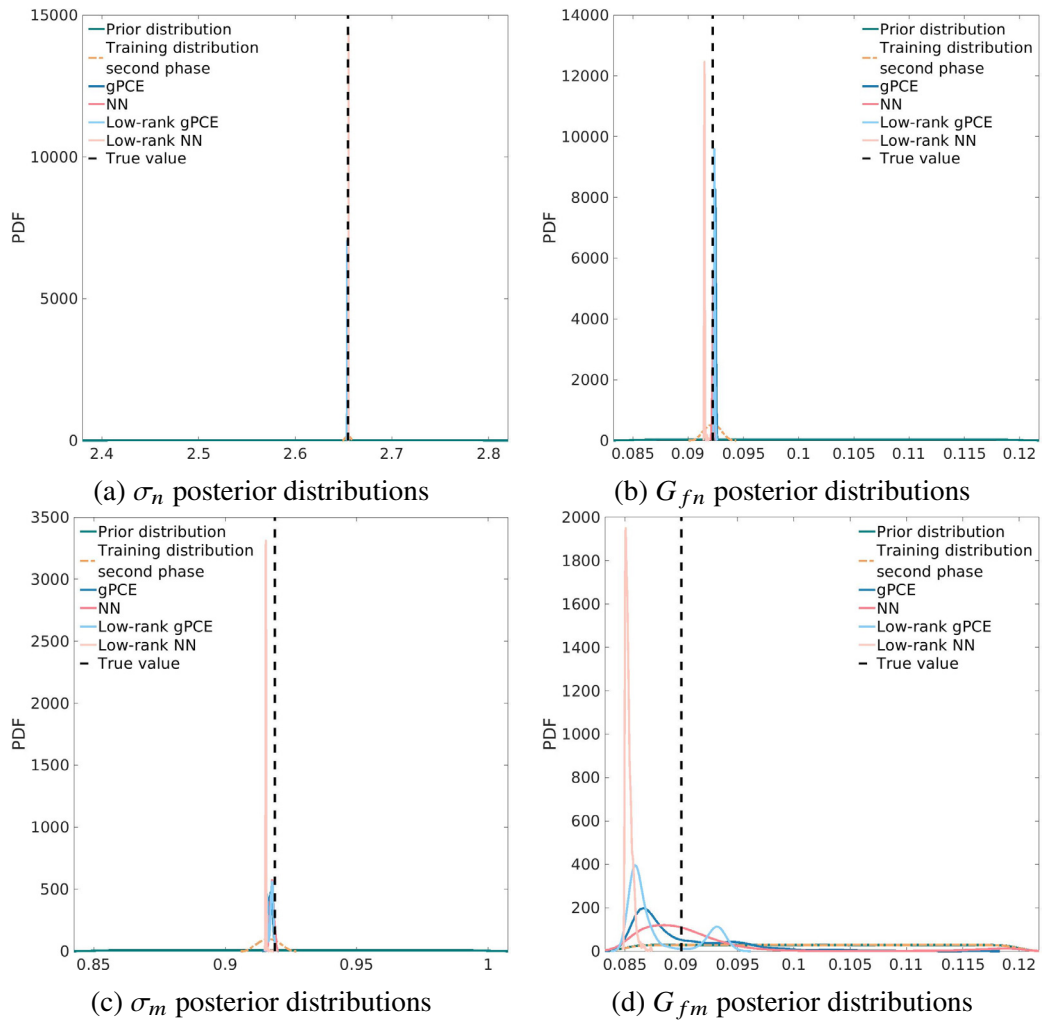
(a) σ_n posterior distributions

(b) G_{fn} posterior distributions

(c) σ_m posterior distributions

(d) G_{fm} posterior distributions

Figure 4.14: Second updating phase: Posterior distributions of tensile strength σ_n, tensile fracture energy G_{fn}, shear strength σ_m, and shear fracture energy G_{fm}.

5. EXPERIMENTAL APPLICATION AND VALIDATION OF METHODOLOGY FRAMEWORK

The third part of this research focuses on the application and validation of the identification methodology developed in Chapter 4, using real materials and laboratory data. Specifically, the study focuses on the identification of uncertain parameters of aluminium alloy 6060. This is achieved through tensile testing of non-standard specimens, including both rectangular and notched geometries, relying solely on simple measurements easily obtainable in standard laboratory settings. To accurately capture ductile material behavior, the numerical model introduced in Section 3.1 is modified to incorporate elastoplastic hardening and ductile fracture mechanisms. In addition, a test design procedure is presented by employing proxy model to evaluate the effectiveness of the identification process prior to data collection. Sections 5.1 to 5.5 present a overview of the methodology and results published in Paper (III) (see Appendix C).

5.1. Numerical model modification for ductile materials

Since the focus of this section is the identification of material parameters for aluminium alloy 6060—a ductile material, the numerical model described in Section 3.1 is modified and further extended to simulate ductile behavior. This is achieved by incorporating a linear hardening law, resulting in a model that now comprises three constitutive laws: an linear elastic law, a linear hardening law and an exponential softening law.

The elastic behavior of the material follows Hooke's law, defined by Young's modulus E and Poisson's ratio v.

During loading, every finite element is checked to determine whether yielding occurs. The von Mises equivalent stress is calculated at each Gaussian integration point according to:

$$\sigma_{\text{eq}} = \sqrt{\sigma_{xx}^2 + \sigma_{yy}^2 - \sigma_{xx}\sigma_{yy} + 3\tau_{xy}^2}. \tag{5.1}$$

The yield function is defined as:

$$f_y = \sigma_{\text{eq}} - \left(\sigma_0 + H \cdot \epsilon_p\right), \tag{5.2}$$

where σ_0 represents the initial yield strength, H denotes the hardening modulus, and ϵ_p corresponds to the equivalent plastic strain. Plastic yielding with isotropic hardening takes place at an integration point where the yield function has positive value. The plastic strain undergoes updating through the radial return algorithm (see [1]), while the stress tensor is recalculated as: $\boldsymbol{\sigma} = \boldsymbol{C}(\overline{\boldsymbol{\epsilon}} - \boldsymbol{\epsilon}_p)$, where $\boldsymbol{\epsilon_p}$ denotes the plastic strain tensor. This approach enables hardening to occur either within

portions of an element or throughout the entire element (active across all four integration points).

As loading continues and stresses exceed material strength, cracks begin to form. Crack behavior is governed by two uncoupled plasticity laws that account for material degradation and energy dissipation, as described in [1]. These laws are better suited for ductile materials as they exhibit damage through permanent plastic deformation rather than stiffness degradation (as is the case for quasi-brittle materials). Once the fracture criterion is met, the framework behaves similarly to that described for quasi-brittle materials in Section 3.3, but with variables redefined in the context of plasticity. The softening traction equation, originally introduced in Eq. 3.10, is now redefined as:

$$\bar{\bar{q}}_n = \sigma_n \left(1 - \exp\left[-\frac{\sigma_n}{G_{fn}}, \bar{\bar{\xi}}_{n,\mathrm{pl}} \right] \right), \tag{5.3}$$

where $\bar{\bar{\xi}}n$, pl is the internal softening variable corresponding to plastic deformation. Mode II (shear) fracture follows the same principle, using softening variables and functions defined in terms of plasticity. An illustration of the applied constitutive laws is given in Figure 5.1.
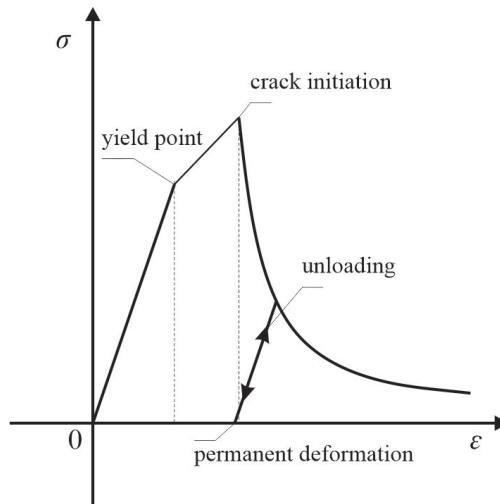

Figure 5.1: Constitutive laws for ductile material (stress–strain curve for one element). The material first follows a linear elastic law. After the occurrence of yielding according to the Von Mises criterion, linear hardening takes place. As the stress increases further, crack initiation occurs, followed by exponential softening law. During unloading, the stress–strain path runs parallel to the elastic stiffness line, resulting in permanent deformation of the material.

Now, based on defined constitutive laws, these parameters are consider uncertain and needs to be identified. Thus they are treated as random variables within Bayesian inference framework, and are collected in vector form as $\mathbf{z}$:

$$\mathbf{z}(\omega) := \left[E(\omega), \nu(\omega), \sigma_0(\omega), H(\omega), \sigma_n(\omega), G_{fn}(\omega) \right], \tag{5.4}$$

for which prior distributions $\pi(\mathbf{z}) = \pi(z_1, ..., z_{N_i})$ must be defined.

5.2. Definitions of errors of identification process

To perform parameter identification via Bayesian inference, it is necessary to define the error terms used to construct the likelihood function $\pi(\mathbf{d}m|\mathbf{z})$. These errors arise from the combined error component $\boldsymbol{\varepsilon}(\omega_e)$ associated with the observed measurements, as introduced in Eq. 4.3. Here, three additive error sources are considered: measurement error, numerical model error, and proxy modeling error.

$$\boldsymbol{\epsilon} = \boldsymbol{\epsilon}_{\text{meas}} + \boldsymbol{\epsilon}_{\text{model}} + \boldsymbol{\epsilon}_{\text{proxy}}. \tag{5.5}$$

The measurement error, $\boldsymbol{\epsilon}_{\text{meas}}$, are usually modeled using a normal distribution, $\boldsymbol{\epsilon}_{\text{meas}} \sim \mathcal{N}(\mathbf{0}, \mathbf{C}_{\text{meas}})$, characterized by zero mean and a diagonal covariance matrix $\mathbf{C}_{\text{meas}}$, under the assumption that individual error components are uncorrelated. The diagonal terms σ_i^2 originate from measurement device specifications, commonly expressed as percentages relative to the recorded values. Here, such percentages represent $3\sigma_i$ value, assuming normally distributed noise. Accordingly, the standard deviation σ_i is computed by dividing the maximum expected error by three.

The numerical model error, $\boldsymbol{\epsilon}_{\text{model}}$, can be treated in multiple ways. One strategy involves incorporating the covariance structure as an unknown parameter to be determined during the identification procedure [53]. As an alternative, these uncertainties can be evaluated deterministically through input-dependent functions, leveraging knowledge about limitations of the constitutive models and through comparison between simulation results and experimental data Modeling and proxy errors are generally systematic and may introduce bias. However, accurately quantifying this bias is often infeasible and, if done incorrectly, can lead to wrong parameter identification. To mitigate this risk, we adopt a simplified approach by assuming all error components to be Gaussian, independent, and unbiased.

The proxy modeling error, $\boldsymbol{\epsilon}_{\text{proxy}}$, results from differences between the predictions of the proxy model and those of the numerical model. Here, the gPCE method is used. As shown in Section 4.5, the gPCE proxy model showed precision comparable to alternative approaches such as NN, especially for the relatively simple fracture scenarios considered (such as uniaxial tension fracture). In addition to its modeling accuracy, gPCE is favored for its computational efficiency, straightforward training process, and straightforward statistical analysis. The standard deviation of the proxy error is estimated from the residuals of an independent validation (testing) dataset.

5.3. Test Design and experimental setup

Parameter identification was conducted on aluminium 6060 alloy specimens with unknown material properties using tensile loading experiments. Three distinct specimen geometries were chosen for the experiments (see Figure 5.2). Before conducting the physical experiments, a virtual testing design was done to evaluate the efficiency of the proposed specimen configurations, measurement methods, and experimental setups. Sobol sensitivity analysis was employed to

assess how individual parameters influence computational outcomes through virtual experiments that replicate the intended experimental tests. This methodology minimizes the probability of experimental failures and guarantees that the planned experiments provide meaningful data for parameter identification purposes.
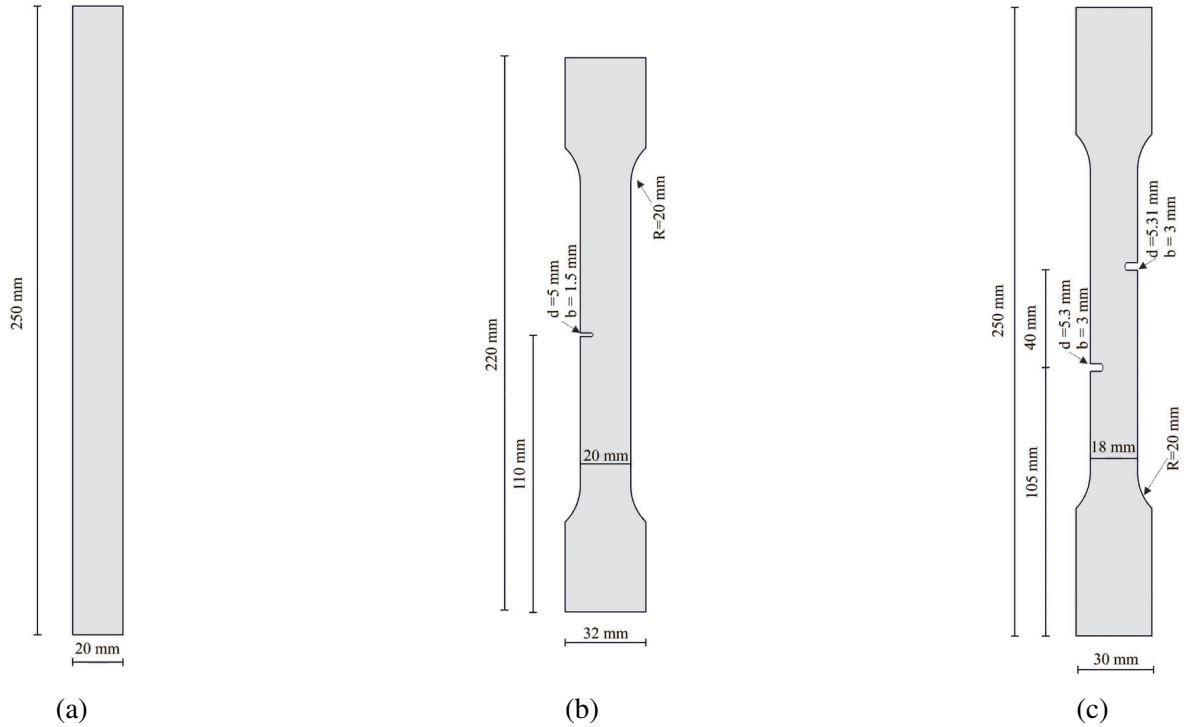

Figure 5.2: Aluminium 6060 alloy specimens: a) Rectangular, b) Dogbone single-notched, c) Dogbone double-notched.

Test Design

The unknown parameters for the aluminium 6060 alloy from Eq.5.4 are modeled as stochastic variables with initial uniform prior distributions, $z_i \sim \mathcal{U}(a, b)$. The corresponding bounds are defined by engineering judgment and are listed in Table 5.1.

Table 5.1: Prior distributions of aluminium alloy parameters.

Parameter	Distribution	Left bound (a)	Right bound (b)
E	$U(a, b)$	50.000 N/mm^2	100.000 N/mm^2
ν	$U(a, b)$	0.2	0.4
σ_0	$U(a, b)$	50 N/mm^2	150 N/mm^2
H	$U(a, b)$	2000 N/mm^2	6000 N/mm^2
σ_n	$U(a, b)$	150 N/mm^2	300 N/mm^2
G_{fn}	$U(a, b)$	100 N/mm	300 N/mm

Identification of parameters is done in two phases. In the first phase, a rectangular specimen (see Figure 5.2a) is used to identify the elastic parameters: Young's modulus E and Poisson's ratio ν. For this identification, a pair of measurements are chosen: force–displacement data and horizontal

deformation data obtained from two locations positioned on opposing lateral faces of the specimen. To verify that these measurements provide enough information, a virtual test design by Sobol sensitivity analysis was conducted. For this purpose, a total of 200 parameter sets were generated using QMC sampling. For each set, virtual measurements were taken at different timesteps under linear displacement-controlled loading. A gPCE surrogate model was trained using 150 samples, with the remaining 50 used for testing. The results, presented in Figures 5.3a and 5.3b, show that both elastic parameters are clearly sensitive to proposed measurements and thus identifiable.

(a) Force–displacement (rectangular)

(b) Lateral deformation (rectangular)

(c) Force–displacement (single-notched)
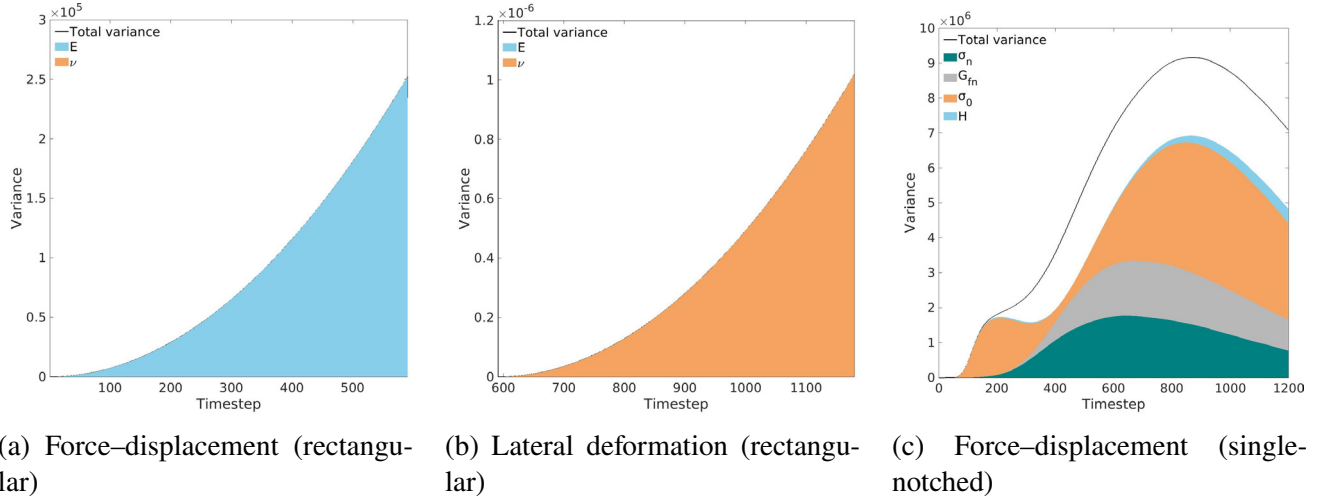
Figure 5.3: Sobol sensitivity analysis results by trained gPCE models. White regions indicate mixed parameter influence.

In the second phase, the elastoplastic hardening (yield strenght σ_0 and hardening modulus H) and fracture parameters (tensile strength σ_n and tensile fracture energy G_{fn}) are identified using a single-notched dog bone specimen (see Figure5.2b). Here, only the force–displacement measurements is proposed. Following the same approach, 2000 QMC samples were generated and a gPCE model was trained. As shown in Figure5.3c, the force–displacement measurement provides enough sensitivity to identify the elastoplastic and fracture parameters.

Experimental Setup

After confirming that the proposed measurements are sensitive to the uncertain parameters, experimental testing was carried out. Several measurement systems were used to accurately record the mechanical response of the test specimens. The aluminium specimens illustrated in Figure 5.2 were machined from 6060 T4 aluminium alloy stock utilizing CNC equipment, in accordance with ISO 6892 specifications.

Tensile loading tests were conducted using a Shimadzu AGX-V 250 kN Universal Testing Machine (UTM). The tests were displacement-controlled with a constant loading rate of 2 mm/min. Forces were measured using a load cell with a nominal capacity of 250 kN and accuracy class 0.5. Data acquisition was performed at a frequency of 100 Hz.

For the determination of Poisson's ratio, additional sensors were used. Longitudinal and transverse strains were recorded using LVDT sensors (HBM WA-L, 0–10 mm range), attached to a

specially designed 3D-printed fixture fabricated from ABS material with a BambuLab X1Carbon printer. The fixture ensured proper alignment and stable attachment of the sensors throughout loading. To ensure consistent measurements, the test cycle was repeated five times within the elastic deformation range prior to data collection.

For verification, an additional optical measurement system was used. A 2560×1440 pixel industrial camera was was oriented with its sensor plane parallel to the specimen face and programmed to acquire images at 0.5 second intervals. Camera operation was coordinated with the data acquisition software to record crosshead position and force measurements corresponding to each captured frame. The system incorporated a 5–50 mm varifocal lens (maximum aperture f/1.6). A random speckle pattern was applied onto the specimen surface to enable Digital Image Correlation (DIC) analysis. DIC processing was implemented in MATLAB utilizing open-source algorithms [94], following procedures outlined in [73]. To assess DIC accuracy, a calibration procedure was performed. Errors in displacement and strain were primarily attributed to lens distortion, surface preparation, and algorithmic constraints. Root-mean-square displacement uncertainty measured 0.1 mm, while strain noise remained below 1×10^{-3}. These errors were mainly due to camera resolution, with minor contributions from specimen surface quality and inherent DIC limitations. Despite this, the DIC data effectively captured the expected strain distribution in critical regions.
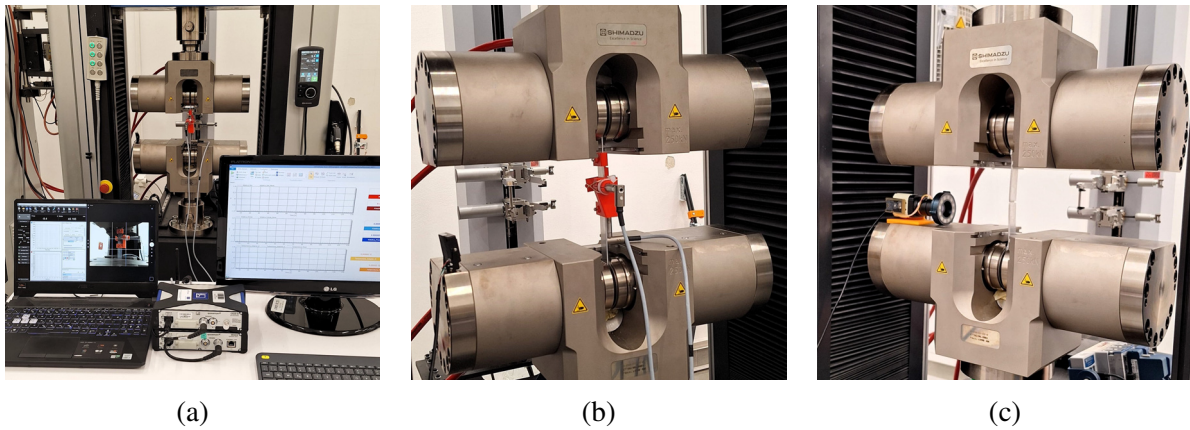

(a)   (b)   (c)

Figure 5.4: Experimental configuration: (a) Instrumentation setup, (b) UTM machine and LVDT sensors, (c) UTM machine and optical measurement system.

5.4. Identification and verification of the results

In this section, the results of the identification of uncertain parameters for aluminium 6060 alloy specimens are presented. The identification was conducted through experimental measurements in combination with a gPCE proxy model of a numerical model and a Markov Chain Monte Carlo (MCMC) method. To ensure consistency with the experimental testing setup, the virtual tests used for proxy model training were configured to reproduce identical boundary conditions and loading rates. Virtual measurements were collected from a timestep-based simulation, where each timestep corresponds to every tenth data point acquired by the measurement equipment. This

discretization produces 590 timesteps for measurements related to elastic parameter identification and 1200 timesteps for the elastoplastic and fracture parameter determination. All virtual test simulations for proxy model training were performed on a cluster computing system.

5.4.1. Identification of elastic parameters

The parameter estimation starts with training a proxy model to approximate the numerical simulation results for the given test. To train the gPCE model, 800 parameter combinations were sampled from the prior distribution using QMC sampling, plus 200 additional samples for testing. Computing the simulation results for these parameter samples on the cluster computer took about five minutes. Based on the Maximum Absolute Error (MAE), the best model was found to be a 4th-order polynomial with 15 coefficients per timestep.

Regarding the error distributions, the measurement error distribution for force–displacement data assumes that the standard deviation σ_i of the normal distribution is 0.167% of the measured value. This is based on the maximum error given by the UTM manufacturer (accuracy class 0.5), assuming this maximum error represents 3σ under normal distribution. For the lateral deformation measurements, the standard deviation is defined similarly using the error given by the LVDT manufacturer (also class 0.5), set to 0.167% of the measured value. A constant noise term of 0.0001 mm is also added to account for other noise sources—like measurement electronics, temperature effects, and similar factors—which show up as spikes because of the small measured values (see Figure 5.5b).

Given that elastic parameter identification involves only linear elastic response, modeling errors are neglected during this stage. The constitutive model employed in the numerical simulation provides sufficient accuracy for this application. The standard deviation of the surrogate model error is computed from the discrepancies between the trained gPCE model predictions and results from the 200 independent test samples. These error distributions, together with the experimental data, are presented in Figure 5.5.

The MCMC analysis used 100 Markov chains with 500 steps each, resulting in 50,000 total parameter combinations. The complete analysis finished in less than one minute. The resulting posterior distributions are shown in Figure 5.6. The results show successful identification of both elastic parameters, as the posterior distributions have low variance, indicating high confidence in the estimated values. The maximum posterior (MAP) values are 66,542 N/mm for Young's modulus E and 0.319 for Poisson's ratio ν. These values are used as known constants in the next phase of parameter identification.
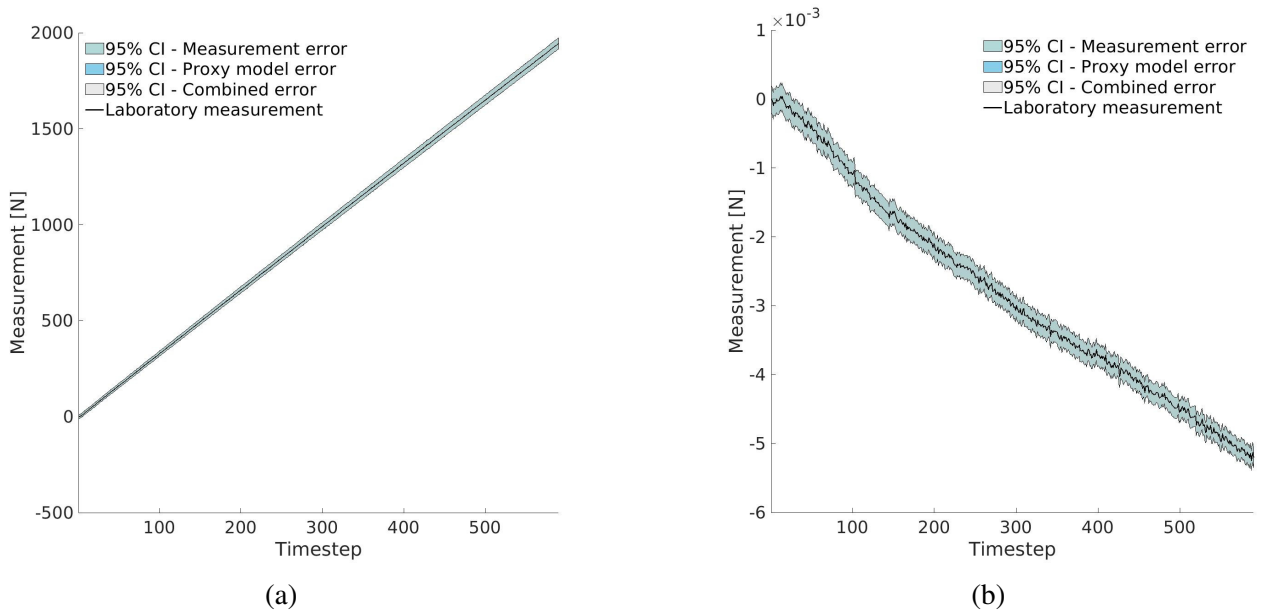
Figure 5.5: Identification of elastic parameters – 95% confidence interval error distributions (rectangular specimen): a) Force–displacement measurements, b) Lateral deformation measurements; Proxy model errors are negligible due to a small values.

5.4.2. Identification of elastoplastic and fracture parameters

This stage of the parameter identification deals with the elastoplastic hardening response of the material, microcrack development, macrocrack formation, and final material failure. These processes create complex datasets that are much more difficult than those from the elastic stage.

To train the gPCE model, 20,000 samples were drawn from the prior distributions, with another 5000 samples for testing and validation. These calculations, run on a cluster computer, took about 70 hours. After testing, a 9th-order polynomial gPCE model with 715 coefficients per timestep gave the best accuracy.

Proper definition of error distributions is important in this stage in order to achieve reliable identification results due to the presence of nonlinearities. The measurement error standard deviation, σ_i, was set to 0.167% of the measured value, based on the accuracy class of the measurement equipment. Modeling error was determined by comparing the numerical model with experimental data and considering the simplifications in the constitutive laws. Thus, this error was divided into two components. The first corresponds to linear elasticity, elastoplastic hardening, and initial microcrack formation. Here, a standard deviation of $\sigma_i = 25$ N was selected to cover natural variability of the material and also influence of nonlinearities by initial microcrack formations. The second component of modeling error covers the progression from initiated microcracks to a dominant macrocrack and final material failure. In the numerical model, this phase is approximated using an exponential softening law, which simplifies the complex fracture process. To reflect the greater uncertainty during failure, the standard deviation was set at $\sigma_i = 100$ N. The proxy model error was defined by comparing proxy model outputs and testing dataset results from numerical model. These error distributions, alongside experimental results, are shown in Figure 5.7.
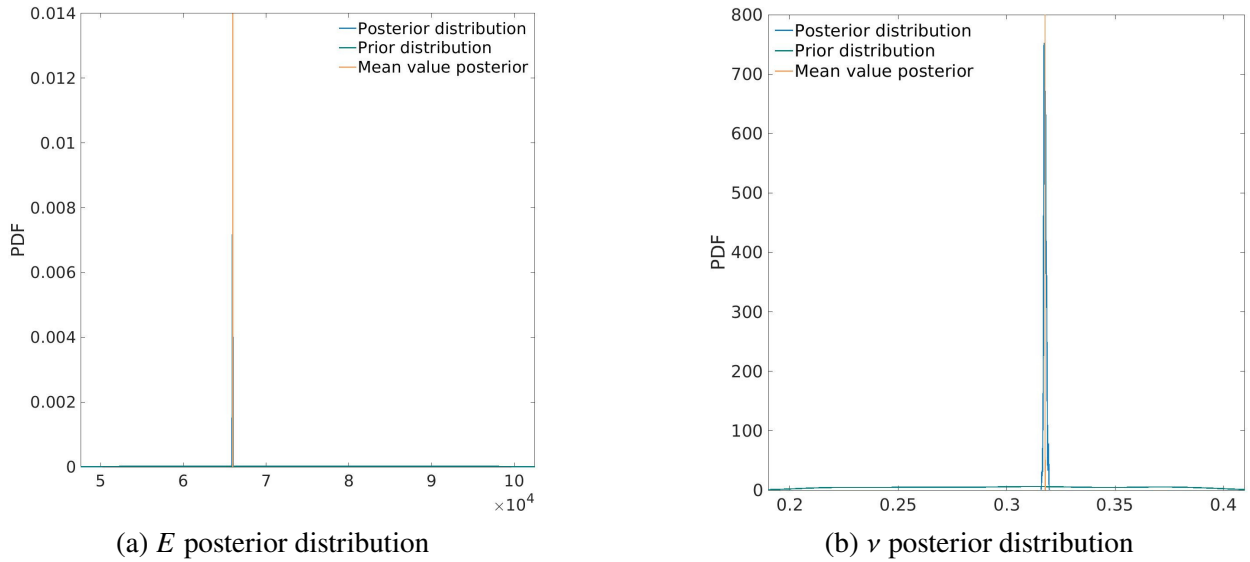
(a) E posterior distribution

(b) ν posterior distribution

Figure 5.6: Posterior distributions of Young's modulus E and Poisson's ratio ν parameters.
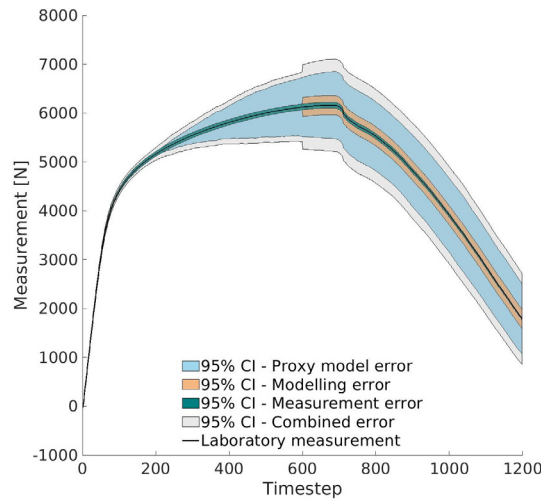

Figure 5.7: Identification of elastoplastic and fracture parameters (single-notched specimen) – 95% confidence interval error distributions.

The identification of elastoplastic and fracture parameters used 200 Markov chains with 5000 sampling steps each, giving 1,000,000 parameter evaluations in total. The complete process took less than 10 minutes. The resulting posterior distributions are shown in Figure 5.8. The posterior distribution of yield strength σ_0 shows very little variation, with a maximum posterior (MAP) value of 76.52 N/mm^2, indicating high confidence. The hardening modulus H also shows only small variation around its MAP value of 1626.01 N/mm^2. Similarly, tensile strength σ_n has a sharp peak at 171.11 N/mm^2, while tensile fracture energy G_{fn} shows somewhat more uncertainty but still has a clear peak around 258.17 N/mm, confirming good accuracy in its identification

These MAP values were employed in both the proxy and numerical models to compare simulated force–displacement response with experimental measurements. As demonstrated in Figure5.9, the proxy model follows the experimental data accurately, with deviations staying within 2%. The numerical model also corresponds well with the experimental outcomes, particularly in the elastic and elastoplastic regions, confirming the reliability of the identification. A minor discrepancy
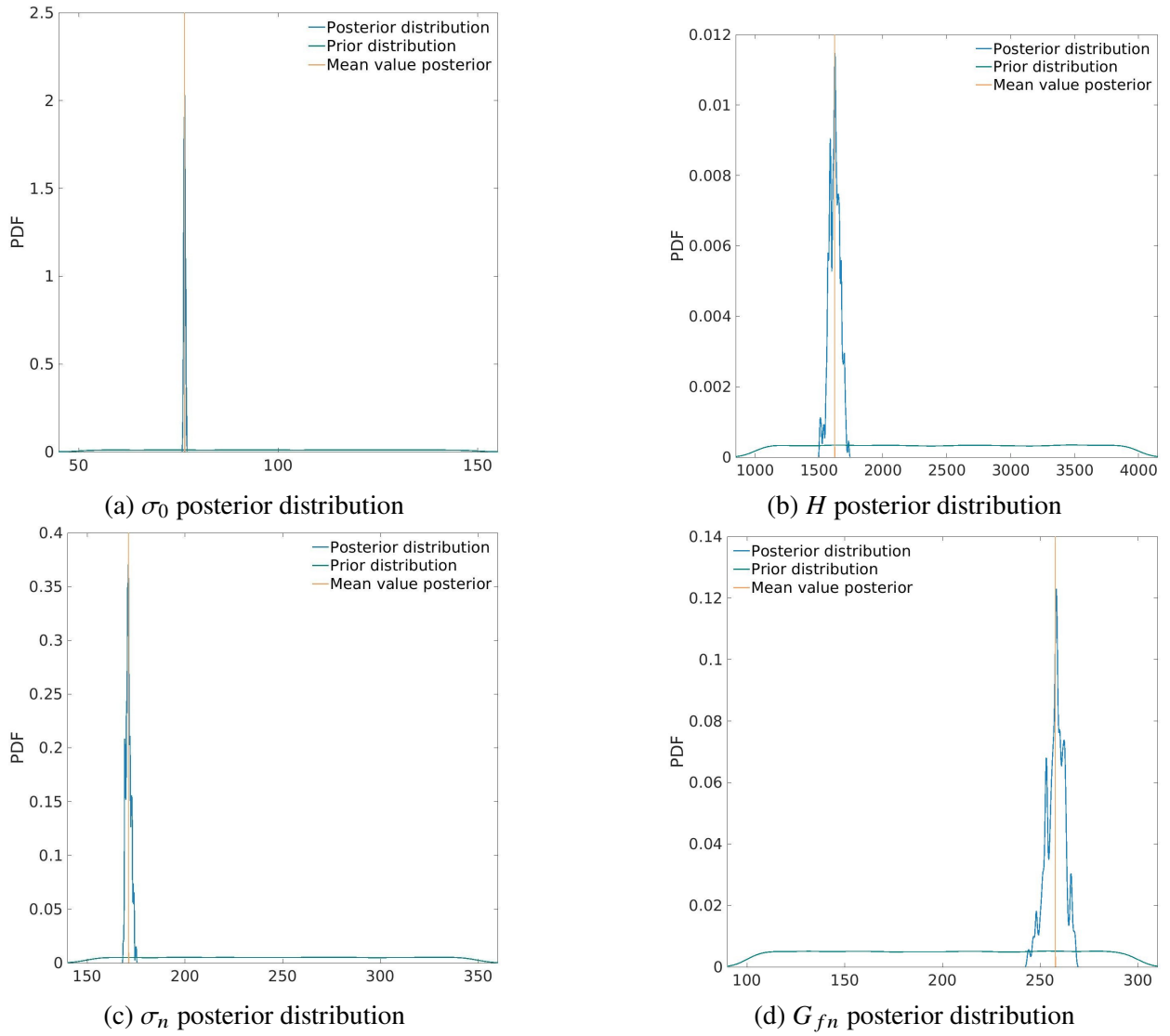
(a) σ_0 posterior distribution

(b) H posterior distribution

(c) σ_n posterior distribution

(d) G_{fn} posterior distribution

Figure 5.8: Posterior distributions for yield strength σ_0, hardening modulus H, tensile strength σ_n, and tensile fracture energy G_{fn}.

emerges after crack initiation, which is primarily attributed to variations between the proxy and numerical model (see also Figure5.7). The maximum error between the numerical simulation and experiment reached 8.9%, which is acceptable given the challenges of modeling nonlinear fracture behavior. Good matching between numerical model simulation and experimental test is also shown in Figure 5.13, where failure mechanisms are compared. For the single-notched dogbone specimen, both the experimental and numerical results (see Figure 5.13a show the development of a single dominant crack that initiates at the notch edge and propagates perpendicularly to the loading direction, toward the specimen's end.

5.4.3. Identification result verification

Verification of the identified elastic, elastoplastic, and fracture parameters was conducted through two test cases by comparing numerical model predictions with experimental measurements.
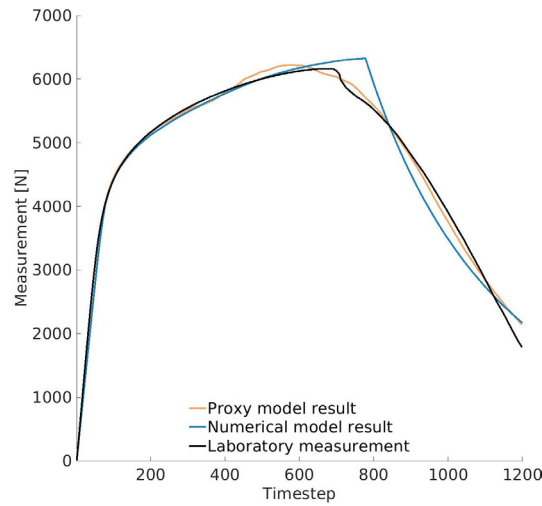
Figure 5.9: Comparison of obtained force–displacement results (single-notched specimen): Laboratory measurement vs. proxy model vs. numerical model.

The first case examined displacements and strain field values on a single-notched dogbone specimen, utilizing data from DIC measurements. The second verification used force-displacement data from a double-notched dogbone specimen (see Figure 5.2c). This approach enabled validation not only against different measurement types from the specimen employed for parameter identification, but also against a specimen with different geometry and thus stress state. For each verification case, 20 samples were drawn from the obtained posterior parameter distributions using QMC sampling. These parameter sets were applied in forward numerical simulations, and the results were compared with experimental measurements to assess the accuracy and reliability of the proposed identification methodology.

In the first verification case, two points were chosen on the single-notched dogbone specimen: (12 mm, 100 mm) and (12 mm, 120 mm), positioned on opposite sides of the expected crack path. The vertical displacement difference between these two points, measured by DIC, was compared with numerical results, as shown in Figure 5.10. Some differences between the DIC and numerical results can be seen, with the largest differences appearing at the start of the test. This is mainly due to the inherent limitations of DIC systems in measuring very small displacements accurately. As the test continues and displacements grow larger, DIC measurements become more reliable. The maximum observed error between DIC and numerical predictions is 11.9%. Towards the end of the test, the differences keep decreasing, leading to close agreement between the model and DIC measurements.

Additionally, strain field comparisons were performed for a total vertical displacement of 3.899 mm. Strain components were calculated from the DIC displacement data using standard post-processing techniques. As shown in Figure 5.11, the numerically predicted and experimentally measured strain fields are in good agreement, both in terms of spatial distribution and magnitude.

The second verification case focused on comparing force-displacement measurements from the double-notched dogbone specimen, which has different notch sizes and geometry compared to the specimens used in parameter identification. As such, this case represents a more rigorous test of
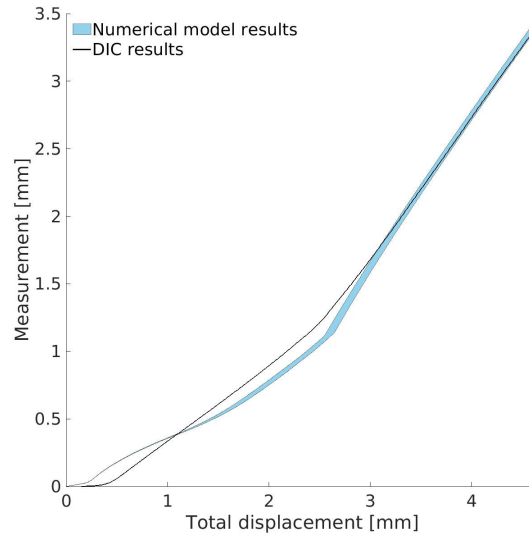
Figure 5.10: Comparison of obtained vertical displacement difference between two points for 20 posterior samples (single-notched dogbone specimen): DIC measurements vs. numerical model.

the identified parameter values generalization. Despite these geometric and loading differences, the comparison in Figure 5.12 shows excellent agreement between experimental and simulated results. The model captures both the elastic and elastoplastic regimes with high precision. Minor deviations are observed in the fracture region, where the maximum error reaches 7.8%.

A comparison of crack patterns for the double-notched dogbone specimen is shown in Figure 5.13b. A main macrocrack starts from the upper notch in both cases and causes complete failure. Additional damage appears around the lower notch in both experiments and simulations. In the numerical results, several microcracks form near the wider notches, though their contribution to energy dissipation stays limited. This behavior closely matches the experimental observations, where minor damage was also limited to the area around the lower notch.

(a)   (b)   (c)
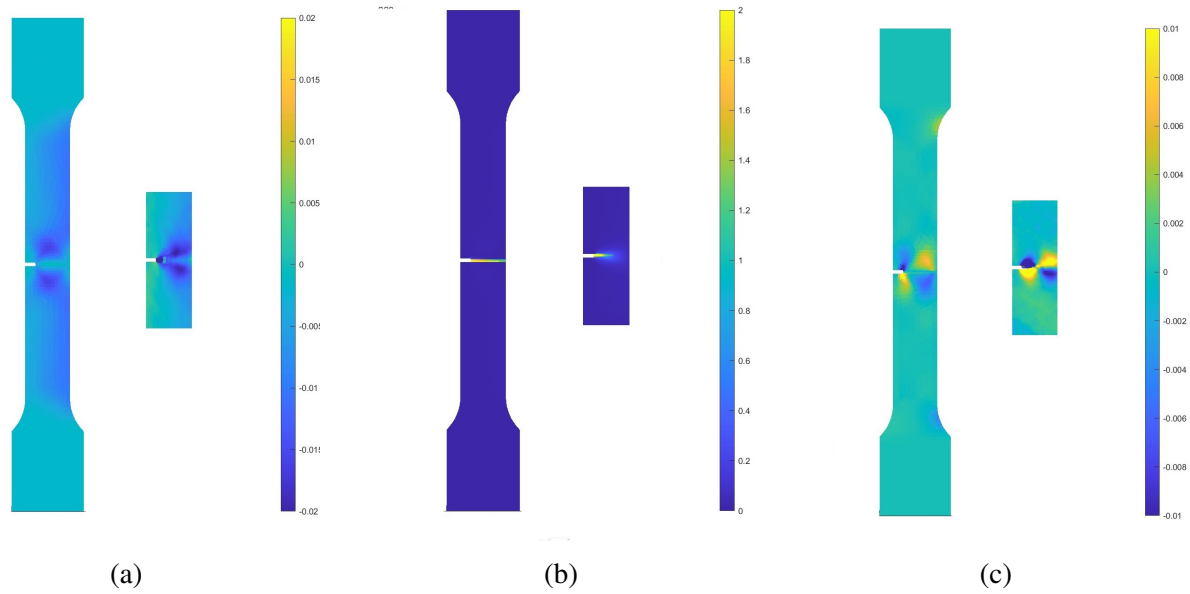
Figure 5.11: Comparison of obtained strain field components between the numerical model and DIC measurements at a displacement of 3.899 mm (single-notched specimen): (a) ϵ_{xx}, (b) ϵ_{yy}, (c) ϵ_{xy}. Left visualization is numerical model results, right zoomed part shows DIC results.
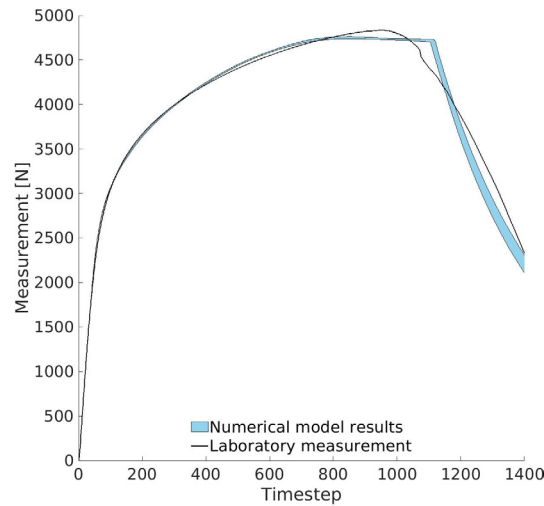

Figure 5.12: Comparison of obtained force-displacement measurement for 20 posterior samples (double-notched specimen): Laboratory measurements vs. numerical model.

(a) Fracture of single-notched specimen in laboratory vs. simulation.

(b) Fracture of double-notched specimen in laboratory vs. simulation.
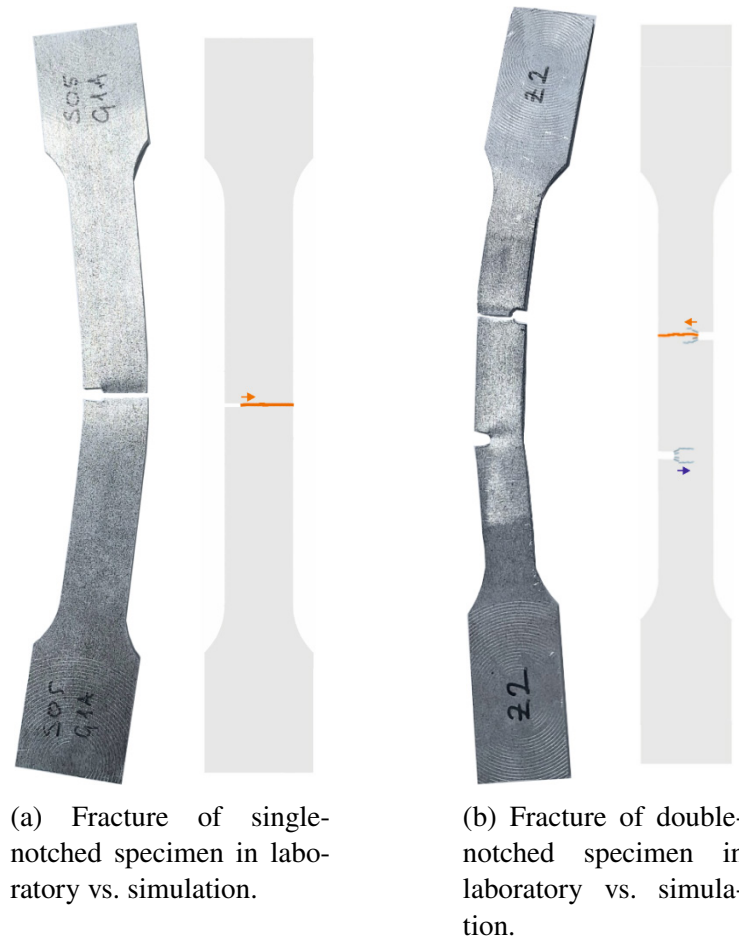
Figure 5.13: Comparison of failure mechanisms for notched dogbone specimens: (a) Fracture of single-notched specimen in laboratory vs. by numerical model in simulation, (b) Fracture of double-notched specimen in laboratory vs. numerical model in simulation. Cracks in the simulation are shown from blue to orange color scale, which represents energy dissipation (blue = low, orange = high). Colored arrows show crack propagation directions.

6. CONCLUSION AND SCIENTIFIC CONTRIBUTION

Every improvement in fracture simulation methods contributes to more accurate and reliable assessment of the safety and durability of both existing and new structural designs. The key to further progress lies in the continued development of precise numerical models, for which reliable values of input parameters must be ensured to accurately simulate the behavior of the analyzed structures.

The numerical model developed in this work enables precise and computationally efficient simulation of fracture in quasi-brittle materials at the macrostructural scale. Its efficiency stems from the localized nature of the embedded discontinuity method, which eliminates mesh sensitivity and avoids redefinition of the global stiffness matrix when new cracks form. Material degradation and energy dissipation is governed by damage exponential softening law, which introduces permanent damage of the material as the crack forms. Fracture initiation, the location and orientation of the crack, is governed by criteria based solely on the local stress state within each finite element. This works introduces a Maximum shear stress criterion for shear-dominated failure alongside Rankine criterion, thus enabling model application to fracture under tensile and compressive loading. The validity and accuracy of the fracture mechanisms were demonstrated through representative examples.

Beyond macrostructural modeling, the approach is extended to the mesostructural level to simulate fracture in heterogeneous materials. Here, the continuum model provides a precise representation of the stress state and unbiased fracture results. This approach allows accurate modeling of the effects of different constituents with varying elastic and fracture parameters on the material's global behavior during fracture. Continuum models based on finite elements with embedded discontinuities for crack propagation have not yet been used to simulate heterogeneous structures, so this approach represents a novelty in the literature. To enable this, specialized algorithms were developed to track crack initiation and propagation throughout the material domain. These algorithms effectively eliminate the "stress-locking" phenomenon, which can compromise simulation performance in complex fracture scenarios. The combination of a crack clustering algorithm based on machine learning with algorithms for continuous tracking of crack propagation at the global level also represents a novel contribution to the literature. The model performance was tested on the new examples of multiphase heterogeneous material. Here, the realistic stress state representation yielded unbiased fracture results for both tensile and compressive load cases. The energy dissipation, displacement field and crack pattern plots proved its accurate and reliable performance.

The development of the fracture parameter identification methodology based on ED-FEM model, determines the optimal and computationally efficient way to establish their reliable values, thereby enhancing the credibility of simulation results for real structures. As part of the method-

ology, the previously developed numerical model is integrated with selected synthetic (virtual) measurements using the Bayesian inference method. The focus is on using simpler measurements, such as horizontal and vertical displacements on the structure. Since the fracture model used relies solely on parameters such as strength and fracture energy, the physical basis of the approach ensures the relevance and further applicability in engineering practice. To approximate the resulting posterior distributions, a robust, model-independent Markov Chain Monte Carlo (MCMC) method based on the Metropolis–Hastings algorithm is employed. To enable computational efficiency and feasibility of the MCMC identification procedure, several types of proxy models are developed to approximate the solutions of the numerical model in a computationally efficient manner. These include General polynomial chaos expansion (gPCE) and neural network (NN) models. A special emphasis was placed on NN based models, which have not yet been applied to crack propagation problems in the literature. In addition, an autoencoder model based on neural networks was introduced to reduce the dimensionality of the measurement data, thereby enhancing computational efficiency and filtering out noise. The precision and efficiency of each proxy models and their impact on the identification results was analyzed to determine the most optimal approach for fracture parameter identification. The methodology was evaluated on both simple and complex fracture cases. Results demonstrated that all applied proxy models within the methodology yielded satisfactory results, with certain differences. In simpler fracture cases, gPCE proved to be the best choice due to its high accuracy, computational efficiency, and straightforward sensitivity analysis. In more complex fracture problems, Neural network models showed to be most suitable with high approximation accuracy.

Finally, the developed framework was experimentally verified to assess its practical applicability and predictive accuracy. An aluminum 6060 alloy with unknown parameters was selected for this purpose. The developed numerical model was modified and extended by introducing a linear isotropic hardening law combined with an exponential softening plasticity model, allowing the simulation of ductile fracture. The yielding of the material is defined by the von Mises criterion, evaluated at each integration point, thereby allowing hardening within part of an element or across its entire domain. The plasticity model introduces permanent plastic deformation as the crack develops. Three specimen geometries with non-standard designs were manufactured from the aluminum material, including rectangular and dogbone shapes with various notch configurations. These notches were introduced to initiate fracture but also resulted in stress concentrations that complicate parameter identification. The specimens were subjected to uniaxial tensile testing using a universal testing machine (UTM). Prior to the experiments, a Sobol sensitivity analysis was conducted through virtual simulations to evaluate the effectiveness of the proposed specimen shapes and measurement techniques for identification of parameters. The selected measurements included simple force–displacement curves and lateral deformation data. Parameter identification was performed in two phases. In the first phase, the elastic parameters were identified using the rectangular specimen. These identified values were then applied to a single-notched dogbone specimen for the identification of elastoplastic and fracture parameters. The narrow posterior distributions obtained in both phases indicated a high degree of certainty in the estimated results.

These results were further verified by running numerical simulations using the identified parameter values and comparing them to experimental measurements from different measurement setups, as well as an independent specimen geometry (a double-notched dogbone). The accurate agreement between the results confirms the predictive accuracy, reliability, and generalizability of the proposed methodological framework.

7.   FUTURE RESEARCH

The numerical model and parameter identification methodology developed in this work provide a solid foundation for a range of future applications and research directions. Several areas for future research are outlined below.

1. Extension to geomechanical applications

Future work will extend the numerical framework to geomechanical applications by incorporating internal friction parameters and adapting the constitutive laws for problems such as landslides, foundation failures, and retaining wall design.

2. Simulation of dynamic loading

The model will be further developed to simulate dynamic loading scenarios, such as seismic events. This will require implementing time–integration schemes and extending the constitutive laws to capture rate-dependent behavior.

3. Transition to three-dimensional modeling

To further enhance the model's applicability to real-world structures, future research will focus on its extension to three dimensions. A 3D implementation would enable the more precise simulation of complex fracture phenomena in large structures.

4. Parameter identification for mesostructural heterogeneous materials

Future work will apply the developed parameter identification approach to mesostructural heterogeneous materials. This will involve both synthetic (virtual) testing and experimental verification to assess the method's robustness in identifying properties of material constituents, thereby supporting the accurate modeling of multiphase composites and other complex materials.

5. Development of physics-informed neural networks (PINNs)

To further improve the accuracy and generalization of the identification methodology, future work will focus on developing Physics-informed neural networks (PINNs) as proxy model. This model will integrate physical laws directly into the training process, which will allow to be trained from limited data and make better predictions for complex fracture cases.

6. Advanced experimental validation

Additional experimental verifications will be carried out to validate both the numerical model and the identification methodology under more complex loading conditions. These experiments

will include multiaxial loading, cyclic loads, and interaction of multiple failure mechanisms. The goal is to assess the predictive capabilities and generalizability of the framework for broader engineering application.

8. LITERATURE

[1]   A. Ibrahimbegovic, *Nonlinear Solid Mechanics*. Springer, 2009, vol. 160. DOI: `10.1007/978-90-481-2331-5_1`.

[2]   E. Karavelić, M. Nikolić, A. Ibrahimbegovic, and A. Kurtović, "Concrete meso-scale model with full set of 3d failure modes with random distribution of aggregate and cement phase. part i: Formulation and numerical implementation," *Computer Methods in Applied Mechanics and Engineering*, vol. 344, pp. 1051–1072, 2019. DOI: `https://doi.org/10.1016/j.cma.2017.09.013`.

[3]   R. Zhou, Z. Song, and Y. Lu, "3d mesoscale finite element modelling of concrete," *Computers & Structures*, vol. 192, 2017. DOI: `https://doi.org/10.1016/j.compstruc.2017.07.009`.

[4]   P. Grassl, "3d lattice meso-scale modelling of the effect of lateral compression on tensile fracture processes in concrete," *International Journal of Solids and Structures*, vol. 262-263, 2023. DOI: `https://doi.org/10.1016/j.ijsolstr.2022.112086`.

[5]   J. Dujc, B. Brank, and A. Ibrahimbegovic, "Quadrilateral finite element with embedded strong discontinuity for failure analysis of solids," *Computer Modeling in Engineering and Sciences*, vol. 69, 2010-01. DOI: `10.3970/cmes.2010.069.223`.

[6]   A. Stanić, B. Brank, A. Ibrahimbegovic, and H. Matthies, "Crack propagation simulation without crack tracking algorithm: Embedded discontinuity formulation with incompatible modes," *Computer Methods in Applied Mechanics and Engineering*, vol. 386, p. 114 090, 2021. DOI: `https://doi.org/10.1016/j.cma.2021.114090`.

[7]   A. Stanić, B. Brank, and D. Brancherie, "Fracture of quasi-brittle solids by continuum and discrete-crack damage models and embedded discontinuity formulation," *Engineering Fracture Mechanics*, vol. 227, 2020. DOI: `https://doi.org/10.1016/j.engfracmech.2020.106924`.

[8]   H. Smoljanović, Ž. Nikolić, and N. Živaljić, "A combined finite–discrete numerical model for analysis of masonry structures," *Engineering Fracture Mechanics*, vol. 136, 2015. DOI: `https://doi.org/10.1016/j.engfracmech.2015.02.006`.

[9]   M. Gimenes, E. A. Rodrigues, L. A. Bitencourt, and O. L. Manzoli, "2d mesoscale modeling of compressive fracture in concrete using a mesh fragmentation technique," *International Journal of Solids and Structures*, vol. 260-261, 2023. DOI: `https://doi.org/10.1016/j.ijsolstr.2022.112031`.

[10] J. Čarija, E. Marenić, T. Jarak, and M. Nikolić, "Discrete lattice element model for fracture propagation with improved elastic response," *Applied Sciences*, vol. 14(3), p. 1287, 2024. DOI: `https://doi.org/10.3390/app14031287`.

[11]   S.-M. Kim and R. K. Abu Al-Rub, "Meso-scale computational modeling of the plastic-damage response of cementitious composites," *Cement and Concrete Research*, vol. 41, 2011. DOI: https://doi.org/10.1016/j.cemconres.2010.12.002.

[12]   A. Lisjak and G. Grasselli, "A review of discrete modeling techniques for fracturing processes in discontinuous rock masses," *Journal of Rock Mechanics and Geotechnical Engineering*, vol. 6, no. 4, pp. 301–314, 2014. DOI: https://doi.org/10.1016/j.jrmge.2013.12.007.

[13]   M. Nikolić, T. roje-Bonacci, and A. Ibrahimbegovic, "Overview of the numerical methods for the modelling of rock mechanics problems," *Tehnicki Vjesnik-technical Gazette*, vol. 23, pp. 627–637, 2016. [Online]. Available: https://api.semanticscholar.org/CorpusID:11755905.

[14]   G. D. Nguyen, A. M. Korsunsky, and I. Einav, "A constitutive modelling framework featuring two scales of behaviour: Fundamentals and applications to quasi-brittle failure," *Engineering Fracture Mechanics*, vol. 115, pp. 221–240, 2014. DOI: https://doi.org/10.1016/j.engfracmech.2013.11.006.

[15]   T. T. Nguyen, J. Yvonnet, M. Bornert, and C. Chateau, "6 - modeling of complex microcracking in quasi-brittle materials: Numerical methods and experimental validations," in *Advances in Multi-Physics and Multi-Scale Couplings in Geo-Environmental Mechanics*, F. Nicot and O. Millet, Eds., Elsevier, 2018, pp. 171–204. DOI: https://doi.org/10.1016/B978-1-78548-278-6.50006-2.

[16]   L. F. Friedrich, I. Iturrioz, A. B. Colpo, and S. Vantadori, "Fracture failure of quasi-brittle materials by a novel peridynamic model," *Composite Structures*, p. 117 402, 2023. DOI: https://doi.org/10.1016/j.compstruct.2023.117402.

[17]   J. Oliver, A. Huespe, and P. Sánchez, "A comparative study on finite elements for capturing strong discontinuities: E-fem vs x-fem," *Computer Methods in Applied Mechanics and Engineering*, vol. 195, pp. 4732–4752, 2006. DOI: https://doi.org/10.1016/j.cma.2005.09.020.

[18]   N. Moës and T. Belytschko, "Extended finite element method for cohesive crack growth," *Engineering Fracture Mechanics*, vol. 69, pp. 813–833, 2002. DOI: https://doi.org/10.1016/S0013-7944(01)00128-X.

[19]   C. Linder and F. Armero, "Finite elements with embedded strong discontinuities for the modeling of failure in solids," *International Journal for Numerical Methods in Engineering*, vol. 72, pp. 1391–1433, 2007. DOI: https://doi.org/10.1002/nme.2042.

[20]   Y. Zhang, R. Lackner, M. Zeiml, and H. A. Mang, "Strong discontinuity embedded approach with standard sos formulation: Element formulation, energy-based crack-tracking strategy, and validations," *Computer Methods in Applied Mechanics and Engineering*, vol. 287, 2015. DOI: https://doi.org/10.1016/j.cma.2015.02.001.

[21] M. Nikolic, E. Karavelić, A. Ibrahimbegovic, and P. Miščević, "Lattice element models and their peculiarities," *Archives of Computational Methods in Engineering*, vol. 25, pp. 753–784, 2018. DOI: `10.1007/s11831-017-9210-y`.

[22] M. Nikolic and A. Ibrahimbegovic, "Rock mechanics model capable of representing initial heterogeneities and full set of 3d failure mechanisms," *Computer Methods in Applied Mechanics and Engineering*, vol. 290, pp. 209–227, 2015. DOI: `https://doi.org/10.1016/j.cma.2015.02.024`.

[23] M. Nikolic, A. Ibrahimbegovic, and P. Miscevic, "Brittle and ductile failure of rocks: Embedded discontinuity approach for representing mode i and mode ii failure mechanisms: Brittle and ductile failure of rocks," *International Journal for Numerical Methods in Engineering*, vol. 102, 2015-05. DOI: `10.1002/nme.4866`.

[24] Z. Rizvi, M. Nikolic, and F. Wuttke, "Lattice element method for simulations of failure in bio-cemented sands," *Granular Matter*, vol. 21, p. 18, 2019. DOI: `10.1007/s10035-019-0878-6`.

[25] M. Nikolić, "Discrete element model for the failure analysis of partially saturated porous media with propagating cracks represented with embedded strong discontinuities," *Computer Methods in Applied Mechanics and Engineering*, vol. 390, p. 114 482, 2022. DOI: `https://doi.org/10.1016/j.cma.2021.114482`.

[26] M. Nikolić, X. N. Do, A. Ibrahimbegovic, and Ž. Nikolić, "Crack propagation in dynamics by embedded strong discontinuity approach: Enhanced solid versus discrete lattice model," *Computer Methods in Applied Mechanics and Engineering*, vol. 340, pp. 480–499, 2018. DOI: `https://doi.org/10.1016/j.cma.2018.06.012`.

[27] M. Nikolic, A. Ibrahimbegovic, and P. Miscevic, "Discrete element model for the analysis of fluid-saturated fractured poro-plastic medium based on sharp crack representation with embedded strong discontinuities," *Computer Methods in Applied Mechanics and Engineering*, vol. 298, pp. 407–427, 2016. DOI: `https://doi.org/10.1016/j.cma.2015.10.009`.

[28] J. Čarija, M. Nikolić, A. Ibrahimbegovic, and Ž. Nikolić, "Discrete softening-damage model for fracture process representation with embedded strong discontinuities," *Engineering Fracture Mechanics*, vol. 236, p. 107 211, 2020. DOI: `https://doi.org/10.1016/j.engfracmech.2020.107211`.

[29] D. Dias-da-Costa, J. Alfaiate, L. Sluys, P. Areias, and E. Júlio, "An embedded formulation with conforming finite elements to capture strong discontinuities," *International Journal for Numerical Methods in Engineering*, vol. 93, no. 2, pp. 224–244, 2013. DOI: `https://doi.org/10.1002/nme.4393`.

[30] I. Dias, J. Oliver, and O. Lloberas-Valls, "Strain-injection and crack-path field techniques for 3d crack-propagation modelling in quasi-brittle materials," *International Journal of Fracture*, vol. 212, pp. 67–87, 2018. DOI: `https://doi.org/10.1007/s10704-018-0293-8`.

[31] J. Oliver, I. Dias, and A. Huespe, "Crack-path field and strain-injection techniques in computational modeling of propagating material failure," *Computer Methods in Applied Mechanics and Engineering*, vol. 274, pp. 289–348, 2014. DOI: `https://doi.org/10.1016/j.cma.2014.01.008`.

[32] D. Brancherie and A. Ibrahimbegovic, "Novel anisotropic continuum-discrete damage model capable of representing localized failure of massive structures: Part i: Theoretical formulation and numerical implementation," *Engineering Computations*, vol. 26, pp. 100–127, 2009. DOI: `https://doi.org/10.1108/02644400910924825`.

[33] J. Oliver, "Modelling strong discontinuities in solid mechanics via strain softening constitutive equations. part 1: Fundamentals," *International Journal for Numerical Methods in Engineering*, vol. 39, no. 21, pp. 3575–3600, 1996. DOI: `https://doi.org/10.1002/(SICI)1097-0207(19961115)39:21<3575::AID-NME65>3.0.CO;2-E`.

[34] S. Saloustros, L. Pelà, M. Cervera, and P. Roca, "Finite element modelling of internal and multiple localized cracks," *Computational Mechanics*, vol. 59, pp. 299–316, 2017. DOI: `https://doi.org/10.1007/s00466-016-1351-6`.

[35] A. Ortega, E. Roubin, Y. Malecot, and L. Daudeville, "A mixed-mode e-fem approach for the study of local fracture processes in heterogeneous quasi-brittle materials," *Materials and Structures*, vol. 55, p. 222, 2022. DOI: `https://doi.org/10.1617/s11527-022-02055-y`.

[36] N. Benkemoun, E. Roubin, and J.-B. Colliat, "Fe design for the numerical modelling of failure induced by differential straining in meso-scale concrete: Algorithmic implementation based on operator split method," *Finite Elements in Analysis and Design*, vol. 137, pp. 11–25, 2017. DOI: `https://doi.org/10.1016/j.finel.2017.08.003`.

[37] Y. Huang, C. Shao, B. Wu, J. L. Beck, and H. Li, "State-of-the-art review on bayesian inference in structural system identification and damage assessment," *Advances in Structural Engineering*, vol. 22, no. 6, pp. 1329–1351, 2019. DOI: `10.1177/1369433218811540`.

[38] B. V. Rosić, A. Kučerová, J. Sýkora, O. Pajonk, A. Litvinenko, and H. G. Matthies, "Parameter identification in a probabilistic setting," *Engineering Structures*, vol. 50, pp. 179–196, 2013. DOI: `https://doi.org/10.1016/j.engstruct.2012.12.029`.

[39] N. Noii, A. Khodadadian, and T. Wick, "Bayesian inversion for anisotropic hydraulic phase-field fracture," *Computer Methods in Applied Mechanics and Engineering*, vol. 386, p. 114 118, 2021. DOI: `https://doi.org/10.1016/j.cma.2021.114118`.

[40] H. G. Matthies, E. Zander, B. V. Rosić, A. Litvinenko, and O. Pajonk, "Inverse problems in a bayesian setting," in *Computational Methods for Solids and Fluids: Multiscale Analysis, Probability Aspects and Model Reduction*. Springer International Publishing, 2016, pp. 245–286. DOI: `10.1007/978-3-319-27996-1_10`.

[41] J. Lee and M. M. Lopez, "An experimental study on fracture energy of plain concrete," *Int J Concr Struct Mater*, 2014. DOI: `10.1007/s40069-014-0068-1`.

[42] E. Markiewicz and B. Langrand, "Characterisation and parameters identification of materials constitutive and damage models: From normalised direct approach to most advanced inverse problem resolution," *Procedia Engineering*, vol. 173, pp. 33–40, 2017. DOI: `https://doi.org/10.1016/j.proeng.2016.12.016`.

[43] X. Ruifeng, X. Xueyong, and Y. Jianlin, "Experimental and numerical investigation of fracture behavior of ultra high performance concrete," *Journal of Materials Research and Technology*, vol. 25, pp. 3109–3119, 2023. DOI: `https://doi.org/10.1016/j.jmrt.2023.06.117`.

[44] I. Rhee, J. S. Lee, and Y.-S. Roh, "Fracture parameters of cement mortar with different structural dimensions under the direct tension test," *Materials*, vol. 12, no. 11, p. 1850, 2019. DOI: `10.3390/ma12111850`.

[45] J. van Mier and M. van Vliet, "Uniaxial tension test for the determination of fracture parameters of concrete: State of the art," *Engineering Fracture Mechanics*, vol. 69, no. 2, pp. 235–247, 2002. DOI: `https://doi.org/10.1016/S0013-7944(01)00087-X`.

[46] W. Brocks and I. Scheider, "Identification of material parameters for structural analyses," *Structural Durability and Health Monitoring*, vol. 6, pp. 189–212, 2010.

[47] B. Conde, P. Eguía, G. Stavroulakis, and E. Granada, "Parameteridentificationmasonryarchbridges," *Engineering Structures*, vol. 172, pp. 275–284, 2018. DOI: `https://doi.org/10.1016/j.engstruct.2018.06.040`.

[48] F. Marsili, N. Friedman, P. Croce, P. Formichi, and F. Landi, "On bayesian identification methods for the analysis of existing structures," 2016, pp. 116–123. DOI: `10.2749/stockholm.2016.0116`.

[49] A. Lye, A. Cicirello, and E. Patelli, "Sampling methods for solving bayesian model updating problems: A tutorial," *Mechanical Systems and Signal Processing*, vol. 159, p. 107 760, 2021. DOI: `https://doi.org/10.1016/j.ymssp.2021.107760`.

[50] R. J. Rossi, "Likelihood-based estimation," in *Mathematical Statistics*. John Wiley & Sons, Ltd, 2018, ch. 5, pp. 223–279. DOI: `https://doi.org/10.1002/9781118771075.ch5`.

[51] B. Kurent, N. Friedman, W. K. Ao, and B. Brank, "Bayesian updating of tall timber building model using modal data," *Engineering Structures*, vol. 266, p. 114 570, 2022. DOI: `https://doi.org/10.1016/j.engstruct.2022.114570`.

[52] R. Ceravolo, A. Faraci, and G. Miraglia, "Bayesian calibration of hysteretic parameters with consideration of the model discrepancy for use in seismic structural health monitoring," *Applied Sciences*, vol. 10, p. 5813, 2020. DOI: `10.3390/app10175813`.

[53] H. Rappel, L. A. A. Beex, J. S. Hale, L. Noels, and S. P. A. Bordas, "A tutorial on bayesian inference to identify material parameters in solid mechanics," *Arch Computat Methods*, vol. 27, pp. 361–385, 2020. DOI: `https://doi.org/10.1007/s11831-018-09311-x`.

[54] D. Xiu, *Numerical Methods for Stochastic Computations: A Spectral Method Approach*. Princeton University Press, 2010. DOI: `https://doi.org/10.2307/j.ctv7h0skv`.

[55] I. Goodfellow, Y. Bengio, and A. Courville, *Deep Learning*. MIT Press, 2016.

[56] B. Ristic, S. Arulampalam, and N. J. Gordon, "Beyond the kalman filter: Particle filters for tracking applications," 2004. [Online]. Available: `https://api.semanticscholar.org/CorpusID:60500010`.

[57] O. G. Ernst, B. Sprungk, and H.-J. Starkloff, "Bayesian inverse problems and kalman filters," in *Extraction of Quantifiable Information from Complex Systems*, S. Dahlke, W. Dahmen, M. Griebel, *et al.*, Eds. Springer International Publishing, 2014, pp. 133–159. DOI: `10.1007/978-3-319-08159-5_7`.

[58] P. F. Shustin, S. Ubaru, V. Kalantzis, L. Horesh, and H. Avron, *Pcenet: High dimensional surrogate modeling for learning uncertainty*, 2022. arXiv: `2202.05063` [`cs.LG`].

[59] C. Soize and R. Ghanem, "Physical systems with random uncertainties: Chaos representations with arbitrary probability measure," *SIAM Journal on Scientific Computing*, vol. 26, pp. 395–410, 2004. DOI: `10.1137/S1064827503424505`.

[60] N. Sanzida and Z. K. Nagy, "Polynomial chaos expansion (pce) based surrogate modeling and optimization for batch crystallization processes," in *24th European Symposium on Computer Aided Process Engineering*. Elsevier, 2014, vol. 33, pp. 565–570. DOI: `https://doi.org/10.1016/B978-0-444-63456-6.50095-8`.

[61] C. E. Rasmussen, "Gaussian processes in machine learning," in *Advanced Lectures on Machine Learning: ML Summer Schools 2003, Canberra, Australia, February 2 - 14, 2003, Tübingen, Germany, August 4 - 16, 2003, Revised Lectures*. Springer Berlin Heidelberg, 2004, pp. 63–71. DOI: `10.1007/978-3-540-28650-9_4`.

[62] Y. Yang, Y. Yang, M. Xiao, M. Wan, and W. Zhang, "A gaussian process regression-based surrogate model of the varying workpiece dynamics for chatter prediction in milling of thin-walled structures," *International Journal of Mechanical System Dynamics*, vol. 2, no. 1, pp. 117–130, 2022. DOI: `https://doi.org/10.1002/msd2.12034`.

[63] D. Williams, I. S. Heng, J. Gair, J. A. Clark, and B. Khamesra, "Precessing numerical relativity waveform surrogate model for binary black holes: A gaussian process regression approach," *Phys. Rev. D*, vol. 101, p. 63 011, 6 2020. DOI: `10.1103/PhysRevD.101.063011`. [Online]. Available: `https://link.aps.org/doi/10.1103/PhysRevD.101.063011`.

[64] R. K. Tripathy and I. Bilionis, "Deep uq: Learning deep neural network surrogate models for high dimensional uncertainty quantification," *Journal of Computational Physics*, vol. 375, pp. 565–588, 2018. DOI: `https://doi.org/10.1016/j.jcp.2018.08.036`.

[65] M. Abdar, F. Pourpanah, S. Hussain, *et al.*, "A review of uncertainty quantification in deep learning: Techniques, applications and challenges," *Information Fusion*, vol. 76, pp. 243–297, 2021. DOI: `https://doi.org/10.1016/j.inffus.2021.05.008`.

[66] W. Wu, M. Malik, S. Cantero-Chinchilla, *et al.*, "Guided waves-based damage identification in plates through an inverse bayesian process," *Ultrasonics*, vol. 125, p. 106 773, 2022. DOI: `https://doi.org/10.1016/j.ultras.2022.106773`.

[67] E. Hernández-Montes, M. L. Jalón, R. Rodríguez-Romero, J. Chiachío, V. Compán-Cardiel, and L. M. Gil-Martín, "Bayesian structural parameter identification from ambient vibration in cultural heritage buildings: The case of the san jerónimo monastery in granada, spain," *Engineering Structures*, vol. 284, p. 115 924, 2023. DOI: `https://doi.org/10.1016/j.engstruct.2023.115924`.

[68] G. Sevieri, M. Andreini, A. De Falco, and H. G. Matthies, "Concrete gravity dams model parameters updating using static measurements," *Engineering Structures*, vol. 196, p. 109 231, 2019. DOI: `https://doi.org/10.1016/j.engstruct.2019.05.072`.

[69] B. Conde, P. Eguía, G. Stavroulakis, and E. Granada, "Parameter identification for damaged condition investigation on masonry arch bridges using a bayesian approach," *Engineering Structures*, vol. 172, pp. 275–284, 2018. DOI: `https://doi.org/10.1016/j.engstruct.2018.06.040`.

[70] S. Dobrilla, M. Lunardelli, M. Nikolić, D. Lowke, and B. Rosić, "Bayesian inference of mesoscale mechanical properties of mortar using experimental data from a double shear test," *Computer Methods in Applied Mechanics and Engineering*, vol. 409, p. 115 964, 2023. DOI: `https://doi.org/10.1016/j.cma.2023.115964`.

[71] T. Wu, B. V. Rosić, L. D. Lorenzis, and H. G. Matthies, "Parameter identification for phase-field modeling of fracture: A bayesian approach with sampling-free update," *Computational Mechanics*, vol. 67, pp. 435–453, 2020. DOI: `https://doi.org/10.1007/s00466-020-01942-x`.

[72] R. D. Taylor, *Feap - finite element analysis program*, `http://projects.ce.berkeley.edu/feap/`.

[73] T. M. Inc., *Matlab r2021b)*, `https://www.mathworks.com`.

[74] D. Bindel, "Matfeap: Matlab interfaces to the feap finite element code," *MATFEAP manual*, 2011. DOI: `https://www.cs.cornell.edu/~bindel//blurbs/matfeap.html`.

[75] E. Zander, *A matlab/octave toolbox for stochastic galerkin methods*, `https://ezander.github.io/sglib/`.

[76] J. Simo and M. Rifai, "A class of mixed assumed strain methods and the method of incompatible modes," *International Journal for Numerical Methods in Engineering*, vol. 29, no. 8, pp. 1595–1638, 1990. DOI: `10.1002/nme.1620290802`.

[77] A. Ibrahimbegovic and E. L. Wilson, "A modified method of incompatible modes," *Communications in Applied Numerical Methods*, vol. 7, pp. 187–194, 1991. DOI: `10.1002/cnm.1630070303`.

[78] M. Jirásek, "Comparative study on finite elements with embedded discontinuities," *Computer Methods in Applied Mechanics and Engineering*, vol. 188, pp. 307–330, 2000. DOI: `https://doi.org/10.1016/S0045-7825(99)00154-1`.

[79] G. Pijaudier-Cabot and Z. Bazant, "Nonlocal damage theory," *Journal of Engineering Mechanics-asce - J ENG MECH-ASCE*, vol. 113, 1987-10. DOI: `10.1061/(ASCE)0733-9399(1987)113:10(1512)`.

[80] G. Cusatis, D. Pelessone, and A. Mencarelli, "Lattice discrete particle model (ldpm) for failure behavior of concrete. i: Theory," *Cement and Concrete Composites*, vol. 33, no. 9, pp. 881–890, 2011. DOI: `https://doi.org/10.1016/j.cemconcomp.2011.02.011`.

[81] P. Grassl, "3d lattice meso-scale modelling of the effect of lateral compression on tensile fracture processes in concrete," *International Journal of Solids and Structures*, vol. 262-263, p. 112 086, 2023. DOI: `https://doi.org/10.1016/j.ijsolstr.2022.112086`.

[82] Z. Qian, E. Schlangen, G. Ye, and K. Breugel, "Modeling framework for fracture in multiscale cement-based material structures," *Materials*, vol. 10, 2017-05. DOI: `10.3390/ma10060587`.

[83] F. Landi, F. Marsili, N. Friedman, and P. Croce, "Gpce-based stochastic inverse methods: A benchmark study from a civil engineer's perspective," *Infrastructures*, vol. 6, p. 158, 2021. DOI: `10.3390/infrastructures6110158`.

[84] J. Chiachio-Ruano, M. Chiachio-Ruano, and S. Sankararaman, "Bayesian inverse problems: Fundamentals and engineering applications (1st ed.)," *CRC Press*, pp. 155–202, 2021. DOI: `https://doi.org/10.1201/b22018`.

[85] M. K. Ramancha, M. A. Vega, J. P. Conte, M. D. Todd, and Z. Hu, "Bayesian model updating with finite element vs surrogate models: Application to a miter gate structural system," *Engineering Structures*, vol. 272, p. 114 901, 2022. DOI: `https://doi.org/10.1016/j.engstruct.2022.114901`.

[86] Y. Li, N. Friedman, P. Teatini, *et al.*, "Sensitivity analysis of factors controlling earth fissures due to excessive groundwater pumping," *Stoch Environ Res Risk Assess*, vol. 36, pp. 3911–3928, 2022. DOI: `https://doi.org/10.1007/s00477-022-02237-8`.

[87] C. M. Bishop, *Neural networks for pattern recognition*. Oxford university press, 1995.

[88] M. Papadrakakis and N. D. Lagaros, "Reliability-based structural optimization using neural networks and monte carlo simulation," *Computer Methods in Applied Mechanics and Engineering*, vol. 191, pp. 3491–3507, 2002. DOI: `https://doi.org/10.1016/S0045-7825(02)00287-6`.

[89] G. E. Hinton, "A practical guide to training restricted boltzmann machines," in *Neural Networks: Tricks of the Trade: Second Edition*. Springer, 2012, pp. 599–619. DOI: `https://doi.org/10.1007/978-3-642-35289-8_32`.

[90] E. Janouchová and A. Kučerová, "Competitive comparison of optimal designs of experiments for sampling-based sensitivity analysis," *Computers & Structures*, vol. 124, pp. 47–60, 2013. DOI: `https://doi.org/10.1016/j.compstruc.2013.04.009`.

[91] A. Saltelli, "Making best use of model evaluations to compute sensitivity indices," *Computer Physics Communications*, vol. 145, pp. 280–297, 2002. DOI: `https://doi.org/10.1016/S0010-4655(02)00280-1`.

[92] A. Saltelli, P. Annoni, I. Azzini, F. Campolongo, M. Ratto, and S. Tarantola, "Variance based sensitivity analysis of model output. design and estimator for the total sensitivity index," *Computer Physics Communications*, vol. 181, pp. 259–270, 2010. DOI: `https://doi.org/10.1016/j.cpc.2009.09.018`.

[93] I. Sobol, "Global sensitivity indices for nonlinear mathematical models and their monte carlo estimates," *Mathematics and Computers in Simulation*, vol. 55, pp. 271–280, 2001. DOI: `https://doi.org/10.1016/S0378-4754(00)00270-6`.

[94] J. Blaber, B. Adair, and A. Antoniou, "Ncorr: Open-source 2d digital image correlation matlab software," *Experimental Mechanics*, vol. 55, pp. 1105–1122, 2015. DOI: `10.1007/s11340-015-0009-1`.

9. LIST OF FIGURES AND TABLES

9.1. List of figures

9.2. List of tables

10.   APPENDIX: PUBLISHED RESEARCH PAPERS

A.   Enhanced solid element model with embedded strong discontinuity for representation of mesoscale quasi-brittle failure - Paper I

Check for updates

RESEARCH

Enhanced solid element model with embedded strong discontinuity for representation of mesoscale quasi-brittle failure

Matej Šodan · Andjelka Stanić · Mijo Nikolić

Abstract This article presents a novel two-dimensional quadrilateral solid finite element model, enhanced by incompatible modes and embedded strong discontinuity for simulation of localized failure in quasi-brittle heterogeneous multi-phase materials. The focus of interest lies in the development of discontinuities and cracks induced by both tensile and compressive loads, considering mesoscale material constituents and very complex meshes. Multiple cracks are initiated within elements using local Gauss-point criteria for crack initiation. Rankine and Maximum shear stress criteria control the crack initiation, location, and orientation depending solely on the stress state within the finite element. The model identifies distinct clusters of cracked elements and merges them into continuous cracks. A tracking algorithm ensures crack continuity, eliminating spurious cracks ahead of the crack tip to prevent crack arrest and stress locking. This approach ensures the formation of various types of cracks within the constituents of composite materials and their spontaneous coalescence forming the final failure mechanisms. The constitutive model for the crack representation is the damage softening model, which accounts for opening and sliding behavior. The efficacy of the proposed model is demonstrated through numerical simulations of heterogeneous 3-phase and 4-phase composites subjected to both tensile and compressive load cases.

Keywords Quasi-brittle failure · Mesoscale modeling · Cracks · Localization · Quadrilateral finite element · Embedded strong discontinuities · Crack tracking

1 Introduction

Quasi-brittle materials are certainly the type of materials that the average civil engineer most often encounters. For instance, concrete, masonry, ceramics and rocks are heterogeneous composites with complex and progressive failure behaviour dependent on the lower scale constituents.

Therefore, it is of vital importance to study further its failure behavior and to put more effort into the development of sophisticated predictive models. With such knowledge and tools, we can improve design and utilization of structures made of quasi-brittle materials.

The main focus of such predictive models should be an accurate estimation in fracture processes of the material and therefore the limit load capacity of the structure by considering its highly uncertain and nonlinear properties. Randomness and nonlinear nature are generated from material constituents, various inclusions and internal imperfections being integral parts of the material, which makes the prediction of crack initia-

M. Šodan · M. Nikolić (✉)
University of Split, Faculty of Civil Engineering, Architecture and Geodesy, Matice hrvatske 15, 21000 Split, Croatia
e-mail: mijo.nikolic@gradst.hr

A. Stanić
Applied Mechanics and Data Analysis, University of Twente, Drienerlolaan 5, 7552 NB Enschede, The Netherlands

tion and propagation a demanding task (Gimenes et al. 2023; Kim and Abu Al-Rub 2011; Hai and Li 2022).

Due to such material heterogeneity, particularly in concrete-like materials, fracture processes tend to be very complex. Each material constituent and any internal flaw affect the cracking process with its mechanical properties, position, and size. Under heavy load, the fracture initiation occurs due to the evolution of microcracks around internal discontinuities and flaws or in one of the weakest material spots such as interfacial transition zones (ITZ) between constituents. Moreover, structural deterioration takes place as microcracks open and close, propagate, coalesce and form macrocracks that irreversibly degrade material and eventually lead to complete structural failure. Given the significant influence that fracture processes have on the macroscopic response of the quasi-brittle materials, it is important that heterogeneity is not neglected (Karavelić et al. 2019; Zhou et al. 2017; Grassl 2023; Du et al. 2023).

However, the majority of solid numerical finite element models which deal with fracture and damage in quasi-brittle materials treat it as homogeneous and at the macroscopic scale. Such a modeling approach can not simulate all the mechanisms that occur inside the material and crack nucleation, position, and propagation are usually predefined. On the other hand, homogeneous macro modeling is justified when the macroscopic scale of consideration is of test interest and a problem is related to the formation and development of mostly one macrocrack. Some such examples that focus on the concrete are the three-point bending test and four-point bending test as shown in many works such as citeBrankIbrahimbegovic,Stanic1,Stanic2. In order to obtain more accurate and reliable results, especially where multiple crack initiation and propagation is expected, lower material scales should be considered in simulations (Gimenes et al. 2023; Carija et al. 2020; Zhou et al. 2017). Thus, mesoscale modeling is often chosen as the most effective and optimal way for considered quasi-brittle and heterogeneous materials encountered in civil engineering. It enables a description of heterogeneous behavior and a more realistic simulation of crack initiation and propagation within the structure. Taking concrete as an example, mesoscale modeling considers it as a three phase or four phase material with aggregate, cement matrix, and interfacial transition zones (ITZ) between aggregates and cement matrix, and voids being the fourth constituent (Gimenes

et al. 2023; Karavelić et al. 2019; Carija et al. 2020; Zhou et al. 2017; Grassl 2023; Kim and Abu Al-Rub 2011).

In order to successfully represent material constituents on mesoscale level and capture the corresponding effects and failure modes, a capable numerical model is needed. In the literature, one can find many numerical models that can reproduce quasi-brittle material cracking (see (Carija et al. 2020; Puccia et al. 2023; Benkemoun et al. 2017; Thongraksa et al. 2023; Qiu et al. 2023; Thilakarathna et al. 2020; Zhang and Mang 2020; Zhang and Zhuang 2018)). Traditionally, most mesoscale models in the literature belong to the discrete group of models such as lattice element models and FEM/DEM. Lattice models, as in Carija et al. (2020); Nikolic et al. (2015); Rizvi et al. (2019); Nikolic et al. (2018), use a combination of material properties related to beam elements and Voronoi cells in order to simulate material heterogeneity. The FEM/DEM method (Smoljanović et al. 2015, 2018) divides the material into small elements that have the possibility of fragmentation and separation. Despite discrete model success in representing crack processes in the mesoscale configuration, they lack stress state representation.

On the other hand, the methods X-FEM (extended finite element method) (Moës and Belytschko 2002) and ED-FEM (embedded discontinuity finite element method) (Linder and Armero 2007; Zhang et al. 2015; Brancherie and Ibrahimbegovic 2009; Oliver 1996; Jirásek 2000) enhance solid finite elements with discontinuity functions that describe material cracking and failure (Oliver et al. 2006). Both methods keep the finite element mesh unchanged, whereas the main difference between them is that X-FEM treats the parameters related to crack opening as nodal enrichment while ED-FEM considers them on the element level. The local (element) nature of embedded discontinuity method does not enforce the continuity of the cracks once they start to develop. Moreover, multiple local cracks can occur followed by their merging and coalescence forming the new large scale fractures with the mechanism of internal force redistribution (Ortega et al. 2022). Given the occasional occurrence of issues such as crack non-continuity and the stress locking phenomenon with this method, one can employ non-local strong discontinuity formulations integrated with crack tracking algorithms (da Costa et al. 2013; Zhang et al. 2015) to ensure crack continuity during crack propaga-

tion modeling. Additionally, strain injection techniques offer a means to alleviate potential stress locking problems (Dias et al. 2018; Oliver et al. 2014). The successful example of using solid elements with embedded strong discontinuities without applying crack tracking algorithms can also be found in Stanić et al. (2021). The embedded discontinuity methods were most often successfully applied at the macro scale, while they were rarely employed in the fracture analysis of heterogeneous multi-phase composites considering multi-crack mechanisms and local dissipation at the mesocale. One such attempt is by using model with tetrahedron embedded discontinuity elements with local representation of fractures for three-dimensional fracture processes in non-homogeneous quasi-brittle materials (Ortega et al. 2022). The local discontinuous nature of embedded discontinuity models is favorable in the context of complex fracture behaviour at the mesoscale of heterogeneous multi-phase composites where larger fractures occur as coalescence of local small scale fractures.

In this work, we propose a 2D plane stress/strain quadrilateral solid finite element model within the framework of ED-FEM method for representation of mesoscale quasi brittle failure in complex geometries. The model is enhanced by incompatible modes (Ibrahimbegovic and Wilson 1991; Simo and Rifai 1990), embedded strong discontinuities (Simo et al. 1993; Ibrahimbegovic 2009) and crack tracking algorithm for following multiple cracks originating from heterogeneous mesostructure (Puccia et al. 2023; Saloustros et al. 2017). The proposed model builds upon the Q6ED element originally introduced in the work (Stanić et al. 2021), where strain softening accounts for stress release as a result of localized failure with propagating discontinuities and incompatible modes which provide higher accuracy of the solutions for bending dominating problems. The novelty with respect to the previous model (Stanić et al. 2021) concerns the inclusion of Maximum shear stress criterion for initiation of cracks in shear and compression dominated problems. Furthermore, a crack tracking algorithm has been implemented to monitor propagation of multiple cracks in complex heterogeneous geometries. Such algorithm maintains the continuity of tensile cracks while eliminating the formation of spurious and blocking cracks ahead of the crack tip. This is essential to prevent crack arrest and stress locking, ensuring the successful merging of cracks and uninterrupted crack propagation. Thus, the proposed model benefits from local nature of

ED-FEM method being able to trigger and propagate multiple cracks, while tracking algorithm help alleviate issues related to stress locking.

The cracks are initially triggered within multiple elements by employing local Gauss-point failure procedures based on the stress state in the mesh containing randomly positioned constituents and voids. The critical stress thresholds are evaluated by one of the two criteria: Rankine or Maximum shear stress, which enable initiation of tension (mode I) or shear cracks (mode II), respectively. Once cracks are formed, they can propagate in the fashion of constant separation mode I and/or constant separation mode II, which is essential for the simulation of complex crack paths spreading throughout interface transition zones around aggregate constituents.

Following the initiation of cracks, a DBSCAN clustering algorithm (Schubert et al. 2017) is used to identify distinct clusters of cracked elements. Within each cluster, the crack tracking algorithm identifies localized elements contributing to the continuous macroscopic tensile crack initiated by the Rankine criterion, retaining these elements and rejecting non-contributing elements back to their non-localized state. In each subsequent load step, the clustering algorithm incorporates new localized elements into clusters. However, the crack tracking algorithm accepts only those localized elements that extend continuous macroscopic cracks within clusters, rejecting other potential localized elements in the mesh. This approach mitigates the presence of spurious cracks throughout the mesh that could prevent crack propagation and cause crack arrest with stress locking. Elements exhibiting initial localization due to the Maximum shear stress criterion are not constrained by the crack tracking algorithm. These elements are allowed to freely initiate and propagate shear cracks based on the stress state within the mesh. This contributes to merging of multiple tensile cracks as shear cracks can merge with existing tensile cracks propagating in different parts of the mesh.

From the thermodynamic point of view, a crack is described by embedded strong discontinuities (jumps in the displacement field) which introduce a localization line placed within a 2D solid finite element. The dissipated energy related to fracture is regularized in terms of softening parameter while not being dependant on the element volume. The fracture energy can thus be considered as material property resulting in fracture analysis being mesh-independent with respect

to softening when using coarser meshes. The material behavior of the bulk is described by a linear elastic model. For the previously mentioned separation modes, two uncoupled associated damage softening models are assigned to describe the fracture processes in the material. The damage exponential softening law allows for the description of material energy dissipation and ensures gradual material failure.

This work explores the capabilities of the developed ED-FEM model enhanced by incompatible modes, embedded strong discontinuities and crack tracking algorithm in representing complex failure mechanisms in heterogeneous mesostructure with randomly positioned constituents and voids. The model can capture multiple crack propagation in 3-phase and 4-phase materials under tensile and compressive loading.

The following sections present the finite element model and its performance. In Sect. 2 we introduce the finite element formulation together with the details related to element localization with incompatible modes and embedded strong discontinuity. Section 3 provides the details about clustering mechanism and crack tracking algorithm. In order to show model capabilities, numerical simulations are presented in Sect. 4. Conclusions are given in Sect. 5.

2 Enhanced quadrilateral finite element model with embedded strong discontinuity

In this section, element localization with ED-FEM model is presented, including a brief description of applied methods, crack initiation procedures and computation strategies. The present numerical model builds upon the Q6ED element originally introduced in the work (Stanić et al. 2021), which served as the theoretical base for the development of the current model.

2.1 Kinematics

A quadrilateral isoparametric finite element with four Gauss points of integration was chosen to be the basis for this numerical model. The element was selected for its simplicity and robustness. Geometry of an element is defined with Cartesian coordinates $\boldsymbol{x} = [x, y]^T$ as $\boldsymbol{x}(\boldsymbol{\xi}) = \sum_{a=1}^{4} N_a(\boldsymbol{\xi})\boldsymbol{x_a}$, where $\boldsymbol{\xi}(\xi, \eta) \in [-1, 1] \times [-1, 1]$ are element's isoparametric coordinates, $\boldsymbol{x_a}$ are

nodal coordinates and $N_a(\boldsymbol{\xi}) = \frac{1}{4}(1 + \xi_a\xi)(1 + \eta_a\eta)$ are standard Lagrange bi-linear interpolation functions.

It is generally known, that the quadrilateral element Q4 exhibits shear stress locking in bending problems, which may lead to a poor stress state in the model. For the efficient simulation of crack propagation in a heterogeneous domain, the correct stress state is required. This is achieved by applying the incompatible modes method (Ibrahimbegovic 2009; Simo and Rifai 1990; Ibrahimbegovic and Wilson 1991) in the linear quadrilateral finite element. The approach is based on a combination of the Hu-Washizu variational principle with displacement field enrichment by adding quadratic terms to the displacement field. In this way, we obtain an improved accuracy of results for bending situations that occur throughout the simulation. This is particularly evident when a crack path kinks or turns as it bypasses aggregates (and causes a bending state in its vicinity). A good example of the favorable effects that incompatible modes have for the formation and simulation of tensile cracks is available in the literature (Stanić et al. 2021). Here, the cracks open in combined tensile and shear modes, where accurate normal and shear stresses are crucial for the successful performance of ED-FEM.

The method of incompatible modes enhances the displacement field of a quadrilateral element by introducing incompatible displacement modes $\boldsymbol{\rho}_1 = [\rho_{11}, \rho_{12}]^T$ and $\boldsymbol{\rho}_2 = [\rho_{12}, \rho_{22}]^T$ that are interpolated with the corresponding quadratic functions $M_1 = 1 - \xi^2$ and $M_2 = 1 - \eta^2$ (see Fig. 1). For all details and conditions related to the method implementation see (Ibrahimbegovic 2009; Ibrahimbegovic and Wilson 1991; Simo and Rifai 1990). The following subsections show the position of incompatible modes in the finite element formulation.

For crack modeling, we use the embedded strong discontinuity method with statically and kinematically optimal nonsymmetric formulation (SKON). This approach has demonstrated efficiency at the macroscopic level, while also showing favorable characteristics in mitigating locking effects (Jirásek 2000). Since the variables related to discontinuity are treated on the element level, the global stiffness matrix has a constant dimension, which in combination with the coarser mesh enables a faster and cheaper solution procedure.

In a quadrilateral element, an embedded discontinuity line (crack) Γ^e with length l_Γ divides the element domain into two subdomains Ω^{e+} and Ω^{e-}. We

Fig. 1 Incompatible shape functions: **a** M_1 and **b** M_2

a)

b)
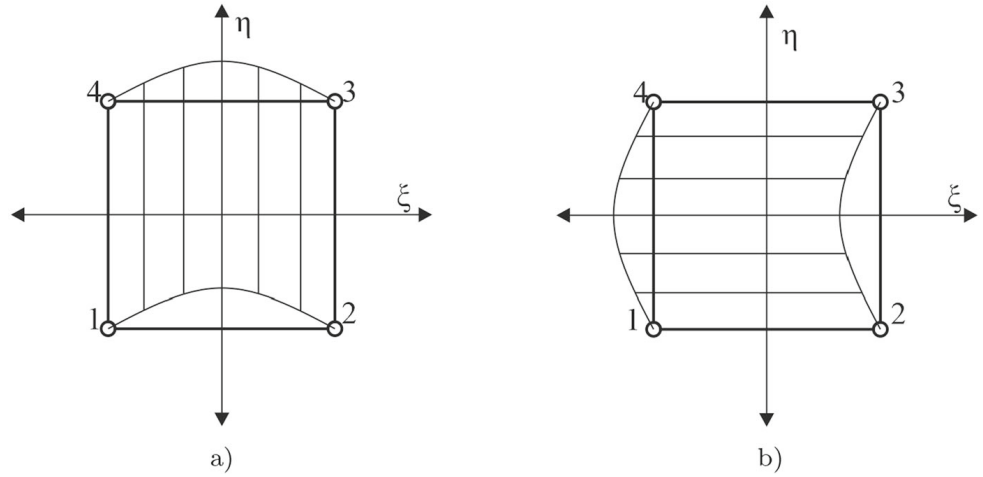
choose two elementary separation modes to describe crack expanding along the discontinuity line: constant Mode I and constant Mode II. The first mode describes crack opening and closing in a normal direction as illustrated in Fig. 2a. The shear Mode II represents sliding along the discontinuity line as shown in Fig. 2b. In this formulation, a crack can grow in the manner of one separation mode only or a combination of both modes. For the selected modes, we introduce corresponding separation parameters $\boldsymbol{\alpha} = [\alpha_1, \alpha_2]^T$. Positive separation parameters α_1 denote opening in Mode I, whereas the negative values are related to the crushing of the material at the discontinuity line. Values of the shear mode parameters α_2 can also have positive or negative values due to the possible shear sliding in both directions.

As in standard ED-FEM formulation, following interpolation functions $\boldsymbol{p}_i = [p_{ix}, p_{iy}]^T$ are obtained by keeping the domain part Ω^{e-} still while the part Ω^{e+} displaces away from or along the discontinuity line. The interpolation functions for the separation Modes I and II are:

$$
\begin{aligned}
\boldsymbol{p}_1 &= (H_\Gamma(x) - \sum_{a \in \Omega^{e+}} N_a)\mathbf{n} \\
\boldsymbol{p}_2 &= (H_\Gamma(x) - \sum_{a \in \Omega^{e+}} N_a)\mathbf{m}.
\end{aligned}
\tag{1}
$$

Here, **n** and **m** represent unit normal and tangent vectors to an embedded discontinuity as shown in Fig. 2. H_Γ is the Heaviside step function with a unit step at a discontinuity line Γ^e. More details about the method and chosen separation modes are available in the following literature (Ibrahimbegovic 2009; Dujc et al. 2010; Stanić et al. 2021, 2020). In the following Subsec-

tion 2.1.1., we introduce the enhanced separation mode parameters and incompatible mode parameters in the kinematic equations.

2.1.1 Modes coupling

The standard displacement based quadrilateral finite element Q4 is enhanced with incompatible mode parameters, which is known as Q6, in order to obtain an accurate stress state that precedes crack initiation. When a crack is initiated, then the Q6 element is enriched with separation parameters related to the embedded discontinuity line. In this subsection, we show the equations that are necessary for building the finite element formulation when a crack is active.

Let's say that a discontinuity line is embedded into an element e. The displacement field over the element is described by taking into account the incompatible modes $\boldsymbol{\rho}_b$ and crack separation modes $\boldsymbol{\alpha}$. The displacement vector $\boldsymbol{u} = [u_x, u_y]^T$ is expressed as:

$$
\begin{aligned}
\boldsymbol{u}(\boldsymbol{\xi}, \Gamma^e) &= \sum_{a=1}^{4} N_a(\boldsymbol{\xi})\boldsymbol{d}_a + \sum_{b=1}^{2} M_b(\boldsymbol{\xi})\boldsymbol{\rho}_b \\
&+ \sum_{i=1}^{2} \boldsymbol{p}_i(\boldsymbol{\xi}, \Gamma^e)\alpha_i.
\end{aligned}
\tag{2}
$$

The infinitesimal strain field in an element is determined as the symmetric gradient of (2) written in a

Fig. 2 Separation modes: **a** tensile opening and **b** shear sliding

a)

b)
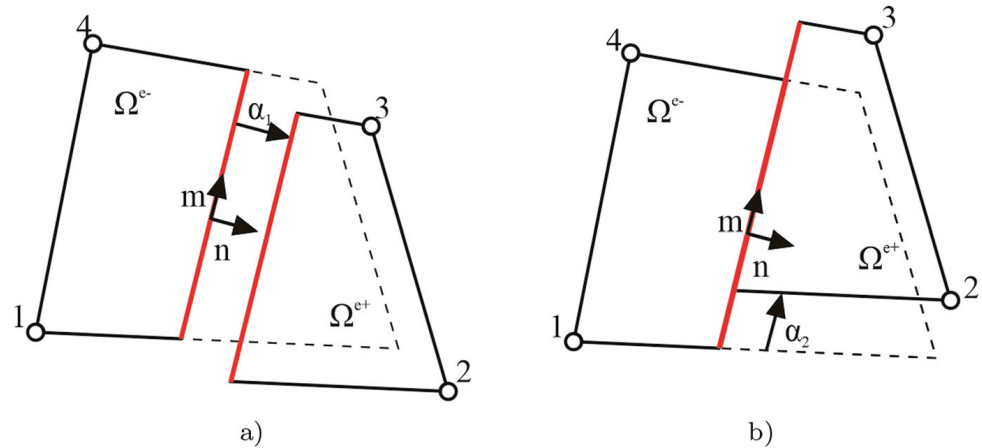
vector form as:

$$\epsilon(\xi, \Gamma^e) = \sum_{a=1}^{4} B_a(\xi)d_a + \sum_{b=1}^{2} \widetilde{G}_b(\xi)\rho_b$$
$$+ \sum_{i=1}^{2} G_i(\xi, \Gamma^e)\alpha_i. \tag{3}$$

While the matrix B_a consists of the derivatives of the interpolations functions N_a, i.e. $B_a = [[\frac{\partial N_a}{\partial x}, 0, \frac{\partial N_a}{\partial y}]^T, [0, \frac{\partial N_a}{\partial y}, \frac{\partial N_a}{\partial x}]^T]$, the matrix $\widetilde{G}_b$ is contructed in the following way:

$$\widetilde{G}_b = G_b - \frac{1}{A_{\Omega^e}} \int_{\Omega^e} G_b d\Omega$$
$$G_b = \begin{bmatrix} \frac{\partial M_b}{\partial x} & 0 \\ 0 & \frac{\partial M_b}{\partial y} \\ \frac{\partial M_b}{\partial y} & \frac{\partial M_b}{\partial x} \end{bmatrix}, \tag{4}$$

where A_{Ω^e} represents area of the element and $\widetilde{G}_b$ is modified so that $\int_{\Omega^e} \widetilde{G}_b d\Omega = 0$. In this way, it fulfills the orthogonality condition between enhanced strains due to incompatible modes and the constant stresses, which guarantees the convergence of the incompatible mode method (Ibrahimbegovic 2009). The terms in the kinematic operator G_i in Eq. (3) are derivatives of the interpolation functions p_i:

$$G_1 = - \underbrace{\sum_{a \in \Omega^{e+}} B_a n}_{G_1} + \underbrace{\delta_\Gamma(x) B_n n}_{\overline{\overline{G}}_1}$$
$$G_2 = - \underbrace{\sum_{a \in \Omega^{e+}} B_a m}_{G_2} + \underbrace{\delta_\Gamma(x) B_n m}_{\overline{\overline{G}}_2}, \tag{5}$$

where $\delta_\Gamma(x)$ is Dirac-δ distribution introduced by the relations $\delta_\Gamma(x)n_x = \frac{\partial H_\Gamma(x)}{\partial x}$ and $\delta_\Gamma(x)n_y = \frac{\partial H_\Gamma(x)}{\partial y}$. The matrix B_n is defined as $B_n = [[n_x, 0, n_y]^T, [0, n_y, n_x]^T]$ with n_x and n_y being the components of normal vector n. By considering the additive decomposition of G_i, we can rewrite the strain field in (3) as:

$$\epsilon(\xi, \Gamma^e) = \underbrace{\sum_{a=1}^{4} B_a(\xi)d_a + \sum_{b=1}^{2} \widetilde{G}_b(\xi)\rho_b + \sum_{i=1}^{2} \overline{G}_i(\xi, \Gamma^e)\alpha_i}_{\overline{\epsilon}}$$
$$+ \underbrace{\sum_{i=1}^{2} \overline{\overline{G}}_i(\xi, \Gamma^e)\alpha_i}_{\overline{\overline{\epsilon}}}. \tag{6}$$

The regular part $\overline{\epsilon}$ represents bulk strains and the singular part $\overline{\overline{\epsilon}}$ is the strain at the discontinuity line.

To formulate the equilibrium equations using the principles of virtual work, it is necessary to define the virtual strain field:

$$\tilde{\epsilon}(\xi, \Gamma^e) = \underbrace{\sum_{a=1}^{4} B_a(\xi)\tilde{d}_a}_{\widetilde{\epsilon}^d} \tag{7}$$

$$+ \sum_{b=1}^{2} \widetilde{\boldsymbol{G}}_b(\boldsymbol{\xi}) \widetilde{\boldsymbol{\rho}}_b + \underbrace{\sum_{i=1}^{2} \widehat{\boldsymbol{G}}_i(\boldsymbol{\xi}, \Gamma^e) \widetilde{\alpha}_i}_{\widetilde{\overline{\boldsymbol{\epsilon}}}^{\beta}} . \qquad (8)$$

In eq. (7), the first part $\widetilde{\overline{\boldsymbol{\epsilon}}}^d$ represents the virtual strains associated with the virtual nodal displacements $\widetilde{\boldsymbol{d}}_a$. The second part $\widetilde{\overline{\boldsymbol{\epsilon}}}^{\beta}$ represents the strains due to the virtual incompatible modes $\widetilde{\boldsymbol{\rho}}_b$ and the virtual separation mode parameters $\widetilde{\alpha}_i$. The operators $\widehat{\boldsymbol{G}}_i$ for virtual separation parameters are modified in the spirit of the incompatible modes method, ensuring:

$$\widehat{\boldsymbol{G}}_i = \boldsymbol{G}_i - \frac{1}{A_{\Omega^e}} \int_{\Omega^e} \boldsymbol{G}_i d\Omega. \qquad (9)$$

Modification (9) is designed in order to ensure $\int_{\Omega^e} \boldsymbol{G}_i d\Omega = 0$ over the domain Ω^e for constant stresses. Applying (5) into (9) and using the relation $\int_{\Omega^e} \delta_{\Gamma} d\Omega = l_{\Gamma}$, the operators $\widehat{\boldsymbol{G}}_i$ for virtual separation parameters have the following form:

$$\widehat{\boldsymbol{G}}_1 = \underbrace{\overline{\boldsymbol{G}}_1 - \frac{1}{A_{\Omega^e}} \int_{\Omega^e} \overline{\boldsymbol{G}}_1 d\Omega - \frac{l_{\Gamma}}{A_{\Omega^e}} \boldsymbol{B}_n \boldsymbol{n}}_{\overline{\overline{\boldsymbol{G}}}_1}$$
$$+ \underbrace{\delta_{\Gamma}(\boldsymbol{x}) \boldsymbol{B}_n \boldsymbol{n}}_{\overline{\overline{\overline{\boldsymbol{G}}}}_1} \qquad (10)$$

$$\widehat{\boldsymbol{G}}_2 = \underbrace{\overline{\boldsymbol{G}}_2 - \frac{1}{A_{\Omega^e}} \int_{\Omega^e} \overline{\boldsymbol{G}}_2 d\Omega - \frac{l_{\Gamma}}{A_{\Omega^e}} \boldsymbol{B}_n \boldsymbol{m}}_{\overline{\overline{\boldsymbol{G}}}_2}$$
$$+ \underbrace{\delta_{\Gamma}(\boldsymbol{x}) \boldsymbol{B}_n \boldsymbol{m}}_{\overline{\overline{\overline{\boldsymbol{G}}}}_2} \qquad (11)$$

More details related to the modifications of operators $\widetilde{\boldsymbol{G}}_b$ and $\widehat{\boldsymbol{G}}_i$ are available in Ibrahimbegovic (2009); Stanić et al. (2021, 2020).

2.2 Global and local equilibrium equations

In this subsection, we derive global and local equations for element localization when a discontinuity line is embedded into a finite element. The same equations can be used for the standard Q6 elements by neglecting the terms related to the crack separation parameters.

For a 2D body discretized with N_{el} quadrilateral finite elements, the principle of virtual work yields:

$$\boldsymbol{\Lambda}_{e=1}^{N_{el}}(G^{int,e} - G^{ext,e}) = 0, \qquad (12)$$

where $\boldsymbol{\Lambda}$ is a finite element assembly operator and $G^{ext,e} = \sum_{a=1}^{4} \widetilde{\boldsymbol{d}}_a{}^T \boldsymbol{f}_a^{ext,e}$ is the virtual work of external forces. By considering the decomposition of the real and virtual strains in eqs. (6) and (7), the internal virtual work can be expressed as:

$$G^{int,e} = t^e \int_{\Omega^e} \sum_{\Omega^e} \widetilde{\overline{\boldsymbol{\epsilon}}}^T \boldsymbol{\sigma} d\Omega = t^e \int \underbrace{(\sum_{a=1}^{4} \boldsymbol{B}_a \widetilde{\boldsymbol{d}}_a)^T \boldsymbol{\sigma} d\Omega}_{\text{standard part}}$$
$$+ \underbrace{t^e \int_{\Omega^e} (\sum_{b=1}^{2} \widetilde{\boldsymbol{G}}_b \widetilde{\boldsymbol{\rho}}_b)^T \boldsymbol{\sigma} d\Omega + t^e \int_{\Omega^e} (\sum_{i=1}^{4} \widehat{\boldsymbol{G}}_i \widetilde{\alpha}_i)^T \boldsymbol{\sigma} d\Omega}_{\text{additional part}} . \qquad (13)$$

In (13), t^e is the element's thickness and $\boldsymbol{\sigma}$ are stresses in bulk. Considering the external virtual work $G^{ext,e}$ and the standard part of internal virtual work in eq. (13), one obtains the set of global equilibrium equations for the finite element mesh:

$$\boldsymbol{\Lambda}_{e=1}^{N_{el}} \underbrace{(\boldsymbol{f}^{int,e} - \boldsymbol{f}^{ext,e})}_{\boldsymbol{R}_d^e} = 0, \qquad (14)$$

where $\boldsymbol{f}^{ext,e} = [\boldsymbol{f}_a^{ext,e,T}]_{a=1,...,4}^T$ and $\boldsymbol{f}^{int,e} = [\boldsymbol{f}_a^{int,e,T}]_{a=1,...,4}^T$.

The additional part of internal virtual work in (13) provides local element equilibrium equations for both incompatible and separation modes enrichments. The first term gives element equilibrium equations for incompatible modes:

$$\underbrace{t^e \int_{\Omega^e} \widetilde{\boldsymbol{G}}_b{}^T \boldsymbol{\sigma} d\Omega}_{\boldsymbol{R}_{\rho,b}^e} = 0, \quad b = 1, 2 \qquad (15)$$

with $\boldsymbol{R}_{\rho,1} = [R_{\rho,11}, R_{\rho,12}]^T$ and $\boldsymbol{R}_{\rho,2} = [R_{\rho,21}, R_{\rho,22}]^T$. By applying the decompositions (10) and (11), and by using the relation $\int_{\Omega_{\Gamma}} \delta(\boldsymbol{x}) f(\boldsymbol{x}) d\Omega = \int_{\Gamma^e} f(\boldsymbol{x}) d\Gamma$, the second term in the additional part of the eq. (13) returns:

$$\underbrace{t^e \int_{\Omega^e} \overline{\overline{\boldsymbol{G}}}_1^T \boldsymbol{\sigma} d\Omega + t^e \int_{\Gamma^e} \underbrace{\boldsymbol{n}^T \boldsymbol{B}_n^T \boldsymbol{\sigma}_{|\Gamma^e}}_{= t_1} d\Gamma = 0}_{h_1^e} \qquad (16)$$

$$t^e \int_{\Omega^e} \overline{\overline{\boldsymbol{G}}}_2^T \boldsymbol{\sigma} \, d\Omega + t^e \underbrace{\int_{\Gamma^e} \underbrace{\boldsymbol{n}^T \boldsymbol{B}_m^T \boldsymbol{\sigma}_{|\Gamma^e}}_{=t_2} \, d\Gamma}_{h_2^e} = 0 \qquad (17)$$

where t_1 and t_2 represent normal and tangential tractions on the discontinuity line. Equations (16) and (17) represent the element's equilibrium equations for separation modes. In order to solve eq. (12) for any discrete time interval, one needs to:

- solve the local eq. (15) on the element level to obtain the incompatible mode parameters $\boldsymbol{\rho}_b$;
- solve the local equilibrium eqs. (16) and (17) to obtain the separation mode parameters α_1 and α_2 for Mode I and Mode II, respectively;
- at the end, to solve a set of global equilibrium eq. (14) to determine the nodal displacements $\boldsymbol{d}_a$.

More details about the solution strategy are provided in Section 2.5.

2.3 Crack initiation

The crack initiation is performed by applying a Gauss-point-based criterion (Stanić et al. 2021). Namely, the embedding of a discontinuity line, its position, and its orientation depend only on the stress state within the corresponding finite element. For every pseudo time increment τ_n, we check Rankine and Maximum shear stress criterion. When one of the criteria is fulfilled, then the orientation and position of a discontinuity line are determined, and the crack is embedded. The geometry of a crack remains fixed throughout the simulation, while the separation parameters (α_1, α_2) may change. In this way, only one crack can appear inside a finite element, but on the mesh level, multiple new cracks can be initiated simultaneously in an increment. The procedure starts with the control of principal stresses in all four integration points:

$$\sigma_{p1,p2}^{e,i} = \frac{\sigma_{xx}^{e,i} + \sigma_{yy}^{e,i}}{2} \pm \sqrt{\left(\frac{\sigma_{xx}^{e,i} - \sigma_{yy}^{e,i}}{2}\right)^2 + \left(\sigma_{xy}^{e,i}\right)^2}$$

$$(18)$$

When evaluating fracture criteria, all Gauss integration points within a single finite element are considered. However, if Rankine criterion is satisfied in one Gauss point and Maximum shear stress is fulfilled in the other Gauss point within the same element, we select the most
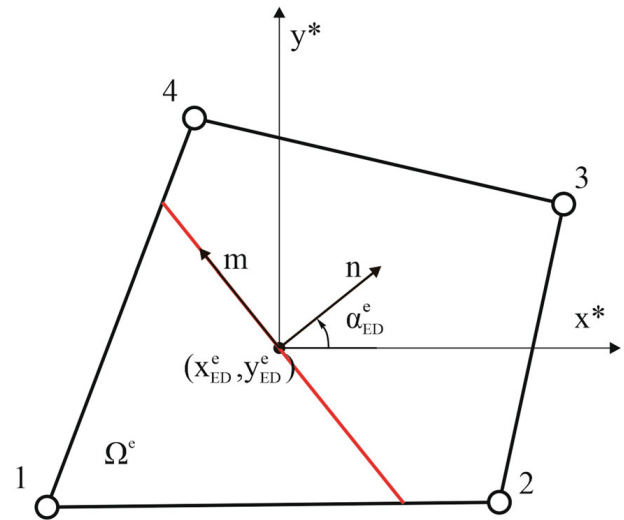
Fig. 3 Quadrilateral finite element with an embedded crack line. The crack line is defined by a point $\boldsymbol{x}_{ED}^e$ and angle α_{ED}^e

critical one. This approach ensures that only one crack type is initiated in a given element, even if multiple criteria are satisfied. When both criteria are negative, the element does not crack and the algorithm proceeds to the next intact element. When one criterion is satisfied, the procedure for the determination of crack position and orientation is performed.

Figure 3 shows a quadrilateral finite element with an embedded discontinuity line, that is defined by the point $\boldsymbol{x}_{ED}^e = [x_{ED}^e, y_{ED}^e]^T$ and angle α_{ED}^e. The coordinate axes x^* and y^* present the element's local coordinate axes—that are parallel to the global ones—with the origin in the point $\boldsymbol{x}_{ED}^e$. The angle α_{ED}^e is the direction of the normal **n** to the discontinuity line. Once a discontinuity is embedded, its location and direction are fixed till the end of the numerical simulation. However, for the selected discontinuity surface, elements can exhibit various behaviors depending on the change in stress state. Specifically, the element can undergo Mode I only, Mode II only, or a combination of mixed mode behavior based on the change in the traction vector value. The following subsections explain the crack initiation criteria and corresponding procedure for determining the point $\boldsymbol{x}_{ED}^e$ and the angle α_{ED}^e.

2.3.1 Rankine criterion

The Rankine failure criterion is used in order to detect tensile fracture by comparing the maximum principle stress and the material tensile strength σ_n. In this

work, we use Rankine criterion in the same manner as in Stanić et al. (2021). The eq. (18) determines the maximum principal stress (i.e. $\sigma_p^{e,i} = \max[\sigma_{p1}^{e,i}, \sigma_{p2}^{e,i}]$), then we single out the maximum one in the element: $\sigma_p^e = \max\limits_{i=1,...,4} \sigma_p^{e,i}$, and compare it with σ_n. If maximum principle stress σ_p^e exceeds material tensile strength σ_n, then the tensile crack is initiated.

First, in order to define crack, we gather all appropriate integration points with maximum principle stress values σ_p^e (within numerical tolerance) in a single set $B^e = \{id \in \{1, 2, 3, 4\} : \sigma_p^{e,id} = \sigma_p^e\}$. By considering the average of the properties of localized Gauss points, the model achieves the right positions and orientations of cracks, which proves to be crucial for obtaining a successful cracking mechanism. From contained integration points of the set B^e, the global coordinates of the geometric center are calculated by averaging:

$$x_{ED}^e = \frac{1}{N_{B^e}} \sum_{i \in B^e} x^{e,i}, \tag{19}$$

where $x^{e,i}$ are global coordinates of included Gauss points and N_{B^e} is the number of elements in the set B^e. The same points are considered to determine the orientation of a crack line. For this purpose, the average stress of points in B^e is calculated as:

$$\sigma_{ED}^e = \frac{1}{N_{B^e}} \sum_{i \in B^e} \sigma^{e,i} \tag{20}$$

where $\sigma^{e,i}$ is stress in an integration points from B^e. Then, the orientation of the crack is determined by the angle α_{ED}^e, which coincides with the slope of the normal vector n to the discontinuity line. By using the average stress components from (20), the principle angle α_{ED}^e, with respect to the global axis x, can be calculated as follows:

$$\alpha_{ED}^e = \frac{1}{2}\arctan\left(\frac{2\sigma_{xyED}^e}{\sigma_{xxED}^e - \sigma_{yyED}^e}\right). \tag{21}$$

Now, with all parameters at hand, the crack definition is quite straightforward. The tangential vector m is perpendicular to the vector n which represents the slope of the discontinuity line. By using the crack's slope (m) and known point x_{ED}^e, the discontinuity line is embedded into the finite element. With the Rankine crack criterion achieved, the element's separation modes can simulate tensile crack opening and shear sliding.

2.3.2 Maximum shear stress

Maximum shear stress criterion for shear crack initiation is checked by comparing the maximum shear stress and material shear strength σ_m. The maximum shear stresses in integration point i is calculated as:

$$\tau_p^{e,i} = \frac{1}{2}|\sigma_{p1}^{e,i} - \sigma_{p2}^{e,i}| \tag{22}$$

Then, each Gauss point's values of shear stress from (22) are compared within the shear cracking criterion:

$$\tau_p^{e,i} \geq \sigma_m, \tag{23}$$

where σ_m is the material shear strength. If one of $\tau_p^{e,i}$ exceeds the material strength in (23), shear crack initiation occurs and the procedure for the definition of a crack is performed. Firstly, the maximal shear stress in the element is found: $\tau_p^e = \max(\tau_p^{e,i})$. The integration points where shear stress attains the highest values are collected in the set $B^e = \{id \in \{1, 2, 3, 4\} : \tau_p^{e,id} = \tau_p^e\}$. The position of a discontinuity line is defined in the same way as for tensile cracking. By applying the location of the points from the set B^e in (19), the point x_{ED}^e is calculated. By using (20) we obtain the average stress σ_{xxED}^e, σ_{yyED}^e and σ_{xyED}^e regarding the shear crack case.

However, the expression to obtain a shear crack angle is different. By applying:

$$\alpha_{ED}^e = \frac{1}{2}arctan\left(\frac{-\sigma_{xxED}^e + \sigma_{yyED}^e}{2\sigma_{xyED}^e}\right), \tag{24}$$

we get the shear principle angle α_{ED}^e with respect to the global x-axis. It represents the slope of the normal n to the discontinuity line (see Fig. 3). Note, when Maximum shear stress failure criterion is fulfilled, the element failure occurs as sliding along the discontinuity line in the fashion of shear Mode II, while the separation Mode I covers tensile opening of the material at the crack. Additionally, when the shear failure line is embedded in the element, compression stress can lead to the rise of negative values of traction vector t_1. In order to enable smooth propagation of shear cracks, one needs to limit the compression stress on the shear failure line with the maximum allowed compression value σ_c. This corresponds to shear failure and compressive crushing which is observable in mesoscale simulations of heterogeneous multi-phase composites as shown in Nikolic et al. (2018).

2.4 Constitutive relations

In order to describe the failure behavior of the model, two material laws have been chosen. For the element's bulk, we adopt a linear elastic material model. Stress is defined as $\sigma = C\bar{\epsilon}$, where C is the constitutive matrix for plane stress or plane strain formulation and $\bar{\epsilon}$ is the strain in bulk defined in eq. (6). The material degradation at the embedded discontinuity is depicted by two damage softening laws (Pijaudier-Cabot and Bazant 1987). More precisely, two uncoupled damage models, related to separation in the fashion of Mode I and Mode II, are formulated in the framework of thermodynamics of interfaces. The Helmholtz free energy for opening crack in Mode I is defined as:

$$\Psi(\bar{\bar{D}}_n, \bar{\bar{u}}_1, \bar{\bar{\xi}}_n) = \frac{1}{2}\bar{\bar{D}}_n^{-1}\bar{\bar{u}}_1^2 + \bar{\bar{\Xi}}(\bar{\bar{\xi}}_n), \tag{25}$$

where $\bar{\bar{D}}_n$ and $\bar{\bar{u}}_1$ are compliance modulus and jump-in-displacements at the crack line in normal direction, $\bar{\bar{\Xi}}$ is softening potential and $\bar{\bar{\xi}}_n$ is internal softening variable. Softening failure function is defined as:

$$\bar{\bar{\phi}}_n(t_1, \bar{\bar{q}}_n) = t_1 - (\sigma_n - \bar{\bar{q}}_n) \leq 0. \tag{26}$$

The variable $\bar{\bar{q}}_n$ represents softening traction:

$$\bar{\bar{q}}_n = \frac{\partial \bar{\bar{\Psi}}_n}{\partial \bar{\bar{\xi}}_n} = \sigma_n \left(1 - \exp\left[-\frac{\sigma_n}{G_{fn}}\bar{\bar{\xi}}_n\right]\right), \tag{27}$$

where σ_n represents material tensile strength and G_{fn} is the tensile Mode I material fracture energy.

Similar models are used for representing the shear Mode II. This work aims to simulate unconfined compression cases where the usual hardening effect, commonly observed at confinement macroscopic scale, is absent. This approach aligns with other models from the literature (Nikolic et al. 2018; Cusatis et al. 2011; Grassl 2023), where it has been demonstrated that at the mesoscale level, compression stress must be limited and followed by softening, in order to allow shear cracks to further propagate in low confinement compression.

It is important to note that under conditions of more confined compression, there would likely be significant overlap between the two sides of the band. Such a situation would be physically unrealistic. Therefore, in cases of higher confinement, alternative (hardening) models should be used for physically accurate representation of failure.

When limiting compression stresses with negative traction t_1 on the shear failure line, one needs to consider additional constitutive equations for compression as well

$$\bar{\bar{\phi}}_c(t_1, \bar{\bar{q}}_c) = t_1 + (\sigma_c - \bar{\bar{q}}_c) \geq 0, \tag{28}$$

with σ_c and G_{fc} being maximum compression stress value and fracture energy in compression.

The tensile Mode I constitutive Eqs. (25)–(27) are used in the same manner for shear Mode II and denoted with indices m. More precisely, σ_m and G_{fm} represent material shear strength and shear fracture energy. The failure function for the shear Mode II is formulated as:

$$\bar{\bar{\phi}}_m(t_2, \bar{\bar{q}}_m) = |t_2| - (\sigma_m - \bar{\bar{q}}_m) \leq 0. \tag{29}$$

In Eq. (29), the absolute value of the traction t_2 indicates that the sliding in Mode II fashion is possible in both directions (upward and downward along the discontinuity line). Additionally, the internal softening variable ξ_m increases together with the maximal shear sliding from both directions. In contrast, the tensile and compressive tractions are considered separately in the model by holding two separate failure functions (26) and (28) and two separate internal variables ξ_n and ξ_c, respectively.

The dissipation of energy in the local (element) form can be obtained with the second law of thermodynamics Ibrahimbegovic (2009) as

$$\dot{D}_P = \sigma\dot{\epsilon} - \frac{d}{dt}\bar{\bar{\Psi}}(\sigma, \bar{\bar{q}}). \tag{30}$$

Furthermore, the total energy balance including the fracture energy can be written in distributional sense (Nikolić et al. 2018), leading to the expression of fracture energy G_f needed to drive the material until the total failure

$$G_f = \int_0^\infty \sigma_u exp\left(-\xi\frac{\sigma_u}{G_f}\right)d\xi \tag{31}$$

The final expression for the dissipated fracture energy in the current time step b can then be computed as

$$D_p = G_f\left(1 - exp\left(-\frac{\sigma_u}{G_f}\xi_b\right)\right). \tag{32}$$

The dissipated fracture energy can be computed for both failure modes.

2.5 Solution procedure

Herein presented, local and global computations are carried out in an iterative way in order to find a solution

at each discrete pseudo-time point $\tau_1, \tau_2, ..., \tau_n, \tau_{n+1},$ ..., T. Procedures are based on an operator-split scheme, so that the local and the global phases are treated separately. The loops of global iterations i and local iterations k are executed until the global convergence for each pseudo time increment τ_{n+1} is obtained.

In order to provide an update of the variables related to the damage model at discontinuity, the local computation for cracked elements is required for every iteration i within a pseudo-time increment τ_{n+1}. For the crack opening in Mode I, in given time increment τ_{n+1}, we know the values of $\boldsymbol{d}_{n+1}, \bar{\bar{\xi}}_n, \alpha_1,$ and $\overline{\overline{D}}_n$ and we are looking for their update. First, the trial value for traction on discontinuity $t_{1,n+1}^{trial}$ is derived from the expression (16) as:

$$t_{1,n+1}^{trial} = -\frac{\int_{\Omega^e} \overline{\boldsymbol{G}}_1^T \boldsymbol{\sigma}_{n+1}^{trial} d\Omega}{L_\Gamma},$$ (33)

The trial values of stress components $\boldsymbol{\sigma}_{n+1}^{trial}$ are computed from the given data. Traction trial values together with softening traction variable $\bar{\bar{q}}_{n,n+1}^{trial} = \bar{\bar{q}}_{n,n}$ from (27) are needed for failure function trial value computation:

$$\overline{\overline{\Phi}}_{n,n+1}^{trial} = t_{1,n+1}^{trial} - (\sigma_n - \bar{\bar{q}}_{n,n+1}^{trial}).$$ (34)

If the failure function's trial value $\overline{\overline{\Phi}}_{n,n+1}^{trial} \leq 0$, then the trial values are accepted: $\bar{\bar{\xi}}_{n,n+1} = \bar{\bar{\xi}}_{n,n}$, $t_{1,n+1} = t_{1,n+1}^{trial}, \bar{\bar{q}}_{n,n+1} = \bar{\bar{q}}_{n,n+1}^{trial}, \overline{\overline{D}}_{n,n+1} = \overline{\overline{D}}_{n,n}$ and $\boldsymbol{\sigma}_{n+1} = \boldsymbol{\sigma}_{n+1}^{trial}$. Otherwise, the internal values have to be updated in order to fulfill (34). The nonlinear function $\overline{\overline{\Phi}}_{n,n+1}(\bar{\bar{\gamma}}_{n,n+1}) = 0$ is solved by the Newton's method iterative procedure to determine the unknown Lagrange multiplier $\bar{\bar{\gamma}}_{n,n+1}$:

$$\bar{\bar{\gamma}}_{n,n+1}^{(k+1)} = \bar{\bar{\gamma}}_{n,n+1}^{(k)} - \left(\frac{d\overline{\overline{\Phi}}_{n,n+1}^{(k)}}{d\bar{\bar{\gamma}}_{n,n+1}^{(k)}}\right)^{-1} \overline{\overline{\Phi}}_{n,n+1}^{(k)}$$ (35)

$$k = 1, ..., \text{convergence} \rightarrow \bar{\bar{\gamma}}_{n,n+1}.$$

With the $\bar{\bar{\gamma}}_{n,n+1}$ at hand, the internal softening variables are updated:

$$\bar{\bar{\xi}}_{n,n+1} = \bar{\bar{\xi}}_{n,n} + \bar{\bar{\gamma}}_{n,n+1},$$ (36)

$$\bar{\bar{q}}_{n,n+1} = \sigma_n \left(1 - \exp\left[-\frac{\sigma_n}{G_{fn}} \bar{\bar{\xi}}_{n,n+1}\right]\right),$$ (37)

$$t_{1,n+1} = \sigma_n - \bar{\bar{q}}_{n,n+1},$$ (38)

$$\overline{\overline{D}}_{n,n+1} = \frac{\bar{\bar{\xi}}_{n,n+1}}{t_{1,n+1}}.$$ (39)

In the case of limiting compression, the same Eqs. (33)–(39) are used, only that the first subscript n is replaced with the letter c. As for the Mode II sliding, $t_{2,n+1}^{trial}$ value is obtained from Eq. (17) and in Eq. (34) softening function from (29) with the absolute value of $t_{m,n+1}^{trial}$ is used. Other equations with the change of the subscripts are the same. Note that the Eqs. (33)–(39) are evaluated on finite element level and the superscript e is omitted for better readability.

After obtaining the updated values of tractions $t_{1,n+1}$ and $t_{2,n+1}$, the local procedures for the calculation of incompatible modes parameters $\boldsymbol{\rho}_b$ and the separation mode parameters $\boldsymbol{\alpha}$ are initiated. For the current increment τ_{n+1}, we know the values of discontinuity tractions $t_{1,n+1}$ and $t_{2,n+1}$, the incompatible modes $\boldsymbol{\rho}_{1,n} = [\rho_{11,n}, \rho_{12,n}]^T$ and $\boldsymbol{\rho}_{2,n} = [\rho_{12,n}, \rho_{22,n}]^T$ and the separation mode parameters $\alpha_{1,n}$ and $\alpha_{2,n}$. In order to get the new updated values of the cracked element's enrichment modes, we need to solve the local Eqs. (15), (16), and (17) with the iterative Newton method:

$$\begin{bmatrix} \Delta\rho_{11}^e \\ \Delta\rho_{12}^e \\ \Delta\rho_{21}^e \\ \Delta\rho_{22}^e \\ \Delta\alpha_1^e \\ \Delta\alpha_2^e \end{bmatrix}_{n+1}^{(i,k)} = -\underbrace{\left(\begin{bmatrix} \boldsymbol{K}_{\rho\rho}^e & \boldsymbol{K}_{\rho\alpha}^e \\ \boldsymbol{K}_{\alpha\rho}^e & \boldsymbol{K}_{\alpha\alpha}^e \end{bmatrix}_{n+1}^{(i,k)}\right)^{-1}}_{\text{6x6 matrix}} \begin{bmatrix} R_{\rho,11}^e \\ R_{\rho,12}^e \\ R_{\rho,21}^e \\ R_{\rho,22}^e \\ h_1^e \\ h_2^e \end{bmatrix}_{n+1}^{(i,k)}$$

$$k = 1, \ldots, \text{convergence}.$$ (40)

The submatrices in (40) read

$$\boldsymbol{K}_{\rho\rho,n+1}^e = \frac{\partial \boldsymbol{R}_\rho^e}{\partial \boldsymbol{\rho}}\bigg|_{n+1}^i, \quad \boldsymbol{K}_{\rho\alpha,n+1}^e = \frac{\partial \boldsymbol{R}_\rho^e}{\partial \boldsymbol{\alpha}}\bigg|_{n+1}^i$$
$$\boldsymbol{K}_{\alpha\rho,n+1}^e = \frac{\partial \boldsymbol{h}^e}{\partial \boldsymbol{\rho}}\bigg|_{n+1}^i, \quad \boldsymbol{K}_{\alpha\alpha,n+1}^e = \frac{\partial \boldsymbol{h}^e}{\partial \boldsymbol{\alpha}}\bigg|_{n+1}^i.$$ (41)

When the Eq. (40) is solved for an i-th global iteration, the enhancing parameters are updated so that:

$$\boldsymbol{\rho}_{1,n+1}^{e,i} = \begin{bmatrix} \rho_{11,n}^e + \Delta\rho_{11,n+1}^{e,i} \\ \rho_{12,n}^e + \Delta\rho_{12,n+1}^{e,i} \end{bmatrix}$$

$$\boldsymbol{\rho}_{2,n+1}^{e,i} = \begin{bmatrix} \rho_{21,n}^e + \Delta\rho_{21,n+1}^{e,i} \\ \rho_{22,n}^e + \Delta\rho_{22,n+1}^{e,i} \end{bmatrix} \tag{42}$$

$$\alpha_{1,n+1}^{e,i} = \alpha_{1,n}^e + \Delta\alpha_{1,n+1}^{e,i}$$
$$\alpha_{2,n+1}^{e,i} = \alpha_{2,n}^e + \Delta\alpha_{2,n+1}^{e,i}. \tag{43}$$

Having the new values of incompatible mode parameters and crack separation parameters at hand, the calculation of the updated stress $\boldsymbol{\sigma}_{n+1}$ is straightforward.

After solving the local equations for i-th iteration, the system of global equations is considered in order to check the solution convergence. The linearization of the local and global equations gives a system of equations

$$\mathbf{\Lambda}_{e=1}^{N_{el}} \left(\boldsymbol{K}_{c,n+1}^{e,i} \Delta\boldsymbol{d}_{c,n+1}^{e,i} \right) = \mathbf{\Lambda}_{e=1}^{N_{el}} \left(-\boldsymbol{R}_{c,n+1}^{e,i} \right), \tag{44}$$

that needs to be solved for a given i-th iteration. The contribution of each finite element in (44) is obtained by performing static condensation of the enhancing parameters from the set of equilibrium equations for a finite element:

$$\begin{bmatrix} \boldsymbol{K}_{dd}^e & \boldsymbol{K}_{d\rho}^e & \boldsymbol{K}_{d\alpha}^e \\ \boldsymbol{K}_{\rho d}^e & \boldsymbol{K}_{\rho\rho}^e & \boldsymbol{K}_{\rho\alpha}^e \\ \boldsymbol{K}_{\alpha d}^e & \boldsymbol{K}_{\alpha\rho}^e & \boldsymbol{K}_{\alpha\alpha}^e \end{bmatrix}_{n+1}^i \begin{bmatrix} \Delta\boldsymbol{d}_{n+1}^{e,i} \\ \Delta\boldsymbol{\rho}_{n+1}^{e,i} \\ \Delta\boldsymbol{\alpha}_{n+1}^{e,i} \end{bmatrix} = - \begin{bmatrix} \boldsymbol{R}_d^e \\ \boldsymbol{0} \\ \boldsymbol{0} \end{bmatrix}_{n+1}^i \tag{45}$$

In (45), zeroes in r.h.s. stand for the satisfied local equilibrium (40) in the current i-th iteration. Some terms in (45) are defined in (41), the other terms are

$$\boldsymbol{K}_{dd,n+1}^e = \frac{\partial \boldsymbol{R}_d^e}{\partial \boldsymbol{d}} \Big|_{n+1}^i,$$

$$\boldsymbol{K}_{d\rho,n+1}^e = \frac{\partial \boldsymbol{R}_d^e}{\partial \boldsymbol{\rho}} \Big|_{n+1}^i, \quad \boldsymbol{K}_{d\alpha,n+1}^e = \frac{\partial \boldsymbol{R}_d^e}{\partial \boldsymbol{\alpha}} \Big|_{n+1}^i,$$

$$\boldsymbol{K}_{\rho d,n+1}^e = \frac{\partial \boldsymbol{R}_\rho^e}{\partial \boldsymbol{d}} \Big|_{n+1}^i,$$

$$\boldsymbol{K}_{\alpha d,n+1}^e = \frac{\partial \boldsymbol{h}^e}{\partial \boldsymbol{d}} \Big|_{n+1}^i.$$

Lets us rewrite the Eq. (45) in a simpler form

$$\begin{bmatrix} \boldsymbol{K}_{dd}^e & \boldsymbol{K}_{d\beta}^e \\ \boldsymbol{K}_{\beta d}^e & \boldsymbol{K}_{\beta\beta}^e \end{bmatrix}_{n+1}^i \begin{bmatrix} \Delta\boldsymbol{d}_{n+1}^{e,i} \\ \Delta\boldsymbol{\beta}_{n+1}^{e,i} \end{bmatrix} = - \begin{bmatrix} \boldsymbol{R}_d^e \\ \boldsymbol{0} \end{bmatrix}_{n+1}^i, \tag{46}$$

where

$$\boldsymbol{K}_{\beta\beta,n+1}^e = \begin{bmatrix} \boldsymbol{K}_{\rho\rho}^e & \boldsymbol{K}_{\rho\alpha}^e \\ \boldsymbol{K}_{\alpha\rho}^e & \boldsymbol{K}_{\alpha\alpha}^e \end{bmatrix}_{n+1}^i,$$

$$\boldsymbol{K}_{d\beta,n+1}^e = \begin{bmatrix} \boldsymbol{K}_{d\rho}^e & \boldsymbol{K}_{d\alpha}^e \end{bmatrix}_{n+1}^i, \tag{47}$$

$$\boldsymbol{K}_{\beta d,n+1}^e = \begin{bmatrix} \boldsymbol{K}_{\rho d}^e \\ \boldsymbol{K}_{\alpha d}^e \end{bmatrix}_{n+1}^i,$$

and

$$\Delta\boldsymbol{\beta}_{n+1}^{e,i} = \begin{bmatrix} \Delta\boldsymbol{\rho}_{n+1}^{e,i} \\ \Delta\boldsymbol{\alpha}_{n+1}^{e,i} \end{bmatrix} \tag{48}$$

By applying static condensation to Eq. (46), we obtain

$$\Delta\boldsymbol{\beta}_{n+1}^{e,i} = - \left[\boldsymbol{K}_{\beta\beta,n+1}^e \right]^{-1} \left(-\boldsymbol{K}_{\beta d,n+1}^e \Delta\boldsymbol{d}_{n+1}^{e,i} \right). \tag{49}$$

and

$$\boldsymbol{K}_{c,n+1}^{e,i} = \boldsymbol{K}_{dd,n+1}^{e,i} - \boldsymbol{K}_{d\beta,n+1}^{e,i} \left[\boldsymbol{K}_{\beta\beta,n+1}^{e,i} \right]^{-1} \boldsymbol{K}_{\beta d,n+1}^{e,i}. \tag{50}$$

We use the expression (50) in (44) in order to get displacement increment $\Delta\boldsymbol{d}_{n+1}^{e,i}$ and a new iterative value of the element nodal displacements $\boldsymbol{d}_{n+1}^{e,i} = \boldsymbol{d}_{n+1}^{e,i-1} + \Delta\boldsymbol{d}_{n+1}^{e,i}$. If the solutions for i-th iteration in the time increment τ_{n+1} do not satisfy the convergence tolerance, a new iteration $i = i + 1$ is performed. Once the convergence is reached, the new values for incompatible mode parameters $\boldsymbol{\rho}_{n+1}^{e,i}$, crack opening parameters $\boldsymbol{\alpha}_{n+1}^{e,i}$ and nodal displacements $\boldsymbol{d}_{n+1}^{e,i}$ are accepted and stored, and the computation advances to the new pseudo-time step τ_{n+2}.

3 Clustering with crack tracking algorithm

The proposed ED-FEM model is based on the local or element approach for crack initiation. With this approach, multiple elements in the mesh can develop initial cracks and localize due to the heterogeneous stress state observed in multi-phase and heterogeneous materials, such as those found in mesoscale configurations of composite materials.

However, while certain localized elements naturally connect and merge into dominant cracks and localized zones, other elements can develop spurious cracks or discontinuities at certain improper angles between these distinct growing cracks such that they cannot

Fig. 4 Localized elements in distinct clusters of elements denoted with different color
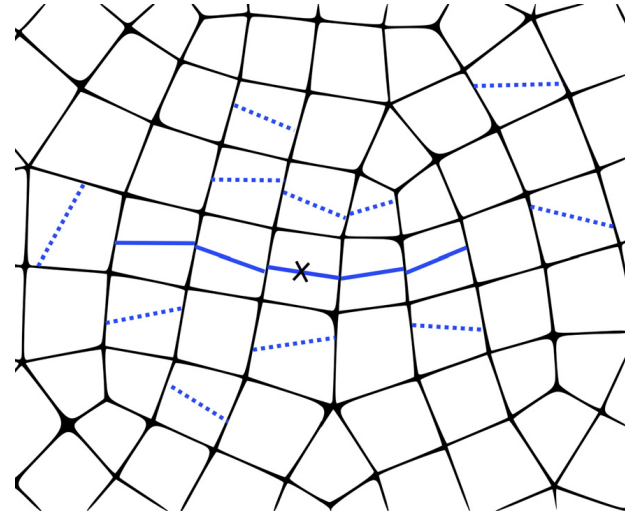

Fig. 5 Crack tracking algorithm identifies the most stressed localized element (cross marked) and searches for the neighbouring localized elements (blue); the rest of the localized elements (dashed blue) are rejected and converted into non-localized state

merge. This phenomenon, known as crack arrest, leads to stress locking and rise in stress levels and energy instead of dissipating it.

The proposed crack tracking algorithm connects localized elements to form continuous tensile cracks and only accepts further localization for elements that extend these continuous cracks. This algorithm specifically targets tensile cracks, corresponding to elements that localized due to a violation of the Rankine criterion for crack initiation.

In contrast, localized elements subjected to high shear stresses, fulfilling the Maximum shear stress criterion, are not necessarily connected through the algorithm. Instead, they are allowed to occur freely as a result of significant shear stresses. This enables shear cracks to merge with existing tensile cracks and formation of a single dominant crack that drives the specimen to full failure.

The proposed crack tracking algorithm is suitable for heterogeneous and multi-phase materials, as it can effectively follow and extend multiple tensile cracks within the mesh. To identify potential tensile cracks, the algorithm employs a DBSCAN clustering mechanism Schubert et al. (2017) to initially identify distinct clusters of localized elements, which may evolve into tensile cracks.

3.1 Clustering of localized elements

Initially, the heterogeneous stress state causes multiple elements to localize due to fulfilling Rankine or Maximum shear stress criteria. In each time step, DBSCAN clustering algorithm identifies distinct clusters of localized elements, which are represented by their centroids (Fig. 4). The clusters are defined with minimum number of localized elements. As soon as the the clusters are defined, the crack tracking algorithm initiates searching for continuous tensile cracks within each cluster.

3.2 Crack tracking algorithm

The proposed algorithm firstly identifies connected tensile cracks within clusters of localized elements such that it finds the most stressed element in each cluster. The algorithm further searches for the localized neighbouring elements that extend on both sides of such element by recognizing neighbouring elements as those that share the edge of the element that is crossed with the discontinuity (Fig. 5). The tensile crack within each cluster is identified with its crack tips represented with the element edges on both sides of the crack. The rest of the localized elements that does not form the continuous tensile crack are rejected and converted back into non-localized state. In the following time steps, the procedure of clustering and crack tracking algo-
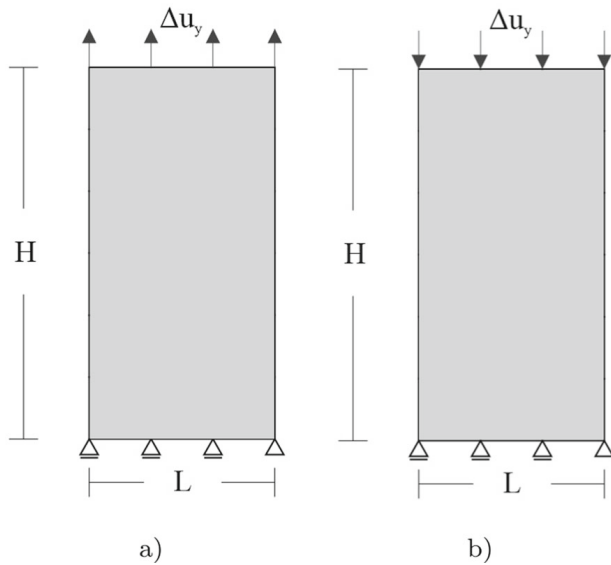
Fig. 6 Homogeneous specimen: **a** Tensile load case, **b** Compressive load case

Fig. 7 Formed cracks at the end of: **a** Tensile load case, **b** Compressive load case. Localized discontinuity lines are depicted in blue (Rankine) and red (Maximum shear stress)

rithm is repeated. The clustering algorithm adds new localized elements as a result of increased stress. Such elements are joined to the previously developed tensile cracks, while the crack tracking algorithm accepts only the localized elements that extend the existing tensile cracks.

Additionally, the crack tracking algorithm follows the crack tips and allows to merge two tensile growing cracks that are close to each other. Namely, the element between the two close crack tips can localize, while the crack angle is the average angle of these two tips.

4 Numerical simulations

In this section, few numerical simulations are presented in order to show the development of failure mechanisms and the capabilities of the proposed numerical model for representation of heterogeneous material on the mesoscale level. Material properties are chosen in order to represent cementitious material, while the fracture parameters are obtained by the trial-and-error method. The aggregate is represented as a stiff elastic material without the possibility of cracking, while the cement matrix and the interface transition zone (ITZ) are modeled with the proposed formulation of enhanced and embedded strong discontinuity solid element model. ITZ zone is constructed as a layer of finite elements distributed around an aggregate. It has lower fracture
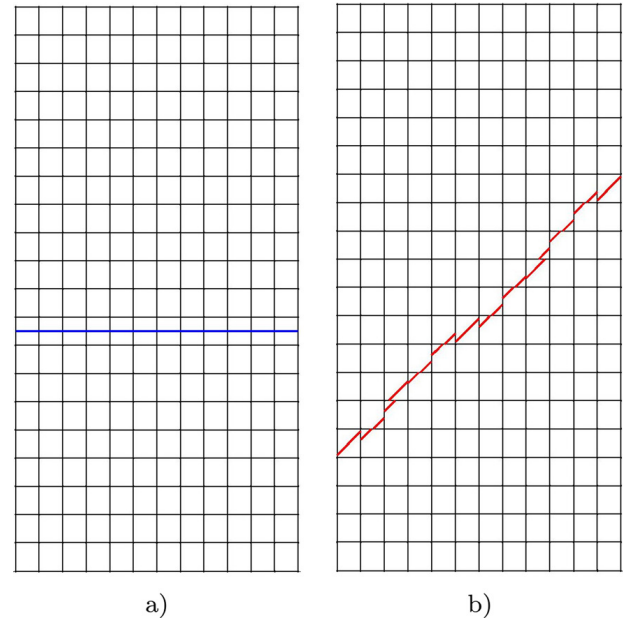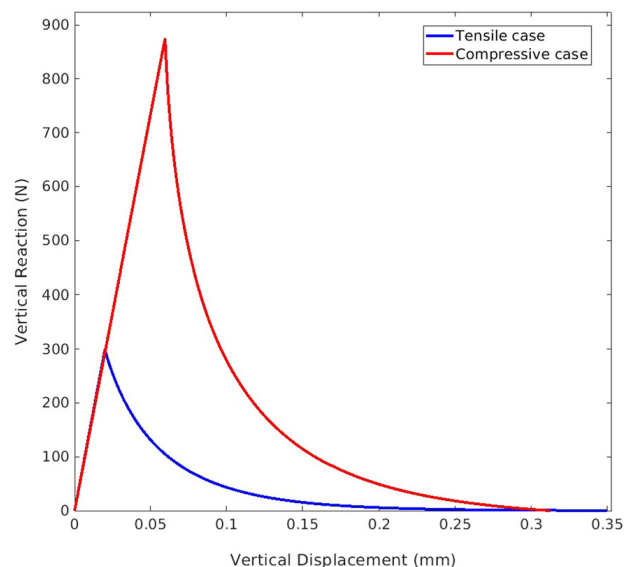

Fig. 8 Homogeneous specimen global response curves

strengths, therefore it is the primary place for the formation of cracks. Firstly, we demonstrate the development of failure mechanism in a simple homogeneous rectangular specimen for tensile and compressive load cases. Next, 3-phase and 4-phase composites are loaded in order to analyze crack formation and propagation in heterogeneous material under tensile and compressive load cases. For the sake of simpler representation, the obtained response curves in the following diagrams are

Table 1 Homogeneous specimen: material properties

Material	ν	E	σ_c	σ_m	σ_n	G_{fc}	G_{fm}	G_{fn}
Homogeneous	0.2	30.000	7	3	2	0.5	0.3	0.1

Material parameters: ν - Poisson's ratio, E - Young's modulus (N/mm^2), σ_c - compressive strength (N/mm^2), σ_m - shear strength (N/mm^2), σ_n - tensile strength (N/mm^2), G_{fc} - compressive fracture energy (N/mm), G_{fm} - shear fracture energy (N/mm), G_{fn} - tensile fracture energy (N/mm)
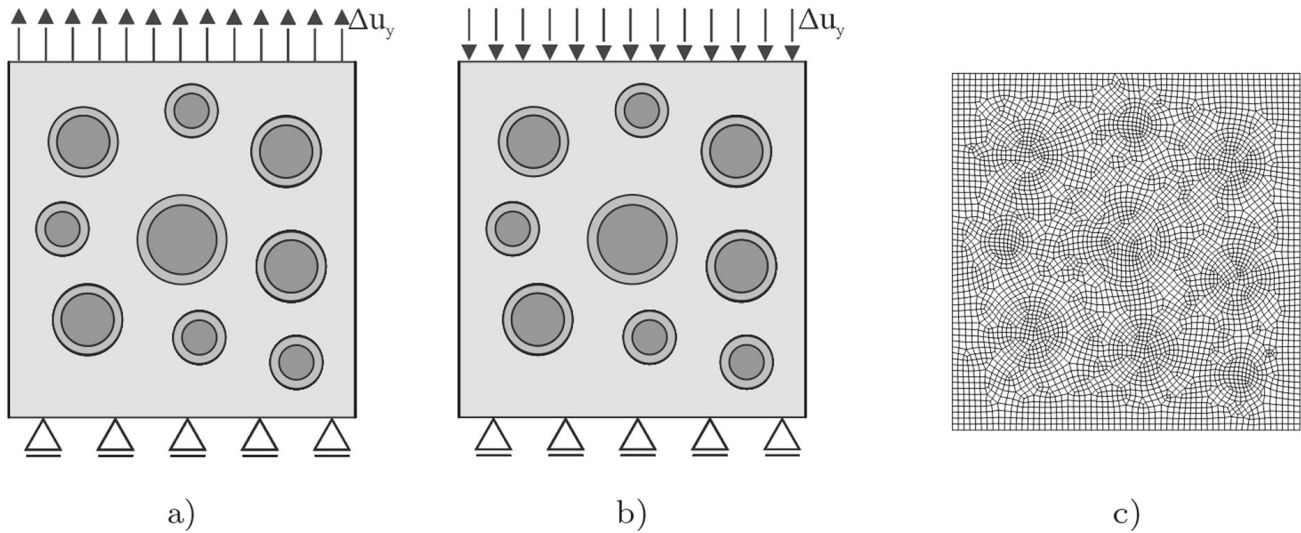
Fig. 9 3-phase test: **a** Tensile load case, **b** Compressive load case and **c** Finite element mesh composed of 4708 elements

Table 2 3-phase test: material properties

Material	ν	E	σ_c	σ_m	σ_n	G_{fc}	G_{fm}	G_{fn}
Cement matrix	0.2	30.000	5	2	1	0.05	0.01	0.003
ITZ	0.2	30.000	2.5	1	0.5	0.015	0.003	0.001
Aggregate	0.2	70.000	–	–	–	–	–	–

presented with positive values for compressive and tensile load cases.

The proposed model and the presented finite element formulations have been implemented in the research version of the computer code FEAP (Taylor 2020). The crack tracking algorithm and clustering have been implemented in MATLAB, while the model also uses MATFEAP interface (Bindel 2011) for exchange of data between the two codes.

4.1 Failure of homogeneous specimen

The specimen is a rectangular plate with thickness t = 1 mm, length L = 150 mm and height H = 300 mm. It is subjected to two different sets of imposed displacement loading cases. The mesh is made of 240 elements that can develop failure mechanisms. The specimen is restrained on the lower side and loaded as illustrated in Figs. 5, 6. The chosen material parameters are presented in Table 2. In order to initiate a crack in a homogeneous environment, the material strengths are lowered by 5 percent in a finite element located in the specimen center.

Figure 7 shows the final crack pattern in the specimen at the end of simulation for each loading case. In the tensile load case, a horizontal and fully aligned crack propagates through the mesh as a result of activation of the Rankine failure criterion. In the compressive load case, the appearance of shear stresses causes
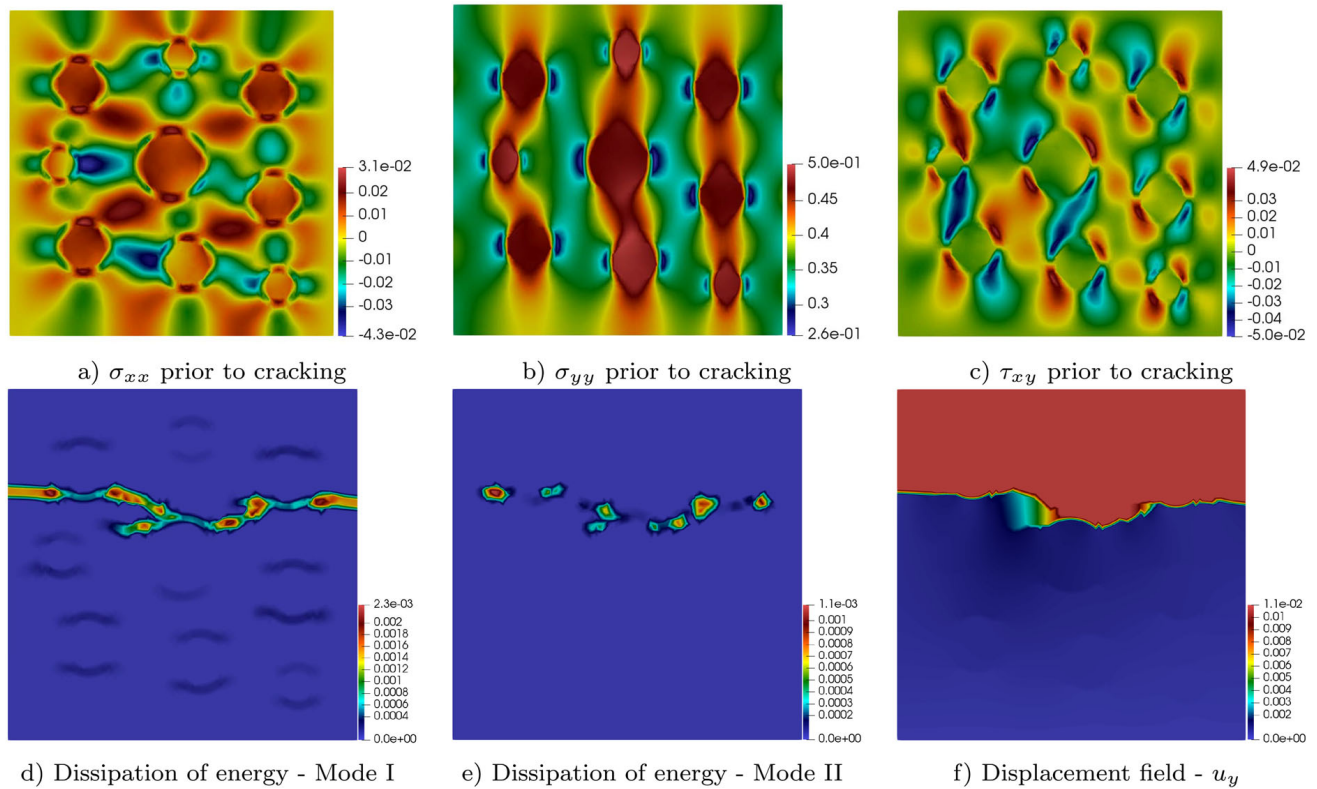
a) σ_{xx} prior to cracking

b) σ_{yy} prior to cracking

c) τ_{xy} prior to cracking

d) Dissipation of energy - Mode I

e) Dissipation of energy - Mode II

f) Displacement field - u_y

Fig. 10 3-phase test: Tensile load case results; stresses are plotted in N/mm^2, energy dissipation in N/mm
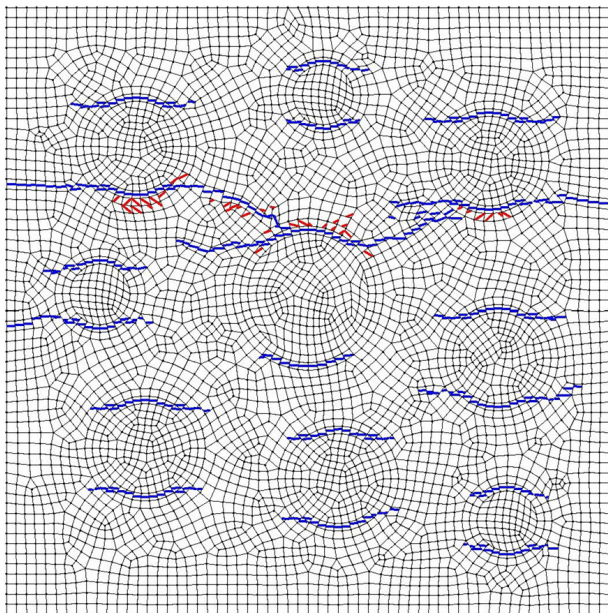

Fig. 11 Formed cracks at the end of 3-phase tensile test. Localized discontinuity lines are depicted in blue (Rankine) and red (Maximum shear stress)

formation of a diagonal crack at an angle of 45° by fulfilling the Maximum shear stress criterion. The specimen is sheared in one direction until the complete failure of the material. Although the shear cracks are not constrained by tracking algorithm and the discontinuity lines are not forced to exactly continue from the previously localized elements, the final shear crack is fully connected from the thermodynamic point of view where all localized neighbouring elements completely softens and undergoes failure. This is manifested from the reaction-imposed displacement curves for both load cases which are presented in Fig. 8. Both graphs show the total loss of specimen resistance.

4.2 3-phase test

In this test, the specimen is regarded as a 3-phase heterogeneous material consisting of several randomly distributed aggregates, with 5 mm wide ITZ, which are surrounded by a cement matrix. A square specimen with the dimensions of length L = 150 mm and thickness t = 1 mm, is supported from the bottom edge and loaded with two types of vertical loading from the
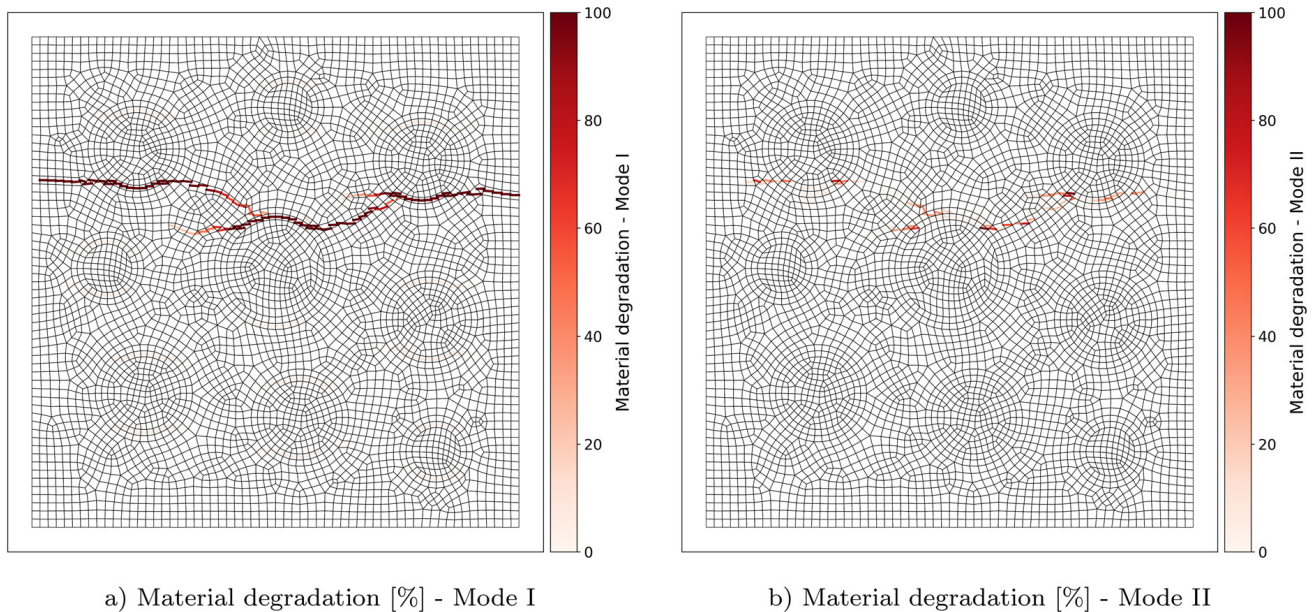
a) Material degradation [%] - Mode I

b) Material degradation [%] - Mode II

Fig. 12 3-phase tensile test: Material degradation data
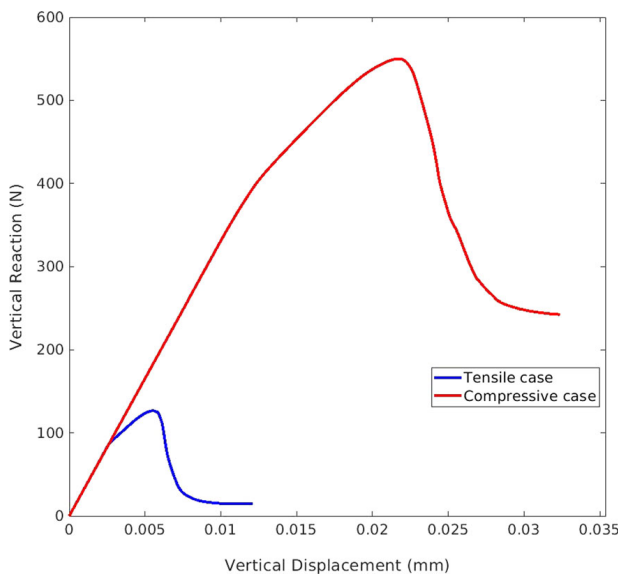

Fig. 13 Reaction-displacement curves in 3-phase fracture test

top side. A detailed view of the geometry, constituent arrangement, finite element mesh and loading conditions are presented in Fig. 9. The material properties of the constituents and their fracture parameters are listed in Table 2.

The tensile load case is conducted with the imposed vertical nodal displacements (Fig.9a). The heterogeneous stress state with higher stress concentrations around the aggregates can be observed prior to crack initiation (Fig. f2a–c). The first cracks initiate with

Rankine criterion in the ITZ zone due to the tensile stresses around the aggregates, primarily at the upper and lower poles. The clustering algorithm recognizes 18 distinct clusters of localized elements, where only elements that form continuous cracks within each cluster are retained. As the load increases, the cracks propagate out of the ITZ through the cement matrix, while the crack tracking algorithm controls the propagation of all cracks that formed from clusters. Among multiple localized elements in the mesh, the algorithm retains only localized elements that initiated with Rankine criterion and that extend continuous tensile cracks. Eventually, the cracks that propagate from clusters of localized elements extend and merge together into one dominant macrocrack that forms from outer edges of the specimen splitting the specimen in two parts. The dissipated energy plots from Fig. 10d–e show that the energy mostly dissipates in mode I, while the dissipation in shear mode II is observable at the locations where cracks merge and change the direction of their path. The final displacement field is plotted in Fig. 10f.

Figure 11 provides the plot of all localized elements and their corresponding embedded discontinuity lines. The discontinuities that are activated by Rankine criterion are depicted in blue, while red embedded lines denote activation by Maximum shear stress criterion. The final macrocrack is formed by merging tensile cracks that originated from weaker elements of ITZ.
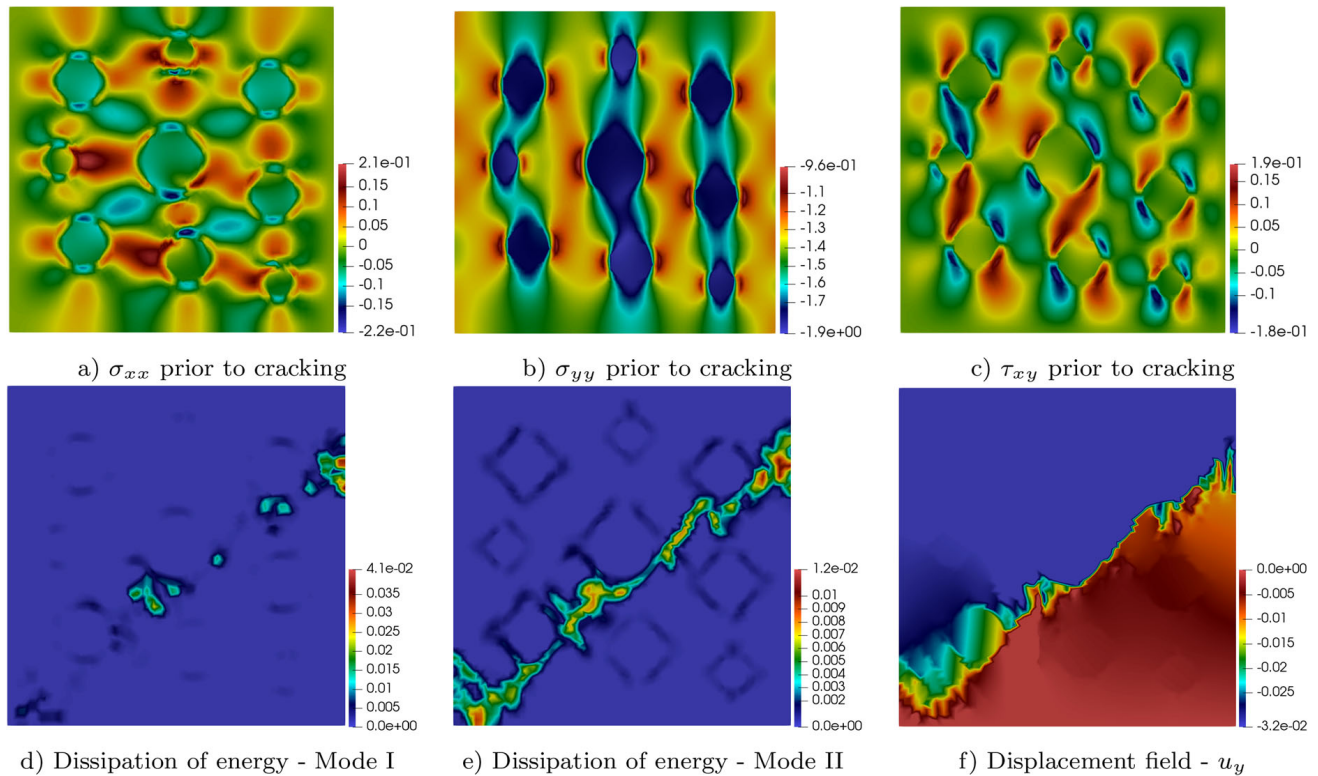
a) σ_{xx} prior to cracking

b) σ_{yy} prior to cracking

c) τ_{xy} prior to cracking

d) Dissipation of energy - Mode I

e) Dissipation of energy - Mode II

f) Displacement field - u_y

Fig. 14 3-phase test: Compressive load case results; stresses are plotted in N/mm^2, energy dissipation in N/mm
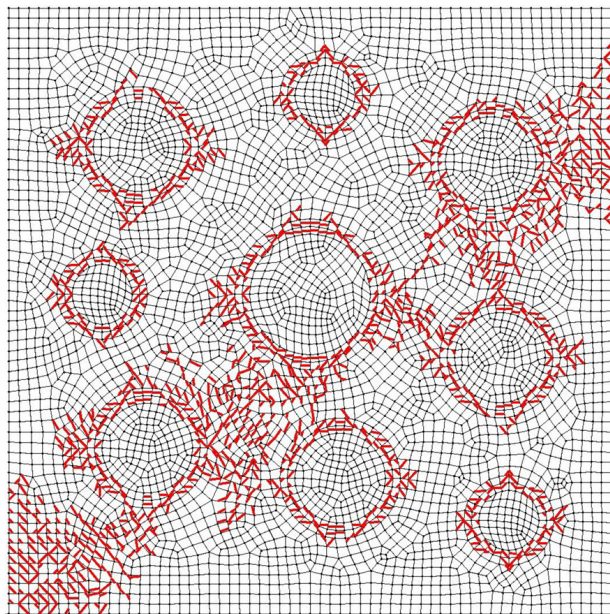

Fig. 15 Formed cracks at the end of 3-phase compressive load case test. Localized discontinuity lines are depicted in blue (Rankine) and red (Maximum shear stress)

Localization of certain elements by activating Maximum shear stress criterion is important for merging of

propagating tensile cracks, which is also observable in Fig. 11. The plot in Fig. 12a-b reveal the dominant crack path highlighted through the material degradation where most elements degraded significantly in mode I, while some elements at the merging points degraded in mode II as well. Figure 13 reveal the macroscopic response curve of the specimen with full softening for the tensile load case.

The compressive load case (Fig. 9b) produces heterogeneous stress field with stress concentrations around the aggregates. Figure 14a–c show the stress field components just before the initiation of the first cracks. The localization of the elements were initiated with the Maximum shear stress criterion and within the ITZ zone as they present the weakest spots of the specimen. Cracks continue to form and propagate through the entire ITZ zone and spread into the cement matrix, which can be observed in the dissipated energy plots (Fig. 14d–e). The energy is dominantly dissipated throughout the specimen in shear mode forming the final failure mechanism. It is also dissipated in mode I in the local regions of the specimen. The final displacement field providing the contours of the failure
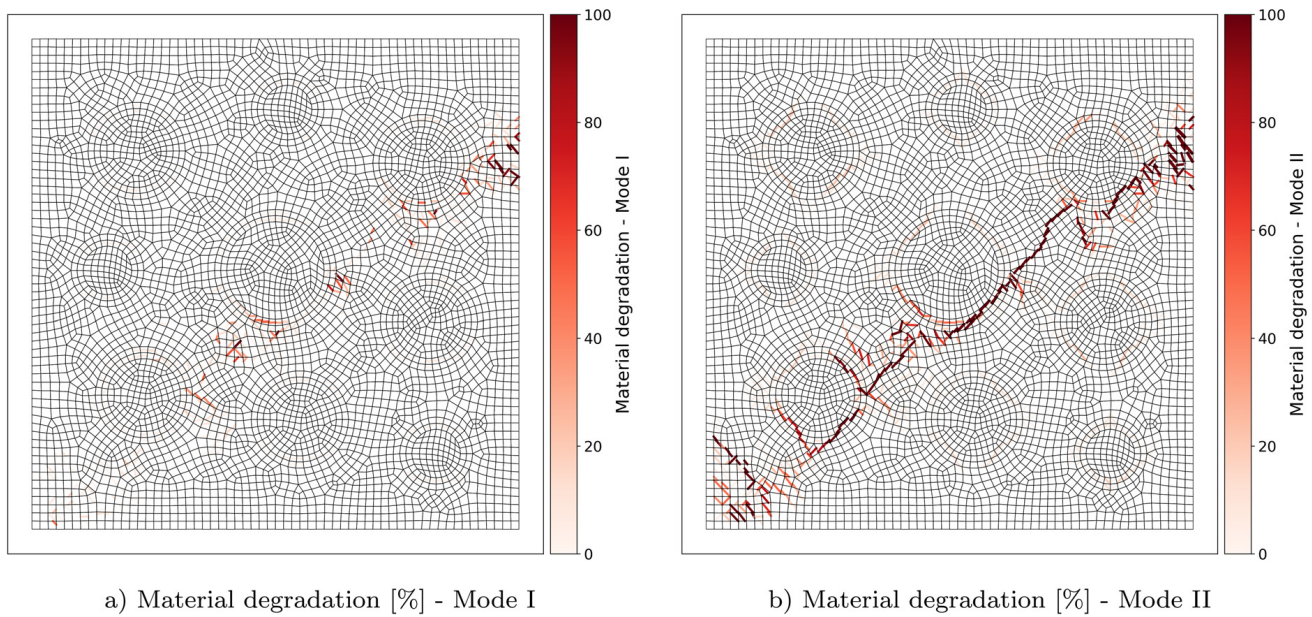
a) Material degradation [%] - Mode I   b) Material degradation [%] - Mode II

Fig. 16 3-phase compressive load case test: Material degradation data
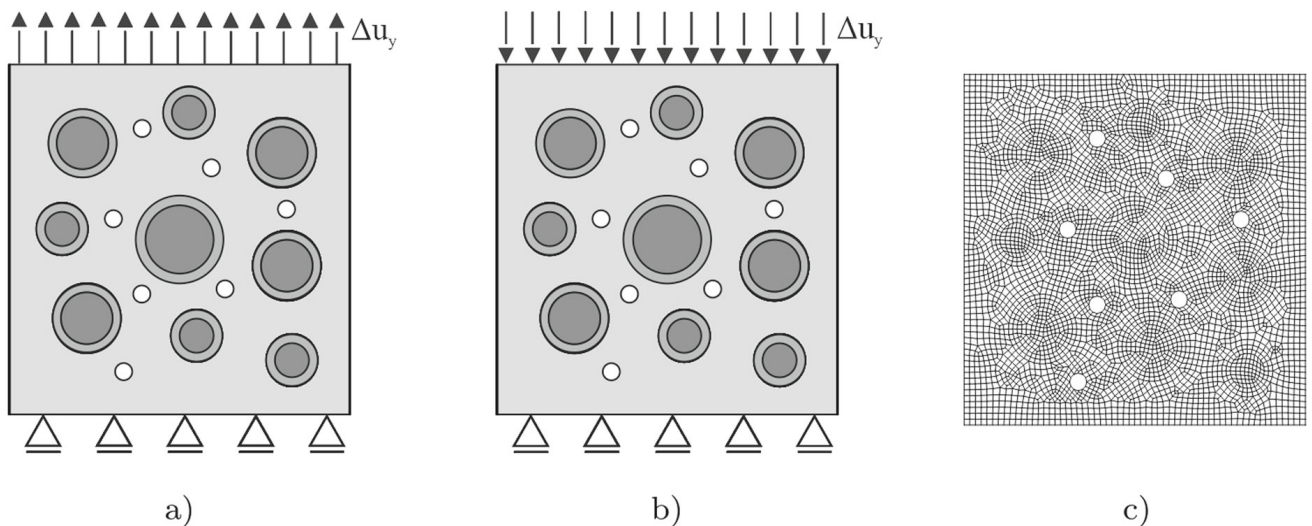

a)   b)   c)

Fig. 17 4-phase test: **a** Tensile load case, **b** Compressive load case and **c** Finite element mesh composed of 4948 elements

mechanism is shown in Fig. 14. Figure 15 shows the localized elements and their discontinuity lines.

In the compressive load case, multiple cracks were initiated and propagated in the mesh. The crack tracking algorithm does not force the shear cracks to be connected, so propagation, collision and merging of cracks occurred as a result of material constituents arrangements and stress state. The dominant macrocrack is also observable for material degradation plot in Fig. 16. The degree of material degradation gives insight into the dominant crack path, highlighting the discon-tinuity lines mostly due to shear. Since the cracks are not bounded to be continuous in shear, many elements localize and form the dominant failure mechanism as shown in Fig. 16. The shear cracks mostly connect, but some cracks do not align with the dominant macro-crack. Due to this reason, more energy is spent in the compression failure of such heterogeneous mate-rials. This phenomena is common in compressive test-ing of cementitious materials, with complicated failure mechanisms, many cracks and crushing of the material (Nikolic et al. 2018).
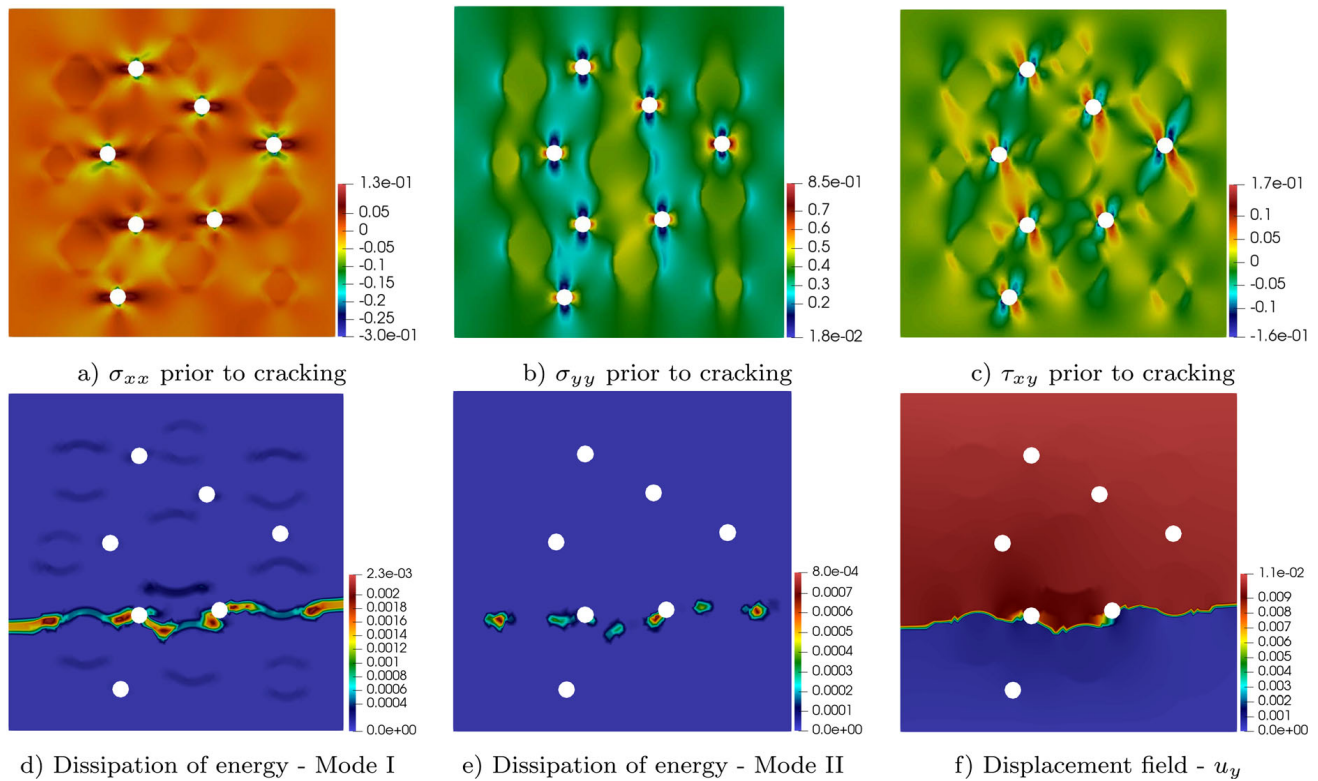
a) σ_{xx} prior to cracking   b) σ_{yy} prior to cracking   c) τ_{xy} prior to cracking

d) Dissipation of energy - Mode I   e) Dissipation of energy - Mode II   f) Displacement field - u_y

Fig. 18 4-phase test: Tensile load case results; stresses are plotted in N/mm^2, energy dissipation in N/mm

The macroscopic reaction curve for compressive load case is shown in Fig. 13, indicating a stiffness reduction of the overall system. Loading of the specimen causes a sudden drop in the reaction force due to the loss of resistance and its ability to support the additional load.

4.3 4-phase test

Several voids with a diameter of 10 mm, representing initial defects in the specimen, were randomly distributed within the previous specimen in order to form the 4-phase material. Material and fracture parameters remain the same as for the 3-phase test specimen. The overall geometry of a specimen, with the distribution of constituents, boundary conditions, finite element mesh, and load cases is shown in Fig. 17.

The presence of voids produces a noticeable effect on the specimen response in the tensile load case. The high-stress concentration regions appear around aggregates and voids (Fig. 18a–c). Therefore, in addition to cracking of the ITZ zone by activating Rankine criterion, tensile cracks also emerge from voids. The failure

mechanism and the formed macrocrack is different than in the 3-phase specimen subjected to tension case. In the present case, the horizontal macrocrack separates the specimen in the bottom half, traversing through the ITZ zone around the aggregates and passing through the voids. Figure 18d–e reveal the dominance of tensile opening through energy dissipation plot in mode I, while the energy dissipates in mode II as well. The displacement field is shown in Fig. 18.

Figure 19 provides the plot of localized elements and discontinuity lines. Majority of elements localize as a result of activation of Rankine criterion. The clustering mechanism initially recognizes 25 clusters of localized elements, including ITZ zone regions and voids. The crack tracking algorithm controls the localization of elements and multiple crack propagation by retaining those elements that extend existing tensile cracks. Material degradation plots in Fig. 20a, b show the highlighted dominant macrocrack, while other cracks did not activate significantly nor dissipated energy. Macroscopic response from Fig. 21 reveals the full softening of the specimen for the tensile case.

When the compression load case is applied, the stress concentrations are present around aggregates and
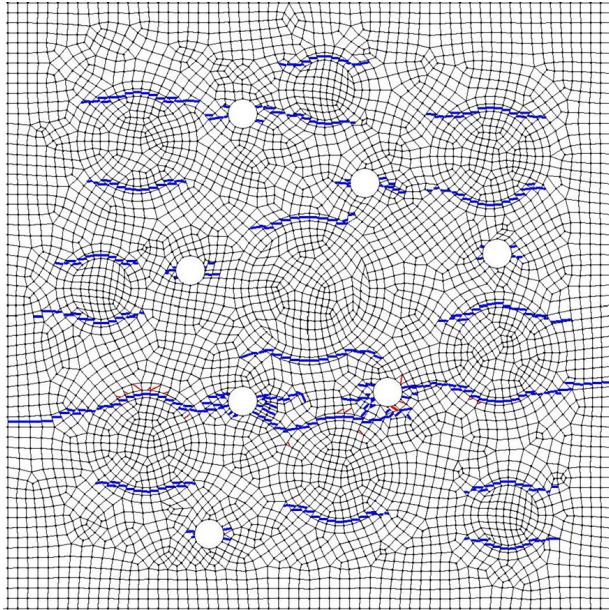
Fig. 19 Formed cracks at the end of 4-phase tensile test. Localized discontinuity lines are depicted in blue (Rankine) and red (Maximum shear stress)

voids (Fig. 22a–c). Multiple cracks are firstly induced with Maximum shear stress criterion around the aggregates and within the ITZ zone and they start propagating through the cement matrix. Further propagation of mode II cracks leads to dominantly diagonal type of the failure mechanism. At the same time, the cement matrix starts cracking around the voids due to high local

tensile stresses by activating Rankine failure criterion. During the load increase, multiple cracks connect and form a dominant failure line. The final failure state can be observed in energy dissipation plots in Fig. 22d–e and displacement field from Fig. 22f. Additionally, Fig. 23 shows the embedded discontinuity lines. Since crack tracking algorithm does not force shear cracks induced by Maximum shear stress criterion to be connected, much more elements tend to localize. Most of localized elements correspond to shear cracks, while tension cracks initiate from voids as well. Material degradation plots in Fig. 23a–b show that shear cracks mostly connect, but there are more cracks that do not necessarily align with others. This depends on the structural heterogeneity since merging is not forced with the algorithm. Due to this mechanism, more energy is needed to drive the specimen to failure. This is also observed from macroscopic response curve for 4-phase compressive case in Fig. 21. For both load cases, the total computed load capacity values were lower than for the 3-phase material. The presence of voids reduces overall material strength. As a result of cracking within the ITZ, a decrease in stiffness is observed in the form of a drop in the slope of the curve.

In comparison to the 3-phase compressive test, the presence of voids causes earlier local cracking of the cement matrix (around voids) which leads to different shape and position of the macrocrack. More precisely,
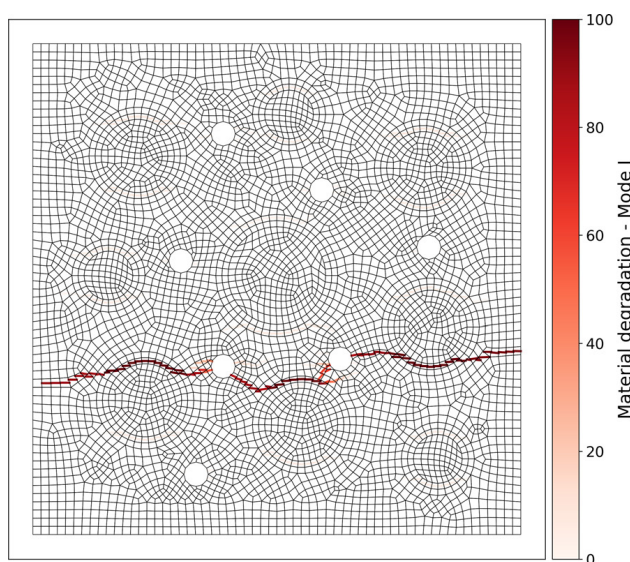
a) Material degradation [%] - Mode I
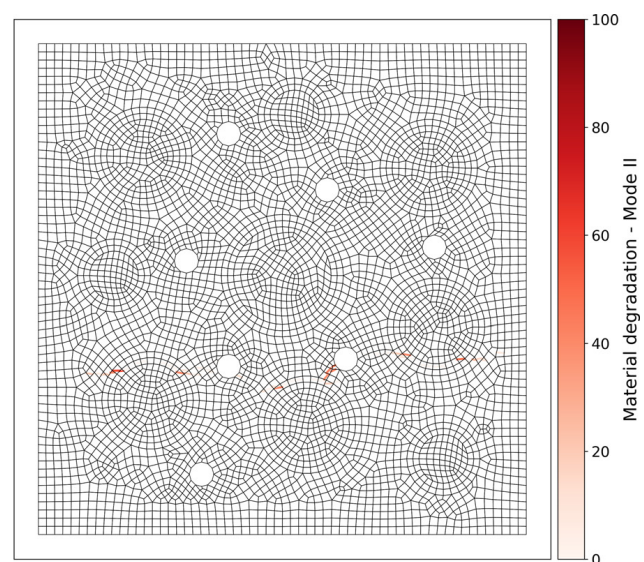
b) Material degradation [%] - Mode II

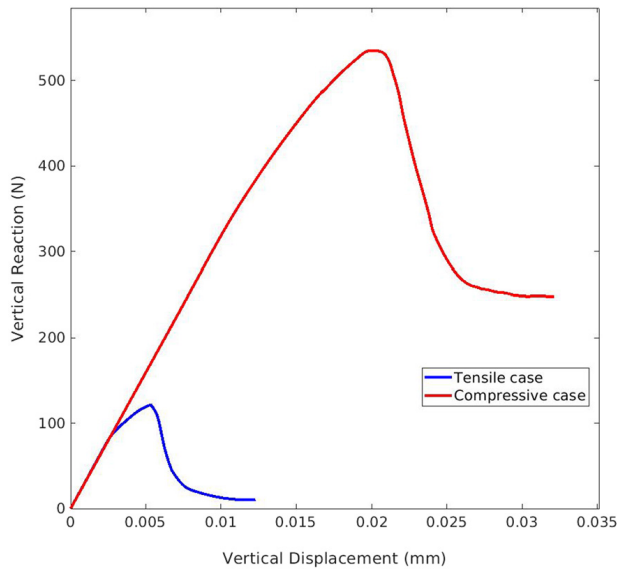**Fig. 20** 4-phase tensile test: material degradation data

Fig. 21 Reaction-displacement curves in 4-phase fracture test

4.4 The model performance

The presented model has demonstrated robustness and efficiency. Specifically, all the presented examples were performed within 2000 time steps (load increments). Two approaches were employed in the solution of global systems of equations. For simpler cases, the Newton-Raphson method was utilized to solve the global matrix of the system reaching the quadratic convergence. However, in examples involving complex geometries, such as those observed in the 3-Phase and 4-Phase examples, the Newton–Raphson method exhibited instability, particularly as material failure occurred, followed by sudden reaction drops. In these cases, the Quasi-Newton method emerged as a notably more stable alternative. To address the issue concerning the non-symmetric finite element's stiffness matrix, the Utangent command feature of the FEAP program coupled with the line search method (Newton–Raphson method) was used and it has proven to be an effective solution.

it begins in the middle of the specimen around the top edge and propagates through ITZ and voids toward the left and right outer edges.

a) σ_{xx} prior to cracking

b) σ_{yy} prior to cracking

c) τ_{xy} prior to cracking

d) Dissipation of energy - Mode I

e) Dissipation of energy - Mode II
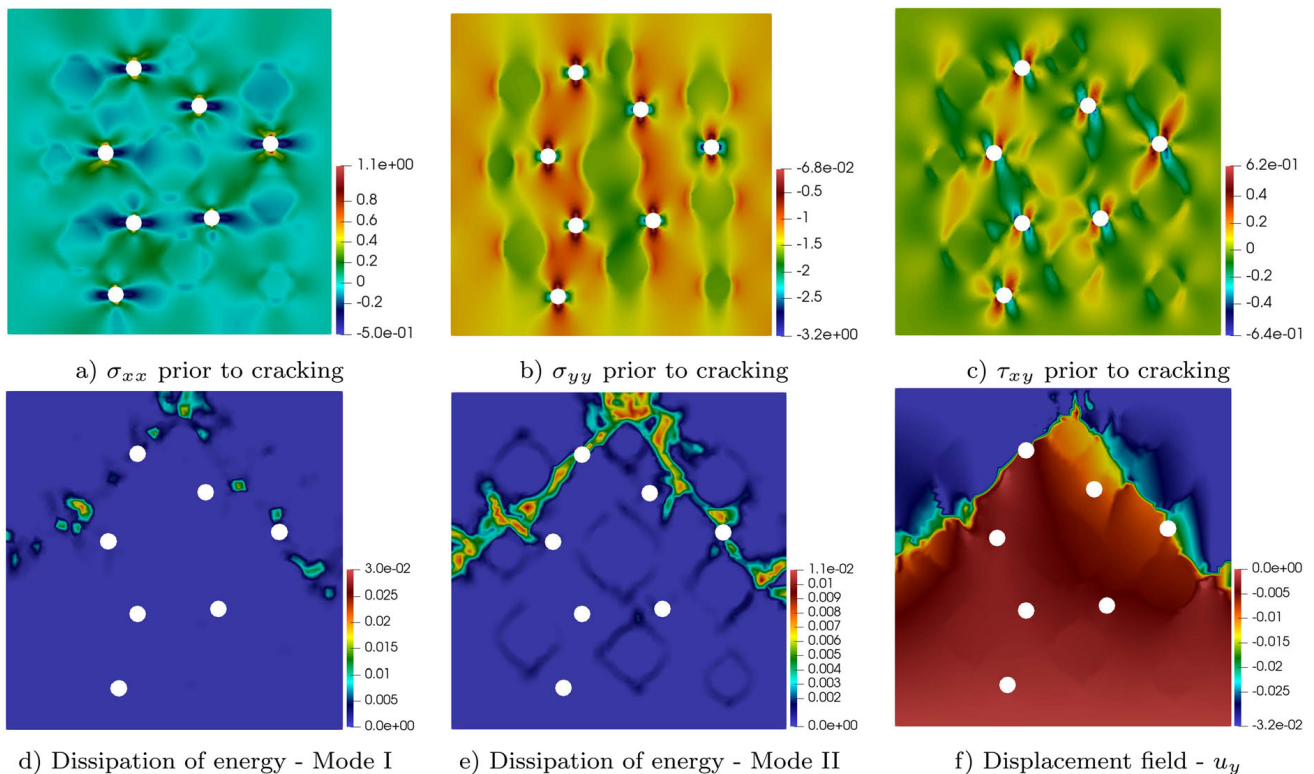
f) Displacement field - u_y

Fig. 22 4-phase test: compressive load case results; stresses are plotted in N/mm^2, energy dissipation in N/mm
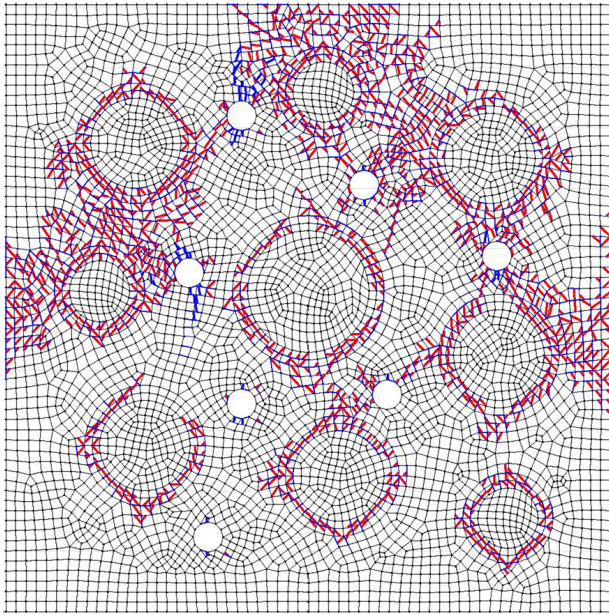
Fig. 23 Formed cracks at the end of 4-phase compressive test. Localized discontinuity lines are depicted in blue (Rankine) and red (Maximum shear stress)

5 Conclusion

In this paper, we presented a quadrilateral solid finite element model enhanced by incompatible modes, embedded strong discontinuities and crack tracking algorithm capable of simulating mesoscale quasi-brittle failure in heterogeneous materials. The model utilizes failure criteria at the local Gauss point level. This approach allows cracks to appear naturally with respect to the stress state within constituents of composite material. Crack initiation, location and orientation and determined solely by the stress state within an individual finite element. However, crack tracking algorithm ensures the continuity of tensile cracks while also eliminating spurious cracks in the mesh which can cause crack arrest and stress locking.

Quasi-brittle materials are known for their ability to absorb energy during the failure process as a result of various internal cracking mechanisms. Nevertheless, as stress levels and the extent of cracking increase, the material undergoes critical failure. The macroscopic failure mechanism results from the formation of multiple cracks within different constituents and their interactions, ultimately leading to crack propagation throughout the specimen and the formation of macrocracks.

The local discontinuous nature of the ED-FEM method and the proposed model is consistent with the behaviour observed in complex heterogeneous materials with multiple cracks at smaller scales contributing to larger ones and creating dissipation mechanisms in the fracture process zones. However, complex meshes such as those presented here and local nature of crack initiation ultimately provides difficult conditions for merging of cracks. It is shown here that crack track-

a) Material degradation [%] - Mode I
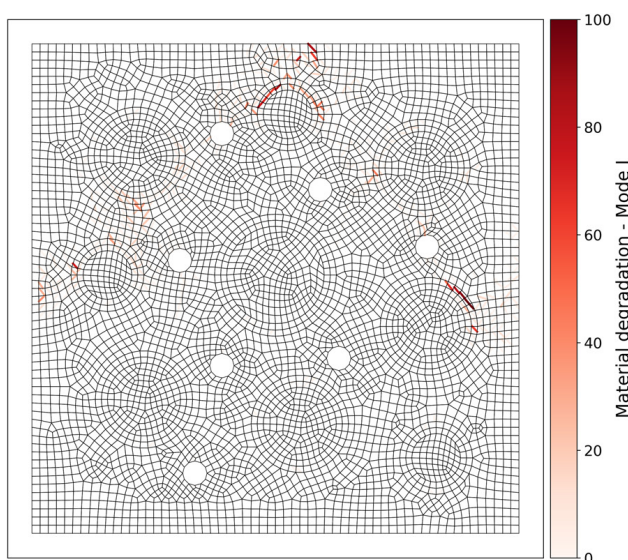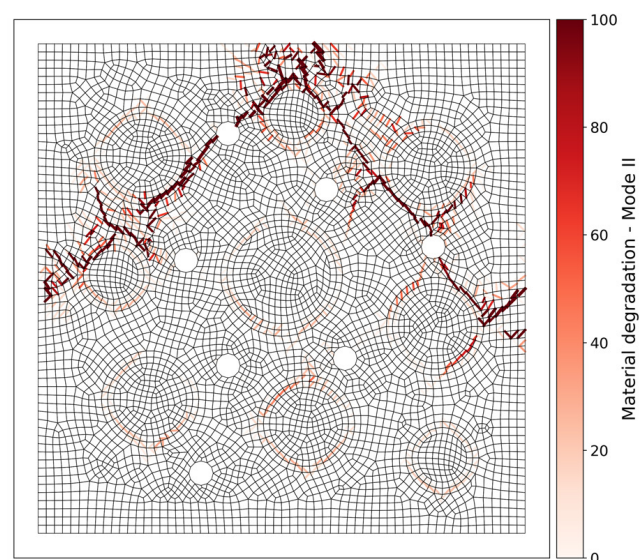
b) Material degradation [%] - Mode II

Fig. 24 4-phase compressive test: Material degradation data

ing algorithm capable of tracking multiple cracks can successfully eliminate spurious cracks and avoid stress locking.

Under tensile loading conditions, this approach predominantly leads to the formation of continuous macrocracks, through which almost all energy is dissipated. The cracking process unfolds as crack propagation advances towards the remaining uncracked elements, displaying a progressive character. In the case of compression load case, numerous elements localize due to Maximum shear stress criterion, indicating the development of microcracks within the material. However, due to stress redistribution and absence of crack tracking mechanism for shear cracks, some of these microcracks cease propagation and subsequently undergo unloading. The failure process consumes more energy for creation of microcracks which contribute to formation of fracture process zone. Meanwhile, other formed cracks become the dominant paths for the majority of energy dissipation. The observed processes in both tensile and compressive tests closely correspond to findings from simulations involving Lattice elements and experimental investigations documented in the literature (Nikolic et al. 2018; Rizvi et al. 2019).

References

Benkemoun N, Roubin E, Colliat J-B (2017) Fe design for the numerical modelling of failure induced by differential straining in meso-scale concrete: Algorithmic implementation based on operator split method. Finite Elem Anal Des 137:11–25. https://doi.org/10.1016/j.finel.2017.08.003

Bindel D (2011) Matfeap: Matlab interfaces to the feap finite element code. MATFEAP manual. https://www.cs.cornell.edu/bindel/blurbs/matfeap.html

Brancherie D, Ibrahimbegovic A (2009) Novel anisotropic continuum-discrete damage model capable of representing localized failure of massive structures: Part i: theoretical formulation and numerical implementation. Eng Comput 26:100–127. https://doi.org/10.1108/02644400910924825

Carija J, Nikolic M, Ibrahimbegovic A, Nikolic Z (2020) Discrete softening-damage model for fracture process representation with embedded strong discontinuities. Eng Fract Mech 236:107211. https://doi.org/10.1016/j.engfracmech.2020.107211

Cusatis G, Pelessone D, Mencarelli A (2011) Lattice discrete particle model (ldpm) for failure behavior of concrete i: Theory. Cement Concrete Compos 33(9):881–890

da Costa DD, Alfaiate J, Sluys L, Areias P, Júlio E (2013) An embedded formulation with conforming finite elements to capture strong discontinuities. Int J Numer Methods Eng 93(2):224–244. https://doi.org/10.1002/nme.4393

Dias I, Oliver J, Lloberas-Valls O (2018) Strain-injection and crack-path field techniques for 3d crack-propagation modelling in quasi-brittle materials. Int J Fract 212:67–87. https://doi.org/10.1007/s10704-018-0293-8

Du C, Huang W, Ghaemian M, Jiang S, Zhao Z (2023) New nonlocal multiscale damage model for modelling damage and cracking in quasi-brittle materials. Eng Fract Mech 277:108927. https://doi.org/10.1016/j.engfracmech.2022.108927

Dujc J, Brank B, Ibrahimbegovic A (2010) Quadrilateral finite element with embedded strong discontinuity for failure analysis of solids. Comput Model Eng Sci 69:223–260. https://doi.org/10.3970/cmes.2010.069.223

Gimenes M, Rodrigues EA, Bitencourt LA, Manzoli OL (2023) 2d mesoscale modeling of compressive fracture in concrete using a mesh fragmentation technique. Int J Solids Struct 260–261:112031. https://doi.org/10.1016/j.ijsolstr.2022.112031

Grassl P (2023) 3d lattice meso-scale modelling of the effect of lateral compression on tensile fracture processes in concrete. Int J Solids Struct 262–263:112086. https://doi.org/10.1016/j.ijsolstr.2022.112086

Hai L, Li J (2022) Modeling tensile damage and fracture of quasi-brittle materials using stochastic phase-field model. Theor Appl Fract Mech 118:103283. https://doi.org/10.1016/j.tafmec.2022.103283

Ibrahimbegovic A (2009) Nonlinear solid mechanics. Solid Mechanics and its Applications, 160

Ibrahimbegovic A, Wilson EL (1991) A modified method of incompatible modes. Commun Appl Numer Methods 7:187–194. https://doi.org/10.1002/cnm.1630070303

Jirásek M (2000) Comparative study on finite elements with embedded discontinuities. Comput Methods Appl Mech Eng 188(1):307–330. https://doi.org/10.1016/S0045-7825(99)00154-1

Karavelić E, Nikolić M, Ibrahimbegovic A, Kurtović A (2019) Concrete meso-scale model with full set of 3d failure modes with random distribution of aggregate and cement phase. part i: Formulation and numerical implementation. Comput Methods Appl Mech Eng 344:1051–1072. https://doi.org/10.1016/j.cma.2017.09.013

Kim S-M, Abu Al-Rub RK (2011) Meso-scale computational modeling of the plastic-damage response of cementitious composites. Cement Concrete Res 41:339–358. https://doi.org/10.1016/j.cemconres.2010.12.002

Linder C, Armero F (2007) Finite elements with embedded strong discontinuities for the modeling of failure in solids. Int J Numer Methods Eng 72:1391–1433. https://doi.org/10.1002/nme.2042

Moës N, Belytschko T (2002) Extended finite element method for cohesive crack growth. Eng Fract Mech 69:813–833. https://doi.org/10.1016/S0013-7944(01)00128-X

Nikolic M, Ibrahimbegovic A, Miscevic P (2015) Brittle and ductile failure of rocks: Embedded discontinuity approach for representing mode i and mode ii failure mechanisms. Int J Numer Methods Eng 102:1507–1526. https://doi.org/10.1002/nme.4866

Nikolic M, Karavelić E, Ibrahimbegovic A, Miščević P (2018) Lattice element models and their peculiarities. Arch Comput Methods Eng 25:753–784. https://doi.org/10.1007/s11831-017-9210-y

Nikolić M, Do XN, Ibrahimbegovic A, Nikolić Z (2018) Crack propagation in dynamics by embedded strong discontinuity approach: Enhanced solid versus discrete lattice model. Comput Methods Appl Mech Eng 340:480–499. https://doi.org/10.1016/j.cma.2018.06.012

Oliver J (1996) Modelling strong discontinuities in solid mechanics via strain softening constitutive equations part 1: Fundamentals. Int J Numer Methods Eng 39(21):3575–3600

Oliver J, Huespe A, Sanchez P (2006) A comparative study on finite elements for capturing strong discontinuities: E-fem vs xfem. Comput Methods Appl Mech Eng 195:4732–4752. https://doi.org/10.1016/j.cma.2005.09.020

Oliver J, Dias I, Huespe A (2014) Crackpath field and strain-injection techniques in computational modeling of propagating material failure. Comput Methods Appl Mech Eng 274:289–348. https://doi.org/10.1016/j.cma.2014.01.008

Ortega A, Roubin E, Malecot Y, Daudeville L (2022) A mixed-mode e-fem approach for the study of local fracture processes in heterogeneous quasi-brittle materials. Mater Struct 55:222. https://doi.org/10.1617/s11527-022-02055-y

Pijaudier-Cabot G, Bazant Z (1987) Nonlocal damage theory. J Eng Mech. https://doi.org/10.1061/(ASCE)0733-9399(1987)113:10(151)

Puccia M, Spada A, Giambanco G (2023) Finite elements with embedded interphases for strain localization in quasi-brittle materials. Eng Fract Mech 277:108956. https://doi.org/10.1016/j.engfracmech.2022.108956

Qiu W, Ueda T, Fu S, Han Y, Wang J, Ye J (2023) Mesoscale computational modeling of the fracture of concrete with complex shaped aggregates under the self-restraint stress. Compos Struct 303:116267. https://doi.org/10.1016/j.compstruct.2022.116267

Rizvi Z, Nikolic M, Wuttke F (2019) Lattice element method for simulations of failure in bio-cemented sands. Granular Matter. https://doi.org/10.1007/s10035-019-0878-6

Saloustros S, Pel'a, L., Cervera, M., & Roca, P. (2017) Finite element modelling of internal and multiple localized cracks. Comput Mech 59:299–316. https://doi.org/10.1007/s00466-016-1351-6

Schubert E, Sander J, Ester M, Kriegel HP, Xu X (2017) Dbscan revisited, revisited: Why and how you should (still) use dbscan. ACM Trans Database Syst 42(3):1–21. https://doi.org/10.1145/3068335

Simo J, Rifai M (1990) A class of mixed assumed strain methods and the method of incompatible modes. Int J Numer Methods Eng 29(8):1595–1638. https://doi.org/10.1002/nme.1620290802

Simo J, Oliver J, Armero F (1993) An analysis of strong discontinuities induced by strainsoftening in rate-independent inelastic solids. Computational Mechanics 12:277–296. https://doi.org/10.1007/BF00372173

Smoljanović H, Nikolić Z, Živaljić N (2015) A combined finite-discrete numerical model for analysis of masonry structures. Eng Fract Mech 136:1–14. https://doi.org/10.1016/j.engfracmech.2015.02.006

Smoljanović H, Živaljić N, Nikolić Z, Munjiza A (2018) Numerical analysis of 3d drystone masonry structures by combined finitediscrete element method. Int J Solids Struct 136–137:150–167. https://doi.org/10.1016/j.ijsolstr.2017.12.012

Stanić A, Brank B, Brancherie D (2020) Fracture of quasi-brittle solids by continuum and discrete-crack damage models and embedded discontinuity formulation. Eng Fract Mech 227:106924. https://doi.org/10.1016/j.engfracmech.2020.106924

Stanić A, Brank B, Ibrahimbegovic A, Matthies H (2021) Crack propagation simulation without crack tracking algorithm: Embedded discontinuity formulation with incompatible modes. Comput Methods Appl Mech Eng 386:114090. https://doi.org/10.1016/j.cma.2021.114090

Taylor RL (2020) Feap - finite element analysis program. http://projects.ce.berkeley.edu/feap/.

Thilakarathna P, Kristombu Baduge K, Mendis P, Vimonsatit V, Lee H (2020) Mesoscale modelling of concrete-a review of geometry generation, placing algorithms, constitutive relations and applications. Eng Fract Mech 231:106974. https://doi.org/10.1016/j.engfracmech.2020.106974

Thongraksa A, Jongpradist P, Nanakorn P, Tunsakul J (2023) Shear fracture propagation in quasi-brittle materials by an elementfree galerkin method. Theor Appl Fract Mech 123:103713. https://doi.org/10.1016/j.tafmec.2022.103713

Zhang Y, Mang HA (2020) Global cracking elements: A novel tool for galerkinbased approaches simulating quasi-brittle fracture. Int J Numer Methods Eng 121(11):2462–2480. https://doi.org/10.1002/nme.6315

Zhang Y, Zhuang X (2018) Cracking elements: A self-propagating strong discontinuity embedded approach for quasi-brittle fracture. Finite Elements Anal Design 144:84–100. https://doi.org/10.1016/j.finel.2017.10.007

Zhang Y, Lackner R, Zeiml M, Mang HA (2015) Strong discontinuity embedded approach with standard sos formulation: Element formulation, energy-based crack-tracking strategy, and validations. Comput Methods Appl Mech Eng 287:335–366. https://doi.org/10.1016/j.cma.2015.02.001

Zhou R, Song Z, Lu Y (2017) 3d mesoscale finite element modelling of concrete. Comput Struct 192:96–113. https://doi.org/10.1016/j.compstruc.2017.07.009

B. Comparison of Machine Learning and gPC-based proxy solutions for an efficient Bayesian identification of fracture parameters - Paper II
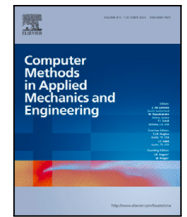
Comparison of Machine Learning and gPC-based proxy solutions for an efficient Bayesian identification of fracture parameters

Matej Šodan [a], András Urbanics [b], Noémi Friedman [b] , Andjelka Stanic [c] ,
Mijo Nikolić [a] ,*

[a] *Faculty of Civil Engineering, Architecture and Geodesy, University of Split, Matice hrvatske 15, Split, 21000, Croatia*
[b] *HUN-REN Institute for Computer Science and Control (SZTAKI), Kende u.13-17, Budapest, 1111, Hungary*
[c] *Faculty of Engineering Technology, University of Twente, Drienerlolaan 5, Enschede, 7522 NB, The Netherlands*

ARTICLE INFO

ABSTRACT

Fracture parameters play an important role in accurately simulating fracture propagation phenomena, which are highly nonlinear and sensitive to various parameters. The main focus of this paper is to offer different proxy modeling techniques to enable the otherwise computationally extremely expensive Bayesian identification procedure performed with Markov Chain Monte Carlo method. The paper contrasts polynomial chaos methods with machine learning techniques, including deep neural networks, in identification of uncertain fracture parameters. In addition, the application of autoencoders to push the stochastic process of deformations to low-dimensional representation is also analyzed. Two fracture scenarios are proposed for parameter identification: the hole tension test and the four point bending test. The 2D fracture propagation model is based on embedded strong discontinuity method, efficiently capturing complex failure mechanisms in modes I and II. The provided results show the successful identification of fracture parameters, including tensile and shear strength, as well as tensile and shear fracture energy using the different proxy modeling techniques and give explanations on the advantages and disadvantages of using different methods.

1. Introduction

The unexpected appearance of cracks in Civil Engineering structures indicates potential structural issues that require investigation. Unstable crack propagation can compromise structural stability, leading to high maintenance costs or catastrophic failure. Consequently, the analysis and prediction of material failure receive significant attention within the engineering community. Understanding fracture mechanics and implementing this knowledge allows civil engineers to enhance the safety and quality of structures. However, despite advancements in this field, fracture analysis remains challenging [1–3]. Modeling crack propagation and material damage is a complex process that involves numerous nonlinearities. Cementitious materials, in particular, are heterogeneous with various constituents, each possessing different material and fracture properties. Their distributions affect the stress states, and thus the initiation and propagation of the cracks. As cracks form and propagate, the material experiences hardening, softening, or

both, followed by permanent damage and/or plastic deformation. While numerous simulation tools exist for modeling material and structural failure, particularly in cases of localized failure and crack propagation, their predictive capabilities heavily rely on the accuracy of uncertain input parameters that reflect the material state and complex microstructure. This work focuses on the inverse problem of identifying (uncertain) fracture parameters by using a Bayesian approach. The general polynomial chaos expansion (gPCE) and neural network (NN) proxy models are proposed together with the application of the autoencoder model for low dimensional representation in order to learn and predict material failure and crack propagation based on data generated from fracture simulations.

A variety of numerical models are used in the literature to simulate material failure processes. Traditionally, discrete crack models and smeared crack models were used mostly for concrete failure. Moreover, non-local damage based models are used to avoid mesh sensitivity and localization problems that arise in traditional damage models [1]. Extended finite element (X-FEM) models enhance the displacement field globally at the nodal level within the basic finite element (FEM) framework to describe crack formation [4,5]. Embedded discontinuity finite element (ED-FEM) models employ a local (element) based approach by adding strong discontinuities and computing it at the local level, which avoids the increase of dimensions of the stiffness matrix of cracked elements [4,6–8]. Phase-field models simulate crack formation through a continuous parameter field over finite elements, describing their current degraded state [9–11]. Another effective approach for modeling failure with crack propagations is by using lattice elements, which represent the material as a set of discrete one-dimensional elements, and Voronoi cells, which describe the cracking of the material through the incorporation of discontinuities within the lattice elements [3,12–14].

In this work, we use the quadrilateral Q6ED model [15] as forward model for fracture propagation, which is based on ED-FEM method for two-dimensional material failure simulation. The integration of strong discontinuities enables the modeling of cracks by introducing the localization line inside the finite element. The displacement field of the element is enhanced by the jump at the place of the crack, thus regularizing the dissipated energy in terms of the local parameter to ensure mesh-independent results when using coarse meshes. Furthermore, local enrichment of the displacement field enables static condensation of the stiffness matrix of each cracked element while preserving the initial dimension. These aspects are particularly noteworthy for complex fracture simulations as it ensures fast computation time. With this model, material failure in constant modes I and II, representing tensile opening and closing processes and crack shear sliding, can be simulated.

Regardless of the type of model used, various material and modeling parameters are necessary to simulate fracture processes. This work focuses only on the material parameters related to fracture propagation (material strengths and fracture energies for modes I and II). Using a numerical model without determining and calibrating its parameters based on the existing structure leads to uncertain predictions. This is particularly evident in the fracture analysis, for which the value of the selected parameters significantly affects the processes. With the available measurements and an initial assumption of parameter values, the goal in traditional calibration is to adjust these parameters to minimize the difference between model predictions and observed measurements. The optimal deterministic values are those that produce the smallest error. The ill-posed nature of the inverse problem may arise here, where solutions are not unique or stable, necessitating regularization techniques [16,17]. In contrast, the stochastic inverse problem offers a more robust, probabilistic approach. By framing the solution process within Bayes theorem, uncertain parameters are treated as random variables. These variables are initially described by a prior distribution, which reflects existing knowledge or assumptions about the parameters. The Bayesian inverse method then integrates this prior distribution with noisy measurements to refine the understanding of the parameters, yielding a solution distribution known as the posterior distribution. Rather than finding a single deterministic solution, this approach provides a comprehensive distribution of possible solutions, effectively transforming the inverse problem into a well-posed one. This probabilistic framework enhances the robustness and reliability of the parameter calibration process. One way to approach this is through sampling methods, such as the Monte Carlo Markov chain (MCMC) method, used in this work. The MCMC method constructs Markov chains whose stationary distribution approximates the desired Bayesian posterior distribution through random walks. Alternative approaches include Kalman filter methods, the Minimum Mean Square Estimator method, and others [18,19].

The Bayesian inverse method has recently gained attraction in Civil Engineering as a tool for estimating material parameters, calibrating FEM models, and facilitating health monitoring. In the literature, numerous applications are found, including the identification of elastic [20–22] and nonlinear elastoplastic and damage parameters [23–25]. Additionally, several studies have focused on identifying fracture parameters. For example, [26] determined the elastic and strength parameters of concrete tram poles, while [27] investigated fracture properties of concrete and steel-concrete bond parameters using ED-FEM and X-FEM models. Furthermore, research presented in [28,29] aimed to identify parameters of lattice models, particularly the mechanical properties of mortar and concrete through different test methods. The work in [30,31] deals with the fracture parameters of the phase-field model for elastic solids and brittle cement mortar, respectively.

As highlighted in the previously mentioned papers, the feasibility of Bayesian calibration in complex fracture mechanics problems hinges on the development of efficient proxy models, also referred to as surrogate models [32]. Without such models, the computational demands become prohibitive. Traditionally, many studies in this domain have relied on general polynomial chaos expansion (gPCE) for surrogate modeling. While gPCE is a powerful tool to represent the parametric dependence of structural responses, it may not always be the optimal choice when dealing with complex, non-smooth functions. In such cases, the approximation capabilities of gPCE may be limited and some alternative machine learning models, such as neural networks (NN), may provide a better solution (see e.g. [33]).

This paper introduces Bayesian inversion method to fracture mechanics problems where the forward fracture model relies on embedded strong discontinuities. For this model, the only parameters involved are those directly representing the material fracture properties such as tensile and shear strengths, as well as corresponding fracture energies in modes I and II. The present paper

also explores and compares various surrogate modeling techniques, including neural networks as proxy models for computationally demanding fracture mechanics simulations. While NN offer significant flexibility in representing the complex, nonlinear behavior inherent in fracture mechanics, we also compare their performance and applicability with simpler linear regression models using gPCE. Although these simpler models are easier to construct with less hyperparameters, they sometimes lack the flexibility needed to accurately capture complex input–output relationships. The paper also contrasts lower dimensional representation of fracture processes using the encoder of a trained autoencoder. Such proxy model can filter out noisy data and can improve the efficiency of the parameter identification process. The proposed modeling strategies represent a comprehensive framework of fracture parameter identification using Bayesian methods demonstrated through the two fracture mechanics problems: hole tension test and four point bending test.

The paper is structured as follows: Section 2 summarizes the forward model used for fracture simulations. Section 3 provides a brief overview of the probabilistic approach of the Bayesian inverse method, MCMC method and applied proxy models. Section 4 elaborates on the test examples. Section 5 includes an accuracy comparison of each selected proxy model and their final identification process results within the MCMC framework. Finally, Section 6 presents the conclusions drawn from the study.

2. Modeling of fracture propagation

As the material undergoes loading, the fracture process starts with the appearance of stress concentrations that lead to the formation of microcracks. This kind of occurrence is inevitable and does not necessarily represent a structural problem. However, with material degradation or increased loading, stress values continue to rise, which causes additional cracking processes. If left unmonitored and untreated, this progression can result in unstable propagation and the formation of macrocracks. The appearance of one or more macrocracks within the material presents a major structural concern that can lead to the complete failure of the construction. Therefore, accurate fracture analysis is imperative to assess structural stability and future performance. However, the simulation of such a complex process poses a significant challenge for numerical models due to its highly nonlinear nature and sensitivity to fracture parameters [1–3].

In this paper, a two-dimensional solid finite element enriched with incompatible modes and embedded strong discontinuities is employed as a deterministic solver to simulate complex fracture phenomena. Its primary parameters that govern the fracture process are material strengths and fracture energies. The strength of material defines the stress limit at which crack formation occurs. Fracture energy parameters govern the energy dissipation, and thus the crack propagation speed. Together, these parameters form the overall cracking process, shaping the formation of crack and its propagation [15,34]. In this section, a brief overview of the model's procedures with cracking criteria and constitutive relations is provided.

2.1. Solid finite element model with the embedded strong discontinuity

A 2D quadrilateral solid finite element enriched with incompatible modes and embedded strong discontinuities (SDA), referred to as the Q6ED element, is employed to simulate fracture propagation processes. By incorporating the incompatible modes, the element displacement field is enriched with additional quadratic terms, which favorably influence fracture analysis based on SDA [1,34]. During the loading process of an uncracked element, the rise of the stress values is governed by a linear elastic model. A fracture occurs when a stress state surpasses the material strength value. The cracking procedure is described by the statically and kinematically optimal nonsymmetric formulation (SKON) of embedded strong discontinuities [8]. Here, the cracks are introduced through locally enhanced jumps over the crack line in the displacement field which ensures result independence of the size of the finite elements [1,34,35].

The cracked Q6ED element is divided into two parts: the intact elastic bulk part and the non-linear crack part. The evolution of the crack part is treated in terms of a thermodynamic framework, where initiation, position, and orientation rely solely on the stress state within the element [34]. Each crack can propagate in constant modes I and/or II characterized by corresponding softening parameters α_i (α_1 and α_2 (see Fig. 1)). Parameter α_1 takes only positive values as the crack can only open or close in tension, while α_2 can be both positive or negative, which allows for shear sliding in both directions. The fracture process involves a dissipation of energy which is controlled by the chosen law of exponential damage softening. This law is governed by the internal damage variables ξ_n and ξ_m, which indicate the level of the element damage and the material softening for both separation modes. The accumulation of these variables is irreversible, which leads to the permanent stiffness reduction due to material cracking [1,34,35].

2.1.1. Kinematics

A geometry of the quadrilateral solid finite element is described by the Cartesian coordinates $x = [x, y]^T$ as $x(\xi) = \sum_{a=1}^{4} N_a(\xi) x_a$. Here, $\xi(\xi, \eta) \in [-1, 1] \times [-1, 1]$ denotes the element's isoparametric coordinates, x_a represents the nodal coordinates, and $N_a(\xi) = \frac{1}{4}(1 + \xi_a \xi)(1 + \eta_a \eta)$ are the Lagrange bi-linear interpolation functions. To simulate fracture phenomena, the quadrilateral solid element is enhanced by incompatible modes and strong embedded discontinuities. Then its displacement field reads:

$$u(\xi, \Gamma^e) = \sum_{a=1}^{4} N_a(\xi) d_a + \sum_{b=1}^{2} M_b(\xi) \rho_b + \sum_{i=1}^{2} p_i(\xi, \Gamma^e) \alpha_i. \tag{1}$$

In Eq. (1), the first part represents the standard quadrilateral formulation, where d_a are the nodal displacements. The second part denotes the incompatible modes enhancement of the field by the additional quadratic shape functions $M_1 = 1 - \xi^2$ and $M_2 = 1 - \eta^2$, along with their corresponding values of the incompatible modes ρ_b [1]. The last part corresponds to the embedded
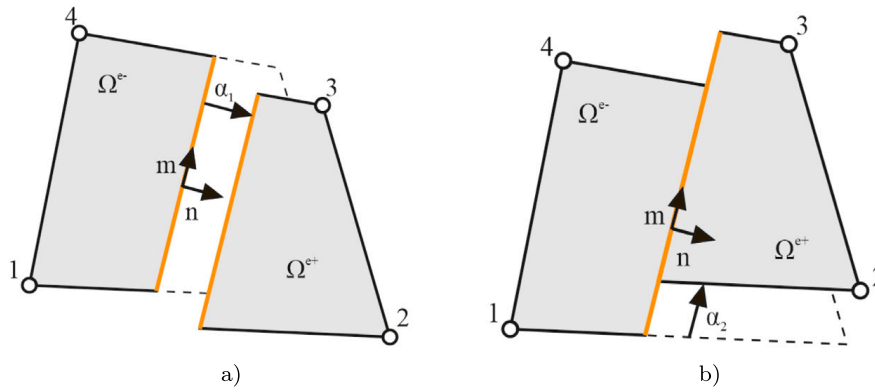
Fig. 1. Separation modes: (a) Tensile opening (Mode I) and (b) Shear sliding (Mode II).

strong discontinuities. Here, $\boldsymbol{p}_i$ are the separation functions assuming that during fracture, one part of the element Ω^{e-} remains still while the other part Ω^{e+} moves (see Fig. 1):

$$\boldsymbol{p}_1 = \left(H_\Gamma(\boldsymbol{x}) - \sum_{a \in \Omega^{e+}} N_a \right) \mathbf{n} \qquad \boldsymbol{p}_2 = \left(H_\Gamma(x) - \sum_{a \in \Omega^{e+}} N_a \right) \mathbf{m}. \tag{2}$$

In Eq. (2), vectors $\boldsymbol{n} = [n_x, n_y]^T$ and $\boldsymbol{m} = [m_x, m_y]^T = [-n_y, n_x]^T$ represent unit normal and tangent vectors to the defined crack line Γ^e within the element. H_Γ denotes the Heaviside step function that introduces displacement jump at the crack $\boldsymbol{x} \in \Omega^{e+}$.

The strain field is obtained by applying the symmetric gradient operator to Eq. (1). The details of this procedure and the model development are given in [15].

2.1.2. Crack initiation procedure

The crack initiation process for the Q6ED element, as outlined in [15,34], is controlled by the stress state at the element's integration points, from which both the location and orientation of the resulting crack are calculated. When the chosen crack criterion is met for the individual element, a crack is embedded. In this work, we use the Rankine criterion, which assumes that fracture in the cementitious material occurs when the maximum principal stress exceeds the material's tensile strength. In each timestep all uncracked elements are evaluated. The procedure begins by calculating the principal stress values at all four integration points:

$$\sigma_{p1,p2}^{e,i} = \frac{\sigma_{xx}^{e,i} + \sigma_{yy}^{e,i}}{2} \pm \sqrt{\left(\frac{\sigma_{xx}^{e,i} - \sigma_{yy}^{e,i}}{2} \right)^2 + \left(\sigma_{xy}^{e,i} \right)^2} \tag{3}$$

From the results of Eq. (3), the maximum principle stress for each integration point is collected (i.e. $\sigma_p^{e,i} = \max[\sigma_{p1}^{e,i}, \sigma_{p2}^{e,i}]$). From the collected values, the maximum one is singled out: $\sigma_p^e = \max_{i=1,\dots,4} \sigma_p^{e,i}$, and compared with the tensile strength σ_n. If σ_p^e surpasses the strength, the fracture occurs, and the crack needs to be embedded in the element. Integration points with maximum principle stress values σ_p^e (within a certain tolerance) are gathered in a set $B^e = \{id \in \{1,2,3,4\} : \sigma_p^{e,id} = \sigma_p^e\}$. By considering only those points that have the maximum principal values, the model calculates the accurate position and orientation of the crack within each element, which proved to be crucial for successful fracture simulation [34]. From the collected values of the set B^e, the global coordinates of crack geometric center are calculated by averaging:

$$\boldsymbol{x}_{ED}^e = \frac{1}{N_{B^e}} \sum_{i \in B^e} \boldsymbol{x}^{e,i}, \tag{4}$$

where N_{B^e} is the number of the used points and $\boldsymbol{x}^{e,i}$ are their global coordinates. The same points are used to determine the crack's orientation. First the average stress of points B^e are calculated by:

$$\sigma_{ED}^e = \frac{1}{N_{B^e}} \sum_{i \in B^e} \sigma^{e,i}, \tag{5}$$

with $\sigma^{e,i}$ being the stress values of integration points from B^e. Now, the orientation of the crack is determined by the α_{ED}^e angle:

$$\alpha_{ED}^e = \frac{1}{2} \arctan \left(\frac{2\sigma_{xyED}^e}{\sigma_{xx_{ED}}^e - \sigma_{yy_{ED}}^e} \right), \tag{6}$$

With the determined location $\boldsymbol{x}_{ED}^e$ and orientation α_{ED}^e, embedding the crack is straightforward (see Fig. 2). The α_{ED}^e represents the crack normal, which coincides with vector $\boldsymbol{n}$. The tangential vector is perpendicular to it. With the known tangential vector $\boldsymbol{m}$ and one point on the crack $\boldsymbol{x}_{ED}^e$, the crack's geometry is fully defined. This geometry remains fixed throughout the simulation, while the separation parameters (α_1, α_2) can change. Consequently, only one crack can emerge within a finite element, but at the mesh level, multiple new cracks can be initiated simultaneously in each timestep. Embedding cracks within finite elements and incorporating
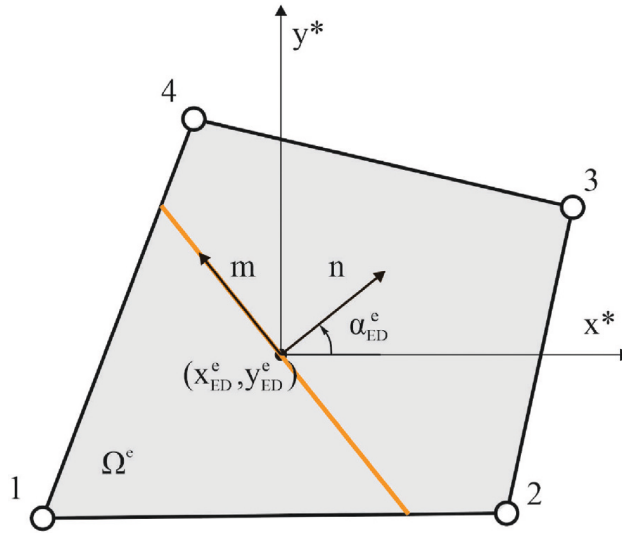
Fig. 2. Quadrilateral finite element with an embedded crack line. The crack line is defined by a point $\boldsymbol{x}_{ED}^e$ and angle α_{ED}^e.

strong discontinuities enables the use of coarser meshes for modeling crack propagation and improves the model's computational efficiency.

2.1.3. Constitutive relations

Two material laws have been selected to simulate the fracture processes of the model. The linear elastic law is applied to the bulk part of the element, where stress is defined as $\boldsymbol{\sigma} = \boldsymbol{C}\bar{\epsilon}$. Here, $\boldsymbol{C}$ represents the constitutive matrix, and $\bar{\epsilon}$ is the strain value of the bulk part. The crack behavior, including material degradation and energy dissipation, is controlled by the two uncoupled damage softening laws [36]. Each law corresponds to the separation of Mode I and Mode II and is formulated within the framework of the thermodynamics by using Helmholtz free energy.

When Rankine failure criterion is activated, the softening failure function $\bar{\bar{\phi}}$ controls the material degradation and evolution of internal variables. For tensile Mode I it is defined as:

$$\bar{\bar{\phi}}_n(t_1, \bar{\bar{q}}_n) = t_1 - (\sigma_n - \bar{\bar{q}}_n) \leq 0, \tag{7}$$

where t_1 is the normal traction value on the crack line and σ_n is the material tensile strength. The variable $\bar{\bar{q}}_n$ represents the softening traction value:

$$\bar{\bar{q}}_n = \frac{\partial \bar{\bar{\Psi}}_n}{\partial \bar{\bar{\xi}}_n} = \sigma_n \left(1 - \exp\left[-\frac{\sigma_n}{G_{fn}} \bar{\bar{\xi}}_n \right] \right), \tag{8}$$

where G_{fn} is the tensile Mode I material fracture energy and $\bar{\bar{\xi}}_n$ is the internal softening variable.

For shear Mode II, the Eq. (8) remain valid, with the notation changed from n to m to represent Mode II parameters. The failure function for shear Mode II is formulated as:

$$\bar{\bar{\phi}}_m(t_2, \bar{\bar{q}}_m) = |t_2| - (\sigma_m - \bar{\bar{q}}_m) \leq 0. \tag{9}$$

Here, t_2 represents the tangential traction on the crack line, and its absolute value is related to the potential for crack sliding in both directions.

2.1.4. Deterministic model formulation

The global and local equations of the cracked Q6ED element are formulated by considering the weak form of the equilibrium equation derived from the principle of virtual work resulting in the set of global equilibrium equations for the finite element mesh

$$\boldsymbol{\Lambda}_{e=1}^{N_{el}} \underbrace{(\boldsymbol{f}^{int,e} - \boldsymbol{f}^{ext,e})}_{\boldsymbol{R}_d^e} = 0, \tag{10}$$

where $\boldsymbol{\Lambda}$ is the finite element assembly operator, $\boldsymbol{f}^{ext,e} = [\boldsymbol{f}_a^{ext,e,T}]_{a=1,\dots,4}^T$ and $\boldsymbol{f}^{int,e} = [\boldsymbol{f}_a^{int,e,T}]_{a=1,\dots,4}^T$. Additionally, the virtual work equation produces local element equilibrium equations for incompatible mode enhancements and for separation modes that correspond to crack opening (more details in [15]).

The operator-split procedure scheme is applied to obtain the solution of both global and local equations of the model for each discrete timestep $\tau = \tau_1, \tau_2, \dots, \tau_n, \tau_{n+1}, \dots, \tau_M$. Initially, the local equations are solved to determine the values of the enhancement parameters ρ and α. Then, the linearization of global equations yields a new system of equations. Since the local equations are

previously satisfied, static condensation of the stiffness matrix of each cracked element preserve the initial dimension, which is beneficial for complex fracture simulations as it ensures fast computation time. Through this procedure, the new values of $d_{a,i}$ for each time increment τ_i are obtained [34].

Furthermore, let us denote this complex deterministic system of equations comprising both global and local components by the operator

$$\mathcal{A}\left(\tau, f_{ext}(\tau), d_a(\tau), \rho_b(\tau), \alpha(\tau)\right) = \mathbf{0}. \tag{11}$$

This implicit operator derived from the discretized system using embedded FE model defines in an abstract way the fracture problem to be solved for the global, compiled coefficients d_a, ρ_b, and α, that define through Eq. (1) the displacement field at the discretized time steps τ_i.

2.2. Stochastic model formulation

As demonstrated in Section 2.1, the operator $\mathcal{A}$, and consequently the results of the material fracture processes, depend heavily on the values of the fracture parameters within the constitutive model. These parameters determine the time, location, and characteristics of the cracks. This work focuses on four fracture parameters: tensile strength σ_n, shear strength σ_m, tensile fracture energy G_{fn}, and shear fracture energy G_{fm}.

Accurately determining these parameter values is crucial for precise simulation of fracture processes and, consequently, for accurately predicting future structural behavior. However, obtaining precise values is a challenging task. Due to the uncertainty surrounding these parameter values, we treat them as random variables. Let us collect these random variables in a vector $\mathbf{z} : \Omega \to \mathbb{R}^n$

$$\mathbf{z}(\omega) := \left[\sigma_n(\omega), G_{fn}(\omega), \sigma_m(\omega), G_{fm}(\omega)\right], \tag{12}$$

where, ω is the actual realization, a sample from the set of all possible realizations Ω, influencing the values of these $n = 4$ parameters, representing their random nature.

Each parameter z_i within the vector $\mathbf{z}$ is characterized by its probability density function $\pi(z_i)$. Assuming mutual independence between the input parameters, their joint probability function $\pi(\mathbf{z})$ can be expressed as [37,38]:

$$\pi(\mathbf{z}) = \pi(z_1, \dots, z_{N_i}) = \prod_{i=1}^{N_i} \pi_i(z_i). \tag{13}$$

The term $\pi(\mathbf{z})$ is called the prior distribution of the parameter values. The choice of the prior distribution depends on several factors such as experience, past identification results, available measurements, or even mere assumptions. While theoretically any type of distribution can be used, in practice, some standard distributions, such as uniform, beta, normal, or lognormal distributions are most often chosen. [37,38].

Using this probabilistic representation of the fracture parameters, the deterministic operator $\mathcal{A}$ becomes a stochastic one, making the coefficients describing the displacement field random variables, dependent on the actual realization. The parametrized abstract notation is given by

$$\mathcal{A}_\omega\left(\mathbf{z}(\omega), \tau, f_{ext}(\tau), d_a(\tau, \omega), \rho_b(\tau, \omega), \alpha(\tau, \omega)\right) = \mathbf{0}, \tag{14}$$

or in a simpler, engineering notation emphasizing the dependence on the uncertain parameters by

$$\mathcal{A}_\mathbf{z}\left(\mathbf{z}, \tau, f_{ext}(\tau), d_a(\tau, \mathbf{z}), \rho_b(\tau, \mathbf{z}), \alpha(\tau, \mathbf{z})\right) = \mathbf{0}. \tag{15}$$

As part of the identification procedure, the Bayesian approach is utilized to update the a-priori knowledge of $\mathbf{z}$ using a set of selected measurements of structural responses, such as strains or relative displacements. This procedure is explained in the next section.

3. Bayesian model calibration

Since direct measurements of parameters might be difficult to perform, we focus here on the case of simpler measurements related to the structural behavior, such as strains or relative displacements, that can be used in Bayesian model calibration. We collect such measurable variables in a vector $\mathbf{u}$, and we assume that this vector can be directly derived from the solution computed from Eq. (11), which is solved for the coefficients of the displacement field. Let us define this measurement operator mapping from the coefficients to the measurable variable

$$\mathbf{u}(\mathbf{z}) = \mathcal{M}(d_a(\tau, \mathbf{z}), \rho_b(\tau, \mathbf{z}), \alpha(\tau, \mathbf{z})), \tag{16}$$

where $\mathbf{u} = [\mathbf{u}^{(1)}, \mathbf{u}^{(2)}, \dots, \mathbf{u}^{(N_u)}]^T \in \mathbb{R}^{N_u \cdot \hat{M}}$ with $\mathbf{u}^{(i)} = [u^{(i)}(\hat{\tau}_1), u^{(i)}(\hat{\tau}_2), \dots, u^{(i)}(\hat{\tau}_{\hat{M}})]^T \in \mathbb{R}^{\hat{M}}$ being the ith variable that can be measured and $\hat{\tau}_j$ the jth snapshot in time when the measurement was taken.[1] For example, one such measurable variable could be the relative displacement between two points. The displacements of these points can be computed from Eq. (1), and the relative displacements

---

[1] Please note, $\hat{\tau}_j$ denotes the snapshots when the measurements were taken and τ_j the snapshots where the numerical solutions were computed. The snapshots as well as their number ($\hat{M}$ or M) do not necessarily have to match. If they do not, the $\mathcal{M}$ operator needs to take care of the interpolation in between the computed snapshots as well.
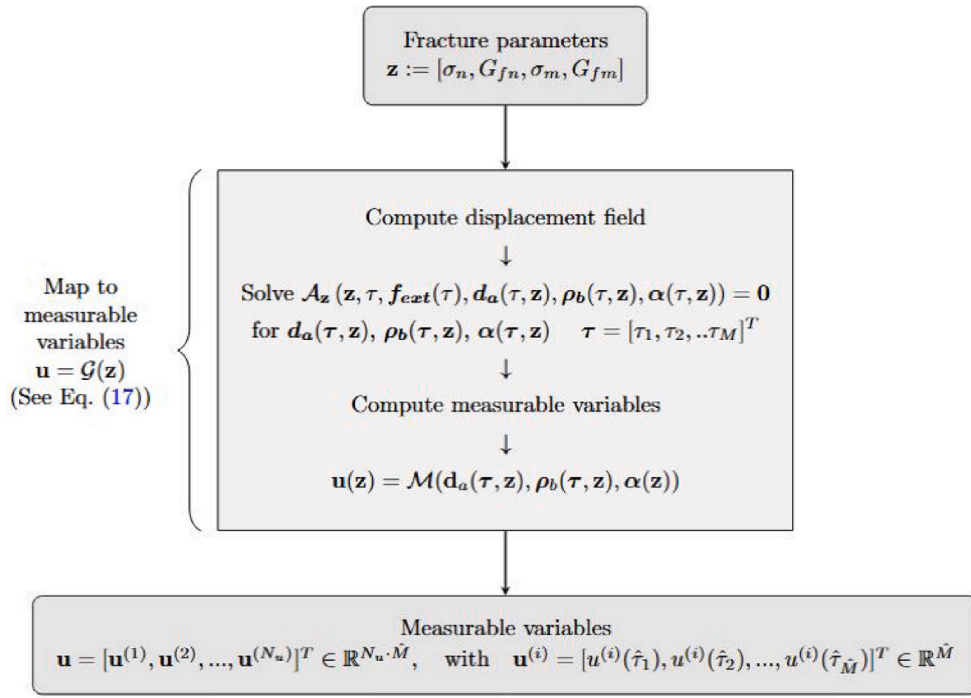
Fig. 3. Flowchart of the deterministic simulation computing from the input parameters the measurable outputs, some relative displacements.

can be obtained by calculating the difference between the two computed values. To conclude, we suppose that N_u different variables can be measured at $\hat{M}$ different snapshots resulting in $Q = N_u \cdot \hat{M}$ components of the measurable vector $\mathbf{u}$.

Accordingly, for a specific realization of the input parameters $\mathbf{z}$, the measurable variables $\mathbf{u}$ can be computed by first solving Eq. (14) for the coefficients of the displacement field and then applying Eq. (16) (see Fig. 3) . To define the relationship between the input parameters and the measurable variables, we introduce the forward model operator $\mathcal{G}$,

$$\mathbf{u} = \mathcal{G}(\mathbf{z}). \tag{17}$$

This abstract operator encapsulates the entire process from the input parameters to the resulting measurable parameters.

Our goal is to calibrate the parameters $\mathbf{z}$ to ensure that the measurable variable $\mathbf{u}$ matches some measured value as closely as possible. This requires us to invert the forward operator $\mathcal{G}$ leading us to solve an inverse problem.

Inverse problems are typically addressed through optimization procedures that minimize a pre-defined loss or cost function. This function, often based on some metric, such as mean squared error, quantifies the deviation between the measured value $\mathbf{z}_m$ and the computed value $\mathcal{G}(\mathbf{z})$. Unfortunately, inverse problems are often ill-posed, meaning that multiple sets of input parameters $\mathbf{z}$ can yield equally good fit, and equally good result for the cost function.

Stochastic methodologies provide an alternative approach. This approach achieves the updating of the initial knowledge of the parameter by combining it with the obtained measurement using the Bayes-rule [16,17,19,39–41]. Unlike the traditional approach of optimization, which yields a deterministic value of the input parameters, potentially a local minimum of the defined cost function, stochastic approaches result in an updated distribution of the parameters. This allows for a more comprehensive understanding of parameter uncertainties and their impact on the model.

Section 3 provides a brief overview of the employed Bayesian inverse method along with its accompanying methodology. Replacing the computationally expensive and cumbersome iterative solution procedure of the forward operator $\mathcal{G}(\mathbf{z})$, it is possible to use a surrogate or proxy model that can effectively capture the dependence of the measurable variable on the uncertain parameters. Such surrogate models can significantly accelerate the updating procedure. The development of surrogate models for the complex fracture mechanics problem is the core focus of this paper and is detailed in Section 3.

3.1. The Bayesian inverse problem

The Bayesian inverse method stands out as a robust and efficient probabilistic approach for solving stochastic inverse problems and thus for the identification of uncertain parameters. The key aspect of the Bayesian inverse method is in the updating of the initial knowledge about uncertain input parameters using measurements of the structural response, which are the outputs of a simulation procedure. Since these measurements do not need to directly measure the required parameters, it is possible to use combinations of simple measurements [17–19,37,38,40–42].

The solution of the forward model $\mathcal{G}$ with the "true" set of input parameters $\mathbf{z}$, $\mathbf{z}_{\text{true}}$, should always match the obtained measurement. But in practice, certain deviations are always inevitable. Such deviations are the product of approximations by the

numerical models, as well as the errors of the measuring devices. Thus, one obtained measurement $\mathbf{d}_m$ is one realization, one instance of the random variable [37,38]:

$$\mathbf{d}_m(\omega_e) = \mathbf{u}_{\text{true}} + \epsilon = \mathcal{G}(\mathbf{z}_{\text{true}}) + \epsilon(\omega_e), \tag{18}$$

Here, $\mathbf{u}_{\text{true}}$ denotes the measurable variable computed (predicted) from the "true" value of the parameters $\mathbf{z}_{\text{true}}$, while $\epsilon : \Omega_e \to \mathbb{R}^Q$ represents the errors depending on the actual realization of the measurement and modeling error ω_e and described by its probability density function π_ϵ. We assume that these realizations are independent of the realization ω of the uncertain input parameters $\mathbf{z}$, so that the random variables of $\mathbf{z}$ and ϵ are independent.

The Bayesian method aims to update the a-priori distribution of the parameter $\pi(\mathbf{z})$ using the given set of observed measurements $\mathbf{d}_m$ by applying Bayes' theorem of conditional probability [18,38]:

$$\pi(\mathbf{z}|\mathbf{d}_m) = \frac{\pi(\mathbf{d}_m|\mathbf{z})\pi(\mathbf{z})}{\pi(\mathbf{d}_m)}. \tag{19}$$

The components of Bayes' theorem can be described as follows:

- **Likelihood:** $\pi(\mathbf{d}_m|\mathbf{z})$ represents the probability (likelihood) function of $\mathbf{z}$ which expresses the likelihood of attaining the value $\mathbf{d}_m$ given a certain parameter value $\mathbf{z}$. This probability function can be defined by determining the probability that the error ϵ takes the value $\mathbf{d}_m - \mathbf{u}$ [38], where $\mathbf{u}$ can be computed from the forward operator $\mathbf{u} = \mathcal{G}(\mathbf{z})$. If we assume, that all elements of the error vector ϵ are independent from each other, the probability function $\pi(\mathbf{d}|\mathbf{z})$ can be expressed as the product of the probability distribution of all components of the measurable vector $\mathbf{u}$, that is

$$\pi(\mathbf{d}_m|\mathbf{z}) = \prod_{i=1}^{Q} \pi_{e_i}(d_{m_i} - u_i(z)). \tag{20}$$

- **Evidence:** The term $\pi(\mathbf{d}_m)$ represents the evidence function, the integral of the nominator in Eq. (19), that acts as a normalization value in Bayes' theorem, to ensure that the integral of $\pi(\mathbf{z}|\mathbf{d}_m)$ equals 1.
- **Posterior:** The expression $\pi(\mathbf{z}|\mathbf{d}_m)$ denotes the posterior distribution of parameter values $\mathbf{z}$. It is the final product of the Bayesian inverse procedure that represents the updated understanding of the parameter distribution based on the measurements $\mathbf{d}_m$.

In most cases, the posterior distribution cannot be formulated explicitly. Consequently, various mathematical techniques have been developed, such as sampling techniques, to approximate shape of the posterior distributions.

Sampling methods generate samples that approximate a stationary distribution that matches the required distribution. In this work, Markov chain Monte Carlo (MCMC) method based on Metropolis Hastings algorithm is chosen as a robust, simple, and model-independent technique [18,37,41–43]. This method utilizes a random walk approach to efficiently gather samples from the desired posterior distribution.

However, when the posterior distribution exhibits a complex shape, effective application of the MCMC method requires evaluating hundreds or even thousands of proposed parameter candidates. The most resource-demanding part of this process is the construction of likelihood functions, for which it is necessary to compute the forward model solutions $\mathcal{G}(\mathbf{z})$ for each candidate parameter. In the case of demanding numerical models, this represents a significant computational burden.

3.2. Proxy models

Performing multiple fracture simulations often necessitates extensive calculations, which can be time-consuming and resource-intensive. Due to these challenges, solving the Bayesian inverse problem using the MCMC method may become prohibitively slow. To accelerate this process, it is beneficial and sometimes necessary to employ mathematical proxy models - often referred to as surrogate, meta, or response surface models [18,19,44]:

$$\mathcal{G}(\mathbf{z}) \approx \tilde{\mathcal{G}}(\mathbf{z}). \tag{21}$$

Here $\tilde{\mathcal{G}}(\mathbf{z})$ represents proxy model approximation of the forward model operator $\mathcal{G}$.

When developing a mathematical proxy model, it is not always necessary to have an in-depth understanding of the underlying numerical model. A proxy model can be constructed using only selected input and output data, following a "black box" approach. In practice, various proxy models exist, each with its advantages and disadvantages, though most follow a similar procedure [19,45]. The process typically begins by selecting a set of input parameter combinations from the predefined prior distribution $\pi(\mathbf{z})$. Forward model calculations are then conducted for these combinations, and their corresponding solutions are gathered. This data is used to train the proxy model. Afterwards, a different set of data is employed to validate the model's accuracy.

The following subsections present the details of the surrogate models selected for this study, namely the generalized polynomial chaos expansion (gPCE) method and the neural network model (NN), both extended with an alternative low-dimensional representation of the measurable vector $\mathbf{u}_r$.

We have chosen the gPCE method because polynomials can be efficiently leveraged for proxy modeling, offering a straightforward way to evaluate sensitivities directly from their coefficients. Additionally, the coefficients of gPCE can be analytically computed by solving a linear regression problem that minimizes the mean squared error (MSE) at the sample points. However, due to the highly nonlinear and occasionally non-smooth nature of response surfaces for fracture problems (see e.g. [33]), achieving accurate

approximations with gPCE sometimes requires high-degree polynomials. These high-degree polynomials, while powerful, can lead to undesirable extrapolation results and erratic behavior between sample points.

To address these limitations, we also incorporated neural networks (NN) which are highly flexible in their representative capabilities, allowing them to model complex, nonlinear relationships effectively. However, unlike gPCE, the parameters of neural networks can only be determined through numerical iterative methods aimed at minimizing a loss function, which can be computationally intensive. By contrasting these two approaches, we aim to balance the strengths and weaknesses of each, providing a comprehensive evaluation of their effectiveness for the specific challenges addressed in this work. Selecting the optimal model with its hyperparameters through training and testing phases is conducted before the MCMC process begins to ensure that it reliably approximates the forward model.

3.2.1. General polynomial chaos expansion (gPCE) model

The core principle of the generalized polynomial chaos expansion (gPCE) method is the approximation of numerical model solutions through a linear combination of multidimensional polynomials and their corresponding coefficients [41,46,47] in the form of:

$$\mathbf{u} = \mathcal{G}(\mathbf{z}) \approx \tilde{\mathcal{G}}(\mathbf{z}) = \tilde{\mathbf{u}} = \sum_{k=0}^{K-1} \boldsymbol{\nu}_k \boldsymbol{\Phi}_k(\mathbf{z}) = \boldsymbol{Y} \boldsymbol{\Phi}(\mathbf{z}). \tag{22}$$

Here, $\tilde{\mathbf{u}}$ represents the approximation of the measurable output, $\boldsymbol{\Phi}$ denotes the chosen set of polynomials collected in the vector $\boldsymbol{\Phi} = [\Phi_0(\mathbf{z}), \Phi_1(\mathbf{z}), \dots, \Phi_{K-1}(\mathbf{z})]^T$ and $\boldsymbol{Y} = [\boldsymbol{\nu}_0, \boldsymbol{\nu}_2, \dots \boldsymbol{\nu}_k \dots \boldsymbol{\nu}_{K-1}]$ stands for the polynomial coefficients of expansion, where $\boldsymbol{\nu}_k \in \mathbb{R}^Q$ corresponds to the polynomial Φ_k.

The main goal of the method is to find the most accurate approximation $\tilde{\mathbf{u}} \approx \mathbf{u}$ of the response surface Eq. (17), in the sense of the least square error approach [18].

First, an appropriate polynomial basis is selected based on the distribution of the input parameters. To ensure the efficiency and simplicity of the gPCE model, polynomials that are orthogonal with respect to the underlying probability space are applied [18,41]. The calculation of the coefficients $\boldsymbol{Y}$ can be computed from the linear regression problem of minimizing the MSE [41]:

$$\mathbb{E}[\tilde{\epsilon}^2] = \mathbb{E}\left[(\mathbf{u} - \tilde{\mathbf{u}})^2\right] = \int_{\mathbb{R}} (\mathbf{u}(\mathbf{z}) - \tilde{\mathbf{u}}(\mathbf{z}))^2 \pi(\mathbf{z}) d\mathbf{z} \approx \frac{1}{N} \sum_{i=1}^{N} \left(\mathbf{u}(\mathbf{z}_i) - \tilde{\mathbf{u}}(\mathbf{z}_i)\right)^2. \tag{23}$$

Introducing the matrix notations:

$$\mathbf{U} = [\mathbf{u}(\mathbf{z}_1), \mathbf{u}(\mathbf{z}_2), \dots, \mathbf{u}(\mathbf{z}_N)],$$

$$\mathbf{F} = [\boldsymbol{\Phi}(\mathbf{z}_1), \boldsymbol{\Phi}(\mathbf{z}_2), \dots, \boldsymbol{\Phi}(\mathbf{z}_N)],$$

the minimization problem boils down to solving the system of equations:

$$\boldsymbol{Y}\mathbf{F}\mathbf{F}^T = \mathbf{U}\mathbf{F}^T \tag{24}$$

for the coefficients $\boldsymbol{Y}$.

A sufficiently precise model provides an analytical representation of the solution of the numerical model, which enables easy analysis of all necessary statistical information with minimal computational effort.

3.2.2. Neural network models

Simple neural networks (NNs), or feedforward networks, consist of an input layer, one or more hidden layers, and an output layer (see Fig. 4). Each layer has interconnected neurons, with weights assigned to connections between them. For the NN's input layer $\mathbf{x}^0 = (z_1, z_2, \dots, z_n)$, corresponding to the parameters of the fracture model, data propagates forward through each layer. In each layer l, neuron j computes a weighted sum of the outputs from the previous layer and applies an activation function:

$$\mathbf{u} = \mathcal{G}(\mathbf{z}) \approx \tilde{\mathcal{G}}(\mathbf{z}) = \tilde{\mathbf{u}} = \mathbf{x}^L(\mathbf{z}), \qquad x_j^l = g^l\left(\hat{y}_j^l\right), \qquad \hat{y}_j^l = \sum_{i=1}^{n^{l-1}} w_{ij}^l x_i^{l-1} + b_j^l, \qquad \mathbf{x}^0 = \mathbf{z}. \tag{25}$$

where w_{ij}^l and b_j^l are weights and biases corresponding to layer l and node i, and $g(\cdot)$ is the activation function. The final output $\mathbf{x}^L$ gives the approximation of the measurable responses $\tilde{\mathbf{u}}$.

The NN's key hyperparameters include the number of neurons per layer, the number of layers, and activation function types. Training the NN involves forward propagation to compute outputs and backpropagation to adjust weights and biases iteratively, minimizing a loss function. This process allows the NN to optimize its predictions over time [43,48–50], in contrast to the gPCE's single-step coefficient calculation.
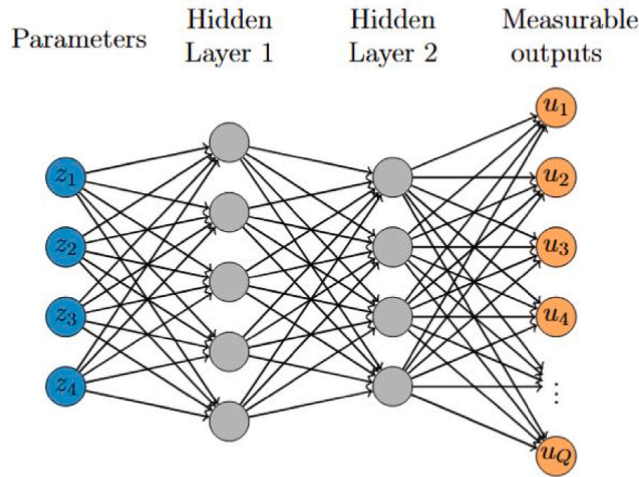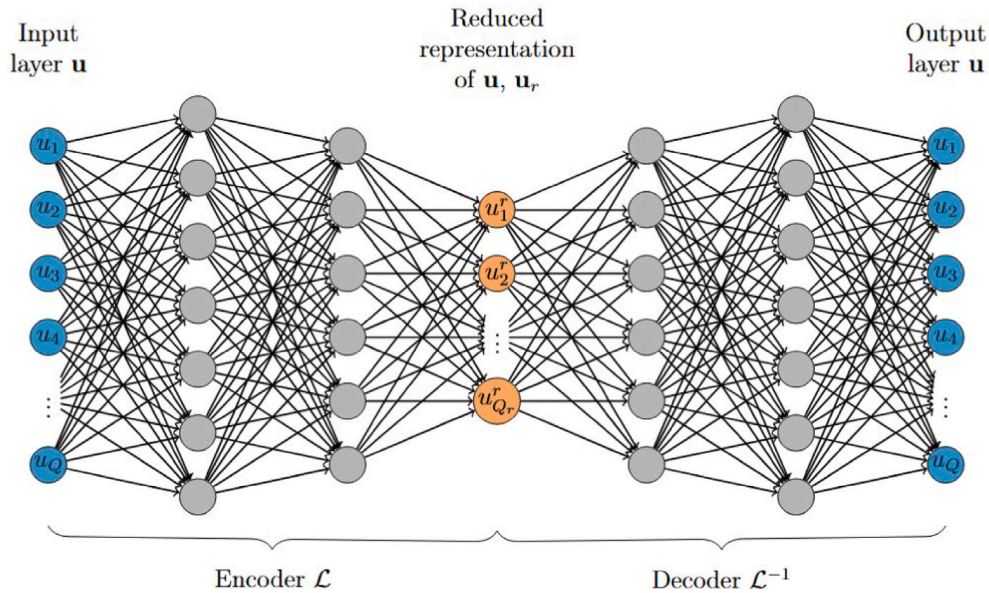
Fig. 4. Surrogating simulation model by NN.

Fig. 5. Reduced, low dimensional representation of the measurable variable by autoencoder.

3.2.3. Low-rank representation of the measurable processes

In both surrogate models discussed, we treated the vector of measurable responses $\mathbf{u}$ without explicitly addressing correlations in its N_u time-dependent components. Since these components are highly correlated, they can be represented in a lower-dimensional space, preserving relevant information with reduced complexity. To achieve this, we use an autoencoder — a neural network designed for dimensionality reduction — consisting of an encoder and decoder. The encoder $\mathcal{L}(\mathbf{u})$ transforms the high-dimensional measurable response vector $\mathbf{u} \in \mathbb{R}^Q$ into a lower-dimensional latent space $\mathbf{u}_r \in \mathbb{R}^{Q_r}$, where $Q_r < Q$. This compact representation, known as the bottleneck layer, captures the primary features of the data while filtering noise from measurement inaccuracies or model errors. The decoder $\mathcal{L}^{-1}(\mathbf{u}_r)$ then reconstructs $\mathbf{u}$ from this latent representation, aiming to minimize the difference between the original and reconstructed data (see Fig. 5). After training the NN of the autoencoder as a hole the network is split into its encoder and decoder components. In the context of our surrogate modeling, we use this low-dimensional representation $\mathbf{u}_r$ as a basis for training the surrogate models, which are then trained on input–output pairs $(\mathbf{z}_i, \mathbf{u}_r(\mathbf{z}_i))$. This approach reduces computational complexity and captures the key structure of the data, potentially improving the efficiency and accuracy of the surrogate model.

To adapt the Bayesian updating process to this modified representation, we modify the MCMC likelihood calculation. We conduct the MCMC procedure directly in the low-dimensional space by mapping the measured data $\mathbf{d}_m$ to the latent space, $\mathbf{d}_{mr} = \mathcal{L}(\mathbf{d}_m)$. We then adjust the posterior and likelihood definitions in terms of $\mathbf{d}_{mr}$:

$$\pi(\mathbf{z}|\mathbf{d}_{mr}) = \frac{\pi(\mathbf{d}_{mr}|\mathbf{z})\pi(\mathbf{z})}{\pi(\mathbf{d}_{mr})}, \tag{26}$$

$$\pi(\mathbf{d}_{mr}|\mathbf{z}) = \pi_{e_r}(\mathbf{d}_{mr} - \mathbf{u}_r(\mathbf{z})). \tag{27}$$

The error distribution π_{e_r} differs from the original error model due to transformations in the latent space. We approximate π_{e_r} by mapping samples of measurable responses, both with and without error, to the low-dimensional space. Then, deviations can be modeled with techniques like Gaussian mixture models to represent the distribution in this reduced space effectively.

3.3. Sobol sensitivity analysis

Sensitivity analysis is valubale in experimental design, helping to determine sensor placement and select the most informative measurable outputs [51]. The use of surrogate models offers the advantage of not only making the update procedure feasible but also simplifying the sensitivity analysis. For gPCE models, the orthogonality of the regressors to the underlying probability space allows partial variances to be directly computed from the coefficients of the gPCE expansion. Partial variance measures the variability of the measurable variable **u** that can be attributed to the variation of one or a combination of independent input parameters. The Sobol index is a relative measure that represents the proportion of partial variance (associated with the variation of a fixed subset of uncertain input parameters) to the total variance (arising from the variation of all uncertain input parameters). For instance, first order (or linear) Sobol indices capture the sensitivity to a single input parameter z_i, while second-order indices reflect the joint contribution of interactions between two parameters z_i and z_j. These indices are mathematically expressed as follows:

$$S_i = \frac{V_i}{V} = \frac{\mathrm{var}_{z_i}\left(\mathbb{E}_{\mathbf{z}_{\sim i}}\left(\mathbf{u}|z_i\right)\right)}{\mathrm{var}(\mathbf{u})} \qquad S_{i,j} = \frac{V_i}{V_{i,j}} = \frac{\mathrm{var}_{z_i,z_j}\left(\mathbb{E}_{\mathbf{z}_{\sim i,j}}\left(\mathbf{u}|z_i,z_j\right)\right)}{\mathrm{var}(\mathbf{u})}, \tag{28}$$

where the $\mathbf{z}_{\sim i}$ notation indicates the set of all variables except z_i, V is the total and V_i, $V_{i,j}$ are the partial variances. Partial variances (and Sobol indices) can be evaluated using sampling-based solutions (see e.g. in [52,53]). Surrogating the FE model significantly accelerates the computationally intensive sampling procedure, making it far more efficient. The gPCE expansion further enhances efficiency, as the orthogonality of the polynomial basis allows direct computation of both partial and total variances from the coefficients of the expansion v [54]:

$$V_{i_1,\dots i_s} = \mathrm{var}\left(\sum_{\boldsymbol{\alpha}\in\mathcal{J}_{i_1,\dots,i_s}} v_{\boldsymbol{\alpha}}\Phi_{\boldsymbol{\alpha}}(z_{i_1},\dots z_{i_s})\right) = \sum_{\boldsymbol{\alpha}\in\mathcal{J}_{i_1,\dots,i_s}} v_{\boldsymbol{\alpha}}^2 \gamma_{\boldsymbol{\alpha}}, \tag{29}$$

where $\mathcal{J}_i$ is defined as a set of all multi-indices that corresponds to the polynomials depending only on parameter z_i, and $\gamma_{\boldsymbol{\alpha}}$ is the norm of the polynomial bases $\Phi_{\boldsymbol{\alpha}}$ [54].

4. Numerical examples

We selected the two examples to investigate the process of identifying fracture propagation: the hole tension test and the four point bending test. Such examples are chosen to avoid bifurcation (e.g. by introducing a hole or notch), as this facilitates identifiability.

The Q6ED model described in Section 2.1 is implemented in the FEAP [55], which was used to generate the results and to solve Eq. (11). For this study, synthetic measurements were used. This approach allows us to know the "true" values of the parameter in advance, which enables a reliable assessment of the identification process and comparison of results using different surrogate models, which is the main focus of this work.

This section provides details about each test example, including geometry and loading conditions and the processes of crack initiation and propagation. Additionally, it shows details of the chosen measurements.

4.1. Hole tension test - case

The hole tension test produces crack formation in pure tension on a dog-bone specimen weakened with a hole. The specimen is 125 mm long, 50 mm wide and has thickness of t = 15 mm. Fig. 6(a) illustrates its detailed geometry, boundary conditions and loading type.

The dog-bone specimen is subjected to vertical tension load which results in the two distinct states of material behavior: an elastic state and a fracture state. In the elastic state, the hole within the sample creates a heterogeneous stress state, with stress concentrations formed along the sides of the hole perpendicular to the loading direction. As the loading increases, first cracks emerge at the hole edges and progressively propagate toward the edges of the specimen (see Fig. 6(b)). During this state, the upper side of the dog-bone continue to move, while the lower side tends to return in its initial position. This behavior is non-linear and is characterized by increased displacement values on the loading edge while stress values decrease.

The analysis of this process using the Q6ED model is relatively straightforward. Convergence for various fracture parameters is easily achieved, and computation time is fast. Consequently, it is possible to use the whole range of the values until the complete failure of the specimen for the identification of parameters.

The elastic properties are predefined to $E = 30.000$ N/mm^2 and $v = 0.2$. Since the test involves only tensile failure, the identification process focuses exclusively on the Mode I fracture parameters. Consequently, the vector from the Eq. (12) can be rewritten as:

$$\mathbf{z}(\omega) := \left[\sigma_n(\omega), G_{f_n}(\omega)\right] \tag{30}$$
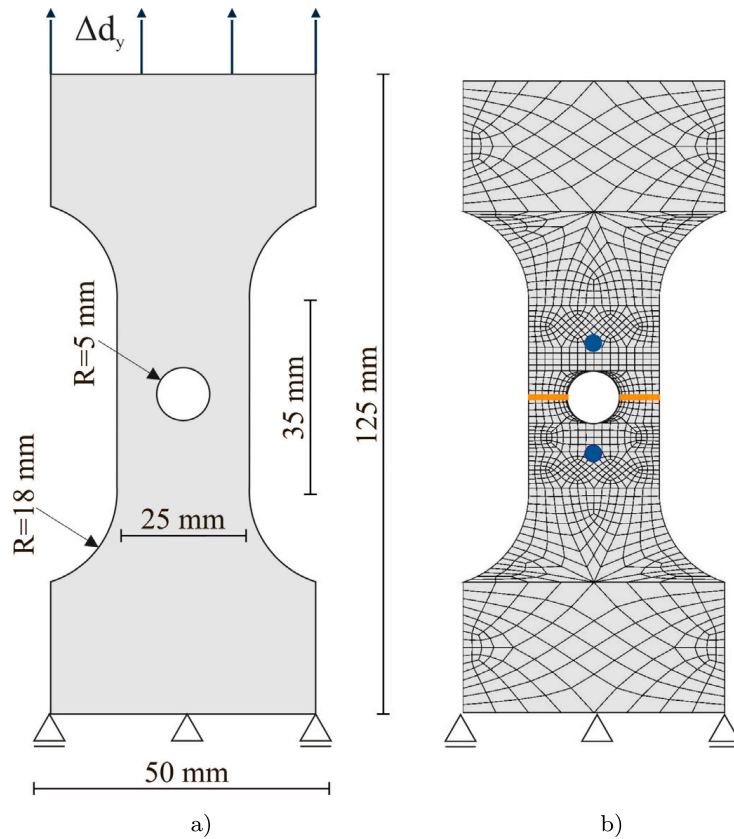
Fig. 6. Hole tension test: (a) problem illustration, (b) FE mesh with the predicted crack pattern (orange lines) and measurement positions (blue dots). (For interpretation of the references to color in this figure legend, the reader is referred to the web version of this article.)

The measurement used for this identification is the relative difference in vertical displacements between the two positions, marked by blue dots in Fig. 6(b). These positions are placed above and below the anticipated crack location to simulate strain gauge readings. Therefore, the measurable variables from Fig. 3 take the form:

$$\mathbf{u} = [\mathbf{u}^{(1)}]^T \in \mathbb{R}^{1 \cdot \hat{M}}, \qquad \mathbf{u}^{(1)} = [u^{(1)}(\hat{\tau}_1), u^{(1)}(\hat{\tau}_2), \dots, u^{(1)}(\hat{\tau}_{\hat{M}})]^T \in \mathbb{R}^{\hat{M}}, \tag{31}$$

where $\hat{M}$ represents a total of 200 timesteps, with 50 $\hat{\tau}$ of 0.005 s and 150 $\hat{\tau}$ of 0.125 s.

4.2. Four point bending test - case

The four point bending test presents a challenging example of crack propagation in a concrete beam. The proposed beam is 1322 mm long, 306 mm high, and has a thickness of 156 mm. It has a predefined notch in the middle (14 mm long and 82 mm high), it is asymmetrically supported and loaded. Fig. 7 shows its geometry, loading, support scheme, and measurement locations. The presence of the middle notch introduces the local stress concentrations that serve as the starting point for the crack initiation. Unlike for the hole tension test, here the crack path cannot be predicted a priori. Variations in strength and fracture energy parameters influence the resulting shape and direction of the crack. However, a general area can be assumed to be from the notch edge to the right upper stiff cap, where the load is applied. This area is marked in Fig. 7 with the dashed lines. The failure of the beam can be characterized by three distinct states: an initial elastic state followed by two cracking states. As the load is applied, the beam begins to bend, which linearly increases the stress values. High stress concentration in the elements close to the notch results in crack formation through the dominant tensile opening mode (Mode I), followed by the appearance of some shear sliding (Mode II). In this first cracking state, more cracks can form, but as the loading increases, mainly the one dominant continues to propagate, while others experience unloading and thus closing. This is visible on Fig. 8 where the material degradation is plotted together for the 20 randomly selected sets of fracture parameters. As the macrocrack grows, the stiffness and stability of the beam degrade, which forces the right side of the beam to rotate under the asymmetric loading. This causes the crack to change its direction vertically towards the upper right stiff cap. These phenomena describe the second cracking state. As the macrocrack propagates to the upper part of the beam, further loss of stability occurs, which leads to complete failure.

Solving the asymmetric four point bending test using the Q6ED model, as well as other models [34,35,56], is a demanding task. The most common approach is by using the Arc length solution strategy, which monitors the speed of change of displacement values at the bottom of the notch to ensure stable computation. To successfully simulate the complete failure of the beam, it is necessary to stabilize the computation and preserve the convergence by limiting the maximum value of the permitted vertical displacements and
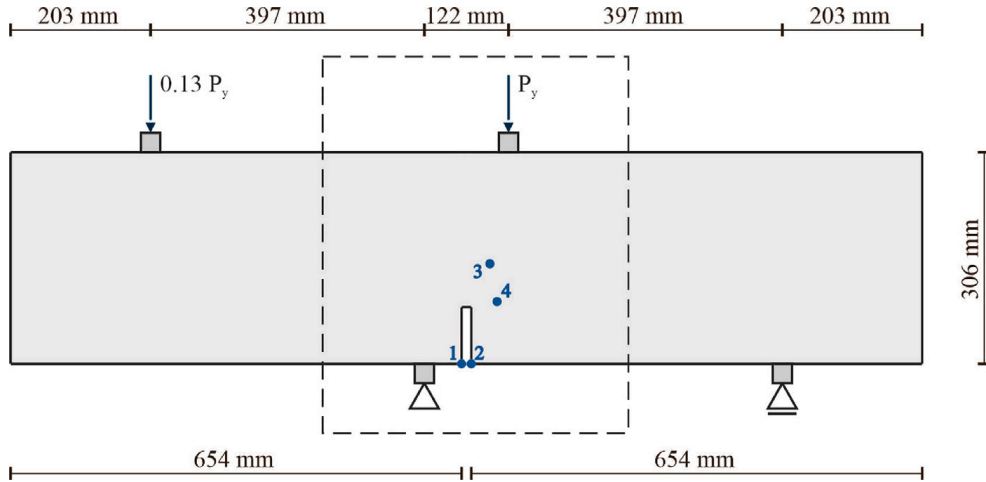
Fig. 7. Four point bending test: problem illustration, area of interest (dashed lines) and measurement positions (blue dots with numbers).
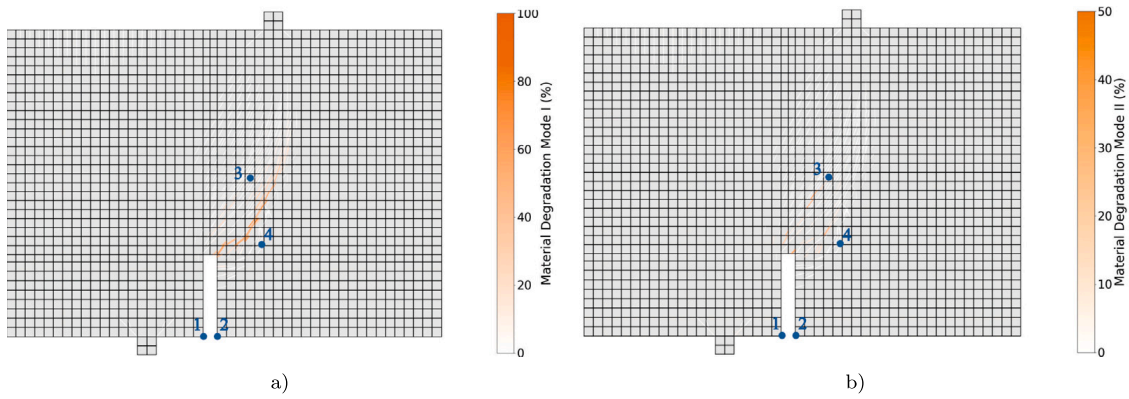

Fig. 8. Four point bending: Material degradation for the first cracking phase (a) Mode I, and (b) Mode II.

varying the size of the timestep. Different combinations of parameters can require different displacement and timestep schemes. In this example, we decided to utilize data from the first state of crack propagation, since both modes of failure are already activated, but a significant loss of system stability has not yet occurred. By focusing on this first state, we reduce the time and convergence requirements, making the identification process feasible.

Regarding the identification of the parameters, the elastic material parameters for the concrete beam are predefined with the values of $E = 32.000$ N/mm^2 and $v = 0.2$. The stiff caps have predefined elastic parameters of $E = 3.2 \times 10^9$ N/mm^2 and $v = 0.2$, and they cannot crack. Fracture parameters for both Mode I and Mode II are considered unknown, and their identification is required. Therefore, vector $\mathbf{z}$ from Eq. (12) still applies. Given the complexity of the fracture phenomena, four different measurement positions were selected on the beam. Two positions are located along the expected crack path, while the other two are at the end of the notch. The macrocrack plot through material degradation (see Fig. 8) confirms good positioning of these local measurements, very close to the positions of generated macrocracks. This allows successful observation of both local and global effects of crack propagation. The measurements are represented by the differences in horizontal and vertical displacements at these positions, with a total of four measurement data sets employed. In this way, we simulate strain gauge readings in both horizontal and vertical directions. The first measurement $\mathbf{u}^{(1)}$ represents the vertical displacement difference between middle positions (3 and 4). The second $\mathbf{u}^{(2)}$ and third $\mathbf{u}^{(3)}$ measurements represent the vertical displacement difference and horizontal displacement difference between notch positions (1 and 2), respectively. The last measurement $\mathbf{u}^{(4)}$ is the horizontal displacement difference between middle positions (3 and 4). Together, these measurements can be expressed as:

$$\mathbf{u} = [\mathbf{u}^{(1)}, \mathbf{u}^{(2)}, \mathbf{u}^{(3)}, \mathbf{u}^{(4)}]^T \in \mathbb{R}^{4 \cdot \hat{M}}, \qquad \mathbf{u}^{(i)} = [u^{(i)}(\hat{\tau}_1), u^{(i)}(\hat{\tau}_2), \dots, u^{(i)}(\hat{\tau}_{\hat{M}})]^T \in \mathbb{R}^{\hat{M}}, \tag{32}$$

with the $\hat{M}$ corresponds to a total of 450 timesteps: 87 timesteps of 0.001 s and 363 timesteps of 0.0001 s.

5. Results

This section presents the results of the fracture parameter identification given the measurement by solving the Bayesian inverse problem with the MCMC method. For both tests we used four different proxy models: a (i) gPCE and (ii) NN approximating the
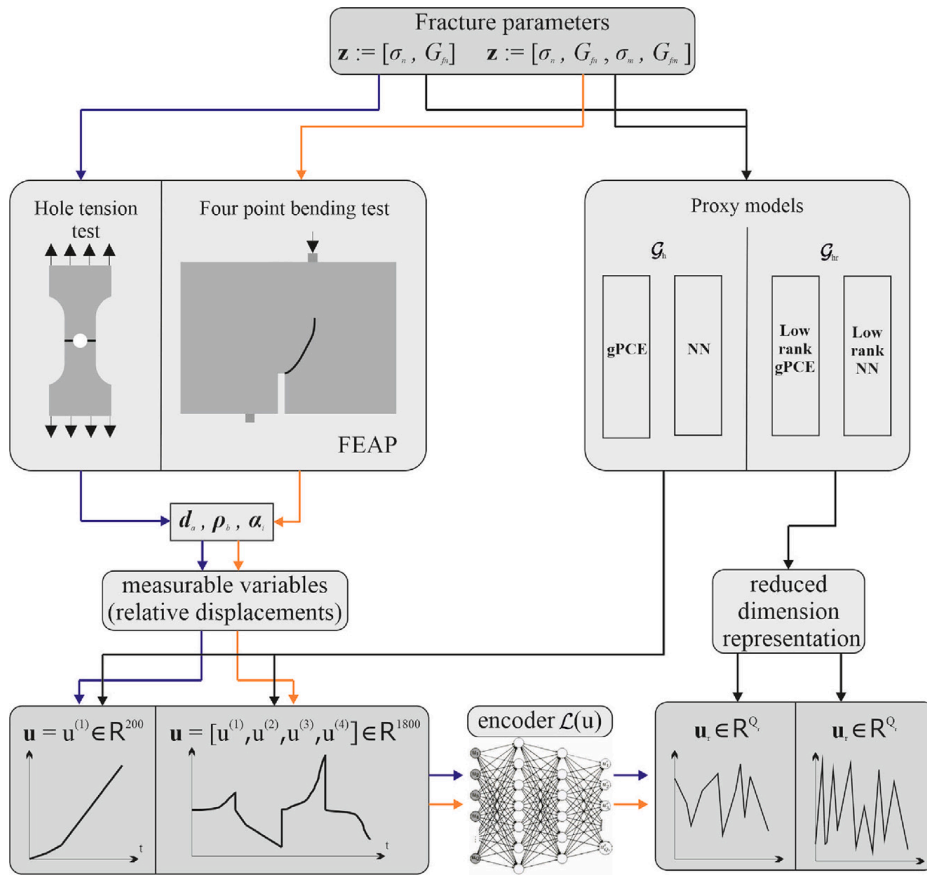
Fig. 9. Flowchart of surrogating the FEM model for the two benchmark tests.

$\mathcal{G}$ operator mapping from the parameter space to the full dimensional representation of the measurable variable $\mathbf{u}$ and (iii) low dimensional gPCE and (iv) low dimensional NN approximating the $\mathcal{G}_r$ operator, mapping the parameters to the low dimensional representation of the measurable variable $\mathbf{u}_r$, which is illustrated in Fig. 9.

The choice of sufficiently precise proxy model is found by hyperparameter search where the optimal model aims at having an error distribution of the prediction that has significantly smaller standard deviation than the a-priori uncertainties of measurable output. An accuracy analysis of each trained proxy model is provided to assess its ability to approximate complex, nonlinear fracture data. This section also includes a comparison of the computational efficiency of the surrogate model optimization processes to evaluate potential computational savings. Finally, a comparative analysis of the identification results for each proxy model is presented, comparing the obtained posterior distributions and assessing identification accuracy by comparing the ground-truth values with the mean posterior estimates.

The open source stochastic library SGLIB [57] was used for identification and construction of gPCE models. The NN models and autoencoder were trained using python based packages. All computational data for training and testing the proxy models were generated using a cluster computer capable of running 100 parallel fracture model simulations.

5.1. Hole tension test

Synthetic measurement values were obtained by choosing a random set of parameters as "true" values, $\mathbf{z}_{true}$ and computing the measurable response from Eq. (31) by evaluating $\mathcal{G}(\mathbf{z}_{true})$. A uniform prior distribution is chosen to represent equal uncertainty for all values. Specifically, parameter σ_n is chosen to follow a uniform distribution $U(2 \text{ N/mm}^2, 4 \text{ N/mm}^2)$, while G_{fn} follows a uniform distribution $U(0.05 \text{ N/mm}, 0.15 \text{ N/mm})$. From the defined prior distribution, Quasi-Monte Carlo (QMC) sampling was used to obtain a set of points for training of proxy models (12.000 samples) and another set (testing set) for estimating their precision (3.000 samples). Each sample computation takes approximately 1 min. Thus, processing all 15.000 samples on the cluster computer requires about 2.5 h. Fig. A.1(a) shows the synthetic measurement together with the computed results for the training set samples.

5.1.1. Proxy model training

gPCE model

The most appropriate model was determined by evaluating the accuracy of trained models with different polynomial basis. For this purpose, the value of the maximum absolute error ($\overline{\text{MAE}}$) is estimated on the difference between $\tilde{\mathbf{u}}(\mathbf{z}_i)$ and $\mathbf{u}(\mathbf{z}_i)$, where $\mathbf{z}_i$ are
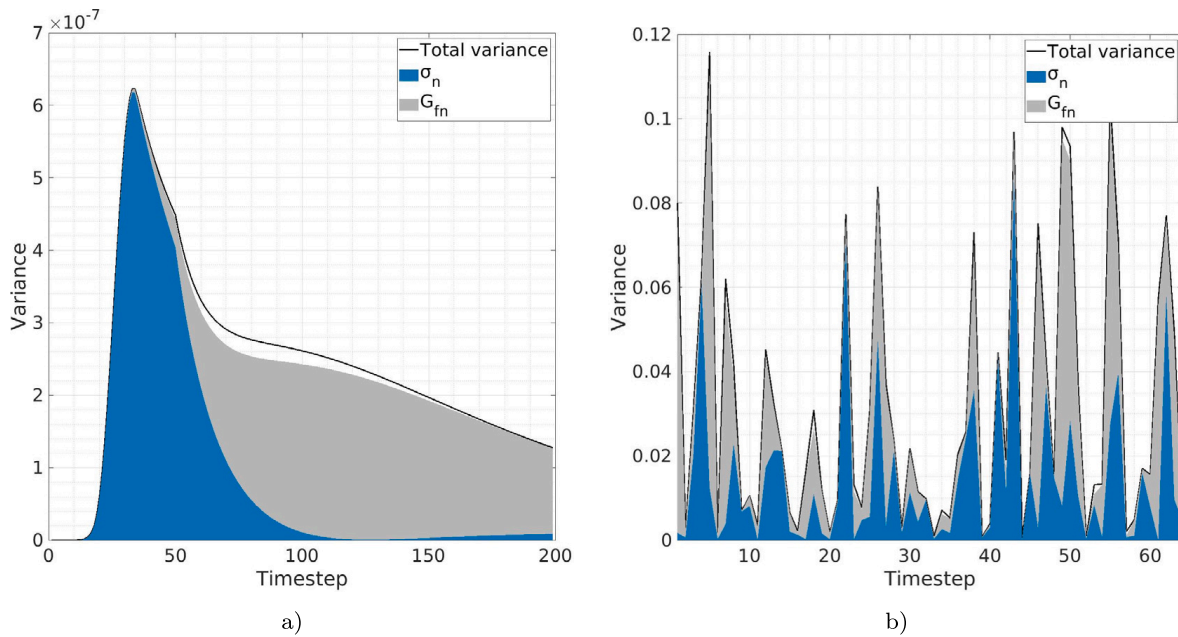
Fig. 10. Hole tension test: (a) Sobol sensitivity by gPCE model (b) Sobol sensitivity by low-rank gPCE model.

set of independent testing and validating samples. The validation set was created by randomly selecting 80% of the samples from the training set, training the model, and then checking its accuracy against the remaining 20% of samples. Fig. A.2(a) illustrates the accuracy of the trained models. Therefore, a basis with a maximum total degree of eight was chosen, resulting in 45 polynomial coefficients per timestep.

Fig. 10(a) shows the Sobol sensitivity results derived from the gPCE surrogate model. The results indicate that both fracture parameters – tensile strength, and fracture energy – play crucial roles in influencing the solution. Initially, tensile strength has a greater impact, as it determines the onset of cracking. As the crack progresses, the influence of fracture energy increases, governing the character of the cracking process. Additionally, the interaction between parameters also has some small influence, presented by the uncolored white area below the total variance in the middle of the time domain.

NN model

Multiple NN models with different hyperparameters, such as number of layers, number of neurons, optimization method and the activation functions, were trained (see Table A.1). The corresponding accuracy metrics such as MAE and root mean squared error (RMSE) averaged over the time domain ($\overline{\text{MAE}}$, $\overline{\text{RMSE}}$, respectively), as well as the maximum of MAE and RMSE over the time domain are provided. The model with the smallest mean MAE was selected, with the total of 15.143 parameters. The output layer of the NN model has 200 neurons, corresponding to the 200 measurable timesteps of relative displacements, represented by the elements of **u**. The Sobol sensitivities of the measurable responses are evaluated from the NN model with Saltelli's sampling based method[2] (Fig. A.3), providing similar results to the one received from the gPCE coefficients (Fig. 10(a)).

Low-rank representation: training Autoencoder

The autoencoder was trained to reduce the measurable output to a lower dimensional space. The inputs and outputs were vectors of the original dimension **u**, with the goal of minimizing the autoencoder's bottleneck by observing the metrics corresponding to different number of neurons. Fig. A.4 illustrates the error metrics of trained models. A 64-dimensional low-rank representation was chosen instead of 200 dimensions. Fig. A.1(b) illustrates the training samples in the lower-dimensional space transformed from the samples shown in Fig. A.1(a).

Low-rank gPCE model

With the generated low-rank representation of the results, a low-rank gPCE model is trained, following the similar procedure as the standard gPCE model. Different degrees of low-rank gPCE models are trained, and their low-rank data results are transformed by decoder and compared with the testing and validation set results (see Fig. A.2(b)). Based on the accuracy results, the 8th-degree polynomial is chosen as the basis for the model, with a total of 45 polynomial coefficients per timestep. With the trained model, sensitivity analysis of the low-rank generated data is made (see Fig. 10(b)). The figure shows the influence of both parameters on the obtained solutions together with the small influence of the mixed mode.

Low-rank NN model

The low-dimensional NN proxy model takes the two scaled and shifted fracture parameters as inputs and maps them to the 64-dimensional representation of the measurable output. As shown in Table A.2., the model with 2 hidden layers with 16, and 32

---

[2] In the subsequent analysis, we will present only the sensitivities of the measurable response obtained from the gPCE approximation, as the different models exhibit similar accuracy and yield nearly identical sensitivity results.

Table 1

Hole tension test: Total computational time required to train and test proxy models including hyperparameter search (18 gPCE models with different polynomial bases, 10 neural network architectures).

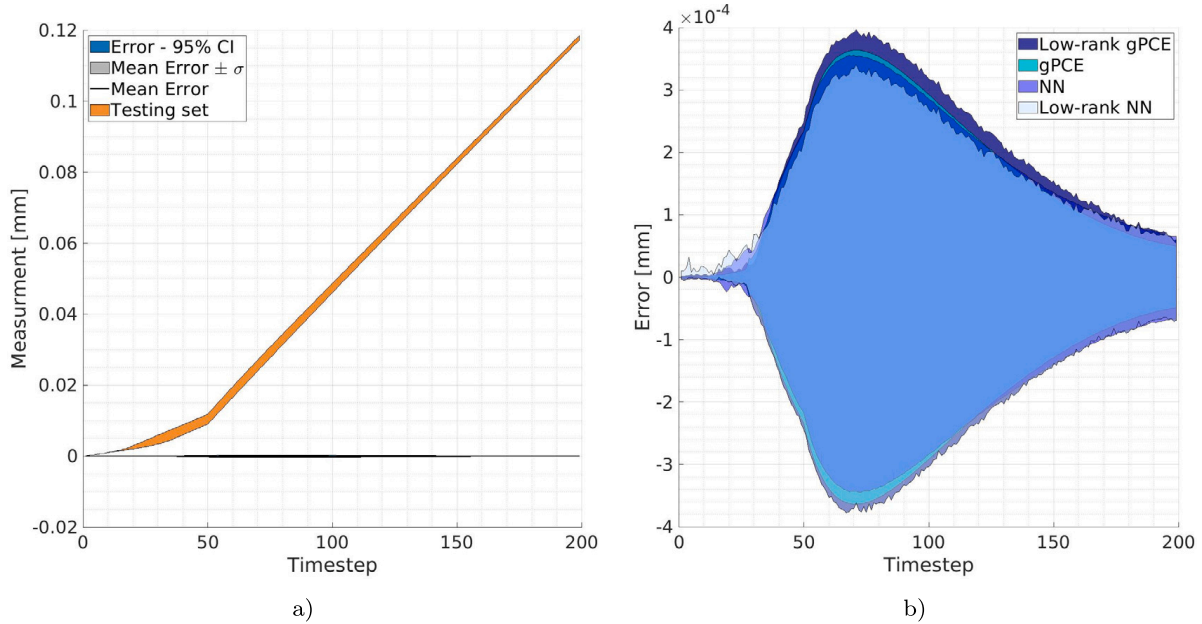|	gPCE	Low-rank gPCE	NN	Low-rank NN
Total computational time [min]	1.5	76	25	110

Fig. 11. Hole tension test: (a) NN model's error metrics together with the envelope of the testing set (b) 95% CI errors of different proxy models.

neurons each with ReLU activation function is selected. A sigmoid activation function was applied on the 64 dimensional output. The total number of model parameters is 2.704.

Proxy model comparison

Table 1 compares the computational time required for training and validating all proxy models including all tested architectures (various polynomial bases for gPCE model and different hyperparameters for NN model). For the low-rank models, computational search time also includes training and optimizing autoencoder (10 autoencoder architectures). The results show that optimization times for all proxy models are small, with the gPCE model being the fastest to optimize.

The accuracy metrics of models are calculated based on the error between the predictions of the trained models and a testing set of 3.000 samples. The results indicate that all four models approximate the forward Q6ED model well with NN models being slightly more accurate (Fig. 11).

5.1.2. Identification results

The MCMC identification process involves searching for parameters that yield the obtained measurements. The definition of the likelihood function requires specifying the obtained measurement d_m by incorporating the error distribution from Eq. (18) into the given synthetic measurement. The measurement error is assumed to be 1% of the synthetic measurement. This value was selected based on available data on the precision of strain gauge devices, as well as supporting evidence from the literature where this specific value is also commonly accepted [17,28]. The modeling error is represented as the standard deviation of the error values obtained by comparing each trained proxy model with the results from the testing samples. These two sources of error are than combined to define the error distribution $X \sim N(0, \epsilon^2)$.

The MCMC results are presented in Fig. 12. It is shown that the MCMC method succesfully identifies parameters with all four proxy models. The results for the first parameter σ_n show minimal variation. For the second parameter G_{fn}, the low-rank models performed slightly better. This suggests that lower-dimensional representations helped filter out the noise and improve accuracy. Additional details on the precision of identification results for each proxy model are provided in Table 2. Here, the mean posterior values are compared with the true values.

The MCMC process involved 100 Markov chains and 1.000 simulation steps, totaling 100.000 simulations. Given the computational capacity to perform 100 parallel runs and a simulation time of approximately 1 min per run, a full MCMC analysis without proxy models would require around 16.7 h. The analysis time by using proxy models significantly reduces. Considering the required computational time to train proxy models (see Table 1), major computational savings are achieved for all models.
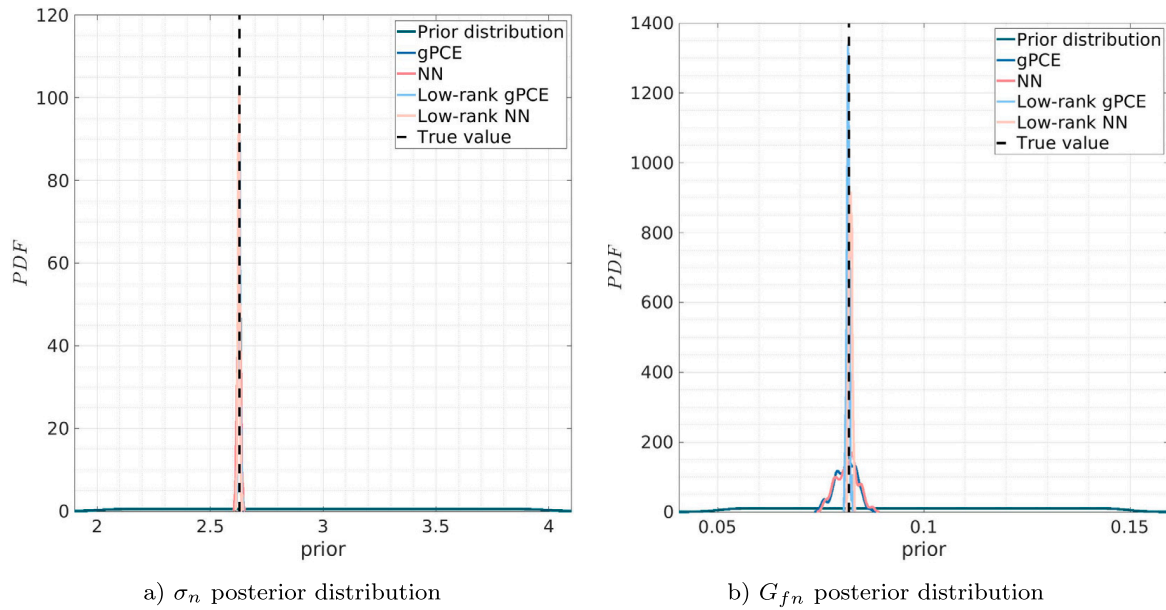
a) σ_n posterior distribution

b) G_{fn} posterior distribution

Fig. 12. Hole tension test: Identification of tensile strenght σ_n and tensile fracture energy G_{fn} parameters.

Table 2

Hole tension test: Identification accuracy of parameters by comparing the ground-truth and posterior mean.[a]

	gPCE	Low-rank gPCE	NN	Low-rank NN
Mean posterior value (σ_n)	2.62908	2.62874	2.62772	2.62729
Error [%]	0.045	0.057	0.096	0.112
Mean posterior value (G_{fn})	0.08111	0.08162	0.08134	0.08222
Error [%]	0.888	0.270	0.617	0.462

[a] True fracture parameter values ($\mathbf{z}_{true}$): $\sigma_n = 2.63025$ N/mm^2, $G_{fn} = 0.08184$ N/mm.

5.2. Four point bending test

In the four-point bending test, the initial prior distribution of unknown parameters is chosen to be uniform, with $\sigma_n \sim U(2.4 \text{ N/mm}^2, 2.8 \text{ N/mm}^2)$, $G_{fn} \sim U(0.085 \text{ N/mm}, 0.12 \text{ N/mm})$, $\sigma_m \sim U(0.85 \text{ N/mm}^2, 1 \text{ N/mm}^2)$, and $G_{fm} \sim U(0.085 \text{ N/mm}, 0.12 \text{ N/mm})$. The synthetic measurements used to identify these parameters are generated by evaluating $\mathcal{G}(\mathbf{z}_{true})$, with $\mathbf{z}_{true}$ being randomly selected, and collecting data from the positions indicated in Fig. 7. These measurements, denoted as $\mathbf{u}^{(1)}, \mathbf{u}^{(2)}, \mathbf{u}^{(3)}, \mathbf{u}^{(4)}$ (see Eq. (32)), each consist of 450 timesteps. To simplify algorithmic calculations, we combine these measurements into a single synthetic measurement spanning 1800 timesteps.

This combined measurement is then divided into two phases. The first phase covers 150 timesteps of each individual measurement (1/3 of the total measurements), as illustrated by the gray regions in Fig. 13. The second phase encompasses the full domain of the measurements. This division is made to enable the sequential identification of parameters, and a reduction of the needed complexity of the surrogate model for the non-gray areas. With an initial prior distribution, uncertainties in input parameters lead to large uncertainties in the results, causing significant discrepancies in the training data set and making it challenging to train proxy models. By adopting this approach, such issues are mitigated due to the reduced parametric uncertainties of the second phase.

5.2.1. First updating phase

The first updating phase covers the time of crack initiation and also the beginning of macrocrack formation. From the initially defined uniform prior distribution, 25.000 samples were created by QMC sampling and computed for the training of the surrogate model, with an additional 5.000 samples to estimate its accuracy. Each sample in this phase requires approximately 5 min of computation time, resulting in a total processing time of about 25 h for all 30.000 samples on the cluster computer. Forward model solutions for the training set are shown in Fig. A.5.

5.2.1.1. Proxy model training.

gPCE model

From the accuracy results of the gPCE model (Fig. A.6(a)), an 8th-degree polynomial model with 495 coefficients per timestep was chosen to approximate the forward model's solutions. The results of the Sobol analysis are shown in Fig. 14(a). From the sensitivity results, it is visible that the majority of the variance of each measurement is attributed to the tensile strength parameter, σ_n. As the
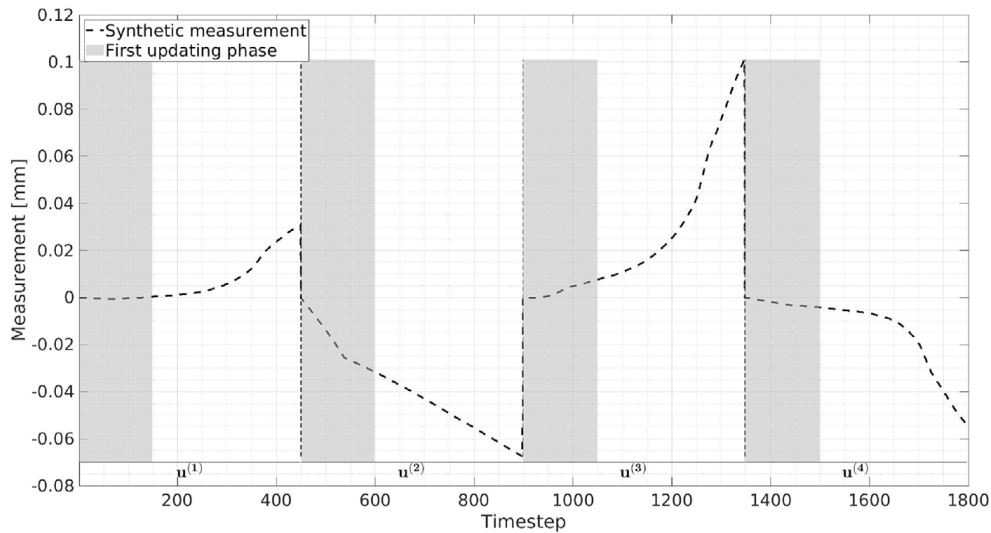
Fig. 13. In the four-point bending test, the measurements $\mathbf{u}^{(1)}, \mathbf{u}^{(2)}, \mathbf{u}^{(3)}, \mathbf{u}^{(4)}$ are represented by Eq. (32). All four synthetic measurements, each consisting of 450 timesteps, are grouped into a single 1.800 timestep measurement, marked by a black dashed line. The gray area indicates the first updating phase of the identification process, while the entire time domain (including both gray and white areas) is later utilized for the second updating phase.

Table 3
Four point bending test (first updating phase): Total computational time required to train and test proxy models including hyperparameter search (18 gPCE models with different polynomial bases, 10 neural network architectures).

	gPCE	Low-rank gPCE	NN	Low-rank NN
Total computational time [min]	12	108	70	183

cracking process progresses, the influence of the other parameters becomes apparent, with the tensile fracture energy parameter, G_{fn}, beginning to mainly impact the result. Additionally, the shear strength parameter, σ_m, affects the second measurement, which is the vertical displacement difference at the notch positions. The sensitivity of the last parameter, shear fracture energy G_{fm}, as well as the mixed modes are not visible in this analysis.

NN model

Table A.3 provides a summary of the performance metrics for different NN configurations. Among the 10 various architectures tested, the configuration with 128 neurons in the first layer and 600 neurons in the output layer (total of 77.524 parameters), using ReLU activation in the first layer and sigmoid activation in the output layer achieved the best performance metrics.

Low-rank representation: training Autoencoder

The autoencoder model with 52 neurons per bottleneck layer and sigmoid activation functions was identified as optimal (Fig. A.7).

Low-rank gPCE model

The 8th-degree polynomial model with 495 coefficients per timestep was selected (Fig. A.6(b)). The Sobol sensitivity analysis (Fig. 14(b)) shows that the first parameter σ_n has a dominant influence on the results. Additionally, there is a noticeable influence from the parameters G_{fn} and σ_m. However, the influence of the fracture shear energy G_{fm} is negligible. These sensitivity results coincide with the previous results gained by the gPCE model.

Low-rank NN model

Table A.4 summarizes the performance metrics for different configurations of the low-rank NN model. The optimal model configuration features two hidden layers with 16 neurons each, both using the tanh activation function, and an output layer with 52 neurons using the sigmoid activation function (total of 1.236 parameters).

Proxy model comparison

The gPCE model requires the least computational time for optimization, followed by the NN model, with the low-rank models requiring the most time (Table 3). The plot of accuracy metrics in Fig. A.8(b) show that all four models demonstrate very similar performance. The current updating phase did not involve significant fracture behavior, and the errors for all four proxy models remain small. This is also observable from Fig. A.8(a) where error vales are significantly smaller compared to plotted dataset.

5.2.1.2. Identification results. Fig. 15 shows that identification of the σ_n produces narrow posterior distributions. Identified G_{fn} distributions varied slightly among the models. The identification of the shear strength parameter σ_m produces pronounced differences within models, with the low-rank ones providing more accurate results. The identification of the G_{fm} parameter was unidentifiable in this phase for all models, which is expected from its absence in the results of the sensitivity analysis shown in Figs. 14(a) and 14(b). Overall no model demonstrated a significant advantage over the others. This is confirmed by the identification metrics in Table 4.
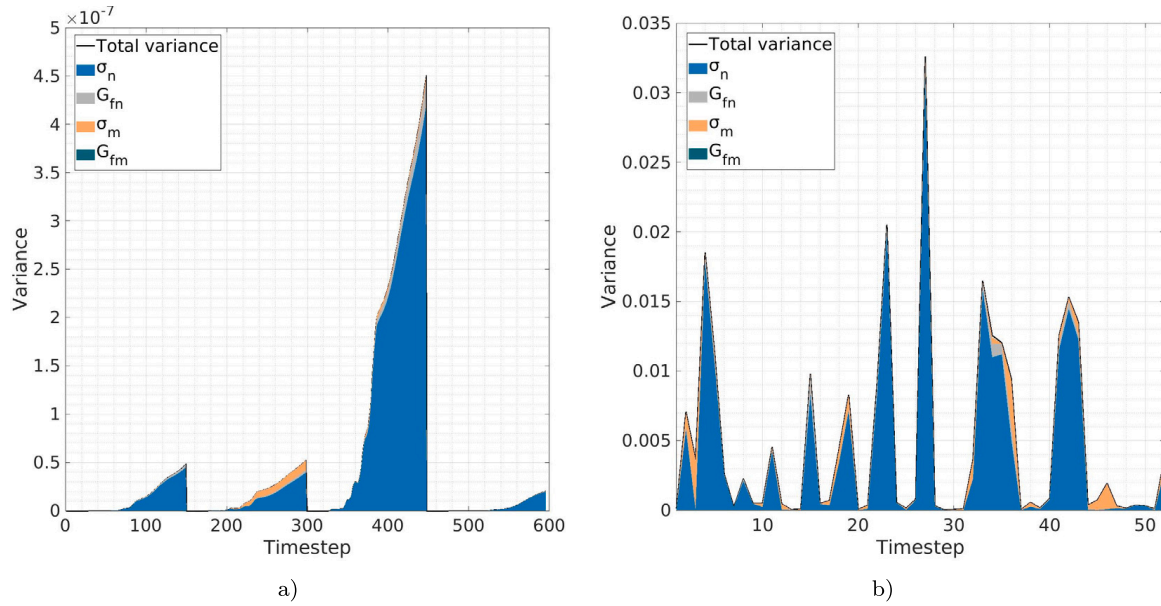
a)

b)

Fig. 14. Four point bending test (first updating phase): (a) Sobol sensitivity by gPCE model (b) Sobol sensitivity by low-rank gPCE model.

Table 4
Four point bending test (first updating phase): Identification accuracy of parameters by comparing the ground-truth and posterior mean.[a]

	gPCE	Low-rank gPCE	NN	Low-rank NN
Mean posterior value (σ_n)	2.65462	2.65448	2.65527	2.65794
Error [%]	0.005	0.001	0.030	0.130
Mean posterior value (G_{fn})	0.09188	0.09220	0.09183	0.09086
Error [%]	0.377	0.035	0.438	0.972
Mean posterior value (σ_m)	0.91677	0.91801	0.91533	0.91828
Error [%]	0.230	0.095	0.387	0.066
Mean posterior value (G_{fm})	0.10232	0.10212	0.10097	0.10242
Error [%]	13.652	13.438	12.150	13.761

[a] True fracture parameter values ($\mathbf{z}_{true}$): $\sigma_n = 2.65448$ N/mm^2, $G_{fn} = 0.09223$ N/mm, $\sigma_m = 0.91888$ N/mm^2, $G_{fm} = 0.09002$ N/mm.

The MCMC analysis involved 2.000 steps with 100 Markov chains. With an average computational time of 5 min per simulation and parallel execution on a cluster computer, the total runtime without using proxy models would be approximately 166.7 h. However, significant reduction is achieved by using proxy models.

Although the dataset from the first updating phase did not capture significant crack propagation or loss of stability in the specimen, the sensitivity analysis revealed a considerable impact of the first three parameters. This shows that the presence of crack initiation was enough to activate these parameters. This phase successfully narrowed our parametric uncertainties for σ_n, G_{fn}, and σ_m. Based on these results, a new training distribution with reduced uncertainty for the unknown fracture parameters was defined for the surrogates of the second phase. The updated distributions were further used in second updating phase to identify the not yet identified parameter G_{fm} and to further refine the identification of the first three parameters.

5.2.2. Second updating phase

The training points for the proxy model were sampled from a new distribution (here quoted as "training distribution second phase"). For training distributions of the first three parameters we have used multivariate beta distribution with $\alpha = 3$ and $\beta = 3$. The original a-priori distribution for the fourth, unidentified parameter was used. The beta distribution was shifted and scaled to have the same mean and covariance as the posterior samples received from the first phase updates, but the later was further upscaled. Fig. 16 shows the training distribution with its samples used for computing the new input–output pairs for the surrogating of the second-phase update. 20.000 QMC sample points were generated for training and 5.000 for testing. Each sample in this phase requires approximately 25 min of computation time, resulting in a total processing time of about 4.5 days to compute all 25.000 samples on the cluster computer. Solutions of the new training set together with the synthetic measurement are shown in Fig. A.9.
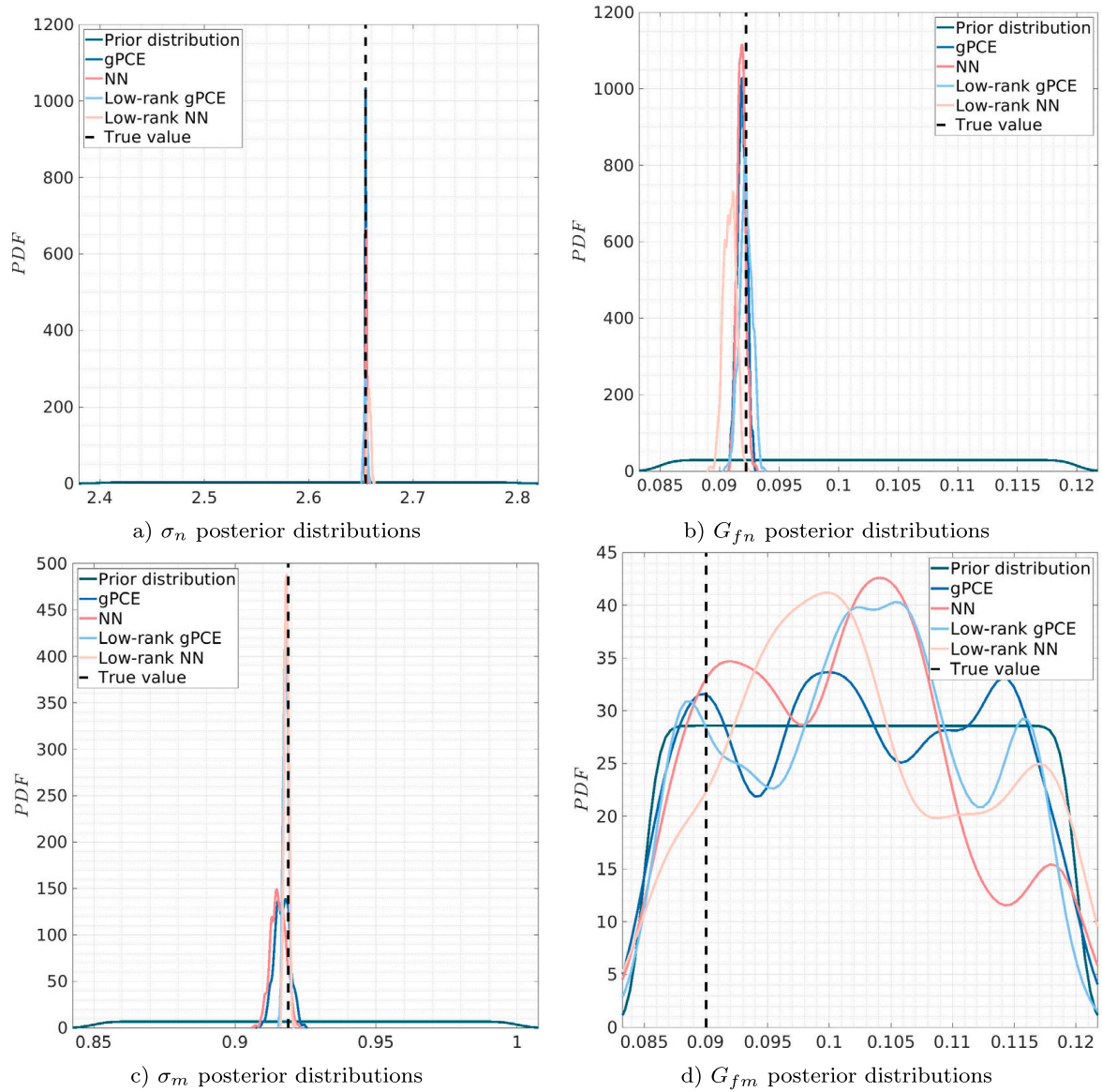
Fig. 15. Four point bending test (first updating phase): Identification of tensile strength σ_n, tensile fracture energy G_{fn}, shear strength σ_m and shear fracture energy G_{fm} parameters.

5.2.2.1. Proxy model training.

gPCE model

The 9th-degree polynomial is chosen with the 715 polynomial coefficients for each timestep based on the accuracy results from Fig. A.10(a). The majority of the variance again refers to the first fracture parameter σ_n (see Fig. 17(a)). As the fracture process progresses, the influence of the other parameters starts to become more noticeable. This is expected, as in the second updating phase, the crack propagates much further than in the first phase. This extended propagation causes the initially formed sections of the cracks to open more, further activating the tensile fracture energy G_{fn}. As the loading continues, the crack's trajectory changes angle due to the combined effects of the applied load and the specimen's cracking. As a result, the influence of the shear strength parameter σ_m increases. It is also observable that the influence of the shear fracture energy G_{fm} exists together with the mixed mode (zoomed part), although limited.

NN Model

The model with three hidden layers of 64 neurons each and an output layer of 1800 neurons (total 125.380 parameters), utilizing GeLU activation functions in the hidden layers and sigmoid in the output layer demonstrated the best performance (see Table A.5).

Low-rank representation: training Autoencoder

Fig. A.11 visually represents the performance of the autoencoder models based on the number of neurons in the bottleneck layer. The configuration with 64 neurons per layer achieved the best performance.
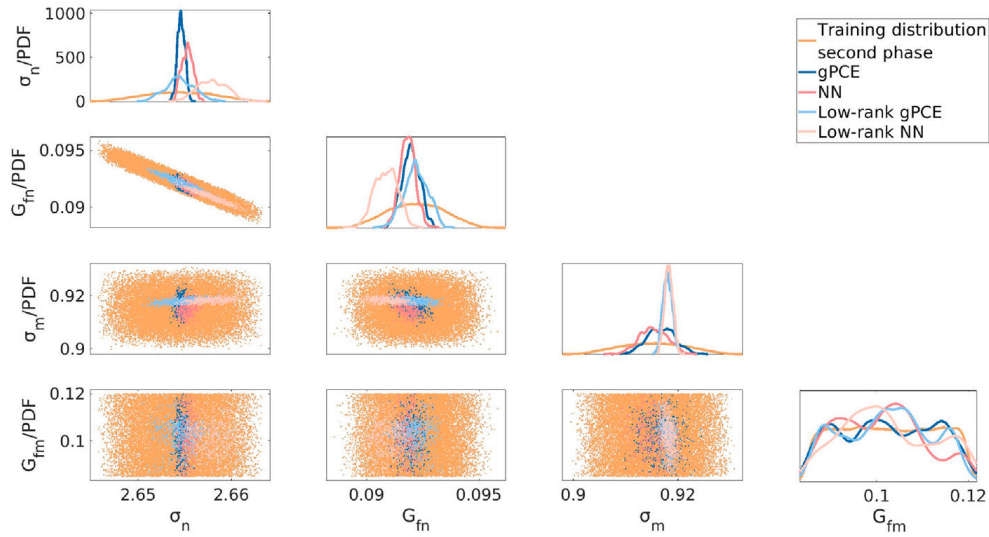
Fig. 16. Second updating phase: Training distribution for the second phase (new prior) is shown together with the posterior distributions of first updating phase of each proxy model.
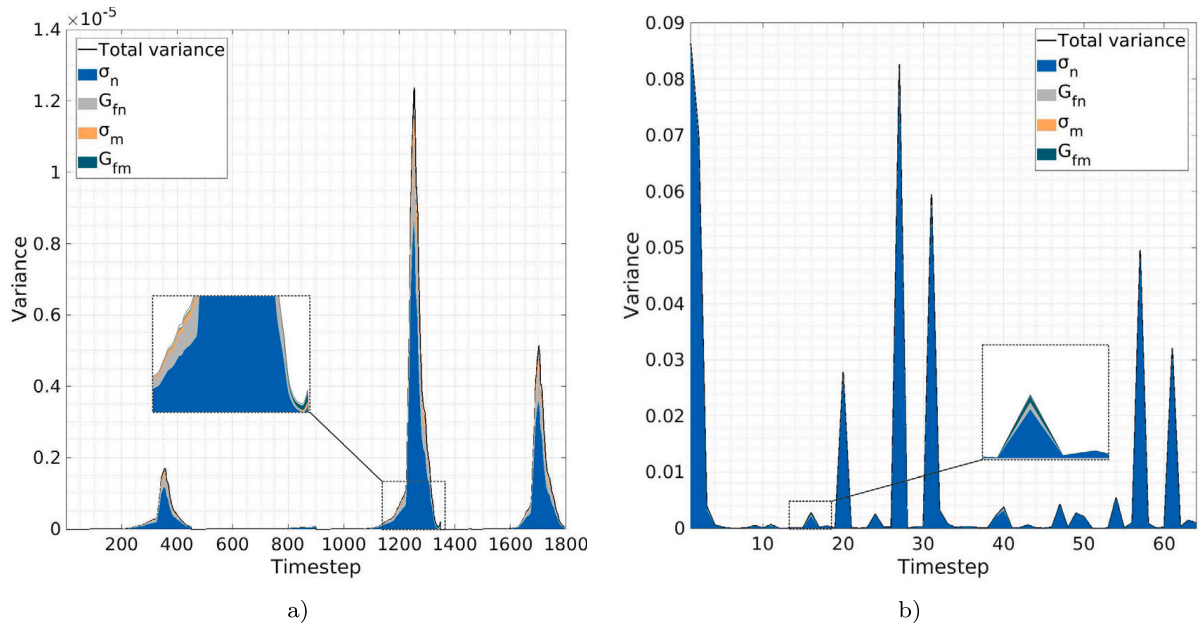

Fig. 17. Four point bending test (second updating phase): (a) Sobol sensitivity by gPCE model (b) Sobol sensitivity by low-rank gPCE model.

Low-rank gPCE model

The 8th-degree polynomial basis with 495 coefficients per timestep was selected (see Fig. A.10(b)). The Sobol sensitivity analysis results are provided in Fig. 17(b). Unlike the previous results of gPCE model, here the influence of the first σ_n parameter is more emphasized. The influence of the other parameters and mixed modes are still present, although they have less influence.

Low-rank NN model

Based on the Table A.6, the optimal model configuration features three hidden layers with 128, 128, and 64 neurons respectively (total 25.408 parameters), all using the ReLU activation function, and an output layer with 64 neurons also utilizing ReLU.

Proxy model comparison

Required computational time (see Table 5) is in the range of that from the first updating phase. However, the measured error values for all proxy models (see Fig. 18) were significantly higher than those observed in the first updating phase. This was anticipated due to the progression of more complex fracture mechanism which introduces more challenging dataset and requires the approximation of rough parameter surfaces.

Variations in input parameters lead to different crack paths and outcomes. As loading increases, this manifests as a bifurcation in results between samples that develop severe cracking, those that do not, and those that form unexpected crack paths. These discrepancies introduce jumps and bifurcations in the results, which are challenging for the proxy models to approximate accurately.

Table 5

Four point bending test (second updating phase): Total computational time required to train and test proxy models including hyperparameter search (12 gPCE models with different polynomial bases, 10 neural network architectures).

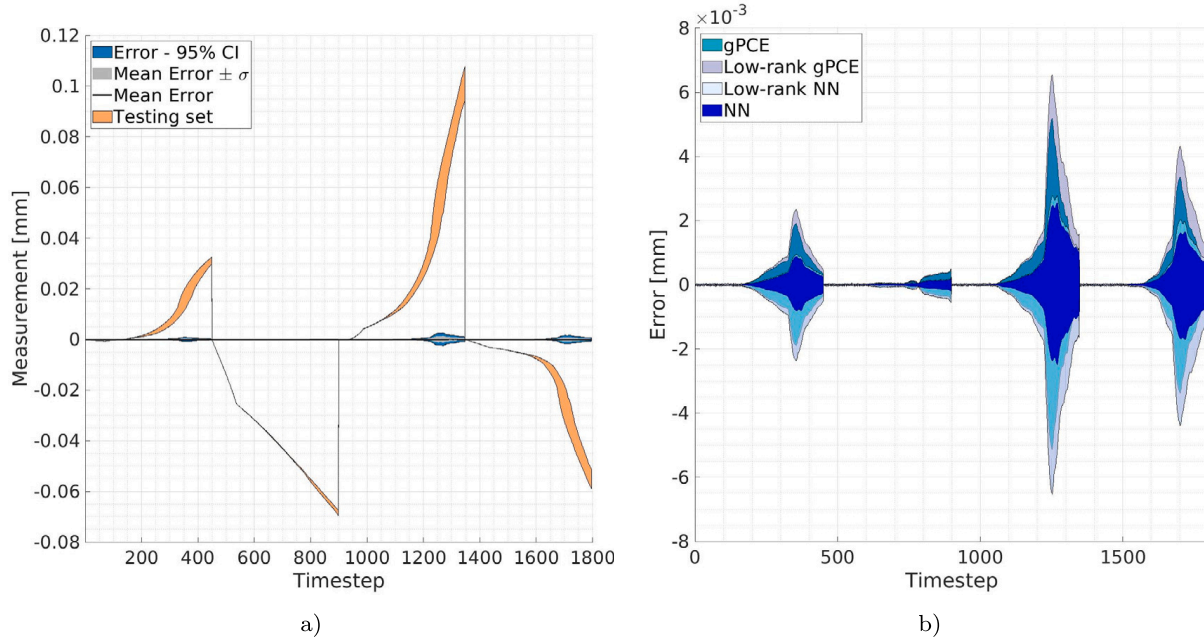|	gPCE	Low-rank gPCE	NN	Low-rank NN
Total computational time [min]	20	103	95	166

Fig. 18. Four point bending test (second updating phase): (a) NN model's error metrics together with the envelope of the testing set (b) 95% CI errors of different proxy models.

As the load continues to increase, the differences in fracture progression become less pronounced, and specimens that initially showed slower cracking begin to catch up. This difficulties highlights the importance of sequential updating, as implemented in this work.

Although the general shapes of the error curves are similar across all models, the magnitude of the errors is significantly smaller for the NN models. This highlights the advantage of deep learning, which excel in universally approximating complex fracture patterns. In contrast, polynomial approximations, while effective for continuous function and capturing smooth surfaces, struggle more to capture the intricacies of more complex fracture behavior.

5.2.2.2. Identification results. The posterior distribution for the first parameter σ_n, has further narrowed for the results of all four models, indicating high certainty and precision in estimating the tensile strength parameter σ_n (Fig. 19). The distributions for the tensile fracture energy G_{fn} also narrows down, except for the low-rank NN model. A similar pattern is observed for the shear strength parameter σ_m. The lower accuracy of the low-rank NN model in this phase likely reflects its lower performance in the first updating phase.

There was a noticeable improvement in the shear fracture energy parameter G_{fm}. Unlike in the first updating phase, where the models failed to reduce the initial uncertainty, this phase demonstrates clear progress. This improvement is likely attributed to the use of the full time domain of the synthetic measurement, which effectively captured the significant propagation of the macrocrack. As a result, the limited influence of shear fracture energy parameter appeared, as shown by the Sobol sensitivity analysis in Fig. 17(a). The gPCE, NN, and low-rank gPCE models significantly reduced the initial uncertainty for G_{fm}, with the NN model providing the most accurate estimate close to the true value. However, the posterior distribution for this parameter remains wider than those of the other parameters, but still informative in an engineering sense.

This is further supported by the accuracy metrics from Table 6, which show a significant change for the final parameter. In this phase, the error metrics for G_{fm} are in the range of 1%–5%, with the NN model being the most precise. Alternatively, the more accurate G_{fm} parameter identification would require a different testing setup.

The estimated required computational time for the direct MCMC analysis with 2.000 steps and 100 Markov chains is 34 day. The estimated proxy model savings is 29.5 days.

6. Conclusion

In this paper, we demonstrated the application of Bayesian identification of parameters in two fracture mechanics problems: a hole tension test and a four point bending test. Additionally, we compared different proxy modeling techniques for identifying
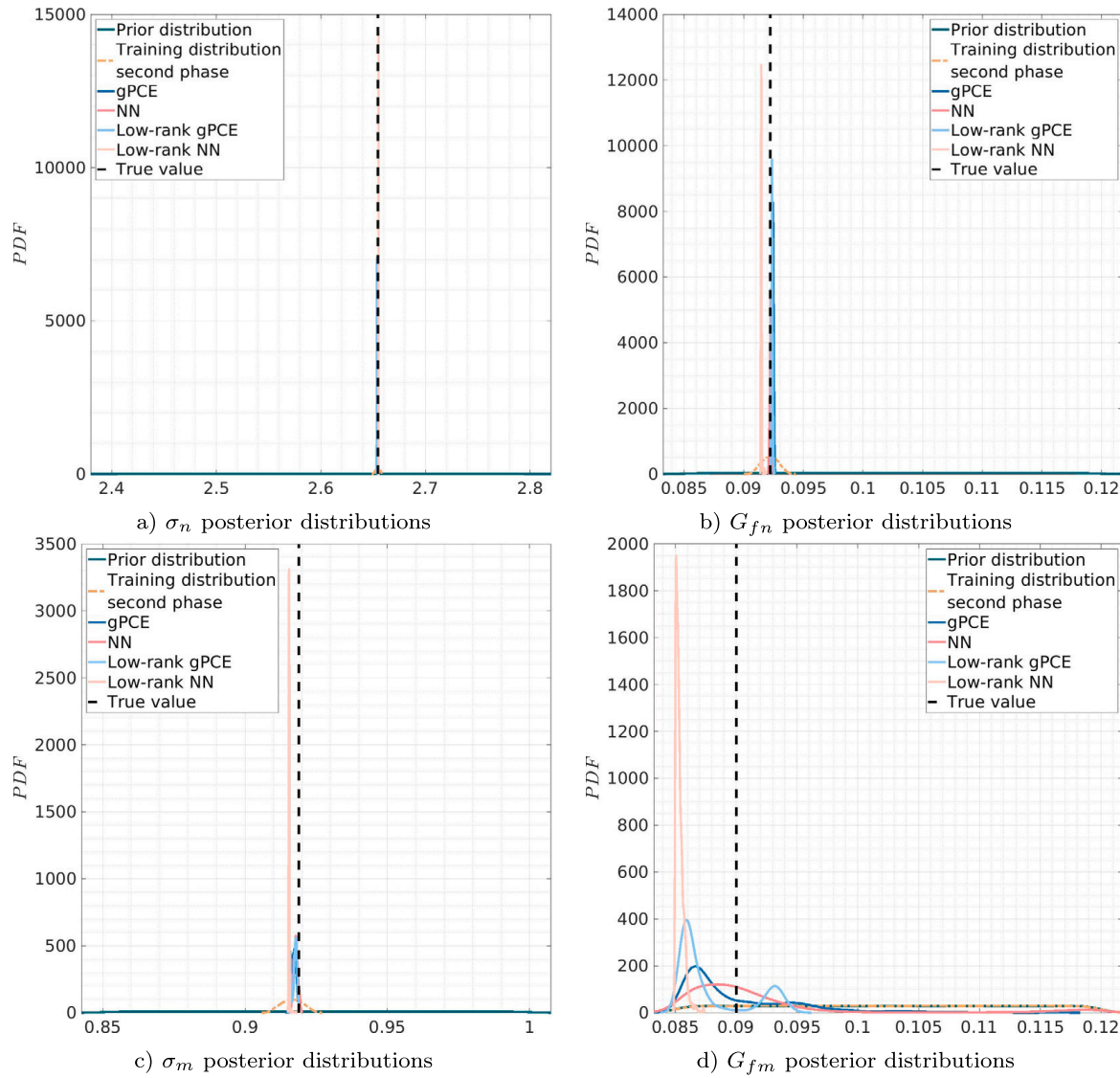
Fig. 19. Four point bending test (second updating phase): Identification of tensile strength σ_n, tensile fracture energy G_{fn}, shear strength σ_m and shear fracture energy G_{fm} parameters.

Table 6

Four point bending test (second updating phase): Identification accuracy of parameters by comparing the ground-truth and posterior mean.[a]

	gPCE	Low-rank gPCE	NN	Low-rank NN
Mean posterior value (σ_n)	2.65400	2.65346	2.65465	2.65515
Error [%]	0.018	0.039	0.006	0.025
Mean posterior value (G_{fn})	0.09247	0.09239	0.09229	0.09148
Error [%]	0.258	0.175	0.062	0.815
Mean posterior value (σ_m)	0.91723	0.91729	0.91784	0.91551
Error [%]	0.180	0.173	0.114	0.367
Mean posterior value (G_{fm})	0.08848	0.08795	0.09078	0.08535
Error [%]	1.711	2.299	0.844	5.188

[a] True fracture parameter values ($\mathbf{z}_{true}$): $\sigma_n = 2.65448$ N/mm^2, $G_{fn} = 0.09223$ N/mm, $\sigma_m = 0.91888$ N/mm^2, $G_{fm} = 0.09002$ N/mm.

fracture parameters. A large number of fracture simulations is carried out by computationally efficient model based on embedded strong discontinuities. Such computational efficiency originates from local nature of embedded strong discontinuities, condensed stiffness matrices and relatively coarse meshes used for crack propagation.

Generalized polynomial chaos expansion models simplify the problem by reducing it to linear regression, which can be solved analytically. Another advantage of gPCE models is that only the polynomial basis needs to be tuned as a hyperparameter, which is

Table A.1

Hole tension test: Hyperparameter optimization of NN models. Used notation: T-tanh, S-sigmoid, R-ReLu.

Neurons/layer	Activation function of layer	$\overline{MAE}$	Max MAE	$\overline{RMSE}$	Max RMSE
64-200	S-S	5.23E−05	6.92E−04	6.55E−05	8.02E−04
64-200	T-S	5.38E−05	7.01E−04	6.80E−05	8.07E−04
64-200	R-S	4.09E−05	7.20E−04	5.07E−05	8.37E−04
32-64-200	R-R-S	3.56E−05	7.27E−04	4.43E−05	8.51E−04
64-128-200	R-R-S	3.37E−05	7.26E−04	4.20E−05	8.51E−04

far less complex than fine-tuning the architecture of a neural network. In contrast, the parameters of deep neural networks require iterative optimization methods like stochastic gradient descent to find local minima. The latter involves adjusting the number of layers, the number of neurons per layer, activation functions, and other elements like dropout rates, making it a more cumbersome and time consuming process. This difference in complexity between surrogate techniques is further confirmed by the optimization time results presented in the paper. Proxy models based on lower-dimensional representation of the time-dependent measurable variables were also tested. Although in our numerical examples, the dimensionality reduction was not significant, in other problems, this reduction could be more substantial.

For the hole tension test, where the fracture pattern was predictable and the response surface was relatively smooth, we found out that all the proxy models performed well. However, the low-rank models demonstrated better accuracy and certainty in identifying the second parameter, highlighting the advantages of a lower-dimensional representation for this test. Computational time savings were achieved across all models, with the greatest reduction observed for the gPCE proxy model.

The four point bending test produced more complex fracture processes and therefore presented greater challenges. The high nonlinearity present in fracture propagation significantly influenced both the identification process and the construction of surrogate models. The complex nature of these nonlinearities produced a challenging dataset, for which all models struggled to accurately approximate the later stages of the fracture process. To address this, we proposed a sequential updating procedure. Initially, the parametric uncertainties were reduced using a preliminary identification using data from the early, less complex stages of fracture. In a second phase, surrogate modeling was performed within this reduced stochastic space. While the first phase yielded results similar to those of the hole tension test, with all methods performing comparably, the second phase revealed the limitations of surrogate models in capturing the complex response surfaces characterized by jumps and bifurcations. In these cases, the NN models outperformed the gPCE models, highlighting their superior ability to handle complicated fracture patterns. Importantly, using proxy models led to substantial computational savings, reducing identification time by several weeks, highlighting the value of these models in identification process in complex fracture problems.

CRediT authorship contribution statement

Matej Šodan: Writing – original draft, Visualization, Software, Investigation. **András Urbanics:** Software, Investigation. **Noémi Friedman:** Writing – review & editing, Writing – original draft, Methodology, Investigation, Conceptualization. **Andjelka Stanic:** Validation, Formal analysis. **Mijo Nikolić:** Writing – review & editing, Supervision, Software, Methodology, Investigation, Funding acquisition, Conceptualization.

Declaration of competing interest

The authors declare that they have no known competing financial interests or personal relationships that could have appeared to influence the work reported in this paper.

Acknowledgments

Appendix. A

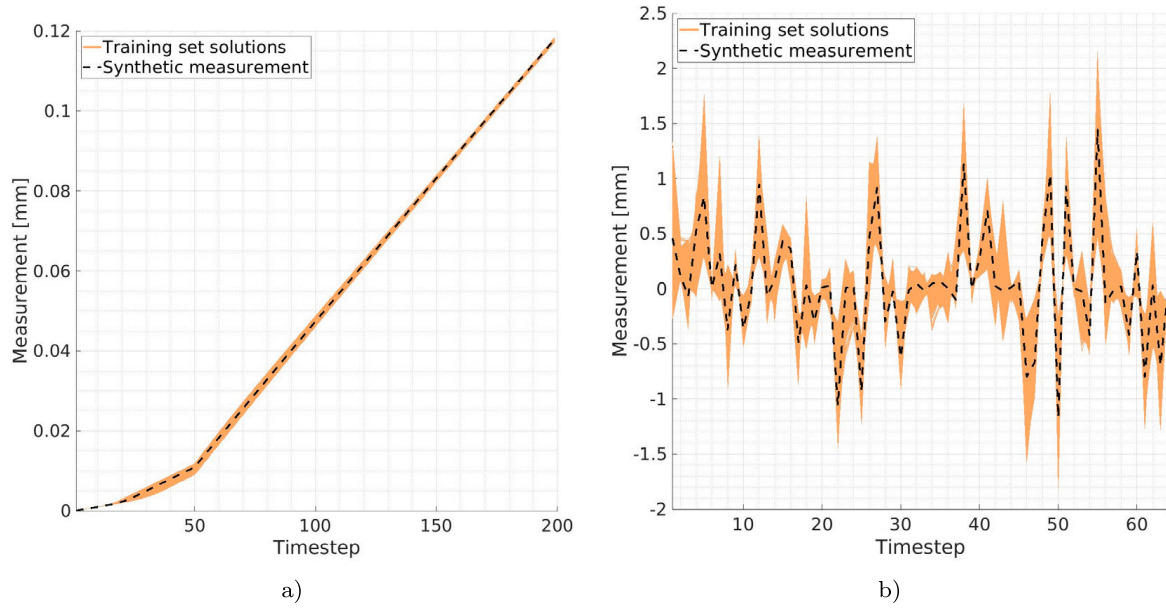See Figs. A.1–A.11 and Tables A.1–A.6.

Fig. A.1. Hole tension test: (a) Training set solutions and synthetic measurement (b) Low-rank representation of (a).
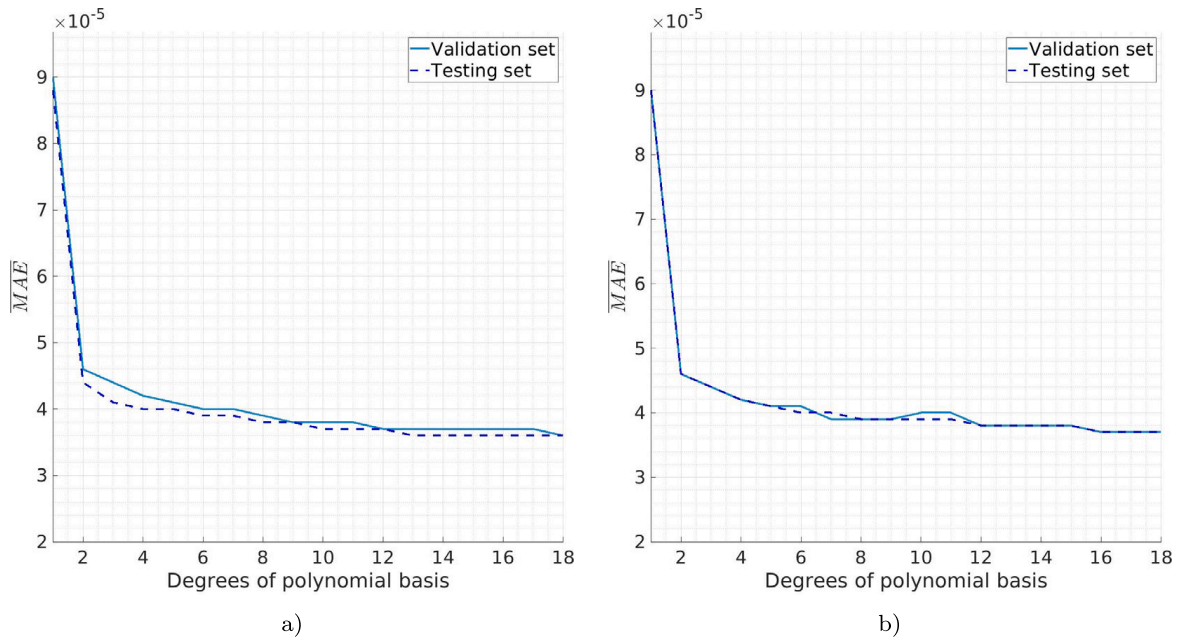

Fig. A.2. Hole tension test: (a) Accuracy assessment of the gPCE proxy models based on polynomial degree (b) Accuracy assessment of the low-rank gPCE proxy models based on polynomial degree.

Table A.2

Hole tension test: Hyperparameter optimization of low-rank NN model. Used notation: T-tanh, S-sigmoid, R-ReLu, Ø-there is no activation function.

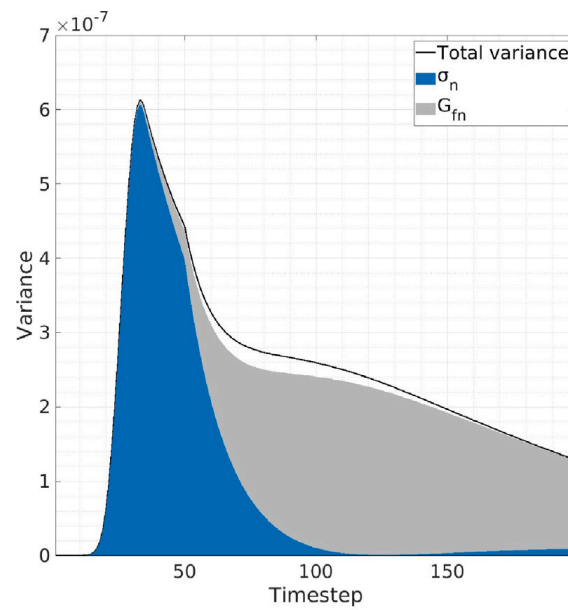| Neurons/layer	Activation function of layer	$\overline{MAE}$	Max MAE	$\overline{RMSE}$	Max RMSE
32-64	R-S	3.96E−05	7.85E−04	4.93E−05	9.09E−04
32-64	Ø-R	8.26-04	1.22E−03	1.03E−03	1.51E−03
32-64	R-T	4.77E−05	7.59E−04	5.92E−05	8.73E−04
16-32-64	**R-R-S**	**3.16E−05**	**7.74E−04**	**3.91E−05**	**8.92E−04**
32-32-64	R-R-S	4.04E−05	7.95E−04	4.93E−05	9.13E−04

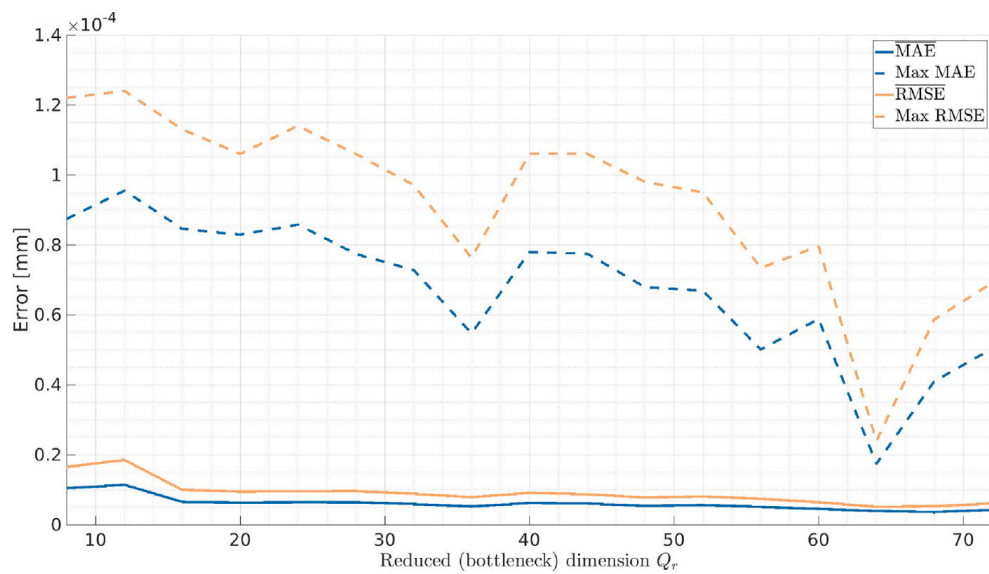**Fig. A.3.** Hole tension test: Sobol sensitivity by the NN model by Saltelli's sampling based method.

Fig. A.4. Hole tension test: Change of errors of the autoencoder models depending on the number of dimensions (subtracted expected value).

Table A.3
Four point bending test (first updating phase): Hyperparameter optimization of NN models. Used notations: S-sigmoid, Ø-there is no activation function, R-ReLu.

Neurons/layer	Activation function of layer	$\overline{\mathrm{MAE}}$	Max MAE	$\overline{\mathrm{RMSE}}$	Max RMSE
4-64-128-64-128-600	S-S-S-S-Ø	6.83E−06	4.23E−05	1.06E−05	8.79E−05
4-128-600	**R-S**	**4.67E−06**	**3.76E−05**	**8.87E−06**	**8.58E−05**
4-128-128-600	R-R-S	4.85E−06	3.84E−05	8.78E−06	8.17E−05
4-64-600	R-S	4.81E−06	3.84E−05	9.35E−06	8.57E−05
4-64-64-600	R-R-S	4.81E−06	3.92E−05	8.97E−06	8.73E−05

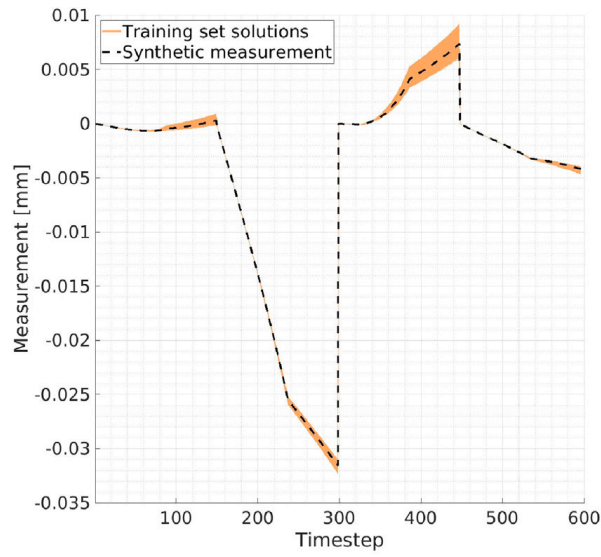**Fig. A.5.** Four point bending test (first updating phase): Training set solutions and synthetic measurement.

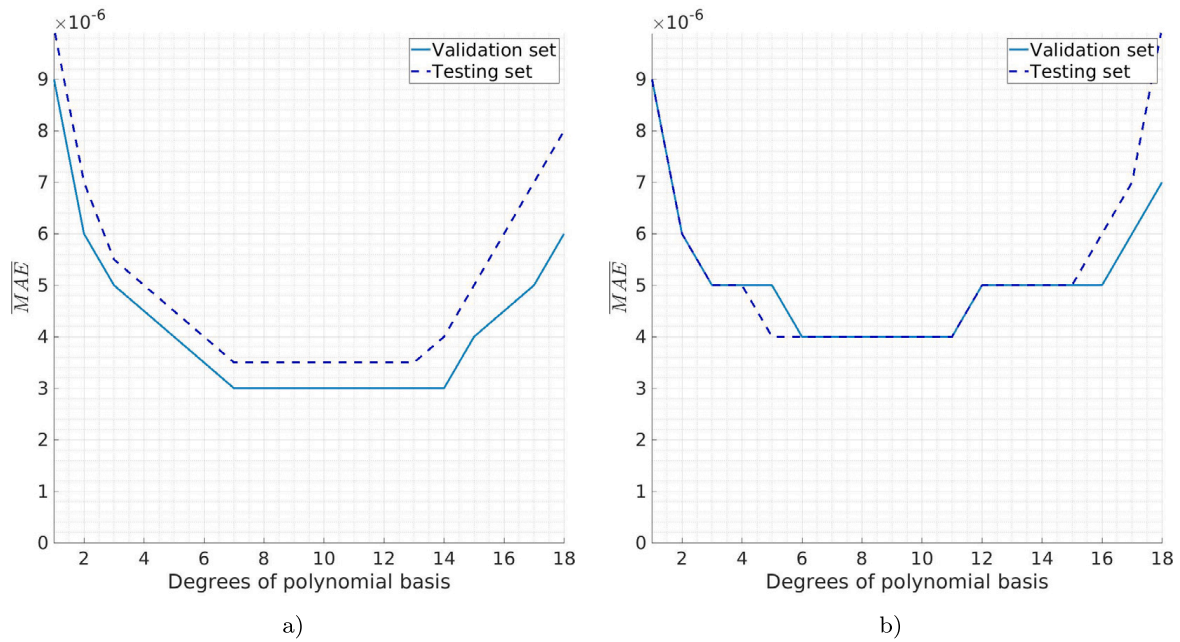a)   b)

Fig. A.6. Four point bending test (first updating phase): (a) Accuracy assessment of the gPCE proxy models based on polynomial degree (b) Accuracy assessment of the low-rank gPCE proxy models based on polynomial degree.

Table A.4
Four point bending test (first updating phase): Hyperparameter optimization of low-rank NN models. Used notations: S-sigmoid, Ø-there is no activation function, T-tanh, G-gelu.

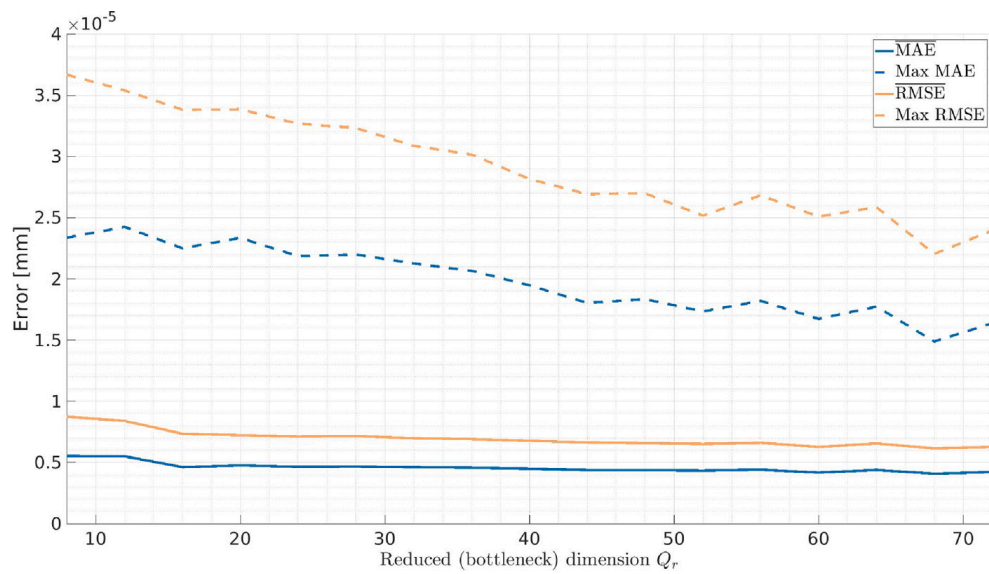| Neurons/layer	Activation function of layer	$\overline{MAE}$	Max MAE	$\overline{RMSE}$	Max RMSE
4-16-52	Ø-G	1.03E−05	3.89E−05	1.71E−05	7.63E−05
4-16-52	T-S	6.10E−06	3.85E−05	1.13E−05	8.17E−05
4-16-16-52	**T-T-S**	**5.61E−06**	**3.98E−05**	**1.05E−05**	**8.45E−05**
4-16-32-52	T-T-S	5.62E−06	3.85E−05	1.04E−05	8.52E−05
4-32-32-52	T-T-S	7.35E−06	3.80E−05	1.30E−05	7.92E−05

Fig. A.7. Four point bending test (first updating phase): change of errors of the autoencoder models depending on the number of dimensions.
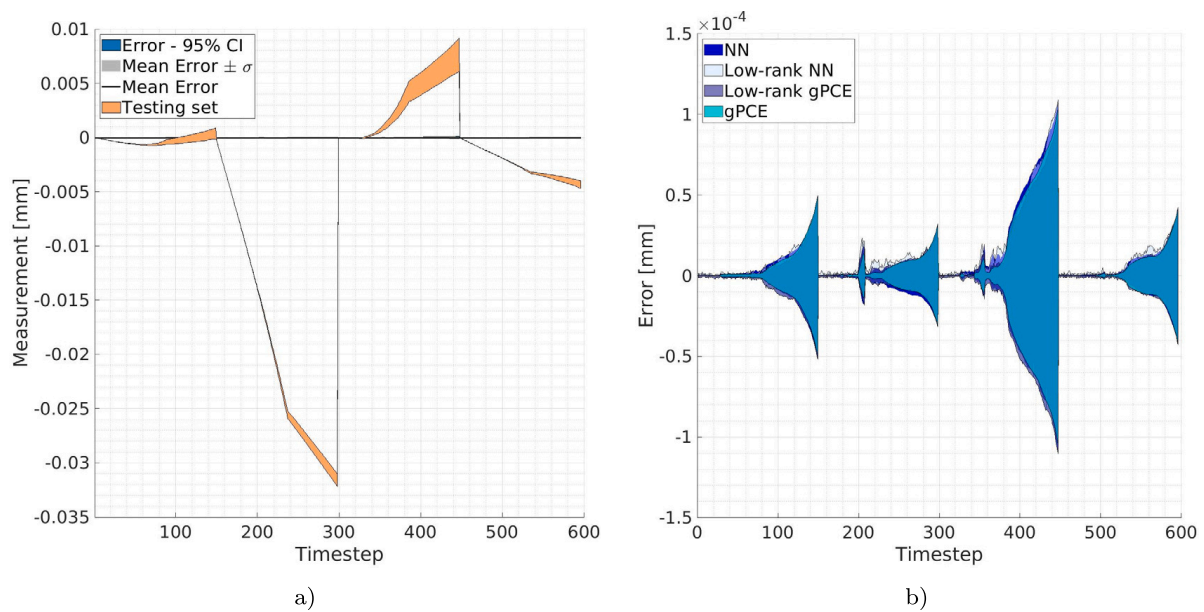

a)

b)

Fig. A.8. Four point bending test (first updating phase): (a) gPCE model's error metrics together with the envelope of the testing set (b) 95% CI errors of different proxy models.

Table A.5
Four point bending test (second updating phase): Hyperparameter optimization of NN models. Used notations: S-sigmoid, Ø-there is no activation function, T-tanh, G-GeLu.

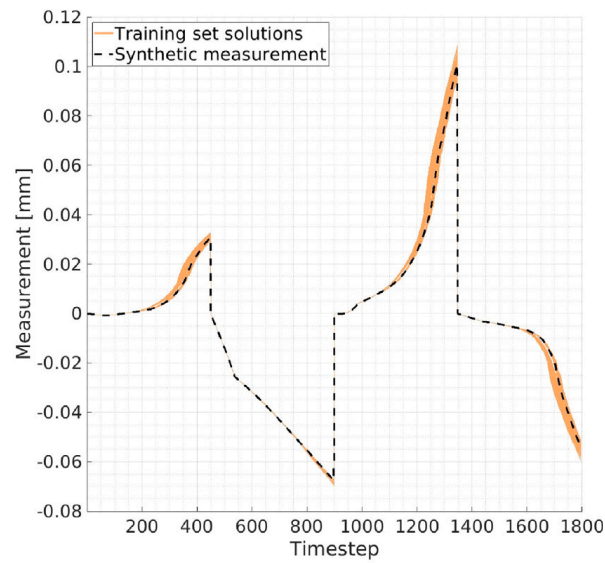| Neurons/layer	Activation function of layer	$\overline{\text{MAE}}$	Max MAE	$\overline{\text{RMSE}}$	Max RMSE
4-64-1800	T-Ø	3.38E−04	1.56E−03	7.06E−04	3.46E−03
4-64-1800	G-S	2.76E−04	1.59E−03	5.82E−04	3.36E−03
4-32-64-1800	G-G-S	1.26E−04	1.46E−03	2.75E−04	3.28E−03
4-32-64-128-1800	G-G-G-S	9.42E−05	1.35E−03	2.09E−04	3.04E−03
4-64-64-64-1800	**G-G-G-S**	**8.10E−05**	**1.24E−03**	**1.86E−04**	**2.56E−03**

Fig. A.9. Four point bending test (second updating phase): Training set solution and synthetic measurement.
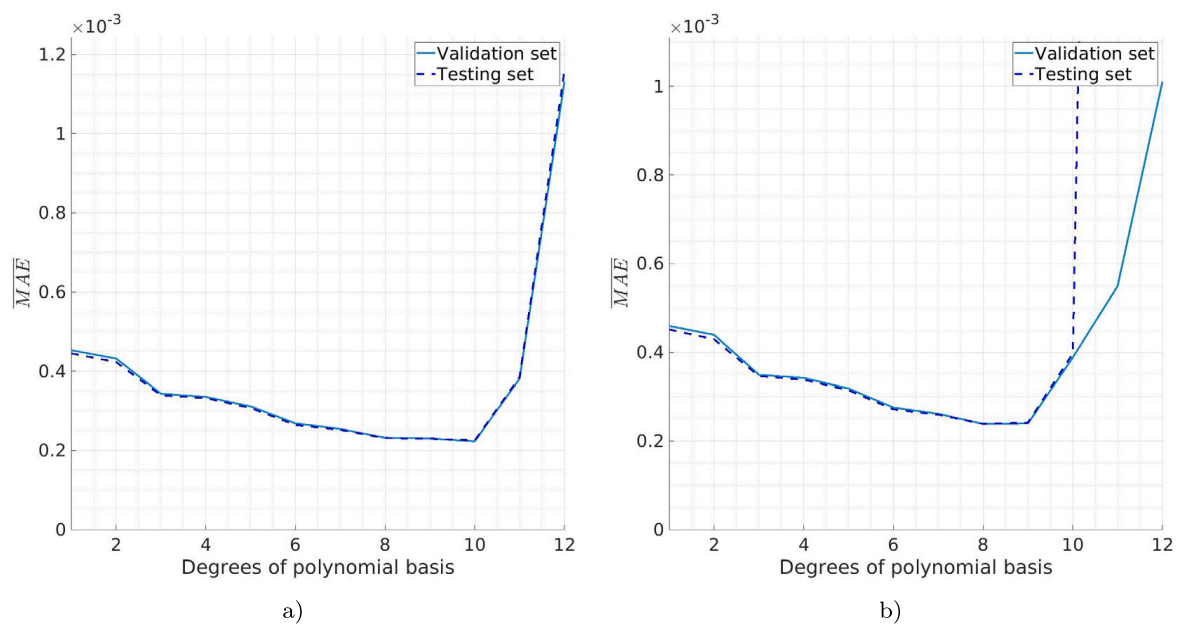

Fig. A.10. Four point bending test (second updating phase): (a) Accuracy assessment of the gPCE proxy models based on polynomial degree (b) Accuracy assessment of the low-rank gPCE proxy models based on polynomial degree.

Table A.6
Four point bending test (second updating phase): Hyperparameter optimization of low-rank NN models. Used notations: S-sigmoid, Ø-there is no activation function, T-tanh, R-ReLu.

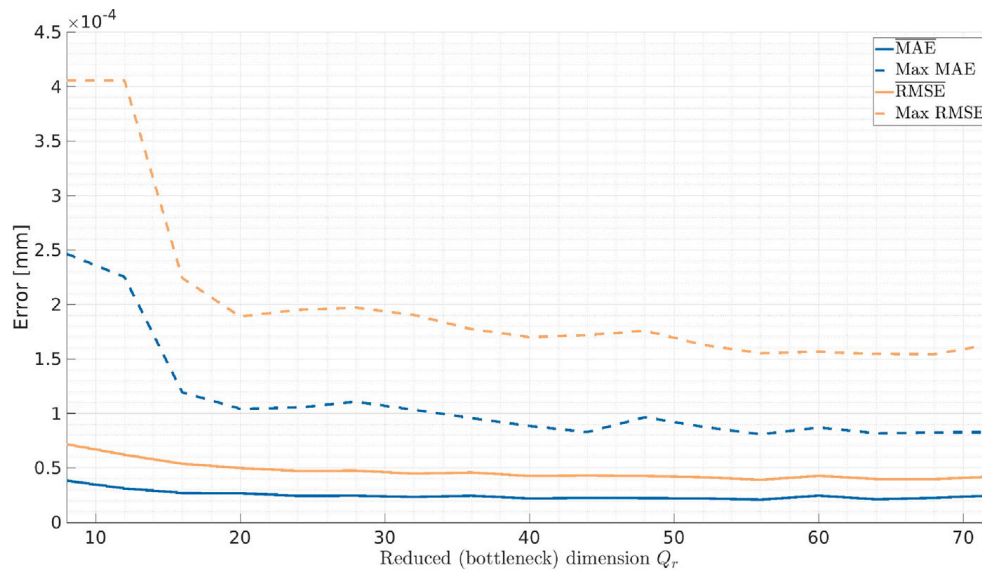| Neurons/layer	Activation function of layer	$\overline{MAE}$	Max MAE	$\overline{RMSE}$	Max RMSE
4-32-64	T-S	2.93E−04	1.45E−03	6.03E−04	3.24E−03
4-32-64	Ø-S	4.49E−04	2.13E−03	9.20E−04	4.25E−03
4-32-64	R-S	1.80E−04	1.35E−03	3.76E−04	2.98E−03
4-64-64-64	R-R-S	1.43E−04	1.31E−03	2.98E−04	2.96E−03
4-128-128-64	**R-R-S**	**9.43E−05**	**1.48E−03**	**2.00E−04**	**3.11E−03**

Fig. A.11. Four point bending test (second updating phase): change of errors of the autoencoder models depending on the number of dimensions.

Data availability

Data will be made available on request.

References

[1] A. Ibrahimbegovic, Nonlinear solid mechanics, 160, 2009, http://dx.doi.org/10.1007/978-90-481-2331-5_1,

[2] A. Lisjak, G. Grasselli, A review of discrete modeling techniques for fracturing processes in discontinuous rock masses, J. Rock Mech. Geotech. Eng. 6 (2014) 301–314, http://dx.doi.org/10.1016/j.jrmge.2013.12.007.

[3] M. Nikolic, E. Karavelić, A. Ibrahimbegovic, P. Miščević, Lattice element models and their peculiarities, Arch. Comput. Methods Eng. 25 (2018) 753–784, http://dx.doi.org/10.1007/s11831-017-9210-y.

[4] J. Oliver, A. Huespe, P. Sánchez, A comparative study on finite elements for capturing strong discontinuities: E-FEM vs X-FEM, Comput. Methods Appl. Mech. Engrg. 195 (2006) 4732–4752, http://dx.doi.org/10.1016/j.cma.2005.09.020.

[5] N. Moës, T. Belytschko, Extended finite element method for cohesive crack growth, Eng. Fract. Mech. 69 (2002) 813–833, http://dx.doi.org/10.1016/S0013-7944(01)00128-X.

[6] C. Linder, F. Armero, Finite elements with embedded strong discontinuities for the modeling of failure in solids, Internat. J. Numer. Methods Engrg. 72 (2007) 1391–1433, http://dx.doi.org/10.1002/nme.2042.

[7] J. Oliver, Modelling strong discontinuities in solid mechanics via strain softening constitutive equations. Part 1: Fundamentals, Internat. J. Numer. Methods Engrg. 39 (1996) 3575–3600, http://dx.doi.org/10.1002/(SICI)1097-0207(19961115)39:21<3575::AID-NME65>3.0.CO;2-E.

[8] M. Jirásek, Comparative study on finite elements with embedded discontinuities, Comput. Methods Appl. Mech. Engrg. 188 (2000) 307–330, http://dx.doi.org/10.1016/S0045-7825(99)00154-1.

[9] X. Li, Y. Xu, Phase field modeling scheme with mesostructure for crack propagation in concrete composite, Int. J. Solids Struct. 234–235 (2022) 111–259, http://dx.doi.org/10.1016/j.ijsolstr.2021.111259.

[10] Y. jie Huang, Z. jun Yang, H. Zhang, S. Natarajan, A phase-field cohesive zone model integrated with cell-based smoothed finite element method for quasi-brittle fracture simulations of concrete at mesoscale, Comput. Methods Appl. Mech. Engrg. 396 (2022) 115074, http://dx.doi.org/10.1016/j.cma.2022.115074.

[11] L. Hai, J. Li, Modeling tensile damage and fracture of quasi-brittle materials using stochastic phase-field model, Theor. Appl. Fract. Mech. 118 (2022) 103283, http://dx.doi.org/10.1016/j.tafmec.2022.103283.

[12] J. Čarija, M. Nikolić, A. Ibrahimbegovic, Ž. Nikolić, Discrete softening-damage model for fracture process representation with embedded strong discontinuities, Eng. Fract. Mech. 236 (2020) 107211, http://dx.doi.org/10.1016/j.engfracmech.2020.107211.

[13] M. Nikolic, A. Ibrahimbegovic, P. Miscevic, Brittle and ductile failure of rocks: Embedded discontinuity approach for representing mode I and mode II failure mechanisms: brittle and ductile failure of rocks, Internat. J. Numer. Methods Engrg. 102 (2015) 1595–1638, http://dx.doi.org/10.1002/nme.4866.

[14] Z. Rizvi, M. Nikolic, F. Wuttke, Lattice element method for simulations of failure in bio-cemented sands, Granul. Matter 21 (2019) 18, http://dx.doi.org/10.1007/s10035-019-0878-6.

[15] M. Šodan, A. Stanic, M. Nikolić, Enhanced solid element model with embedded strong discontinuity for representation of mesoscale quasi-brittle failure, Int. J. Fract. 248 (2024) 1–25, http://dx.doi.org/10.1007/s10704-024-00797-0.

[16] H.G. Matthies, E. Zander, B.V. Rosić, A. Litvinenko, O. Pajonk, Inverse problems in a Bayesian setting, in: Computational Methods for Solids and Fluids: Multiscale Analysis, Probability Aspects and Model Reduction, Springer International Publishing, 2016, pp. 245–286, http://dx.doi.org/10.1007/978-3-319-27996-1_10.

[17] B.V. Rosić, A. Kučerová, J. Sýkora, O. Pajonk, A. Litvinenko, H.G. Matthies, Parameter identification in a probabilistic setting, Eng. Struct. 50 (2013) 179–196, http://dx.doi.org/10.1016/j.engstruct.2012.12.029.

[18] J. Chiachio-Ruano, M. Chiachio-Ruano, S. Sankararaman, Bayesian Inverse Problems: Fundamentals and Engineering Applications, first ed., CRC Press, 2021, pp. 155–202, http://dx.doi.org/10.1201/b22018.

[19] F. Landi, F. Marsili, N. Friedman, P. Croce, gPCE-based stochastic inverse methods: A benchmark study from a civil engineer's perspective, Infrastructures 6 (2021) 158, http://dx.doi.org/10.3390/infrastructures6110158.

[20] F. Daghia, S. de Miranda, F. Ubertini, E. Viola, Estimation of elastic constants of thick laminated plates within a Bayesian framework, Compos. Struct. 80 (2007) 461–473, http://dx.doi.org/10.1016/j.compstruct.2006.06.030.

[21] G. Sevieri, M. Andreini, A. De Falco, H.G. Matthies, Concrete gravity dams model parameters updating using static measurements, Eng. Struct. 196 (2019) 109231, http://dx.doi.org/10.1016/j.engstruct.2019.05.072.

[22] G. Sevieri, A.D. Falco, Dynamic structural health monitoring for concrete gravity dams based on the Bayesian inference, J. Civ. Struct. Health Monit. 10 (2020) 235–250, http://dx.doi.org/10.1007/s13349-020-00380-w.

[23] H. Rappel, L. Beex, L. Noels, S. Bordas, Identifying elastoplastic parameters with Bayes' theorem considering output error, input error and model uncertainty, Probab. Eng. Mech. 55 (2019) 28–41, http://dx.doi.org/10.1016/j.probengmech.2018.08.004.

[24] J. Waeytens, B. Rosić, Comparison of deterministic and probabilistic approaches to identify the dynamic moving load and damages of a reinforced concrete beam, Appl. Math. Comput. 267 (2015) 3–16, http://dx.doi.org/10.1016/j.amc.2015.07.121.

[25] B. Conde, P. Eguía, G. Stavroulakis, E. Granada, Parameter identification for damaged condition investigation on masonry arch bridges using a Bayesian approach, Eng. Struct. 172 (2018) 275–284, http://dx.doi.org/10.1016/j.engstruct.2018.06.040.

[26] F. Alkam, I. Pereira, T. Lahmer, Qualitatively-improved identified parameters of prestressed concrete catenary poles using sensitivity-based Bayesian approach, Results Eng. 6 (2020) 100104, http://dx.doi.org/10.1016/j.rineng.2020.100104.

[27] S. Dobrilla, H.G. Matthies, A. Ibrahimbegovic, Considerations on the identifiability of fracture and bond properties of reinforced concrete, Internat. J. Numer. Methods Engrg. 124 (2023) 3662–3686, http://dx.doi.org/10.1002/nme.7289.

[28] S. Dobrilla, M. Lunardelli, M. Nikolić, D. Lowke, B. Rosić, Bayesian inference of mesoscale mechanical properties of mortar using experimental data from a double shear test, Comput. Methods Appl. Mech. Engrg. 409 (2023) 115964, http://dx.doi.org/10.1016/j.cma.2023.115964.

[29] E. Janouchová, A. Kučerová, J. Sýkora, J. Vorel, R. Wan-Wendner, Robust probabilistic calibration of a stochastic lattice discrete particle model for concrete, Eng. Struct. 236 (2021) 112000, http://dx.doi.org/10.1016/j.engstruct.2021.112000.

[30] T. Wu, B.V. Rosić, L.D. Lorenzis, H.G. Matthies, Parameter identification for phase-field modeling of fracture: A Bayesian approach with sampling-free update, Comput. Mech. 67 (2020) 435–453, http://dx.doi.org/10.1007/s00466-020-01942-x.

[31] A. Khodadadian, N. Noii, M. Parvizi, M. Abbaszadeh, T. Wick, C. Heitzinger, A Bayesian estimation method for variational phase-field fracture problems, Comput. Mech. 66 (2020) 827–849, http://dx.doi.org/10.1007/s00466-020-01876-4.

[32] B. Sudret, S. Marelli, J. Wiart, Surrogate models for uncertainty quantification: An overview, in: 2017 11th European Conference on Antennas and Propagation, EUCAP, 2017, pp. 793–797, http://dx.doi.org/10.23919/EuCAP.2017.7928679.

[33] Y. Li, N. Friedman, P. Teatini, A. Benczur, S. Ye, L. Zhu, C. Zoccarato, Sensitivity analysis of factors controlling earth fissures due to excessive groundwater pumping, in: Stoch Environ Res Risk Assess, vol. 36, 2022, pp. 3911–3928, http://dx.doi.org/10.1007/s00477-022-02237-8.

[34] A. Stanić, B. Brank, A. Ibrahimbegovic, H. Matthies, Crack propagation simulation without crack tracking algorithm: Embedded discontinuity formulation with incompatible modes, Comput. Methods Appl. Mech. Engrg. 386 (2021) 114090, http://dx.doi.org/10.1016/j.cma.2021.114090.

[35] A. Stanić, B. Brank, D. Brancherie, Fracture of quasi-brittle solids by continuum and discrete-crack damage models and embedded discontinuity formulation, Eng. Fract. Mech. 227 (2020) 106924, http://dx.doi.org/10.1016/j.engfracmech.2020.106924.

[36] G. Pijaudier-Cabot, Z. Bazant, Nonlocal damage theory, J. Eng. Mech.-ASCE - J ENG MECH-ASCE 113 (1987) http://dx.doi.org/10.1061/(ASCE)0733-9399(1987)113:10(1512).

[37] A. Lye, A. Cicirello, E. Patelli, Sampling methods for solving Bayesian model updating problems: A tutorial, Mech. Syst. Signal Process. 159 (2021) 107760, http://dx.doi.org/10.1016/j.ymssp.2021.107760.

[38] B. Kurent, N. Friedman, W.K. Ao, B. Brank, Bayesian updating of tall timber building model using modal data, Eng. Struct. 266 (2022) 114570, http://dx.doi.org/10.1016/j.engstruct.2022.114570.

[39] N. Noii, A. Khodadadian, T. Wick, Bayesian inversion for anisotropic hydraulic phase-field fracture, Comput. Methods Appl. Mech. Engrg. 386 (2021) 114118, http://dx.doi.org/10.1016/j.cma.2021.114118.

[40] Y. Huang, C. Shao, B. Wu, J.L. Beck, H. Li, State-of-the-art review on Bayesian inference in structural system identification and damage assessment, Adv. Struct. Eng. 22 (2019) 1329–1351, http://dx.doi.org/10.1177/1369433218811540.

[41] D. Xiu, Numerical Methods for Stochastic Computations: A Spectral Method Approach, Princeton University Press, 2010, http://dx.doi.org/10.2307/j.ctv7h0skv.

[42] F. Marsili, N. Friedman, P. Croce, P. Formichi, F. Landi, On Bayesian identification methods for the analysis of existing structures, 2016, pp. 116–123, http://dx.doi.org/10.2749/stockholm.2016.0116.

[43] I. Goodfellow, Y. Bengio, A. Courville, Deep Learning, MIT Press, 2016.

[44] M.K. Ramancha, M.A. Vega, J.P. Conte, M.D. Todd, Z. Hu, Bayesian model updating with finite element vs surrogate models: Application to a miter gate structural system, Eng. Struct. 272 (2022) 114901, http://dx.doi.org/10.1016/j.engstruct.2022.114901.

[45] P.F. Shustin, S. Ubaru, V. Kalantzis, L. Horesh, H. Avron, PCENet: High dimensional surrogate modeling for learning uncertainty, 2022, http://dx.doi.org/10.48550/arXiv.2202.05063, ArXiv.

[46] C. Soize, R. Ghanem, Physical systems with random uncertainties: Chaos representations with arbitrary probability measure, SIAM J. Sci. Comput. 26 (2004) 395–410, http://dx.doi.org/10.1137/S1064827503424505.

[47] N. Sanzida, Z.K. Nagy, Polynomial chaos expansion (PCE) based surrogate modeling and optimization for batch crystallization processes, in: 24th European Symposium on Computer Aided Process Engineering, vol. 33, Elsevier, 2014, pp. 565–570, http://dx.doi.org/10.1016/B978-0-444-63456-6.50095-8.

[48] C.M. Bishop, Neural Networks for Pattern Recognition, Oxford University Press, 1995.

[49] M. Papadrakakis, N.D. Lagaros, Reliability-based structural optimization using neural networks and Monte Carlo simulation, Comput. Methods Appl. Mech. Engrg. 191 (2002) 3491–3507, http://dx.doi.org/10.1016/S0045-7825(02)00287-6.

[50] G.E. Hinton, A practical guide to training restricted Boltzmann machines, in: Neural Networks: Tricks of the Trade, second ed., Springer, 2012, pp. 599–619, http://dx.doi.org/10.1007/978-3-642-35289-8_32.

[51] E. Janouchová, A. Kučerová, Competitive comparison of optimal designs of experiments for sampling-based sensitivity analysis, Comput. Struct. 124 (2013) 47–60, http://dx.doi.org/10.1016/j.compstruc.2013.04.009.

[52] A. Saltelli, Making best use of model evaluations to compute sensitivity indices, Comput. Phys. Comm. 145 (2002) 280–297, http://dx.doi.org/10.1016/S0010-4655(02)00280-1.

[53] A. Saltelli, P. Annoni, I. Azzini, F. Campolongo, M. Ratto, S. Tarantola, Variance based sensitivity analysis of model output. Design and estimator for the total sensitivity index, Comput. Phys. Comm. 181 (2010) 259–270, http://dx.doi.org/10.1016/j.cpc.2009.09.018.

[54] I. Sobol, Global sensitivity indices for nonlinear mathematical models and their Monte Carlo estimates, Math. Comput. Simulation 55 (2001) 271–280, http://dx.doi.org/10.1016/S0378-4754(00)00270-6.

[55] R.D. Taylor, FEAP - Finite Element Analysis Program, http://projects.ce.berkeley.edu/feap/.

[56] J. Dujc, B. Brank, A. Ibrahimbegovic, Quadrilateral finite element with embedded strong discontinuity for failure analysis of solids, Comput. Model. Eng. Sci. 69 (2010) 223–260, http://dx.doi.org/10.3970/cmes.2010.069.223.

[57] E. Zander, A Matlab/Octave toolbox for stochastic Galerkin methods, https://ezander.github.io/sglib/.

C. Investigating Bayesian Parameter Identification Using Non-Standard Laboratory Specimens - Paper III

Article

Investigating Bayesian Parameter Identification Using Non-Standard Laboratory Specimens

Matej Šodan [1] **, Vladimir Divić** [1] **, Noémi Friedman** [2] **and Mijo Nikolić** [1,*]

[1] Faculty of Civil Engineering, Architecture and Geodesy, University of Split, Matice Hrvatske 15, 21000 Split, Croatia; msodan@gradst.hr (M.Š.); vdivic@gradst.hr (V.D.)
[2] HUN-REN Institute for Computer Science and Control (SZTAKI), Kende u.13-17, 1111 Budapest, Hungary; n.friedman@ilab.sztaki.hu
[*] Correspondence: mijo.nikolic@gradst.hr

Abstract: This work investigates the applicability of Bayesian inverse analysis for identifying parameters from non-standard aluminum specimens with notches that induce stress concentrations. Unlike conventional standardized specimens, the notched samples used in this work are typically unsuitable for direct parameter extraction due to geometric irregularities and size effects. The experimental procedure involved tensile tests conducted using a universal testing machine, with deformation data collected via LVDT sensors and optical measurements with digital image correlation. The numerical simulations were performed using a quadrilateral finite element model with embedded strong discontinuities to capture the complete material response, including elastic, plastic, and fracture behavior. The proposed identification procedure successfully provided reliable posterior parameter estimates on aluminum rectangular and single-notch specimens. Furthermore, the identified parameters were validated on a double-notch specimen made of the same material. The results highlight the importance of parameter interpretation and show that the Bayesian framework can reliably identify key material and model-dependent parameters from non-standard specimens while accounting for uncertainty in both measurements and model formulation.

Keywords: Bayesian identification; embedded strong discontinuity; laboratory measurements; material parameters; material failure; non-standard specimen

1. Introduction

Numerical models are essential tools in engineering for analyzing complex physical processes, including both linear and nonlinear material behaviors [1]. While they are traditionally used to simulate the performance of future structures and systems, their application also extends to advanced tasks, such as reliability assessment [2], remaining useful life (RUL) prediction [3,4], and system-level optimization [5] for existing structures. The predictive performance of these models depends on how accurately they represent the underlying physical phenomena, which is influenced by the selected approximations and parameter choices [6,7]. In particular, material behavior, governed by constitutive laws, is sensitive to these input parameters, which play a critical role in analyzing the underlying physical processes [8]. These parameters are typically determined through experimental testing, which includes both standardized and non-standardized procedures. While standardized tests provide baseline values suitable for general use, non-standard tests are often required to investigate localized phenomena and nonlinear behavior. However, the parameters obtained from such tests are highly sensitive to size effect and specimen

geometry, which can complicate the interpretation and limit the general applicability of the derived parameters.

This work focuses on the identification of input parameters that govern the elastic, plastic hardening, and failure behavior of aluminum alloy specimens. Some parameters may reflect intrinsic material properties, while others may be model-dependent, relying on the specific type of model. To identify these parameters, this work goes beyond standardized laboratory tests by examining non-standard tests using notched specimens, which introduce stress concentrations and weaken the material. To extract these parameters from non-standard tests, a Bayesian inverse procedure [6,9] is applied with an embedded strong discontinuity Q6ED model [10,11] on laboratory samples tested until failure. Furthermore, the study demonstrates the capability of Bayesian identification to derive material parameters from experimental tests not originally intended for their targeted calibration, or when it is not possible to test ideal specimens.

The process of determining parameter values to align model predictions with experimental measurements of a particular problem is known as parameter identification or model calibration [6,8], which aims to find parameters independent of sample size, geometry, and boundary conditions to ensure the applicability of the model to a wide range of engineering problems [8]. A traditional approach to parameter identification relies on standardized tests and direct laboratory measurements that are related to specific parameters. In the context of material failure, different tests are recommended to determine the necessary material parameters. For example, uniaxial tension and splitting tests are commonly used to determine material strength, while three and four-point notched bending tests are employed to evaluate fracture energy [12]. However, beyond the dependence on the test design, several challenges arise from this approach [12,13]. As numerical models are increasingly complex with a range of parameters, finding the proper measurements becomes challenging. Even when such measurements exist, the sheer volume of collected data can influence the results. For example, in [14], it was shown that fracture energy values depend on the timing of test termination. Additionally, the obtained results can also be affected by the nonlinear processes occurring within the material during testing. Stress concentrations caused by notches, holes and imperfections can lead to inaccuracies and the general applicability can thus be influenced by the size and shape of these notches [15,16]. Finally, the existence of various uncertainties, such as measurement and numerical model errors cannot be incorporated into the direct laboratory identification process which leads to unreliable parameter identification.

The limitations of relating parameters to direct laboratory measurements can be overcome by solving an inverse problem, where numerical model predictions are compared to experimental measurements to identify the optimal set of model parameters. There are two distinct frameworks for solving the inverse problem: deterministic and probabilistic [16,17]. Deterministic approaches, also known as optimization techniques, rely on defining a loss function that quantifies the discrepancy between the numerical output of the model and the experimental measurements. The parameter set that minimizes the loss function is considered the "best" estimate and is assumed to approximate the true values [8,9,18]. This approach is effective when experimental data are highly informative and the inverse problem is well-posed. However, in more complex settings, especially those involving nonlinearity, deterministic methods have important limitations. They do not account for uncertainties in the identification process, such as measurement inaccuracies and modeling errors. Furthermore, due to the ill-posed nature of many inverse problems, multiple parameter sets may yield similarly low loss values, leading to non-unique solutions. To address this issue, additional constraints or regularization techniques are typically employed to ensure a stable and well-posed solution [9,19]. An example of such a parameter identification

procedure with nonstandard metallic specimens by instrumented indentation and small punch can be found in [20–22].

Probabilistic approaches, on the other hand, represent parameters through probability distributions. This approach ensures that the inverse problem is well defined. A widely used probabilistic method is the Bayesian inverse method (Bayesian inference) [9], which is based on Bayes's theorem of conditional probability. Here, the unknown parameters are treated as random variables, described by a prior distribution based on existing knowledge or experience. The prior distributions are then updated using experimental measurements from a specimen or structure. Notably, the required parameters do not need to be directly measured. Instead, the combinations of simpler measurements can be used to indirectly provide valuable information for parameter estimation. This enables the incorporation of a broader range of experimental data into the identification process. The end result of the identification is the posterior distributions that reflect the updated parameter estimates. The key strength of this approach lies in the ability to account for uncertainties by treating the discrepancy between numerical model predictions and experimental measurements as a variable within the error model. The error model is defined by accounting measurement and modeling errors. By directly incorporating these uncertainties into the identification process, the Bayesian approach provides a more comprehensive and realistic estimation of model parameters [9,23–25]. Solving the inverse problem of parameter identification across the full range of material behavior, from the elastic and plastic phases to complete failure, requires advanced nonlinear numerical models and methods. Several approaches have been developed for this purpose, including the Extended Finite Element Method (X-FEM) [26,27], the Embedded Strong Discontinuity Finite Element Method (ED-FEM) [11,28,29], the Phase-Field Method [30,31], the Lattice Element Method [32–35] and cohesive zone models [36].

Various applications of Bayesian parameter identification can be found in the literature. Namely, the combined isotropic/kinematic hardening model was calibrated based on the cyclic response of cantilever steel specimens, employing a Gaussian process model [37]. In [38], hierarchical Bayesian identification was performed to identify the elastic parameters of the spring mass model in the dynamic test using acceleration measurements. Ultrasonic experiments were performed on a large aluminum plate containing a hole, where a semi-analytical numerical model in conjunction with the MCMC method was used to estimate transmission coefficients [39]. The Bayesian method was also applied to full-scale structures, such as a seven-story cross-laminated timber building [23], where gPCE and MCMC methods together with results of a vibration tests were used to identify elastic constants. Similarly, in [40], the elastic parameters of cultural heritage buildings were identified using a simplified finite element model, MCMC methods, and ambient vibration measurements. Furthermore, the elastic parameters of the concrete dams have been identified through gPCE and MCMC methods and by monitoring displacement data [41]. A hierarchical Bayesian approach combined with ambient vibration tests and gPCE was used in another dam study [42]. In [18], the goal was to identify mechanical model parameters based on existing damage patterns using the Bayesian inference method and a Gaussian process model.

Several studies have also focused on the identification of fracture parameters. For instance, the elastic and strength parameters for FEM model of concrete tram poles were determined in [17] using a Kriging proxy model, MCMC, and vibration testing on pole specimens. In [43], the fracture properties of concrete and steel-concrete bond parameters were investigated using ED-FEM and X-FEM models, based on tensile tests on concrete beams. Here, gPCE and Kalman filtering were used alongside displacement measurements and cyclic fracture energy tests for parameter identification. Additionally, in [44], the parameters of a lattice model for mortar prisms reinforced with carbon fiber polymer

plates were identified by double shear test, using gPCE and Kalman filtering with Digital Image Correlation (DIC) measurements. In [45], the focus was on identifying parameters of lattice models, specifically the mechanical properties of mortar and concrete, through unconfined compression cube tests and notched three-point bending tests by applying gPCE, MCMC, and Crack Mouth Opening Displacement (CMOD) measurements. The study presented in [46] focused on fracture parameters, such as strength and toughness in a phase-field model for elastic solids and brittle cement mortar, utilizing notched three-point bending tests with sequential updating, gPCE, and MCMC methods. Finally, the study presented in [47] addressed the identification of phase-field model parameters for metals through both synthetic and experimental measurements. For the experimental part, load-displacement measurements from I-shaped Al-5005 and Sandia Al-5052 specimens were used in combination with MCMC-based methods.

Despite the progress made in identifying fracture parameters, these studies reveal some common challenges. Parameters associated with the later stages of failure tend to yield more uncertain results. Furthermore, the applicability of the identified parameters across different specimen geometries and stress states is not generally investigated.

This study applies a Bayesian identification methodology to full-stage parameter identification in the mechanical testing of non-standard aluminum 6060 alloy specimens, covering the entire material response from elastic and plastic deformation to fracture and complete failure. The methodology uses the embedded discontinuity model (Q6ED) with general polynomial chaos expansion (gPCE) as a proxy model. The Q6ED model is capable of representing material plasticity with isotropic hardening and simulating crack initiation and propagation. Cracks are introduced within the elements as discontinuity lines (displacement jumps) with independent location and orientation, ensuring that the computed fracture energy dissipation remains independent of element size. A novelty lies in the combination of these methods applied to non-standard and unsuitable specimens for direct parameter extraction, as they do not represent standardized testing protocols. Three different specimen geometries were tested to evaluate the general applicability of the identified parameters regardless of geometry, shape, or stress conditions, assuming the material remains the same. Specifically, elastic parameters were identified from rectangular specimens, plastic and fracture parameters from notched dogbone specimens, and the full parameter set was verified using a double−notched specimen. This process allows not only the identification of uncertain parameters but also their validation across different geometries and stress states. For parameter identification, all specimens were subjected to uniaxial tensile testing with simple laboratory measurements from LVDT sensors, complemented by an optical measurement system.

The structure of this paper is as follows. Section 2 describes the numerical model used for simulating material failure. Section 3 provides an overview of the Bayesian inverse method. Section 4 details the test design process and experimental setup. Section 5 presents the parameter identification results, while Section 6 gives conclusions.

2. Modeling of Fracture Propagation

As material is subjected to loading, stress level increases, which leads to the formation of stress concentrations. These concentrations typically occur in areas of imperfections, such as pores, inclusions, pre-existing damages, as well as around geometric features like holes, notches, and corners. First, the material exhibits plastic hardening. Furthermore, as the stress increases, microcrack initiation starts leading to macrocrack formation.

This work provides the simulation of fracture propagation mechanisms with a 2D solid quadrilateral finite element enhanced with incompatible modes method and the embedded strong discontinuity, known as Q6ED [10,11]. The incompatible modes method

enriches the displacement field of the finite element with additional quadratic terms, which has a beneficial influence on the accuracy of the model [1,10]. The embedded strong discontinuity method is used to simulate crack initiation and propagation processes. This section provides a brief overview of the model's formulation, together with the crack nucleation criteria and used constitutive laws. Further formulation and implementation details of the model can be found in the following works [11].

2.1. Q6ED Model with the Embedded Strong Discontinuity

During the simulation of material failure, each finite element in the Q6ED model consists of two parts: the bulk material and a crack. Initially, as long as the stress within a finite element remains below the defined material strength, the entire element behaves as bulk material, which is first modeled using a linear elastic law, followed by an elastoplastic isotropic hardening model. However, when the stress exceeds the defined material strength of a given element, a crack followed by material softening is introduced.

The crack embedding follows the statically and kinematically optimal nonsymmetric formulation (SKON) formulation of the embedded strong discontinuity method [48], which has demonstrated effectiveness in capturing complex fracture behaviors in materials [10]. In this approach, the crack inside each finite element is represented by a local jump in the displacement field over the defined crack line. This approach ensures that the results remain independent of the finite element size. Figure 1 illustrates the Q6ED finite element, which is capable of simulating the constant separation of material during cracking in both Mode I and Mode II. The separation of the material is controlled by softening parameters α_i (α_1 and α_2).
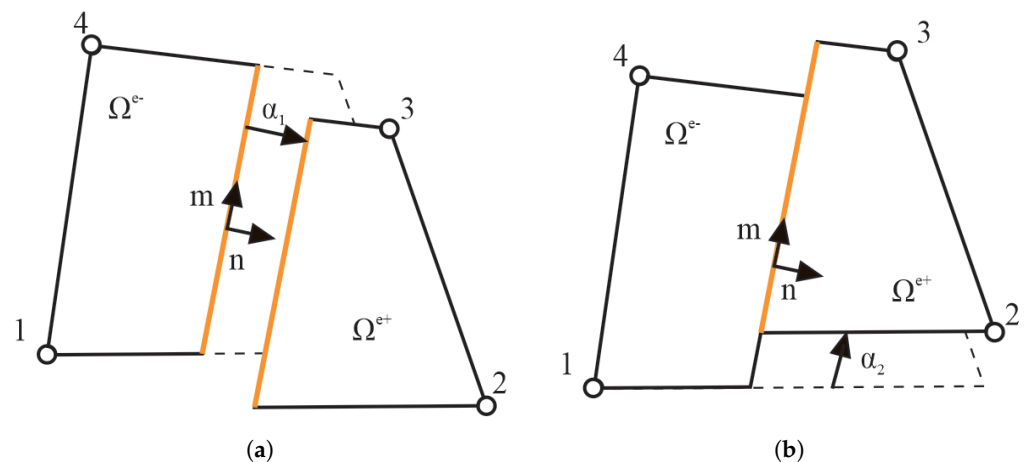

Figure 1. Q6ED element separation modes: (**a**) Tensile opening (**b**) Shear sliding.

As the crack is formed and keeps opening, the phenomenon of energy dissipation occurs. This phenomenon is defined by the exponential softening law and its internal variables ξ_n and ξ_m. The values of the variables indicate the level of element degradation for both separation modes.

2.2. Kinematics

The quadrilateral finite element formulation is enhanced by incompatible modes and embedded discontinuities methods. The resulting displacement field is defined as follows:

$$\mathbf{u}(\boldsymbol{\xi}, \Gamma^e) = \sum_{a=1}^{4} \mathbf{N}_a(\boldsymbol{\xi})\mathbf{d}_a + \sum_{b=1}^{2} \mathbf{M}_b(\boldsymbol{\xi})\boldsymbol{\rho}_b + \sum_{i=1}^{2} \mathbf{p}_i(\boldsymbol{\xi}, \Gamma^e)\boldsymbol{\alpha}_i. \tag{1}$$

The first term represents the standard finite element part, where N_a bilinear Lagrange interpolation functions and $\mathbf{d}_a$ are nodal displacement values. The second term introduces enhancements through the incompatible mode method, defined through the $M_1 = 1 - \xi^2$ and $M_2 = 1 - \eta^2$ shape functions and corresponding incompatible mode parameters $\boldsymbol{\rho}_b$. The last term accounts for embedded discontinuities, where $\mathbf{p}_i$ are discontinuity shape functions which are defined by assuming that during the fracture, Ω^{e-} part of the element remains still while the counterpart Ω^{e+} moves (see Figure 1):

$$\mathbf{p}_1 = \left(H_\Gamma(\mathbf{x}) \sum_{a \in \Omega^{e+}} N_a \right) \mathbf{n} \qquad \mathbf{p}_2 = \left(H_\Gamma(\mathbf{x}) - \sum_{a \in \Omega^{e+}} N_a \right) \mathbf{m}. \tag{2}$$

The unit normal and tangent vectors to the crack Γ^e from Equation (2) are represented by $\mathbf{n} = [n_x, n_y]^T$ and $\mathbf{m} = [m_x, m_y]^T = [-n_y, n_x]^T$. The function H_Γ represents the Heaviside step function, which introduces a displacement jump across the crack for $\mathbf{x} \in \Omega^{e+}$.

2.3. Crack Nucleation

The nucleation of cracks within each Q6ED element is governed by the stress state at the element's four integration points, which determine both the crack's location and orientation. The procedure, first introduced by [10], consists of two key processes: the fracture initiation and the definition of crack position and orientation.

Fracture initiation is regulated using the Rankine criterion, which assumes that a crack forms when the maximum principal stress exceeds the material's tensile strength. At each simulation timestep, all uncracked finite elements are evaluated using this criterion. First, the principal stress values $\sigma_{p1,p2}^{e,i}$ at the four integration points are computed. The maximum principal stress at each integration point is determined by $\sigma_p^{e,i} = \max[\sigma_{p1}^{e,i}, \sigma_{p2}^{e,i}]$. The highest value among these is selected $\sigma_p^e = \max_{i=1,\ldots,4} \sigma_p^{e,i}$. This value is then compared with the tensile strength of the material σ_n. If σ_p^e exceeds this value, the element fractures, and a crack within the element is initiated.

Once a crack is initiated, its position and orientation need to be defined. The integration points where σ_p^e reaches its maximum value (within a tolerance) are collected in the set: $B^e = id \in {1, 2, 3, 4} : \sigma_p^{e,id} = \sigma_p^e$. The geometric center of the crack is obtained by averaging the global coordinates of the points in B^e:

$$\mathbf{x}_{ED}^e = \frac{1}{N_{B^e}} \sum_{i \in B^e} \mathbf{x}^{e,i}, \tag{3}$$

where N_{B^e} is the number of contributing points, and $\mathbf{x}^{e,i}$ are their global coordinates. The average stress at points B^e is calculated as follows:

$$\sigma_{ED}^e = \frac{1}{N_{B^e}} \sum_{i \in B^e} \sigma^{e,i}, \tag{4}$$

where $\sigma^{e,i}$ are the stress values of each contributing point. The crack orientation angle α_{ED}^e is then derived from these averaged stress values:

$$\alpha_{ED}^e = \frac{1}{2} \arctan \left(\frac{2\sigma_{xyED}^e}{\sigma_{xxED}^e - \sigma_{yyED}^e} \right). \tag{5}$$

With the calculated position $\mathbf{x}_{ED}^e$ and orientation α_{ED}^e, embedding the crack is straightforward (see Figure 2). The crack normal, represented by the angle α_{ED}^e, aligns with the vector $\mathbf{n}$, while the tangential vector $\mathbf{m}$ is perpendicular to it. Once defined, the crack's

geometry remains fixed throughout the simulation, with only the separation parameters (α_1, α_2) evolving over time. Each finite element can have only one crack, but multiple cracks can emerge across the mesh during each timestep.
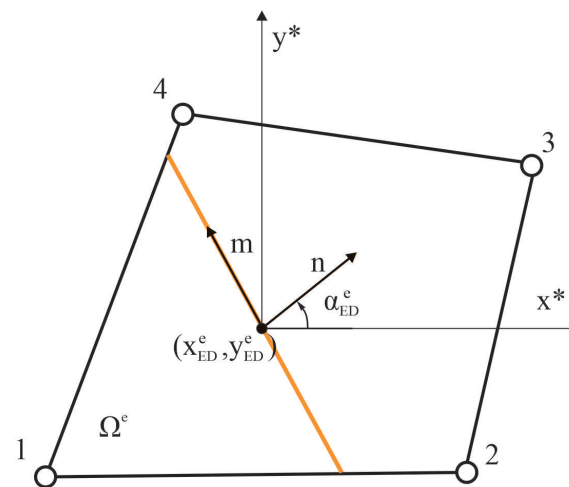

Figure 2. Quadrilateral finite element with an embedded crack line, defined by point $\mathbf{x}^e_{ED}$ and angle α^e_{ED}. Symbol * represents the local coordinate system.

2.4. Constitutive Law

The material initially deforms elastically, following the principles of Hooke's law. The linear elastic behavior is applied to the bulk region of the element, where the stress is defined as $\sigma = C\bar{\epsilon}$. Here, C represents the constitutive matrix, determined by Young's modulus E and Poisson's ratio ν, while $\bar{\epsilon}$ denotes the strain in the bulk material.

During the loading process, each finite element is evaluated for elastoplastic behavior with isotropic hardening. At every Gaussian integration point, the equivalent stress is calculated based on the von Mises yield criterion:

$$\sigma_{eq} = \sqrt{\sigma_{xx}^2 + \sigma_{yy}^2 - \sigma_{xx}\sigma_{yy} + 3\tau_{xy}^2}. \tag{6}$$

The corresponding yield function is defined as follows:

$$f = \sigma_{eq} - \left(\sigma_0 + H \cdot \varepsilon_p^*\right), \tag{7}$$

where σ_0 is the yield strength, H is the hardening modulus, and ε_p is the equivalent plastic strain for each Gauss integration point. If the yield function returns a positive value, elastoplastic isotropic hardening occurs at that integration point. The plastic strain is then updated using the radial return algorithm (see [1]), and the stress tensor is subsequently computed as follows: $\sigma = C(\bar{\epsilon} - \epsilon_p)$, where ϵ_p represents the plastic strain tensor.

As the stress continues to increase and surpasses the material strength, the first cracks begin to form. At this phase, the finite element is divided into the crack domain and the remaining bulk material. Crack behavior, including material degradation and energy dissipation, is governed by two uncoupled plasticity softening laws [1]. Each law corresponds to the separation modes, Mode I (opening) and Mode II (sliding), and is formulated within the framework of thermodynamics using Helmholtz free energy. These laws describe the dissipation of energy during the fracture process of material by irreversible accumulation of plastic deformations while preserving the stiffness of the material.

When the Rankine failure criterion is activated, the softening failure function $\bar{\bar{\phi}}$ controls the material degradation and evolution of internal variables. For tensile Mode I, it is defined as follows:

$$\bar{\bar{\phi}}_n(t_1, \bar{\bar{q}}_n) = t_1 - (\sigma_n - \bar{\bar{q}}_n) \leq 0, \tag{8}$$

where t_1 is the normal traction value on the crack line and σ_n is the material tensile strength. The variable $\bar{\bar{q}}_n$ represents the softening traction value:

$$\bar{\bar{q}}_n = \frac{\partial \bar{\bar{\Psi}}_n}{\partial \bar{\bar{\xi}}_n} = \sigma_n \left(1 - \exp\left[-\frac{\sigma_n}{G_{fn}} \bar{\bar{\xi}}_n \right] \right), \tag{9}$$

where G_{fn} is the Mode I material fracture energy and $\bar{\bar{\xi}}_n$ is the internal softening variable.

For shear Mode II, Equation (9) remains valid, with the notation changed from n to m to represent Mode II parameters. The failure function for shear Mode II is formulated as follows:

$$\bar{\bar{\phi}}_m(t_2, \bar{\bar{q}}_m) = |t_2| - (\sigma_m - \bar{\bar{q}}_m) \leq 0. \tag{10}$$

Here, t_2 represents the tangential traction on the crack line, and its absolute value is related to the potential for the crack to slide in both directions.

With the constitutive laws defined, the entire fracture process of the material in the Q6ED model is determined by the previously introduced elastic, elastoplastic and fracture model parameters. Since this paper deals with only tensile fracture of the material, shear fracture parameters are neglected. So, uncertain parameters subjected to the identification procedure can be collected into a single vector **z**:

$$\mathbf{z} = \left[E, \nu, \sigma_0, H, \sigma_n, G_{fn} \right] \tag{11}$$

3. Bayesian Model Calibration

Material failure is a complex, nonlinear process governed by constitutive laws and their corresponding input parameters, which play a crucial role in simulations by influencing both crack initiation and propagation. Accurately determining these parameters is essential for achieving reliable simulation outcomes.

This work relies on minimizing the discrepancy between numerical model predictions and experimental observations by using simple measurements such as those shown in [49]. The relationship between the parameters **z** and measurable test behavior is expressed as follows:

$$\mathbf{u} = \mathcal{G}(\mathbf{z}) \quad \mathbf{u} \in \Re^Q. \tag{12}$$

Here, **u** represents the vector of measurable model outputs, and $\mathcal{G}$ denotes the numerical model operator, often referred to as the forward model, that predicts these measurements based on the values of model parameters **z**. The objective of identification is to determine the optimal values of **z** such that the model output **u** closely matches observed data. This leads to an inverse problem, where the forward model $\mathcal{G}$ must be inverted to estimate the unknown parameters accurately. This section provides a brief overview of probabilistic Bayesian inverse method used in this work, along with its accompanying methodology. For more details, refer to [49].

3.1. The Bayesian Inverse Method

The Bayesian inverse method is a robust and efficient probabilistic approach for identifying uncertain parameter values by solving the inverse problem. In this work, the

uncertain parameters are defined in Equation (11). These parameters are treated as random variables and are expressed in vector form as $\mathbf{z} : \Omega \to \mathbb{R}^n$

$$\mathbf{z}(\omega) := \Big[E(\omega), \nu(\omega), \sigma_0(\omega), H(\omega), \sigma_n(\omega), G_{fn}(\omega) \Big], \tag{13}$$

where ω represents one realization from the set of all possible realizations Ω. Each model parameter z_i within the vector $\mathbf{z}$ is described by its probability density function $\pi(z_i)$. Assuming that the input parameters are mutually independent, their joint probability function $\pi(\mathbf{z})$ can be expressed as [23,50]:

$$\pi(\mathbf{z}) = \pi(z_1, \ldots, z_{N_i}) = \prod_{i=1}^{N_i} \pi_i(z_i). \tag{14}$$

The term $\pi(\mathbf{z})$ is referred to as the prior distribution of the parameter values. The selection of the prior distribution is influenced by various factors, including prior experience, results from previous identification efforts, available measurement data, or even mere assumptions [23,50].

The solution of the numerical forward model, $\mathcal{G}$, with the "true" set of input parameters should ideally match the obtained measurements from the analyzed structure or specimen. However, in practice, this is not achievable due to inherent errors and imperfections in both the measurement and modeling processes, especially when dealing with nonlinear phenomena. Taking this into account, an obtained measurement $\mathbf{d}_m$ can be expressed as a realization of a random variable [23,50]:

$$\mathbf{d}_m(\omega_e) = \mathbf{u}_{\text{true}} + \boldsymbol{\epsilon}(\omega_e) = \mathcal{G}(\mathbf{z}_{\text{true}}) + \boldsymbol{\epsilon}(\omega_e). \tag{15}$$

Here, $\mathbf{u}_{\text{true}}$ represents the measurable variable predicted by using the "true" parameter values $\mathbf{z}_{\text{true}}$, while $\boldsymbol{\epsilon}$ accounts for the the combined errors in the measurement and the modeling, depending on the specific realization ω_e. These errors are described by their probability density function π_ϵ. It is further assumed that the realizations of the errors $\boldsymbol{\epsilon}$ are independent of the realizations of the uncertain input parameters $\mathbf{z}$, ensuring that the random variables $\mathbf{z}$ and $\boldsymbol{\epsilon}$ are independent. Accurately defining the error distribution is a crucial step in the identification process. This work considers three types of additive errors: measurement errors, numerical model errors, and proxy modeling errors

$$\boldsymbol{\epsilon} = \boldsymbol{\epsilon}_{\text{meas}} + \boldsymbol{\epsilon}_{\text{model}} + \boldsymbol{\epsilon}_{\text{proxy}}, \tag{16}$$

where the last term, $\boldsymbol{\epsilon}_{\text{proxy}}$, arises when the computationally expensive numerical simulation is replaced by a proxy model. These three error components are assumed to be mutually independent.

The measurement error $\boldsymbol{\epsilon}_{\text{meas}}$ is often assumed to follow a normal distribution, $\boldsymbol{\epsilon}_{\text{meas}} \sim \mathcal{N}(\mathbf{0}, \mathbf{C}_{\text{meas}})$, centered around the experimental measurements. This assumption is justified by the use of standardized calibration and testing procedures, which ensure consistent and reliable measurement performance. The covariance matrix $\mathbf{C}_{\text{meas}}$ is taken as diagonal, assuming independent error components. The diagonal entries σ_i^2 are defined based on the manufacturer's specifications of the measurement device, which may be expressed as a percentage of the measured values. This percentage typically reflects the maximum possible error, which is here interpreted as a $3\sigma_i$ deviation under the normal distribution assumption. Consequently, the standard deviation σ_i of the measurement error is calculated by dividing the maximum error by three.

In contrast, modeling and proxy errors are inherently more complex. They may exhibit correlation, systematic bias, or non-Gaussian behavior, especially near crack initiation. If not properly addressed, such simplifications can lead to underestimated uncertainties and biased parameter estimates, even if the model fits the experimental data. Various strategies exist to handle numerical model errors. One approach is to treat the associated covariance matrix as an additional unknown within the identification process [25]. Alternatively, it can be estimated separately as a deterministic, input-dependent function, based on the constitutive laws employed and comparisons between model predictions and experimental data. To avoid the risk of incorporating incorrectly estimated bias and correlations, a simple analysis was conducted comparing model predictions with experimental results for non-linear data. This revealed that modeling error exhibited noticeable bias only in the later stages of testing, where increased uncertainty was already anticipated. In contrast, proxy model errors were generally small and only weakly correlated, with a negligible impact on the later parts of the response. Based on these findings, we adopt the simplifying assumption that these error components are also zero-mean, mutually independent, and Gaussian. This is considered a pragmatic compromise in the absence of reliable bias quantification. Thus, the modeling errors $\epsilon_{\mathrm{model}}$ were modeled as heteroscedastic measurement noise, where the variance is an input-dependent function of the chosen quantities. For the proxy modeling error $\epsilon_{\mathrm{proxy}}$, the standard deviation is estimated from the variance of proxy errors evaluated on an independent validation dataset, i.e., input–output pairs not used during proxy model training.

The main idea of the Bayesian method is to update the prior distribution of the parameters $\pi(\mathbf{z})$ using the obtained measurements $\mathbf{d}_m$ by applying Bayes' theorem of conditional probability [23,51,52]:

$$\pi(\mathbf{z}|\mathbf{d}_m) = \frac{\pi(\mathbf{d}_m|\mathbf{z})\pi(\mathbf{z})}{\pi(\mathbf{d}_m)}. \tag{17}$$

Here, $\pi(\mathbf{d}_m|\mathbf{z})$ represents the likelihood function, which quantifies the probability of obtaining the measurement $\mathbf{d}_m$ given a specific set of parameter values $\mathbf{z}$. This likelihood function is defined by the probability that the error ϵ equals $\mathbf{d}_m - \mathbf{u}$ [23], where $\mathbf{u}$ is computed from the forward operator $\mathbf{u} = \mathcal{G}(\mathbf{z})$.

The term $\pi(\mathbf{d}_m)$ is referred to as the evidence function. It serves as a normalization constant in Bayes' theorem, ensuring that the posterior distribution $\pi(\mathbf{z}|\mathbf{d}_m)$ integrates to 1.

The expression $\pi(\mathbf{z}|\mathbf{d}_m)$ represents the posterior distribution of the parameter values $\mathbf{z}$. This distribution is the final result of the Bayesian inverse procedure, representing the updated understanding of the parameter values based on the used measurements $\mathbf{d}_m$.

A common challenge with the Bayesian inverse method is that, in most cases, the posterior distribution cannot be formulated explicitly. To address this, various mathematical techniques, such as sampling methods, have been developed to approximate its shape.

Sampling methods generate samples that approximate a stationary distribution matching the desired posterior distribution. In this work, the Markov Chain Monte Carlo (MCMC) method, based on the Metropolis–Hastings algorithm, is chosen as a robust, simple, and model-independent technique [19,50,51,53,54]. This method employs a random walk approach to efficiently generate samples from the posterior distribution.

However, when the posterior distribution exhibits a complex shape, the effective application of the MCMC method requires evaluating hundreds or even thousands of proposed parameter candidates. The most computationally intensive part of this process is constructing the likelihood function, which involves computing the forward model solutions $\mathcal{G}(\mathbf{z})$ for each candidate parameter. For complex numerical models, such as

models to simulate fracture processes, this represents a significant computational burden. To mitigate this, mathematical proxy models are often employed.

3.2. General Polynomial Chaos Expansion (gPCE) Proxy Model

Performing multiple fracture simulations often requires extensive computational efforts, which can be both time and resource-consuming. These can make solving the Bayesian inverse problem using the MCMC method excessively slow or even impossible. To address this issue, mathematical proxy models are necessary. These models, also known as surrogate, meta, or response surface models, provide approximate results of numerical simulations with a certain degree of precision, thereby significantly accelerating the computational process [51,55,56]:

$$\mathcal{G}(\mathbf{z}) \approx \tilde{\mathcal{G}}(\mathbf{z}). \tag{18}$$

Here, $\tilde{\mathcal{G}}(\mathbf{z})$ represents the proxy model's approximation of the forward model operator $\mathcal{G}$.

The choice of proxy model must be made carefully, taking into account the characteristics of the analyzed problem. The study [49] compares the accuracy of various proxy models used to approximate numerical simulation results in crack propagation problems. With respect to performance, for simpler fracture propagation cases, the gPCE model demonstrated accuracy comparable to other approaches, such as neural networks, and was effective in achieving precise parameter identification. From a practical standpoint, the gPCE model is well-regarded for its computational efficiency and ease of training. Additionally, a sufficiently accurate gPCE model provides an analytical representation of the numerical model's output, enabling efficient statistical analysis with minimal computational cost. Based on these considerations, the gPCE proxy model is selected. However, it is important to note that for more complex fracture problems, gPCE may not be the most suitable proxy model, as highlighted in the same study.

The gPCE method approximates numerical model solutions through a linear combination of multidimensional polynomials and their corresponding coefficients [53,57,58], as expressed by the following:

$$\mathbf{u} = \mathcal{G}(\mathbf{z}) \approx \tilde{\mathcal{G}}(\mathbf{z}) = \tilde{\mathbf{u}} = \sum_{k=0}^{K-1} \boldsymbol{\nu}_k \Phi_k(\mathbf{z}) = \mathbf{Y}\boldsymbol{\Phi}(\mathbf{z}), \tag{19}$$

where $\tilde{\mathbf{u}}$ represents the approximation of the numerical model's output, $\boldsymbol{\Phi}$ is the selected set of polynomials collected in the vector $\boldsymbol{\Phi} = [\Phi_0(\mathbf{z}), \Phi_1(\mathbf{z}), \ldots, \Phi_{K-1}(\mathbf{z})]^T$, and $\mathbf{Y} = [\boldsymbol{\nu}_0, \boldsymbol{\nu}_1, \ldots, \boldsymbol{\nu}_{K-1}]$ denotes the coefficients of the polynomial expansion, where $\boldsymbol{\nu}_k \in \mathbb{R}^Q$ corresponds to the polynomial Φ_k.

To accurately approximate the forward model, a polynomial basis is first selected based on the prior distribution of the model parameters. The coefficients $\mathbf{Y}$ are then determined by solving a linear regression problem that minimizes the mean squared error (MSE) [53]:

$$\mathbb{E}[\tilde{\boldsymbol{\epsilon}}^2] = \mathbb{E}\left[(\mathbf{u} - \tilde{\mathbf{u}})^2\right] = \int_{\mathbb{R}} (\mathbf{u}(\mathbf{z}) - \tilde{\mathbf{u}}(\mathbf{z}))^2 \pi(\mathbf{z}) d\mathbf{z} \approx \frac{1}{N} \sum_{i=1}^{N} \left(\mathbf{u}(\mathbf{z}_i) - \tilde{\mathbf{u}}(\mathbf{z}_i)\right)^2. \tag{20}$$

One significant advantage of the gPCE method is its ability to compute sensitivities directly from its coefficients [59]. Sensitivity analysis plays an essential role in experimental design, helping to optimize sensor placement and identify the most informative measurable outputs [60]. In this study, we used Sobol Sensitivity Analysis, a method for evaluating the contribution of input variables (i.e., model parameters) to the variance in the model's output. This method decomposes the total variance in the output into partial variances, which can be calculated directly from the coefficients of the gPCE model. Partial variance

measures the extent to which the variability in the solutions $\boldsymbol{u}$ can be attributed to the changes in the values of one or more model parameters. Sobol indices represent this relative measure by the ratio of partial variance (caused by variations in a specific subset of model parameters) to the total variance (resulting from all model parameters) [49,61–63].

4. Test Design and Experimental Setup

The identification of parameters was performed for aluminum 6060 alloy specimens with unknown properties through the tensile loading tests. Three different specimen designs were selected for the experiments (see Figure 3).

Before conducting physical experiments, it is important to carry out a test design procedure to evaluate the effectiveness of the planned tests, specimen geometries, and measurement techniques for identifying the target parameters. This helps reduce the risk of test failure. As a part of this process, sensitivity analysis is used to gain insights into how strongly different parameters influence the planned measurements. In this study, Sobol sensitivity analysis was applied to quantify the effect of parameter variations on the simulated responses. To support this, virtual simulations were created to replicate the planned experiments. By examining how different combinations of parameter values affect the measured responses, the most informative measurements and configurations can be selected. Following the sensitivity analysis, the chosen measurements were applied in the laboratory in order to identify the uncertain parameters and to verify their results.
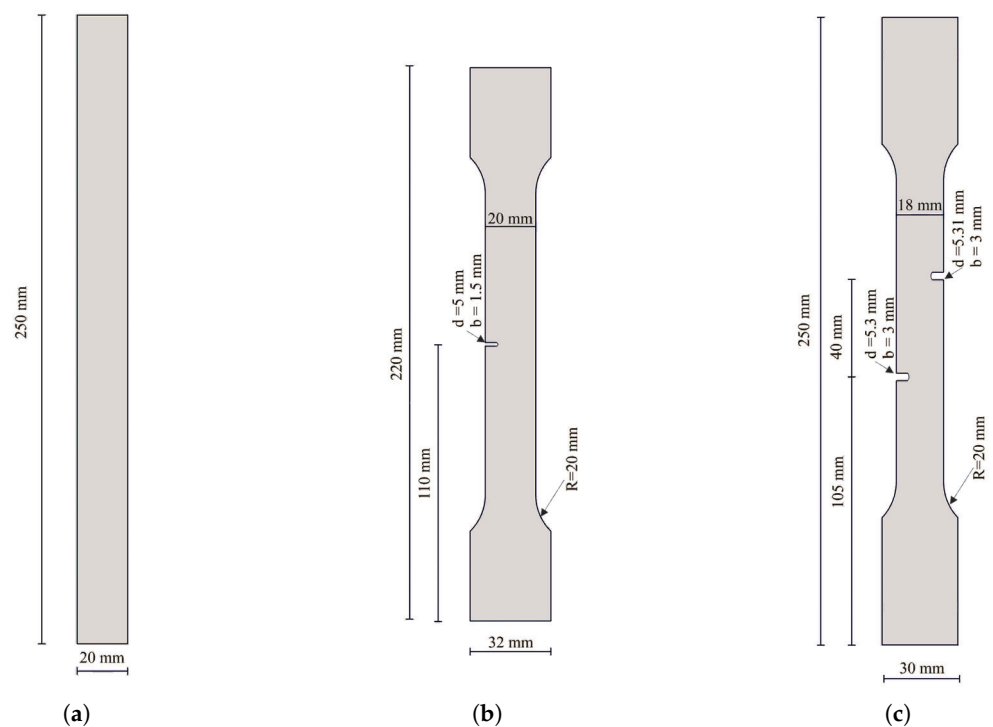

Figure 3. Aluminum alloy specimens: (**a**) Rectangular (**b**) Dogbone single−notched (**c**) Dogbone double−notched.

4.1. Test Design

The uncertain parameters of the aluminum alloy are treated as random variables, initially characterized by a uniform prior distribution $z_i \sim \mathcal{U}(a, b)$. This choice reflects a non-informative prior defined between the bounds given based on the best engineering judgment. These bounds are given in Table 1. The parameter identification process is conducted in two phases. In the first phase, the rectangular specimen (see Figure 3a) is used to identify the elastic parameters (E and ν). Although Young's modulus E and Poisson's

ratio ν are standard parameters in engineering, for stochastic computations, it is often more advantageous to work with the bulk modulus K and shear modulus G, as they directly correspond to the eigenvalues of the constitutive matrix. Ensuring the positivity of K and G automatically guarantees the positive definiteness of the constitutive matrix. Nevertheless, in this work, we use the parameter pair (E, ν), and enforce the positivity of K and G through appropriately bounded distributions of these parameters.

Table 1. Prior distributions for material parameters.

Parameter	Distribution	Left Bound (a)	Right Bound (b)
E	$U(a, b)$	$50,000 \, \text{N/mm}^2$	$100,000 \, \text{N/mm}^2$
ν	$U(a, b)$	0.2	0.4
σ_0	$U(a, b)$	$50 \, \text{N/mm}^2$	$150 \, \text{N/mm}^2$
H	$U(a, b)$	$2000 \, \text{N/mm}^2$	$6000 \, \text{N/mm}^2$
σ_n	$U(a, b)$	$150 \, \text{N/mm}^2$	$300 \, \text{N/mm}^2$
G_{fn}	$U(a, b)$	$100 \, \text{N/mm}$	$300 \, \text{N/mm}$

The proposed laboratory setup for parameter identification includes both force−displacement measurements and deformation measurements taken from the specimen's lateral surfaces. In the middle of the specimen, two points were selected on opposite sides of the lateral boundary, and the sum of their horizontal displacements is used as a measurement. To validate the feasibility of this approach prior to experimental testing, a Sobol sensitivity analysis was performed. A set of 200 parameter combinations from the prior distribution was generated using a Quasi-Monte Carlo (QMC) sampling technique, ensuring a well-distributed sample set. For each generated sample, virtual measurements were collected at different time steps using a linearly incrementing displacement control. Then a gPCE model was trained using 150 random samples, while 50 were used for accuracy testing. The degree of the polynomial basis was optimized to achieve the best accuracy. The results of the sensitivity analysis, presented in Figure 4, confirm that the selected measurements effectively capture the influence of both elastic parameters.
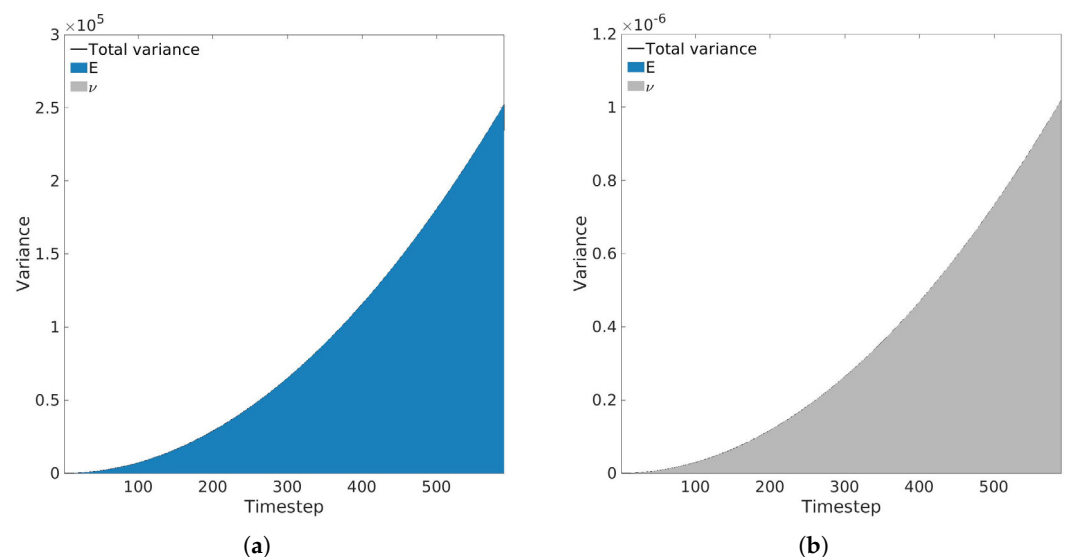

Figure 4. Sobol sensitivity analysis (rectangular specimen): Partial variances of (**a**) The force−displacement measurement (**b**) Lateral deformation measurement.

For the identification of the elastoplastic hardening and fracture parameters, the single−notched dog bone specimen is used (see Figure 3b). For this case, only a

force−displacement measurement was selected for the identification process. Following the same procedure as the elastic parameter identification, a set of 2000 combinations of parameters was generated using QMC sampling and a corresponding gPCE model was trained. The results, presented in Figure 5, show that force−displacement measurement is sufficient to capture the influences of the elastoplastic and fracture model parameters.
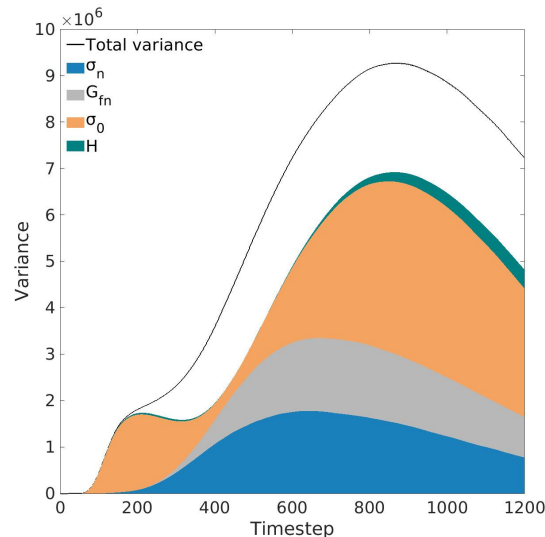

Figure 5. Sobol sensitivity (single−notched specimen): Partial variances of force due to changes in elastoplastic and fracture parameters (white area represents mixed modes influence).

4.2. Experimental Setup

Experimental investigations were conducted in the Structures Laboratory of FCEAG at the University of Split. Multiple measurement systems were used to obtain precise data on the physical properties of the test specimens (see Figure 6). The samples were fabricated from 6060 T4 aluminum alloy stock using a CNC milling machine, in accordance with the ISO 6892 standard. Additionally, some of the specimen was notched to induce stress concentration areas, as illustrated in Figure 3. Dimensional accuracy was verified prior to every test.

Specimens were loaded using a Shimadzu AGX-V 250 kN Universal Testing Machine (UTM), Shimadzu, Singapore. Strains were measured with an SIE extensometer and a crossbar positional sensor; both devices are classified as accuracy class 0.5. Forces were recorded using a load cell (nominal capacity 250 kN, accuracy class 0.5). Testing was performed under displacement control of the upper jaw at a constant speed of 2 mm/min, chosen to match the strain rate from ISO 6892. The termination condition was defined as a 10% drop in subsequent force, and data were sampled at 100 Hz.

To determine Poisson's ratio, additional sensors and measurement systems were utilized. Longitudinal and transverse strains were measured using LVDT sensors (HBM WA-L, 0–10 mm nominal range). A custom made 3D-printed jig, manufactured from ABS plastic on a BambuLab X1Carbon desktop 3D printer, was used to hold the sensors orthogonally and maintain attachment to the sample during loading. The testing regime for measuring Poisson's ratio was limited to the elastic deformation region and cycled five times before data collection to ensure the positional stability of all components in the measurement chain. The LVDT sensors were connected to an HBM Quantum MX840B universal amplifier, which acquired data independently of the UTM. To synchronize the two data sources (the UTM and the MX840B), analog signals representing crossbar displacement and force were recorded by the MX840B.

In addition to the mechanical measurements, an optical measurement system was employed. An industrial camera (2560 × 1440 pixels) was positioned with its imaging plane parallel to the specimen plane and configured to capture an image every 0.5 s. It was synchronized with the data acquisition software so that crossbar displacement and force values were recorded for each frame. The camera used a varifocal lens (5–50 mm) with a maximum aperture of f/1.6. Captured images were undistorted to remove radial and tangential distortions using camera parameters obtained through a checkerboard calibration procedure; this step was repeated for every experimental setup to account for the variable zoom setting. Camera parameter determination and image undistortion were carried out in MATLAB (version 9.13.0, R2022b, The MathWorks Inc.: Natick, MA, USA, 2022).

A random speckle pattern was applied to the samples to facilitate Digital Image Correlation (DIC). The DIC analysis was performed using the open-source software [64], implemented in the MATLAB environment [65].

To assess the accuracy of the DIC system, a calibration run was carried out. Before each tensile test, the specimen was translated through the camera's field of view using the UTM crossbar. The sample was held only by the upper jaw, leaving the lower end free. The position of the sample was recorded using the MX840B amplifier. Analysis of the calibration run revealed displacement accuracy and apparent strain values related to lens irregularities, specimen preparation, and DIC limitations. The root-mean-square error in displacement was 0.1 mm, and the strain noise was below 1×10^{-3}, primarily due to camera limitations (and to a lesser extent, specimen preparation and inherent DIC constraints). Nevertheless, the DIC data were qualitatively accurate in capturing the expected strain distributions near critical stress zones.
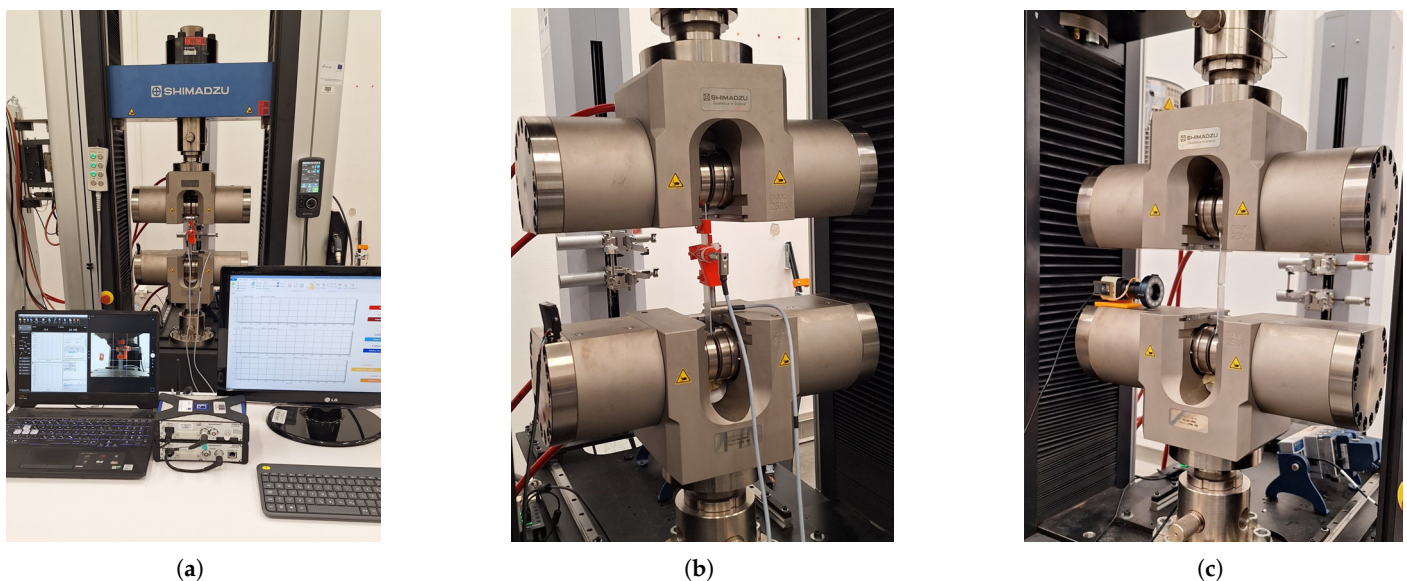

<div align="center">(a)   (b)   (c)</div>

Figure 6. Laboratory setup: (**a**) Measurement equipment (**b**) UTM machine and LVDT sensors (**c**) UTM machine and optical measurement system.

A summary of the identification procedures for elastic, elastoplastic, and fracture parameters—along with details on specimen types, measurement methods, and equipment used—is provided in Table 2.

Table 2. Identification of elastic, elastoplastic, and fracture parameters.

Parameter	Specimen	Measurement	Equipment
E	Rectangular	Force−displacement	UTM
ν	Rectangular	Lateral deformation	LVDT
$\sigma_0, H, \sigma_n, G_{fn}$	Single−notched	Force−displacement	UTM

5. Results

This section presents the results of the Bayesian identification process for the uncertain parameters of aluminum 6060 alloy specimens. The identification was performed using experimental measurements in conjunction with a trained generalized Polynomial Chaos Expansion (gPCE) proxy model, developed from virtual test data, and a Markov Chain Monte Carlo (MCMC) analysis within a Bayesian framework. The numerical simulations were implemented within the FEAP finite element framework [66], while the gPCE model training and MCMC sampling were carried out using the open-source library SGLIB [67].

To ensure consistency with the experimental setup, the virtual tests used for training the proxy model were designed to replicate the same boundary conditions and loading rates. Virtual measurements were gathered from a timestep-based simulation, where each timestep represents every tenth data point collected by the measurement equipment. This discretization yields 590 timesteps for measurement regarding the identification of the elastic parameters and 1200 timesteps for the elastoplastic and fracture ones. All virtual test simulations were executed on a high-performance cluster computer, which is capable of running 400 parallel computations.

5.1. Identification of Elastic Parameters

The identification process begins with the training of a proxy model to ensure a fast yet precise approximation of virtual test results of the numerical model. To train the gPCE proxy model, a dataset of 800 parameter combinations was generated from the prior distribution using QMC sampling, with an additional set of 200 for accuracy testing. The computation of the results for this parameter sample by cluster computer took around 5 min to complete. Training the optimal gPCE model involves solving Equation (20) and selecting the polynomial degree that minimizes the error metrics between the proxy model and the generated test sample results from the numerical model. In this work, the mean Maximum Absolute Error (MAE) averaged over the timestep domain is used. A fourth-degree polynomial with 15 coefficients per timestep was found to provide the best fit.

With the trained proxy model, the next step is to define the error distributions. First, we consider the measurement error distribution. For the force–displacement data, the standard deviation σ_i is set to 0.167% of the measured value. This is based on the maximum error specified by the UTM machine (class 0.5), assuming the maximum error represents 3σ under a normal distribution. For the lateral deformation measurements, the standard deviation is determined in the same way using the error specified by the LDTV manufacturer (class 0.5), and is also set to 0.167% of the measured value. Additionally, a constant component of 0.0001 mm is included to account for other sources of noise, such as those originating from the measuring circuitry, thermal fluctuations, and similar effects, which manifest as spikes due to the small magnitude of measured values (see Figure 7b).Since the identification of elastic parameters focuses on the material's linear elastic behavior, modeling errors are not considered at this stage. The constitutive law used in the numerical model is sufficiently accurate for this purpose. The standard deviation of the proxy model error is defined based on the differences between the predictions of the trained gPCE model

and the results obtained from 200 independent testing samples. These error distributions, along with the collected laboratory measurements, are presented in Figure 7. Here, only the measurement errors are visible, as the proxy model errors are very small due to the linear nature of the problem.
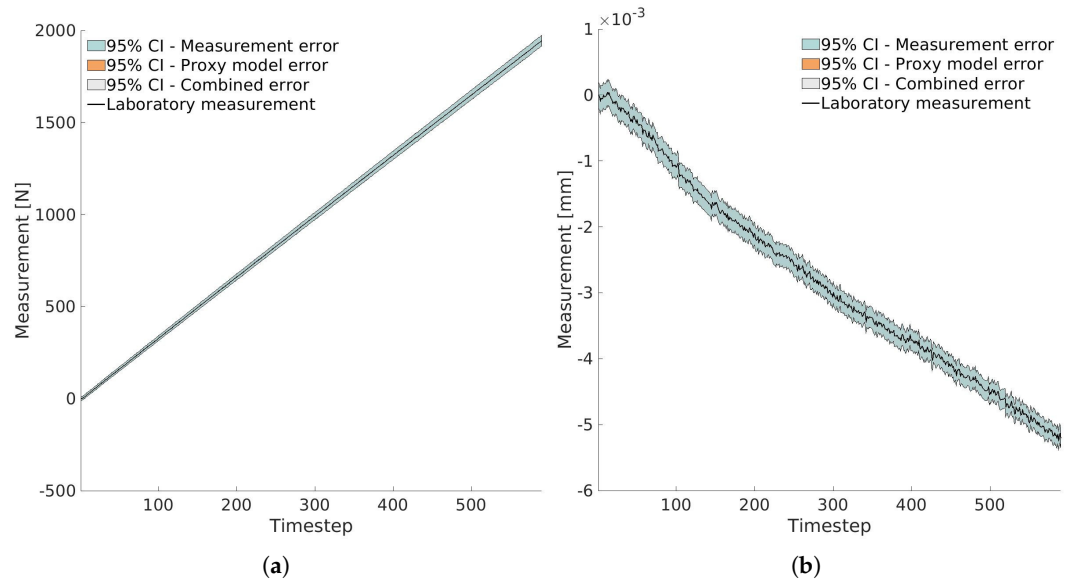

Figure 7. Identification of elastic parameters−95% CI error distributions (rectangular specimen): (**a**) Measurement of force−displacement measurement (**b**) Lateral deformation measurement.

The MCMC analysis is conducted using 100 Markov chains and 500 simulation steps, totaling 50,000 computed results for the combinations of the elastic parameters. The entire analysis was completed in less than a minute. The results of the identification are shown in Figure 8. The results shows a successful identification of both elastic parameters, as their posterior distributions have minimal variation, which ensures a high degree of certainty. The maximum a-posterior (MAP) value—the point estimate of the parameter, maximizing the posterior distribution—for Young's modulus E is 66,542 N/mm^2, while the Poisson's ratio ν is 0.319. These values are considered certain and are used as constants in the next phase of the identification.
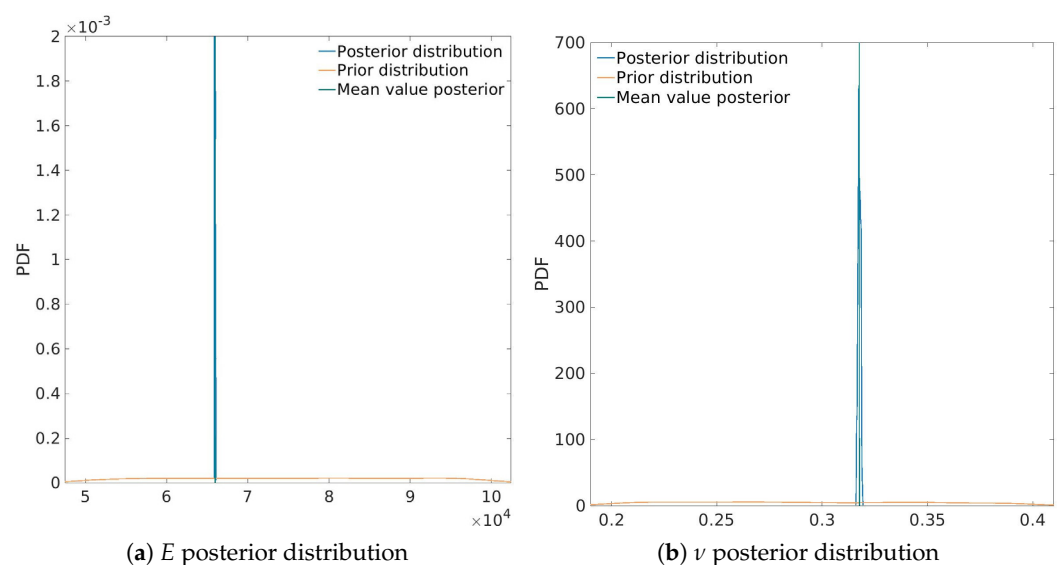

Figure 8. Identification of Young's modulus E and Poisson ratio ν parameters.

5.2. Identification of Elastoplastic and Fracture Parameters

This phase of the identification process involves the elastoplastic hardening of the material, the development of microcracks, the formation of the macrocrack, and finally, the material failure. These processes result in complex datasets that are much more challenging to interpret compared to elastic parameters, resulting in significantly higher computational effort needed.

To train the gPCE model, 20,000 samples were generated from the prior distributions using QMC sampling, with an additional 5000 samples used for testing. These computations performed on a cluster computer required approximately 70 h to complete. After validation and testing, a ninth-degree polynomial gPCE with 715 coefficients per timestep was found to provide the most accurate results.

Regarding the definition of the error distributions, the standard deviation of the measurement error σ_i was set to 0.167% of the measured value. The modeling error is defined by comparing the laboratory measurements with the results from the numerical model, based on knowledge of the constitutive laws used. Here, we divide the modeling error into two parts. The first part relates to the linear elastic and elastoplastic hardening behavior, as well as the onset of microcrack formation. For this part, a standard deviation of $\sigma_i = 25$ N is chosen. This value is selected because the numerical model produces identical outputs for the same input parameters, whereas real materials exhibit inherent variations. Since the elastic parameters were fixed in the previous phase and by considering the small influence of the nonlinear behavior of microcracks, this error distribution is selected to cover potential variations. The second part of the modeling error relates to the merging of microcracks, the formation of macrocracks, and the final material failure. In the numerical model, energy dissipation is represented by an exponential softening law. However, this is only an approximation of a highly nonlinear real-world phenomenon. Given the potential for larger variations when sudden material failure occurs, the error distribution for this part is set to be significantly larger, with $\sigma_i = 100$ N. Finally, the proxy model error is determined by comparing its predictions for the testing samples with the results from the numerical model. These error distributions, along with laboratory measurements, are presented in Figure 9.
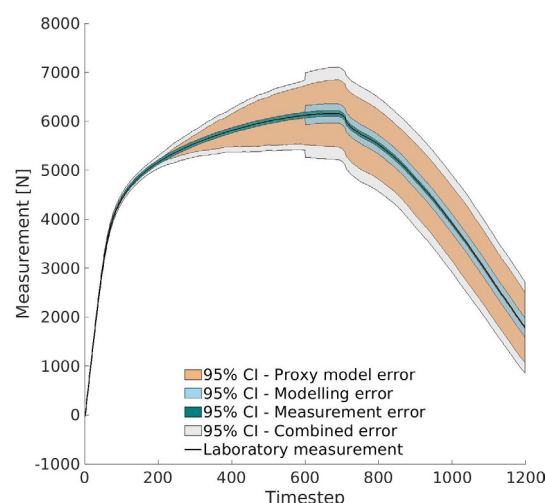

Figure 9. Identification of elastoplastic and fracture parameters (single−notched specimen)−95% CI error distributions.

The biggest error comes from the proxy modeling. This is primarily due to the complex and nonlinear nature of the problem, for which we have a complex, nonsmooth response surface that is difficult to approximate. Because a wide range of prior distributions was

considered, the samples in the testing set exhibit substantial variation. At a given timestep, some samples remain in the linear elastic regime, others undergo elastoplastic hardening, some initiate cracking, and others may approach complete failure. Capturing such a diverse dataset is challenging for different proxy modeling techniques [49]. Therefore, when analyzing fracture propagation problems, it is inevitable that relatively larger errors will be encountered in proxy modeling. That is why it is important to include these errors inside the identification process through the error model to ensure that the uncertainty introduced by the proxy is properly reflected in the posterior distributions of the identified parameters.

One suggested strategy to reduce proxy modeling errors is to perform multiple iterations of the identification process for the same test. After the initial identification, the resulting posterior distributions can be broadened using a chosen uncertainty coefficient and then used as new prior distributions. These updated priors typically exhibit less variability, which simplifies the response surface and improves the quality of the proxy model in subsequent iterations. Additionally, ongoing developments in advanced proxy modeling, particularly in Physics-Informed Neural Networks (PINNs), offer promising prospects for further reducing these errors. However, a robust PINN framework capable of effectively handling embedded discontinuities in fracture mechanics has not yet been established.

The identification of elastoplastic and fracture parameters was performed using 200 Markov chains and 5000 computational steps, resulting in a total of 1,000,000 evaluations for different parameter combinations. The entire process took less than 10 min to complete. The results are presented in Figure 10.
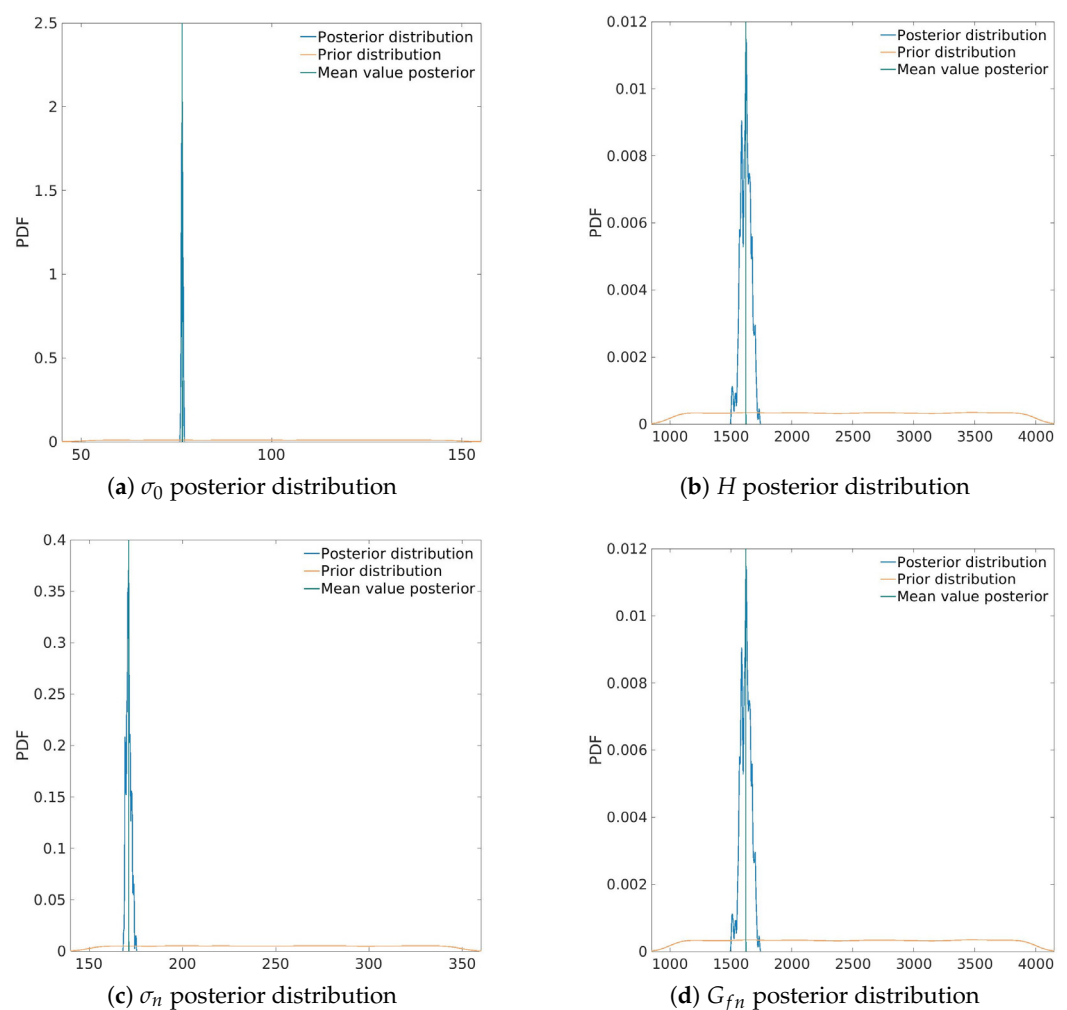

(a) σ_0 posterior distribution

(b) H posterior distribution

(c) σ_n posterior distribution

(d) G_{fn} posterior distribution

Figure 10. Identification of yield strength σ_0, hardening modulus H, tensile strength σ_n and tensile fracture energy G_{fn} parameters.

The posterior distribution of yield strength σ_0 exhibits minimal variation, indicating a high level of certainty, with a maximum posterior value of 76.52 N/mm^2. Similarly, the hardening modulus H shows only slight variation around its maximum posterior value of 1626.01 N/mm^2. The posterior distribution of tensile strength σ_n also demonstrates high certainty, with a well-defined peak at 171.11 N/mm^2. Finally, while the posterior distribution of tensile fracture energy G_{fn} shows slightly greater uncertainty compared to the other parameters, it still features a strong peak around its maximum posterior value of 258.17 N/mm.

These maximum posterior values were used in both the proxy model and the full numerical model to compare against the experimental data. The comparison is presented in Figure 11. As shown, the proxy model closely follows the lab measurements throughout the test, with only small deviations (with a maximum error of 2%). The numerical model also aligns very well with the experimental results, particularly in the elastic and elastoplastic regions, which confirms the accuracy of the identification process. A slight discrepancy emerges after the onset of fracture, mainly due to differences between the proxy model and the numerical simulation results (see Figure 9). The maximum error between the laboratory measurement and the numerical model is 8.9%. Nevertheless, the accuracy remains good, especially considering the challenges of modeling nonlinear fracture behavior.
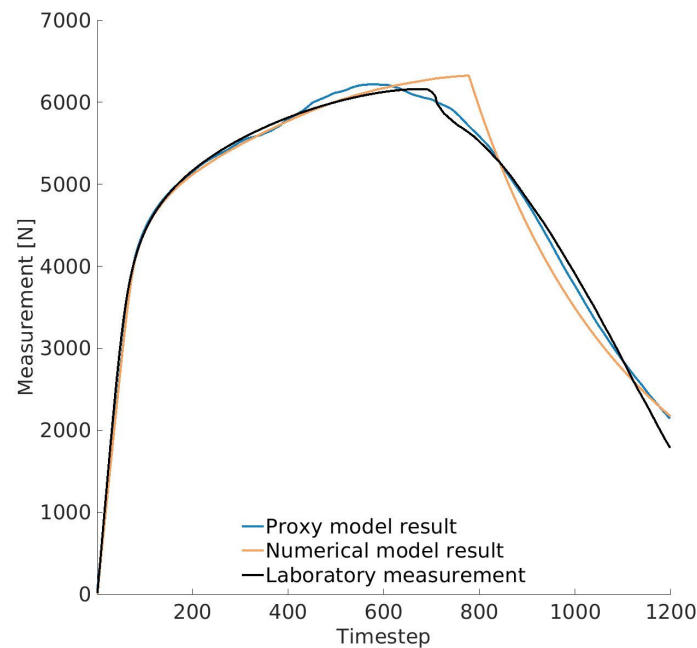

Figure 11. Comparison of the force−displacement results (single−notched specimen): Laboratory measurement vs. proxy model result vs. numerical model result.

Figure 12 shows a comparison of specimen failure observed in the laboratory tests and in the numerical simulations. For the simulation results, cracks are visualized using a color scale ranging from blue to orange, representing the level of energy dissipation, where blue indicates lower values and orange higher ones. For the single−notched dogbone specimen, both the experimental and numerical results (see Figure 12a,b) confirm the formation of a single dominant crack. This crack initiates at the edge of the notch and propagates toward the end of the specimen perpendicular to the direction of the loading. This confirms that the model accurately captured the failure mechanism.
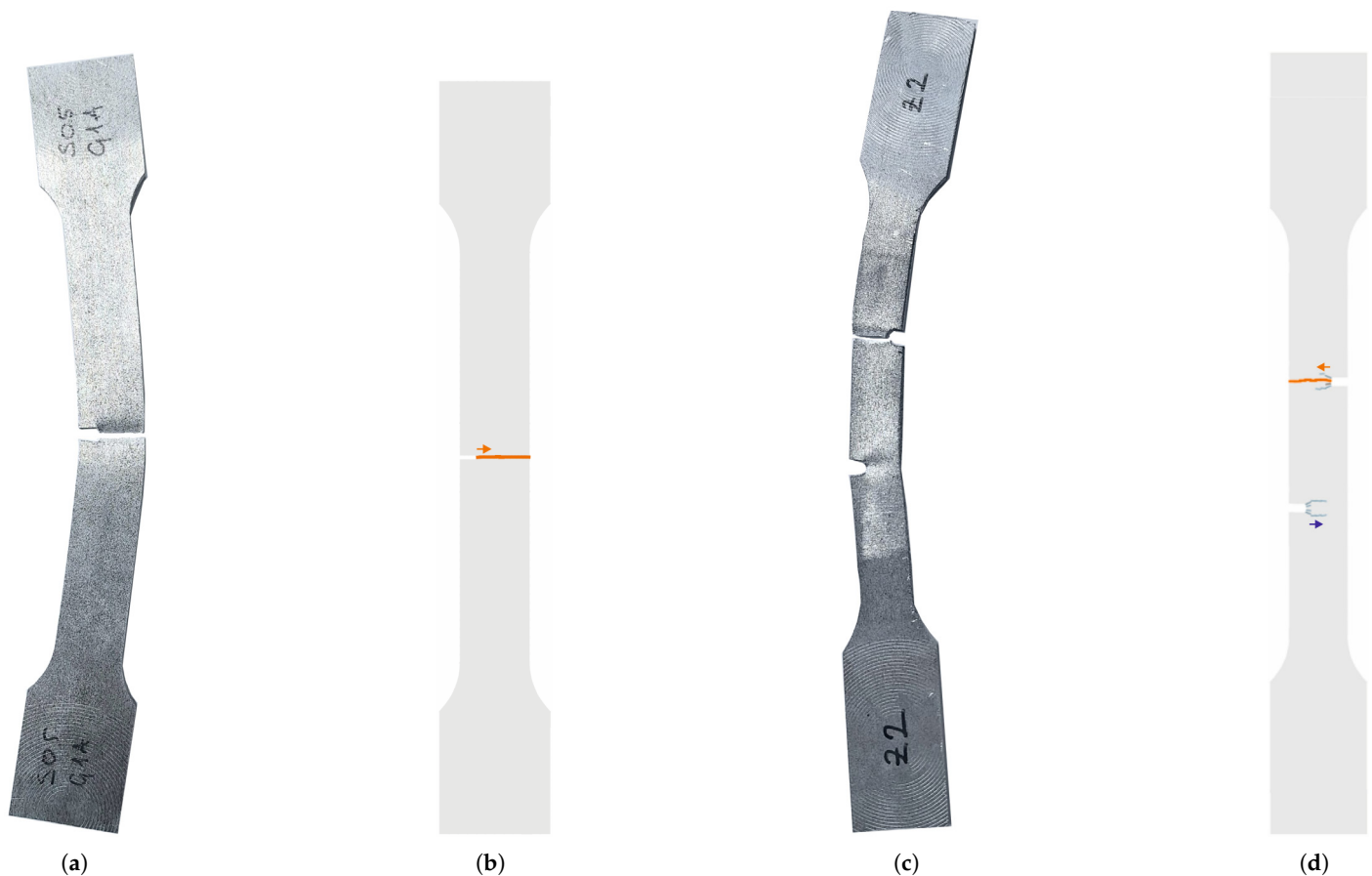
Figure 12. Comparison of the failure mechanism for the notched dogbone specimens: (**a**) Failure of the single−notched specimen in laboratory (**b**) Failure of the single−notched specimen in numerical simulation (**c**) Failure of the double−notched specimen in laboratory (**d**) Failure of the double−notched specimen in numerical simulation. Colored arrows indicate crack propagation directions.

5.3. Result Verification

The verification of the identified elastic, elastoplastic, and fracture parameters was carried out for two cases by comparing the numerical model results using the MAP estimate of the parameters with two distinct sets of experimental data. The first case involved a comparison of displacements and strain field values on a single−notched dogbone specimen, with data obtained by DIC camera. The second verification used force−displacement data from a double−notched dogbone specimen (see Figure 3c). This approach allowed for validation not only against different types of measurements from the specimen used for identification but also against specimens with different geometries (see Table 3).

For each verification case, 20 samples were generated from the posterior parameter distributions using QMC sampling. These parameter sets were then used in simulations, and the resulting outputs were compared with experimental data to evaluate the accuracy and robustness of the identification methodology.

Table 3. Verification process of elastic, elastoplastic, and fracture parameters through comparison of laboratory measurements and numerical model predictions (two verification cases) [1].

Parameter	Specimen	Measurement
$\sigma_0, H, \sigma_n, G_{fn}$	single$-$notched	Vertical displacements and strain fields (DIC)
$\sigma_0, H, \sigma_n, G_{fn}$	double$-$notched	Force–displacement (UTM)

[1] Accuracy of the identified elastic parameter values (E, ν) was confirmed by matching of numerical model results with experimental measurements in the linear elastic region of force$-$displacement measurements for the single-notch and double-notch specimens.

For the first verification case, two points on the specimen were selected: (12 mm, 100 mm) and (12 mm, 120 mm). These points were located on opposite sides of the crack. The vertical displacement difference between these points was extracted from DIC measurements and compared with numerical results, as shown in Figure 13. The results reveal some differences between the numerical and DIC data. The largest discrepancy appears at the beginning of the test, mainly due to the difficulty of DIC systems in capturing very small displacement values accurately. As the test progresses and displacements become larger, the measurements from DIC become more reliable. In the middle of the test, where the measured values are higher, the DIC measurements become more reliable. At this stage, the observed differences are largely attributed to the same sources of error noted in the force$-$displacement comparison, particularly those arising from the proxy model. The maximum error between the DIC measurements and the numerical model is 11.9%. Toward the end of the test, these differences continue to decrease, resulting in an increasingly close match between the numerical predictions and the DIC data.
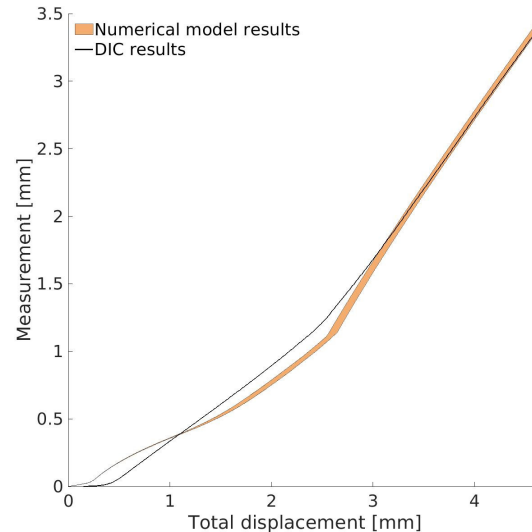
Figure 13. Comparison of the vertical displacement difference between two points (single$-$notched specimen): DIC measurements vs. numerical model results using 20 samples of parameter values drawn from the posterior distribution.

Additionally, a comparison of strain field values was performed for a total displacement of 3.899 mm. The strain components were computed from the displacement gradients using standard DIC post-processing methods. This comparison also showed very good agreement between the two results, both in the shape of the strain fields and the magnitude of the strain values (see Figure 14).
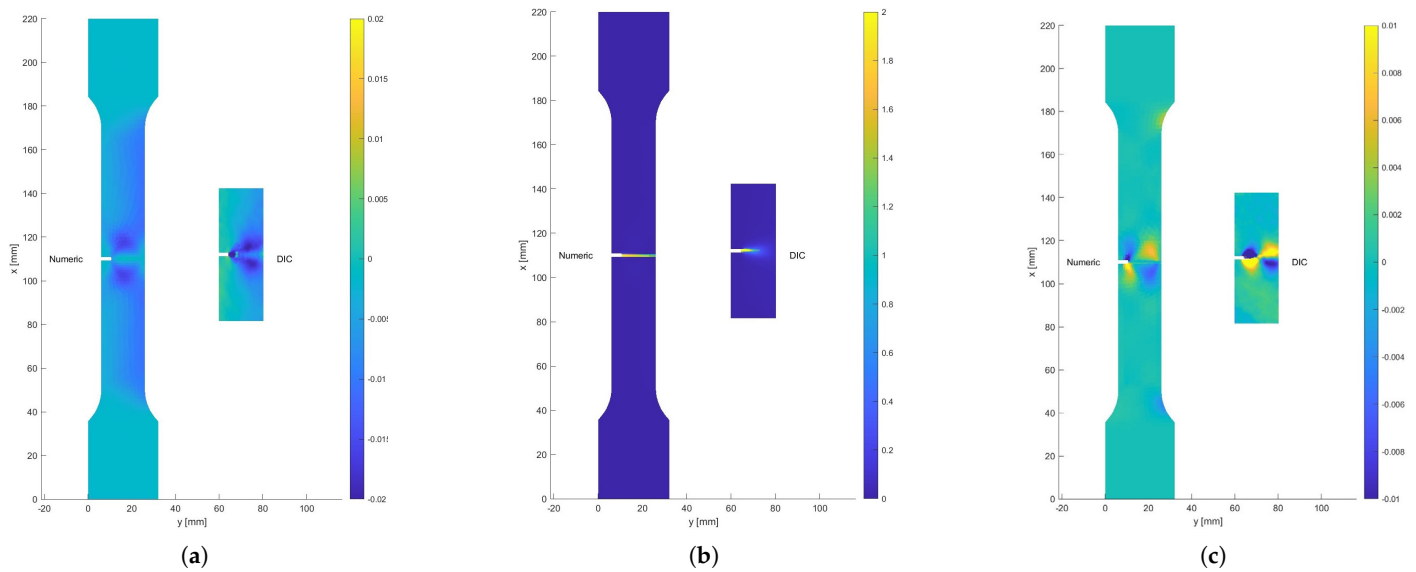
Figure 14. Comparison of strain field components between the numerical model and DIC measurements at a displacement of 3.899 mm (single−notched specimen): (**a**) ϵ_{xx} field values (**b**) ϵ_{yy} field values (**c**) ϵ_{xy} field values. Strain localization patterns and magnitudes with both methods capturing similar regions of high strain concentration.

The second verification case was conducted by comparing the force−displacement results from the laboratory with numerical simulation results. This specimen had a different geometry and featured two notches of different sizes, which led to a stress distribution and failure mode different from the ones used for parameter identification. Despite these differences, the comparison shown in Figure 15 demonstrates that the numerical model performed with high accuracy. The elastic and elastoplastic regions were matched almost perfectly. Some discrepancies appeared in the fracture region, similar to what was observed in previous comparisons, with the maximum error reaching 7.8%. These results further support the reliability of the identified parameters, even when the fracture mechanism is different.
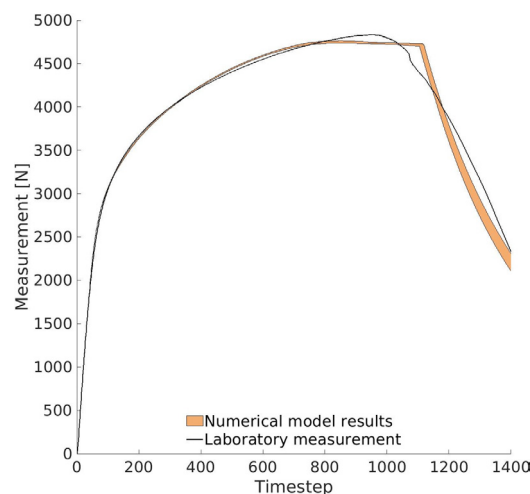

Figure 15. Comparison of the force−displacement measurement (double−notched specimen): Laboratory measurements vs. numerical model.

A comparison of the failure behavior of the double−notched specimen in both the laboratory and numerical simulation (see Figure 12c,d) shows similar fracture mechanisms. In the laboratory, a macrocrack formed at the upper notch, leading to complete failure, with additional damage observed around the lower notch. The numerical model result

follows the same pattern, with a main macrocrack forming from the upper notch, causing total failure. Additionally, due to the wider notches, the formation of several microcracks is visible alongside the macrocrack, though they contribute little to energy dissipation. For the lower notch, a few microcracks are also seen, but they do not significantly dissipate energy, which matches the laboratory results, where only limited damage is visible.

6. Conclusions

This work demonstrates the potential of the Bayesian approach for solving the inverse problem of material parameter identification, specifically applied to the failure behavior of aluminum 6060 alloy specimens.

Within the applied methodology, a numerical model based on the embedded discontinuity method (Q6ED) is used, in which cracks are modeled locally with their own location and orientation. This allows for realistic and mesh-independent fracture results.

To achieve a computationally efficient approach, a generalized polynomial chaos expansion (gPCE) was used as a proxy model. This approach has already proven to be efficient and accurate for simpler fracture cases, while also supporting straightforward sensitivity analysis, which is valuable for both test design and understanding parameter influence. However, gPCE introduces approximation errors that must be carefully controlled across the entire response surface. If not adequately managed, these errors can bias the identification process by overfitting regions with lower proxy error, thereby compromising the accuracy of the identified parameters.

The experimental setup involved tensile testing using a universal testing machine (UTM), with deformation monitored through simple yet effective measurements, including internal UTM sensors (force, crossbar position, and extensometers), LVDT sensors with an additional data acquisition unit, and an optical measurement system. Unlike standard laboratory specimens, the aluminum samples in this study were intentionally designed with notches to induce stress concentrations, which makes them non-standard and typically unsuitable for direct parameter extraction from test data alone.

A key aspect of the Bayesian method is the definition of the error model. In this study, measurement error, modeling error, and proxy model error were assumed to be mutually independent and normally distributed with zero mean. While this assumption is widely used due to its simplicity and analytical convenience, it may not always hold, particularly in the context of nonlinear fracture mechanics. In this work, the assumption of unbiased and uncorrelated measurement errors was considered reasonable due to reliable calibration and stable testing conditions. In contrast, modeling and proxy errors are inherently more complex. They may exhibit correlation, systematic bias, or non-Gaussian behavior, especially near crack initiation. Nevertheless, the error analysis for non-linear data showed that the impact of such limitations was limited. Consequently, the adopted simplifications were deemed justified and did not significantly compromise the validity of the results within the scope of this study.

The Bayesian inversion process successfully provided credible posterior values for key parameters across all behavioral phases: elastic (Young's modulus E, Poisson's ratio ν), elastoplastic (yield strength σ_0, hardening modulus H), and fracture parameters (tensile strength σ_n, tensile fracture energy G_{fn}). The resulting posterior distributions show limited variability, highlighting the robustness of the Bayesian methodology and the effectiveness of the integrated numerical and experimental framework. However, this level of certainty may not be achieved with different numerical models or experimental conditions. This highlights the importance of applying probabilistic methods for nonlinear and non-standard measurements over deterministic approaches, as they provide a means to quantify uncertainty, which is essential for the reliability and interpretability of the results.

The identified elastic parameters from the rectangular specimen were shown to be applicable to all the subsequently tested specimens. The maximum a posteriori (MAP) values of the elastoplastic and fracture parameters, obtained from the single−notched specimen, were validated through comparisons with independent measurement data and additional results from the double−notched specimen. These comparisons demonstrated a strong agreement with the experimental observations, further confirming the robustness and reliability of the identified parameters within the scope of the conducted tests. However, confirming the broader applicability of the methodology will require further validation through more diverse specimen geometries and multiaxial loading scenarios.

It is important to recognize that the identified parameters are not purely material constants in the classical sense, but are model-dependent. While elastic parameters E and ν, as well as σ_0 and σ_n may closely reflect intrinsic material properties, hardening modulus H and tensile fracture energy G_{fn} are the parameters calibrated for the specific numerical model applied in the identification process. In this case, isotropic linear hardening and exponential softening were assumed to approximate the complex plastic and failure behavior, respectively. Therefore, while the results support the robustness of the Bayesian approach even with non-standard specimens, the interpretation of the identified parameters should always consider the modeling framework used.

Finally, the demonstrated methodology shows strong potential when complemented with experimental investigations, offering the ability to identify multiple parameters from a single test, even under suboptimal sample geometry. As a part of future work, we aim to refine the error modeling by explicitly accounting for correlations in proxy and modeling errors. Additionally, broader experimental validation will be necessary to confirm the generalizability of the approach. With further development and testing, this framework could be extended to a wide range of engineering applications, particularly where standard specimens are unavailable or full-scale testing is impractical.

Institutional Review Board Statement: Not applicable.

Informed Consent Statement: Not applicable.

Data Availability Statement: The data presented in this study are available on request from the corresponding author. The data are not publicly available due to dependency on our software implementation.

Conflicts of Interest: The authors declare no conflicts of interest.

References

1. Ibrahimbegovic, A. *Nonlinear Solid Mechanics*; Springer: Berlin/Heidelberg, Germany, 2009; Volume 160. [CrossRef]
2. Xu, A.; Fang, G.; Zhuang, L.; Gu, C. A multivariate student-t process model for dependent tail-weighted degradation data. *IISE Trans.* **2024**, 1–17. [CrossRef]
3. Fei, C.W.; Han, Y.J.; Wen, J.R.; Li, C.; Han, L.; Choy, Y.S. Deep learning-based modeling method for probabilistic LCF life prediction of turbine blisk. *Propuls. Power Res.* **2024**, *13*, 12–25. [CrossRef]
4. Xu, A.; Wang, R.; Weng, X.; Wu, Q.; Zhuang, L. Strategic integration of adaptive sampling and ensemble techniques in federated learning for aircraft engine remaining useful life prediction. *Appl. Soft Comput.* **2025**, *175*, 113067. [CrossRef]
5. Fei, C.W.; Li, C.; Lin, J.Y.; Han, Y.J.; Choy, Y.S.; Chen, C.H. Structural design of aeroengine radiators: State of the art and perspectives. *Propuls. Power Res.* **2024**, *13*, 319–334. [CrossRef]
6. Kennedy, M.C.; O'Hagan, A. Bayesian Calibration of Computer Models. *J. R. Stat. Soc. Ser. B Stat. Methodol.* **2002**, *63*, 425–464. [CrossRef]
7. Azad, M.S.; Eum, D.M.; Moriguchi, S.; Han, T.S. A Short Review on the Application of Bayesian Updating of the Mechanical Property Evaluation on Cementitious Materials. *Multiscale Sci. Eng.* **2024**. [CrossRef]
8. Brocks, W.; Scheider, I. Identification of material parameters for structural analyses. *Struct. Durab. Health Monit.* **2010**, *6*, 189–212.
9. Matthies, H.G.; Zander, E.; Rosić, B.V.; Litvinenko, A.; Pajonk, O. Inverse Problems in a Bayesian Setting. In *Computational Methods for Solids and Fluids: Multiscale Analysis, Probability Aspects and Model Reduction*; Springer International Publishing: Berlin/Heidelberg, Germany, 2016; pp. 245–286. [CrossRef]
10. Stanić, A.; Brank, B.; Ibrahimbegovic, A.; Matthies, H. Crack propagation simulation without crack tracking algorithm: Embedded discontinuity formulation with incompatible modes. *Comput. Methods Appl. Mech. Eng.* **2021**, *386*, 114090. [CrossRef]
11. Šodan, M.; Stanic, A.; Nikolić, M. Enhanced solid element model with embedded strong discontinuity for representation of mesoscale quasi-brittle failure. *Int. J. Fract.* **2024**, *248*, 1–25. [CrossRef]
12. Lee, J.; Lopez, M.M. An Experimental Study on Fracture Energy of Plain Concrete. *Int. J. Concr. Struct. Mater.* **2014**, *8*, 129–139. [CrossRef]
13. Markiewicz, E.; Langrand, B. Characterisation and Parameters Identification of Materials Constitutive and Damage Models: From Normalised Direct Approach to Most Advanced Inverse Problem Resolution. *Procedia Eng.* **2017**, *173*, 33–40. [CrossRef]
14. Ruifeng, X.; Xueyong, X.; Jianlin, Y. Experimental and numerical investigation of fracture behavior of ultra high performance concrete. *J. Mater. Res. Technol.* **2023**, *25*, 3109–3119. [CrossRef]
15. Rhee, I.; Lee, J.S.; Roh, Y.S. Fracture Parameters of Cement Mortar with Different Structural Dimensions Under the Direct Tension Test. *Materials* **2019**, *12*, 1850. [CrossRef] [PubMed]
16. van Mier, J.; van Vliet, M. Uniaxial tension test for the determination of fracture parameters of concrete: State of the art. *Eng. Fract. Mech.* **2002**, *69*, 235–247. [CrossRef]
17. Alkam, F.; Pereira, I.; Lahmer, T. Qualitatively-improved identified parameters of prestressed concrete catenary poles using sensitivity-based Bayesian approach. *Results Eng.* **2020**, *6*, 100104. [CrossRef]
18. Conde, B.; Eguía, P.; Stavroulakis, G.; Granada, E. Parameteridentificationmasonryarchbridges. *Eng. Struct.* **2018**, *172*, 275–284. [CrossRef]
19. Marsili, F.; Friedman, N.; Croce, P.; Formichi, P.; Landi, F. On Bayesian Identification Methods for the Analysis of Existing Structures. In Proceedings of the 2016 IABSE Congress: Challenges in Design and Construction of an Innovative and Sustainable Built Environment, Stockholm, Sweden, 21–23 September 2016; pp. 116–123. [CrossRef]
20. Cornaggia, A.; Cocchetti, G.; Maier, G.; Buljak, V. Inverse Structural Analyses on Small Punch Tests, with Model Reduction and Stochastic Approach. In Proceedings of the 2018 International Conference on Environment and Electrical Engineering (EEEIC), Palermo, Italy, 12–15 June 2018; pp. 1–5. [CrossRef]
21. Buljak, V.; Cocchetti, G.; Cornaggia, A.; Maier, G. Parameter identification in elastoplastic material models by Small Punch Tests and inverse analysis with model reduction. *Meccanica* **2018**, *53*, 3815–3829. [CrossRef]
22. Buljak, V.; Cocchetti, G.; Cornaggia, A.; Maier, G. Estimation of residual stresses by inverse analysis based on experimental data from sample removal for "small punch" tests. *Eng. Struct.* **2017**, *136*, 77–86. [CrossRef]
23. Kurent, B.; Friedman, N.; Ao, W.K.; Brank, B. Bayesian updating of tall timber building model using modal data. *Eng. Struct.* **2022**, *266*, 114570. [CrossRef]
24. Ceravolo, R.; Faraci, A.; Miraglia, G. Bayesian Calibration of Hysteretic Parameters with Consideration of the Model Discrepancy for Use in Seismic Structural Health Monitoring. *Appl. Sci.* **2020**, *10*, 5813. [CrossRef]
25. Rappel, H.; Beex, L.A.A.; Hale, J.S.; Noels, L.; Bordas, S.P.A. A Tutorial on Bayesian Inference to Identify Material Parameters in Solid Mechanics. *Arch Comput. Methods* **2020**, *27*, 361–385. [CrossRef]
26. Moës, N.; Belytschko, T. Extended finite element method for cohesive crack growth. *Eng. Fract. Mech.* **2002**, *69*, 813–833. [CrossRef]

27. Oliver, J.; Huespe, A.; Sánchez, P. A comparative study on finite elements for capturing strong discontinuities: E-FEM vs X-FEM. *Comput. Methods Appl. Mech. Eng.* **2006**, *195*, 4732–4752. [CrossRef]

28. Linder, C.; Armero, F. Finite elements with embedded strong discontinuities for the modeling of failure in solids. *Int. J. Numer. Methods Eng.* **2007**, *72*, 1391–1433. [CrossRef]

29. Brancherie, D.; Ibrahimbegovic, A. Novel anisotropic continuum-discrete damage model capable of representing localized failure of massive structures: Part I: Theoretical formulation and numerical implementation. *Eng. Comput.* **2009**, *26*, 100–127. [CrossRef]

30. Li, X.; Xu, Y. Phase field modeling scheme with mesostructure for crack propagation in concrete composite. *Int. J. Solids Struct.* **2022**, *234–235*, 111–259. [CrossRef]

31. Huang, Y.; jun Yang, Z.; Zhang, H.; Natarajan, S. A phase-field cohesive zone model integrated with cell-based smoothed finite element method for quasi-brittle fracture simulations of concrete at mesoscale. *Comput. Methods Appl. Mech. Eng.* **2022**, *396*, 115074. [CrossRef]

32. Nikolic, M.; Karavelić, E.; Ibrahimbegovic, A.; Miščević, P. Lattice Element Models and Their Peculiarities. *Arch. Comput. Methods Eng.* **2018**, *25*, 753–784. [CrossRef]

33. Nikolic, M.; Ibrahimbegovic, A. Rock mechanics model capable of representing initial heterogeneities and full set of 3D failure mechanisms. *Comput. Methods Appl. Mech. Eng.* **2015**, *290*, 209–227. [CrossRef]

34. Čarija, J.; Marenić, E.; Jarak, T.; Nikolić, M. Discrete Lattice Element Model for Fracture Propagation with Improved Elastic Response. *Appl. Sci.* **2024**, *14*, 1287. [CrossRef]

35. Rizvi, Z.; Nikolic, M.; Wuttke, F. Lattice element method for simulations of failure in bio-cemented sands. *Granul. Matter* **2019**, *21*, 18. [CrossRef]

36. Buljak, V.; Cocchetti, G.; Maier, G. Calibration of brittle fracture models by sharp indenters and inverse analysis. *Int. J. Fract.* **2013**, *184*, 123–136. [CrossRef]

37. Do, B.; Ohsaki, M. Bayesian optimization for inverse identification of cyclic constitutive law of structural steels from cyclic structural tests. *Structures* **2022**, *38*, 1079–1097. [CrossRef]

38. Jia, X.; Hou, W.; Papadimitriou, C. Hierarchical Bayesian modeling for uncertainty quantification and reliability updating using data. *J. Reliab. Sci. Eng.* **2025**, *1*, 025002. [CrossRef]

39. Wu, W.; Malik, M.; Cantero-Chinchilla, S.; Lawrie, T.; Yan, W.; Tanner, G.; Remenyte-Prescott, R.; Chronopoulos, D. Guided waves-based damage identification in plates through an inverse Bayesian process. *Ultrasonics* **2022**, *125*, 106773. [CrossRef]

40. Hernández-Montes, E.; Jalón, M.L.; Rodríguez-Romero, R.; Chiachío, J.; Compán-Cardiel, V.; Gil-Martín, L.M. Bayesian structural parameter identification from ambient vibration in cultural heritage buildings: The case of the San Jerónimo monastery in Granada, Spain. *Eng. Struct.* **2023**, *284*, 115924. [CrossRef]

41. Sevieri, G.; Andreini, M.; De Falco, A.; Matthies, H.G. Concrete gravity dams model parameters updating using static measurements. *Eng. Struct.* **2019**, *196*, 109231. [CrossRef]

42. Sevieri, G.; Falco, A.D. Dynamic structural health monitoring for concrete gravity dams based on the Bayesian inference. *J. Civ. Struct. Health Monit.* **2020**, *10*, 235–250. [CrossRef]

43. Dobrilla, S.; Matthies, H.G.; Ibrahimbegovic, A. Considerations on the identifiability of fracture and bond properties of reinforced concrete. *Int. J. Numer. Methods Eng.* **2023**, *124*, 3662–3686. [CrossRef]

44. Dobrilla, S.; Lunardelli, M.; Nikolić, M.; Lowke, D.; Rosić, B. Bayesian inference of mesoscale mechanical properties of mortar using experimental data from a double shear test. *Comput. Methods Appl. Mech. Eng.* **2023**, *409*, 115964. [CrossRef]

45. Janouchová, E.; Kučerová, A.; Sýkora, J.; Vorel, J.; Wan-Wendner, R. Robust probabilistic calibration of a stochastic lattice discrete particle model for concrete. *Eng. Struct.* **2021**, *236*, 112000. [CrossRef]

46. Wu, T.; Rosić, B.V.; Lorenzis, L.D.; Matthies, H.G. Parameter identification for phase-field modeling of fracture: A Bayesian approach with sampling-free update. *Comput. Mech.* **2020**, *67*, 435–453. [CrossRef]

47. Noii, N.; Khodadadian, A.; Ulloa, J.; Aldakheel, F.; Wick, T.; François, S.; Wriggers, P. Bayesian inversion for unified ductile phase-field fracture. *Comput. Mech.* **2021**, *68*, 943–980. [CrossRef]

48. Jirásek, M. Comparative study on finite elements with embedded discontinuities. *Comput. Methods Appl. Mech. Eng.* **2000**, *188*, 307–330. [CrossRef]

49. Šodan, M.; Urbanics, A.; Friedman, N.; Stanic, A.; Nikolić, M. Comparison of Machine Learning and gPC-based proxy solutions for an efficient Bayesian identification of fracture parameters. *Comput. Methods Appl. Mech. Eng.* **2025**, *436*, 117686. [CrossRef]

50. Lye, A.; Cicirello, A.; Patelli, E. Sampling methods for solving Bayesian model updating problems: A tutorial. *Mech. Syst. Signal Process.* **2021**, *159*, 107760. [CrossRef]

51. Chiachio-Ruano, J.; Chiachio-Ruano, M.; Sankararaman, S. *Bayesian Inverse Problems: Fundamentals and Engineering Applications*, 1st ed.; CRC Press: Boca Raton, FL, USA, 2021; pp. 155–202. [CrossRef]

52. Hadwin, P.J.; Motie-Shirazi, M.; Erath, B.D.; Peterson, S.D. Bayesian Inference of Vocal Fold Material Properties from Glottal Area Waveforms Using a 2D Finite Element Model. *Appl. Sci.* **2019**, *9*, 2735. [CrossRef]

53. Xiu, D. *Numerical Methods for Stochastic Computations: A Spectral Method Approach*; Princeton University Press: Princeton, NJ, USA, 2010. [CrossRef]

54. Goodfellow, I.; Bengio, Y.; Courville, A. *Deep Learning*; MIT Press: Cambridge, MA, USA, 2016.

55. Ramancha, M.K.; Vega, M.A.; Conte, J.P.; Todd, M.D.; Hu, Z. Bayesian model updating with finite element vs surrogate models: Application to a miter gate structural system. *Eng. Struct.* **2022**, *272*, 114901. [CrossRef]

56. Landi, F.; Marsili, F.; Friedman, N.; Croce, P. gPCE-Based Stochastic Inverse Methods: A Benchmark Study from a Civil Engineer's Perspective. *Infrastructures* **2021**, *6*, 158. [CrossRef]

57. Soize, C.; Ghanem, R. Physical Systems with Random Uncertainties: Chaos Representations with Arbitrary Probability Measure. *SIAM J. Sci. Comput.* **2004**, *26*, 395–410. [CrossRef]

58. Sanzida, N.; Nagy, Z.K. Polynomial Chaos Expansion (PCE) Based Surrogate Modeling and Optimization for Batch Crystallization Processes. In *Computer Aided Chemical Engineering*; Elsevier: Amsterdam, The Netherlands, 2014; Volume 33, pp. 565–570. [CrossRef]

59. Sudret, B. Global sensitivity analysis using polynomial chaos expansions. *Reliab. Eng. Syst. Saf.* **2008**, *93*, 964–979. [CrossRef]

60. Janouchová, E.; Kučerová, A. Competitive comparison of optimal designs of experiments for sampling-based sensitivity analysis. *Comput. Struct.* **2013**, *124*, 47–60. [CrossRef]

61. Saltelli, A. Making best use of model evaluations to compute sensitivity indices. *Comput. Phys. Commun.* **2002**, *145*, 280–297. [CrossRef]

62. Saltelli, A.; Annoni, P.; Azzini, I.; Campolongo, F.; Ratto, M.; Tarantola, S. Variance based sensitivity analysis of model output. Design and estimator for the total sensitivity index. *Comput. Phys. Commun.* **2010**, *181*, 259–270. [CrossRef]

63. Sobol, I. Global sensitivity indices for nonlinear mathematical models and their Monte Carlo estimates. *Math. Comput. Simul.* **2001**, *55*, 271–280. [CrossRef]

64. Blaber, J.; Adair, B.; Antoniou, A. Ncorr: Open-Source 2D Digital Image Correlation Matlab Software. *Exp. Mech.* **2015**, *55*, 1105–1122. [CrossRef]

65. MathWorks Inc. MATLAB R2021b. Available online: https://www.mathworks.com (accessed on 12 March 2025)

66. Taylor, R.D. FEAP-Finite Element Analysis Program. Available online: http://projects.ce.berkeley.edu/feap/ (accessed on 12 March 2025)

67. Zander, E. A Matlab/Octave Toolbox for Stochastic Galerkin Methods. Available online: https://ezander.github.io/sglib/ (accessed on 12 March 2025)

11. CURRICULUM VITAE

I was born on July 20, 1997, in Split, Croatia. I completed my secondary education at the III. Natural Science and Mathematics Gymnasium in Split. I earned my bachelor's degree in civil engineering in 2019 with a GPA of 4.21 (very good), defending a thesis titled "Selection and coordination of machine operation for selected construction works of a small airport." I continued my studies at the same faculty and completed my master's degree in 2021 with a GPA of 4.88 (excellent), defending the thesis "Analysis of masonry structures using the combined finite and discrete element method (FDEM)."

During my studies, I was demonstrator in several courses, including Probability and Statistics, Structural Statics 1 and 2, and Dynamic Models of Earthquake Engineering. For my academic performance, I was awarded two Dean's Awards and the Rector's Award for Excellence.

Since October 2021, I have been employed at FCEAG in Split as a research associate on the HRZZ project "Methodology for estimating parameters in problems of crack propagation caused by extreme mechanical loads." In June 2022, I enrolled in a Postgraduate Doctoral Study of Civil Engineering.

As part of my doctoral development, I participated in a number of international workshops and courses. In 2023, I attended the five-day "SEA-EU Training Event and Entrepreneurship Skills" workshop in Cádiz, Spain, which focused on creative thinking and communication. In 2024, I took part in the "64th ESReDA Seminar – Doctoral Workshop on Digital Twin" in Bilbao, Spain, where we explored digital surrogate modeling of real systems. The same year, I attended the "CEACM S4ML 2024 Conference Course," a two-day workshop focused on connecting numerical modeling with machine learning.

Through the Erasmus+ program, I completed two international training periods – one at the Czech Technical University in Prague, lasting 12 days, and another at the Institut National des Sciences Appliquées de Toulouse in France, lasting 10 days.

I have presented my research at several domestic and international scientific conferences, including the 10th International Congress of the Croatian Society of Mechanics (ICCSM 2022) in Pula, the 12th Meeting of the Croatian Society of Mechanics in Split in 2023, and the 6th International Conference on Multi-scale Computational Methods for Solids and Fluids in Sarajevo. In 2024, I also presented at the ECCOMAS Congress in Lisbon and the CEACM S4ML Conference in Prague, where I received the award for the best presentation by a young researcher.

My research is based in the Numerical Laboratory of FCEAG and focuses on the development of numerical models for analyzing material failure. This includes both theoretical work and programming using Fortran and Matlab. I have also developed stochastic parameter identification methods using Python and Matlab, worked with artificial intelligence models, and performed

computations on cluster computers. In addition, I have conducted experimental testing in the Laboratory for Constructions, where I helped in operating the UTM machine and other testing and measurement tools.

To date, I have published three scientific papers in international journals indexed in the Web of Science, all of which are in Q1 journals: International Journal of Fracture, Computer Methods in Applied Mechanics and Engineering (CMAME), and Applied Sciences, where I was the first author. I am currently working on two more papers, which are being prepared for submission to international journals. I have also contributed to ten international conference and other publications, six of which I authored as the first author.